



Design of innovative zero power reactor configurations for modeling coupling/decoupling phenomena : Application to kinetics transients

Korniliос Routsonis

► To cite this version:

Korniliос Routsonis. Design of innovative zero power reactor configurations for modeling coupling/decoupling phenomena: Application to kinetics transients. Génie civil nucléaire. Université Grenoble Alpes [2020-..], 2021. English. NNT: 2021GRALI049 . tel-03320762

HAL Id: tel-03320762

<https://theses.hal.science/tel-03320762>

Submitted on 16 Aug 2021

HAL is a multi-disciplinary open access archive for the deposit and dissemination of scientific research documents, whether they are published or not. The documents may come from teaching and research institutions in France or abroad, or from public or private research centers.

L'archive ouverte pluridisciplinaire **HAL**, est destinée au dépôt et à la diffusion de documents scientifiques de niveau recherche, publiés ou non, émanant des établissements d'enseignement et de recherche français ou étrangers, des laboratoires publics ou privés.



THÈSE

Pour obtenir le grade de

DOCTEUR DE L'UNIVERSITÉ GRENOBLE ALPES

Spécialité : MEP : Mécanique des fluides Energétique, Procédés

Arrêté ministériel : 25 mai 2016

Présentée par

Korniliос ROUTSONIS

Thèse dirigée par **Patrick BLAISE**, Directeur de Recherche et codirigée par **Jean TOMMASI**

préparée au sein du **Laboratoire CEA Cadarache** dans l'**École Doctorale I-MEP2 - Ingénierie - Matériaux, Mécanique, Environnement, Energétique, Procédés, Production**

Conception de configurations innovantes en maquette critique pour la modélisation des phénomènes de couplages / découplages : Application aux transitoires cinétiques

Design of innovative zero power reactor configurations for modeling coupling/decoupling phenomena: Application to kinetics transients

Thèse soutenue publiquement le **12 mai 2021**, devant le jury composé de :

Monsieur Benoit GALL

PROFESSEUR, Institut Pluridisciplinaire Hubert CURIEN (IPHC), Université de Strasbourg, Président du jury

Monsieur Benoit FORGET

PROFESSEUR, Department of Nuclear Science & Engineering, Massachusetts Institute of Technology (MIT), Cambridge, USA, Rapporteur

Madame Sandra DULLA

PROFESSEUR, Department of Energy « Galileo Ferraris », Politecnico de Turin, Rapporteure

Monsieur Adrien BIDAUD

INGENIEUR HDR, Grenoble INP/PHELMA, LPSC, Examinateur

Monsieur Patrick BLAISE

DIRECTEUR DE RECHERCHE, CEA Saclay, Directeur de thèse

Monsieur Jean TOMMASI

INGENIEUR HDR, CEA Cadarache, Co-encadrant de thèse



Commissariat à l'énergie atomique et aux énergies alternatives
Direction des énergies
Institut de recherche sur les systèmes nucléaires pour la production d'énergie bas
carbone
Département d'études des réacteurs
Service de physique expérimentale, d'essais en sûreté et d'instrumentation
Laboratoire des programmes expérimentaux et d'essais en sûreté

This thesis was conducted in the LP2E laboratory of the Energy Division, at the Research Institute for Nuclear Systems for Low Carbon Energy Production, located at the center of Cadarache, of the French Alternative Energies and Atomic Energy Commission (CEA).

To my mother.

I wish you were here.

You were my best friend and I will always miss you.

Abstract

The study of space-time neutronic behavior of a nuclear reactor is the subject of both computational and experimental fields. Future and existing experimental facilities are called to answer questions on issues such as core stability and response to perturbations, that are commonly seen in large power reactors and are related to spatial decoupling. Calculations with accurate neutron kinetics models are required to characterize such decoupling effects in nuclear systems, both at small and large scales. The end goal of this work is to propose an innovative approach to analyze and reproduce such spatial effects in smaller ZPR (Zero Power Reactor) configurations. This is achieved by using the dominance ratio or eigenvalue separation as design criteria and connecting them to the characteristics of the system.

The methodology followed here relies on two main approaches. A hybrid stochastic – deterministic method based on the Transient Fission Matrix (TFM) model, implemented in the Serpent 2 Monte Carlo code and a deterministic calculation scheme based on Kobayashi’s multipoint kinetics model, running on the ERANOS 2.4 system of codes. The two approaches complement each other well, each covering the other’s limitations and enable the evaluation of both complex geometries and the design of decoupled high dominance ratio configurations. At their core, both methods track the neutron population across the system and relate it to its kinetic behavior. This allows one to access higher source distribution modes related to the flux harmonics, whose study is key to understanding nuclear reactor spatial effects.

The TFM model, permitting one-dimensional analysis with a fine nodal mesh, is an ideal tool for determining the dominance ratio and getting a detailed look at how prompt and delayed neutrons propagate in a geometry. On the other hand, the deterministic calculation scheme based on Kobayashi’s model allows for a lower calculation time and memory requirements, while enabling the study of three-dimensional coupling effects at the cost of a reduced number of nodes.

A fast/thermal coupled core ZPR concept, developed at CEA in the context of the ZEPHYR versatile facility, unfortunately frozen at the moment, is analyzed using the above methodology. This complicated geometry offers a good way to both test the validity of the models and gain an understanding of the associated coupling effects. Additionally, a simple coupled fuel assemblies benchmark problem was developed, for testing coupled core system calculations, models, and methodologies. The system’s kinetic behavior is analyzed in response to geometry and material changes. The distance between the assemblies is changed, fuels of different reactivities are used, control rods are introduced to parts of the system and finally, different levels of boron dilution in the moderator are

tested. This study enables us to better understand how the coupling is affected by various parameters and it deals with commonly encountered scenarios, in both experimental programs and power reactor operation.

Finally, the developed methodology is applied towards producing high dominance ratio configurations in the VENUS-F zero power reactor of the SCK-CEN, in the frame of a potential collaboration project between CEA and SCK CEN, part of which would be focused around developing a better understanding of space-time kinetics effects. This is done through a progressive optimization process that aims to gradually redesign the VENUS-F core, while keeping certain considerations in mind.

Résumé

Le comportement neutronique d'un réacteur nucléaire en transitoire est étudié à la fois de façon théorique et expérimentale. Les installations de type « maquettes critiques » existantes ainsi que les futures installations sont sollicitées afin de répondre aux questions concernant des problématiques telles que la stabilité de la nappe de puissance ou les diverses réponses aux perturbations, souvent observées dans des grands cœurs, et liées au découplage spatial. Afin de pouvoir caractériser de tels découplages au sein de systèmes nucléaires, il est nécessaire de se baser sur des modèles de cinétique spatiale à la fois en grande et petite échelle. L'objectif des études menées dans le cadre de cette thèse est de proposer une approche innovante d'analyse et de reproduction de tels effets spatiaux au sein de plus petites configurations (maquettes critiques). L'approche proposée est basée sur l'utilisation du facteur de séparation des valeurs propres (SVP) dans la conception des configurations expérimentales.

La méthodologie suivie dans cette étude s'appuie sur deux approches principales : une méthode hybride stochastique / déterministe basée sur le modèle Transient Fission Matrix (TFM), implémentée dans le code Serpent 2 et un schéma de calcul déterministe basé sur le modèle cinétique multipoint de Kobayashi, implémenté dans le système de codes ERANOS 2,4. Ces deux approches sont complémentaires, chacune remédiant aux limitations de l'autre, permettant l'analyse de géométries complexes et de la conception de configurations à haute SVP. Essentiellement, les deux méthodes suivent les neutrons à travers le système nucléaire et les relient au paramètres cinétiques. Ceci permet d'accéder à des modes de distribution de sources relatives aux harmoniques du flux, essentielles à la compréhension des effets spatiaux nucléaires.

Le modèle TFM, permettant une analyse unidimensionnelle détaillée, est l'outil idéal pour déterminer la SVP et ainsi permettre de visualiser en détail la propagation des neutrons prompts et des neutrons retardés au sein d'une géométrie. Au delà, le schéma déterministe basé sur le modèle de Kobayashi permet de réduire les temps de calcul et les besoins en mémoire, tout en rendant possible l'étude des effets de couplage tridimensionnels, mais au détriment du nombre de zones traitées.

La méthodologie d'approche combinée est utilisée pour l'analyse d'un concept de maquette critique à cœur rapide / thermique développé au sein du programme ZEPHYR au CEA, actuellement à l'arrêt. Cette géométrie complexe constitue un excellent test de la validité des modèles ainsi qu'un outil pour la compréhension des effets de couplage associés. De plus, un benchmark d'assemblages REP couplés a été développé, afin de permettre de tester des calculs sur les systèmes couplés, les modèles et méthodologies associées. Le comportement cinétique du système est analysé en réponse à des change-

ments géométriques et matériels. La distance entre les assemblages est modifiée, des combustibles de compositions différentes sont employés, les barres de contrôle sont introduites dans certaines parties du système et, enfin, plusieurs niveaux de dilution de bore dans le modérateur sont examinés. Cette étude permet de mieux comprendre comment le couplage est affecté par divers paramètres et explore divers cas de figure courants, à la fois au sein de programmes expérimentaux et du fonctionnement des réacteurs de puissance.

Pour finir, la méthodologie est appliquée à la conception préliminaire de configurations à haute SVP au sein de la maquette critique VENUS-F du SCK-CEN, dans le cadre d'un projet de collaboration entre le CEA et SCK CEN, centrée en partie autour d'une meilleure compréhension des effets de cinétique spatiale des cœurs. Ceci est réalisé à l'aide d'un processus d'optimisation progressive permettant de redesigner le cœur de VENUS-F.

Acknowledgments

First and foremost, I would like to thank my thesis director, Patrick Blaise and my supervisor, Jean Tommasi. Their continuous support, guidance and patience has helped me on numerous occasions over the years. Full of ideas and experience, Patrick always steered me in the right direction and remained present and approachable, both in and out of the office. Jean was a grounding presence, keeping me on track, always ready to help, with a keen eye for detail.

I would like to thank my reviewers, Sandra Dulla and Benoit Forget, for providing valuable input on my work and for their suggestions, which ultimately lead to a more concise and complete manuscript and fostered interesting discussion. I also wish to thank Adrien Bidaud for participating in my defense and last but not least, Benoit Gall, for presiding over it and bringing the whole thing together.

I would like to thank my colleagues and friends at CEA, for accompanying me during this period in my life.

I thank my partner, Victoria, for standing by my side during the difficult times, helping me organize my work when I was feeling overwhelmed and always assisting however she could. I am happy to be starting the next chapter of my life with her by my side.

Finally, I would like to thank my parents. I am the person I am, largely because of them. Their teachings, guidance and support allowed me to be here, today, writing this.

Contents

1	Introduction	1
1.1	Context and incentive	1
1.2	Layout of the thesis	4
1.3	Publications	6
2	Multipoint kinetics theory	7
2.1	Avery's multipoint kinetics	8
2.1.1	Introduction to coupled systems	8
2.1.2	Direct kinetics equations	11
2.1.3	Adjoint kinetics equations	12
2.1.4	Prompt neutron lifetime	13
2.2	Kobayashi's Multipoint Kinetics	14
2.2.1	Static problem	14
2.2.2	Time-dependent problem	17
2.2.3	Diffusion problem	18
2.2.4	Implementation in ERANOS	19
2.3	The Transient Fission Matrix method	20
3	Flux harmonics, dominance ratio and eigenvalue separation	24
3.1	Reduced order model for the dominance ratio	26
3.2	Experimental results of eigenvalue separation measurements in the KUCA reactor	31

4 The ZEPHYR fast-thermal coupled core	35
4.1 General characteristics and flux profiles	35
4.1.1 Development of the control rod assemblies	40
4.2 Analysis with the TFM model in Serpent 2	43
4.2.1 TFM analysis of a control rod insertion scenario	52
4.3 Analysis with Kobayashi's multipoint kinetics model in ERANOS	56
4.3.1 Traverse geometry	57
4.3.2 Full square geometry	61
4.4 Remarks	63
5 Coupled assemblies benchmark	64
5.1 Calculation setup	65
5.2 TFM calculations	67
5.2.1 Results for the UOX-UOX case	67
5.2.2 Results for the UOX-MOX case	81
5.3 ERANOS k_{ij} calculations	89
5.3.1 Results for the UOX-UOX case	90
5.3.2 Results for the UOX-MOX case	99
5.4 Remarks	105
6 High dominance ratio configurations in the VENUS-F zero power reactor	106
6.1 Characteristics of the VENUS-F core	107
6.1.1 k_0 , k_1 and dominance ratio sensitivities	113
6.1.2 Three-dimensional coupling	114
6.2 Increasing the dominance ratio	117
6.2.1 Moderator changes	117
6.2.2 Zones modification	120
6.2.3 Perturbation of the Design 2 configuration	128

6.3	Remarks	132
7	Conclusions	133
A	Dominance ratio model additional data	137
B	Calculation settings	138
C	Convergence of $\frac{k_{1,0,0}}{k_{0,0,0}}$ in the TFM model	143
D	ZEPHYR coupled core additional data	144
E	Coupled assemblies benchmark additional data	146
F	VENUS-F additional data	151
F.1	CR0* configuration results	151
F.2	Design 1 and Design 2 configurations results	155
F.3	Résumé en français	162
F.3.1	Contexte et motivation	162
F.3.2	Structure de la thèse	164
F.3.3	Conclusions	166

List of Figures

3.1	Dominance ratio versus material properties of the system.	29
3.2	The effect of geometry size.	30
3.3	Dependency on migration length and geometry size.	30
4.1	Top-down view of a ZEPHYR ZONA1 cell.	36
4.2	X-Y representation of the Serpent 2 modeling of the ZEPHYR fast-thermal coupled core configuration. Blue: light water, Orange: UO ₂ 3.7% enrichment, Green: metallic U 30.2% enrichment, Pink: natural UO ₂ , Yellow: B ₄ C absorber, White: air. The central cell design is the one presented in Fig. 4.1.	37
4.3	X-Z representation of the Serpent 2 modeling of the ZEPHYR fast-thermal coupled core configuration.	38
4.4	Flux profiles in the ZEPHYR fast-thermal coupled core configuration, calculated in Serpent 2. The geometry zones are marked on the figure. . . .	38
4.5	1G radial adjoint flux in the ZEPHYR fast-thermal coupled core, calculated in ERANOS.	39
4.6	Neutron spectra in the different areas of the fast-thermal coupled core (upper left) together with the neutron flux maps calculated with the Serpent 2 code: total flux (upper-right), and thermal/epithermal/fast flux (bottom).	39
4.7	ZEPHYR ZONA1 control assemblies (marked with yellow).	41
4.8	ZEPHYR final design in shutdown configuration, with control assemblies in ZONA1 and ZONA3 (marked with yellow).	42
4.9	Total flux map of the ZEPHYR core, with and without inserted control elements. Normalized to one source neutron.	42

4.10	Square representation of the ZEPHYR core. Blue: light water, Orange: UO ₂ 3.7% enrichment, Green: metallic U 30.2% enrichment, Pink: natural UO ₂ , Yellow: B ₄ C absorber, White: air. The central cell design is the one presented in Fig. 4.1.	44
4.11	Top-down view of the traverse of the square geometry used in the TFM calculation. The region discretization is also shown.	45
4.12	Fission rate, for the traverse of the square geometry. The error is on the order of 10 ⁻⁴ . Normalized to one source neutron.	45
4.13	TFM example of a $\underline{G}_{\chi_p \nu_p}$ matrix.	46
4.14	Prompt production matrices for 0% rod insertion.	47
4.15	Delayed production matrices for 0% rod insertion.	48
4.16	$\underline{T}_{\chi_p \nu_p}$ matrix.	49
4.17	Eigenvectors of the $\underline{G}_{\chi_p \nu_p}$ matrix.	50
4.18	\underline{G}_{all} block matrix first 72 eigenvalues (real parts).	51
4.19	Top-down view of the "1D" geometry used in the TFM calculation, with control rods inserted. The TFM discretization is also shown.	52
4.20	Side view of the "1D" geometry used in the TFM calculation, at 50% control rod insertion.	52
4.21	Fission rate, for the traverse of the square geometry, for all rod insertion cases.	53
4.22	$\underline{G}_{\chi_p \nu_p}$ matrices for various levels of control rod insertion.	54
4.23	$\underline{T}_{\chi_p \nu_p}$ matrix, for 100% rod insertion.	55
4.24	Eigenvectors of the $\underline{G}_{\chi_p \nu_p}$ matrix, for 100% rod insertion.	56
4.25	Homogenized squared geometry in ERANOS. The coupling zones and the center traverse are marked. Blue: light water, Orange: UO ₂ 3.7% enrichment, Green: metallic U 30.2% enrichment, Pink: natural UO ₂ , Yellow: B ₄ C absorber, Red: ZONA1 homogenized cell (4.1).	57
4.26	Coupling matrix for the traverse geometry, generated with ERANOS.	58
4.27	k_{ij} matrix eigenvectors for the traverse geometry, as calculated in ERANOS in this work and in APOLLO3®.	60

4.28	Non-converged forward first harmonic flux, before system symmetries were used.	60
4.29	First harmonic total flux profiles for the square ZEPHYR traverse, calculated in ERANOS.	61
4.30	First two eigenvectors of the square geometry, obtained with the k_{ij} model implemented in ERANOS.	62
5.1	X-Y view of the UOX-UOX geometry, with a separation of 5.04 cm (4x). The total length of the geometry is 78.12 cm (62x).	65
5.2	X-Z view of the UOX-UOX geometry. The pins and guide tubes are on top of steel supports placed at the bottom of the geometry.	66
5.3	X-Y view of the UOX-MOX geometry, with a separation of 20.16 cm (16x). The total length of the geometry is 78.12 cm (62x).	66
5.4	$G_{\chi_p \nu_p}$ matrices for the UOX-UOX geometry, for different levels of assembly separation.	68
5.5	$G_{\chi_p \nu_p}$ matrix eigenvector for the UOX-UOX geometry, for different levels of assembly separation.	69
5.6	Prompt-to-prompt matrix eigenvector for a single UOX fuel assembly. . .	70
5.7	G matrices for the UOX-UOX geometry, for a separation of 2.52 cm (2x). . .	71
5.8	$T_{\chi_p \nu_p}$ matrices for the UOX-UOX geometry, for different levels of assembly separation.	72
5.9	$\frac{k_{1,0,0}}{k_{0,0,0}}$ value versus assembly separation, for the UOX-UOX case.	74
5.10	$G_{\chi_p \nu_p}$ matrix eigenvector for the first five modes, for the UOX-UOX 5.04 cm case.	75
5.11	X-Y view of the UOX-UOX geometry, with a separation of 5.04 cm (4x) and B ₄ C control rods inserted into the right assembly.	76
5.12	$G_{\chi_p \nu_p}$ matrices for the UOX-UOX geometry, for a separation of 5.04 cm (4x), showing the effects of control rod insertion.	76
5.13	Prompt-to-prompt matrix eigenvector for a single UOX assembly (left) , the system of Fig. 5.11 (middle) and a single UOX assembly with control rods inserted (right).	77

5.14 $\underline{G}_{\chi_p \nu_p}$ matrices for the UOX-UOX geometry, for a separation of 5.04 cm (4x), showing the effects of control rod insertion.	78
5.15 1D thermal flux for the UOX-UOX geometry, including the case of control rod insertion (5.04cm CR), for the entire system size. Error bars are shown only for the 0 cm case, to avoid cluttering the graph. Normalized to one source neutron.	79
5.16 Boron dilution effect on the $\frac{k_{1,0,0}}{k_{0,0,0}}$ value. The linear fit is $\frac{k_{1,0,0}}{k_{0,0,0}} = (5.19716 \times 10^{-5})ppm + 0.82622$, with $R^2 = 0.99791$	81
5.17 $\underline{G}_{\chi_p \nu_p}$ matrices for the UOX-MOX geometry, for different levels of assembly separation.	82
5.18 \underline{G} matrices for the UOX-MOX geometry, for a separation of 2.52 cm (2x).	83
5.19 $\underline{T}_{\chi_p \nu_p}$ matrices for the UOX-MOX geometry, for different levels of assembly separation.	84
5.20 $\underline{G}_{\chi_p \nu_p}$ matrix eigenvector for the UOX-MOX geometry, for different levels of assembly separation.	85
5.21 $\frac{k_{1,0,0}}{k_{0,0,0}}$ versus assembly separation, compared between the UOX-UOX and UOX-MOX cases.	87
5.22 1D flux below 1 eV for the UOX-MOX geometry, for the entire system size. Error bars are shown only for the 0 cm case, to avoid cluttering the graph. Normalized to one source neutron.	88
5.23 1D flux above 1 eV for the UOX-MOX geometry, for the entire system size. Error bars are shown only for the 0 cm case, to avoid cluttering the graph. Normalized to one source neutron.	89
5.24 X-Y view of the UOX-UOX geometry, with the homogenized coupling regions marked.	90
5.25 $\frac{k_{1,0,0}}{k_{0,0,0}}$ versus separation for the UOX-UOX case, as calculated with ERA-NOS and with the TFM model.	91
5.26 First six eigenvectors for the 20.16 cm UOX-UOX case.	93
5.27 First six eigenvectors for the 0 cm UOX-UOX case.	94
5.28 Even modes ($n = 0, 2, 4$) for a perfectly symmetric k_{ij} matrix. Observe that the second ($n = 2$) and fourth ($n = 4$) modes are completely flat between regions 3 and 4, indicating a perfectly even source distribution.	95

5.29	First mode azimuthal flux harmonics for the 0 cm, 2.52 cm and 20.16 cm cases.	97
5.30	Fundamental and first mode eigenvectors of the 12 region, 0 cm separation case, before and after control rods were inserted in the (3/12) region.	98
5.31	X-Y view of the UOX-MOX geometry, with the homogenized coupling regions marked.	99
5.32	$\frac{k_{1,0,0}}{k_{0,0,0}}$ value versus separation for both the UOX-UOX and UOX-MOX cases, as calculated with ERANOS and with the TFM model. A TFM plateau is assumed for UOX-MOX at 0.85837.	100
5.33	$\frac{k_{1,0,0}}{k_{0,0,0}}$ value % difference versus separation for both the UOX-UOX and UOX-MOX cases, of the k_{ij} method in ERANOS, using the TFM method in Serpent 2 as reference. A TFM plateau is assumed for UOX-MOX at 0.85837.	101
5.34	First six modes for the 20.16 cm UOX-MOX case.	102
5.35	First six modes for the 0 cm UOX-MOX case.	103
6.1	Top-down view of the Serpent 2 model of the VENUS-F core. Yellow: metallic U 30.2% enrichment, Orange: B ₄ C safety rod position, Black: void (B ₄ C pilot rod position), White: air.	108
6.2	Side view of the Serpent 2 model of the VENUS-F core.	108
6.3	Core-wide flux spectrum of the VENUS-F core.	109
6.4	$G_{\chi_p \nu_p}$ matrix eigenvectors for the default VENUS-F core configuration. .	110
6.5	Geometry discretization for the k_{ij} model in ERANOS.	111
6.6	k_{ij} matrix eigenvector for the default VENUS-F core configuration.	112
6.7	First flux harmonic distribution in the core mid-plane, calculated in ER-ANOS. The z axis represents the harmonic flux in arbitrary units.	112
6.8	Nuclear data sensitivity profiles for the CR0* core.	113
6.9	Radial discretizations.	115
6.10	3D coupling for the VENUS-F core in the CR0* configuration. Regions 1-6 refer to the top part and regions 7-12 refer to the bottom part.	116

6.11 $\underline{G}_{\chi_p \nu_p}$ matrices and their difference, for the CR0* and graphite VENUS-F configurations. The material changes only refer to the 12×12 lattice, not the radial reflector.	118
6.12 $\underline{G}_{\chi_p \nu_p}$ matrix, its fundamental eigenvector and it difference from CR0*, for the VENUS-F core with polyethylene moderator.	120
6.13 VENUS-F configuration with polyethylene moderator and a ring of natural uranium assemblies around the core center. Yellow: metallic U 30.2% enrichment, Brown: CH_2 , Pink: natural UO_2 , Black: void (B_4C pilot rod position), White: air.	121
6.14 VENUS-F high dominance ratio designs. Yellow: metallic U 30.2% enrichment, Brown: CH_2 , Pink: natural UO_2 , Orange: B_4C , Black: void (B_4C pilot rod position), White: air.	124
6.15 $\underline{G}_{\chi_p \nu_p}$ matrix fundamental eigenvector.	125
6.16 $\underline{G}_{\chi_p \nu_p}$ matrix first mode eigenvector.	125
6.17 $\underline{G}_{\chi_p \nu_p}$ matrices and their difference.	126
6.18 Radial discretization for the k_{ij} model in ERANOS, for the two high dominance ratio configurations.	127
6.19 $\underline{G}_{\chi_p \nu_p}$ differences from the default Design 2 geometry, $x = j$, $y = i$ nodes, respectively.	128
6.20 $\underline{G}_{\chi_p \nu_p}$ fundamental and first mode eigenvectors and their redistribution, for the pilot rod insertion in Design 2.	129
6.21 Flux maps for the Design 2 configuration, with all control elements withdrawn (left) and with one safety rod inserted (right). A red square marks the point of insertion. Th.	130
6.22 $\underline{G}_{\chi_p \nu_p}$ fundamental and first mode eigenvectors and their redistribution, for the safety rod insertion in Design 2.	130
6.23 S_{k_1}/S_{k_0} sensitivities ratio for Design 2.	131
C.1 Convergence of $\frac{k_{1,0,0}}{k_{0,0,0}}$, versus number of regions in the TFM model.	143
D.1 Total forward flux for the square ZEPHYR traverse, for all rod insertion levels, calculated in Serpent 2.	144

D.2	Total fundamental flux profiles for the square ZEPHYR traverse, calculated in ERANOS.	144
D.3	All accessed $G_{\chi_p \nu_p}$ eigenvectors. Rows indicate the modes and columns indicate the coupling regions.	145
E.1	Normalized fission reaction rate for the UOX-UOX geometry.	146
E.2	Normalized fission reaction rate for the UOX-MOX geometry.	147
F.1	Flux profiles for the VENUS-F core in the CR0* configuration. The thermal component of the flux is very small and not visible at this scale.	151
F.2	Flux spectrum for the 4 central assemblies for the VENUS-F core in the CR0* configuration.	152
F.3	Total flux map for the VENUS-F core in the CR0* configuration.	152
F.4	Fission rate map for the VENUS-F core in the CR0* configuration.	153
F.5	First six flux modes for the VENUS-F core in the CR0* configuration.	154
F.6	Flux spectra for Design 1.	155
F.7	Flux profiles for Design 1.	155
F.8	Total flux map for Design 1.	156
F.9	Fission rate map for Design 1.	156
F.10	Flux spectra for Design 2.	157
F.11	Flux profiles for Design 2.	158
F.12	Total flux map for Design 2.	158
F.13	Fission rate map for Design 2.	159
F.14	Fission rate map for safety rod insertion in the Design 2 configuration.	159
F.15	Nuclear data sensitivity profiles for Design 2.	160
F.16	Fundamental and first mode eigenvectors as calculated in ERANOS, for Design 1 and Design 2.	161

List of Tables

4.1	Control rod material selection results.	40
4.2	G_{all} block matrix first 72 eigenvalues (real parts), calculated with the TFM model.	51
4.3	k_{ij} coupling coefficients matrix for the traverse.	58
4.4	First eight eigenvalues of the ZEPHYR traverse geometry, calculated in ERANOS.	59
4.5	First eight eigenvalues of the full square geometry, calculated in ERANOS.	62
5.1	$k_{0,0,0}$, $k_{1,0,0}$ and $\frac{k_{1,0,0}}{k_{0,0,0}}$ as a function of the assembly separation for the UOX-UOX case.	73
5.2	β_{eff} and Λ_{eff} as a function of the assembly separation for the the UOX-UOX case.	73
5.3	Comparison between values calculated with the TFM model versus reference data calculated natively in Serpent 2.	74
5.4	$k_{0,0,0}$, $k_{1,0,0}$ and $\frac{k_{1,0,0}}{k_{0,0,0}}$ as a function of the assembly separation for the rod insertion case.	78
5.5	β_{eff} and Λ_{eff} as a function of the assembly separation for the rod insertion case.	78
5.6	$k_{0,0,0}$, $k_{1,0,0}$ and $\frac{k_{1,0,0}}{k_{0,0,0}}$ as a function of boron concentration in the moderator.	80
5.7	$k_{0,0,0}$, $k_{1,0,0}$ and $\frac{k_{1,0,0}}{k_{0,0,0}}$ as a function of the assembly separation for the UOX-MOX case.	86
5.8	β_{eff} and Λ_{eff} as a function of the assembly separation for the the UOX-MOX case.	87

5.9	$k_{0,0,0}$, $k_{1,0,0}$ and $\frac{k_{1,0,0}}{k_{0,0,0}}$ as a function of the assembly separation for the UOX-UOX case, calculated in ERANOS.	90
5.10	k_{ij} coupling coefficients for the 20.16 cm UOX-UOX case.	92
5.11	β_{ij} for the 20.16 cm UOX-UOX case.	95
5.12	β_i for different levels of assembly separation for the UOX-UOX case. Results are given in pcm .	96
5.13	ℓ_i for different levels of assembly separation for the UOX-UOX case. Results are given in μs .	96
5.14	$k_{1,0,0}$ eigenvalues calculated via a harmonic flux calculation on one half of the symmetric geometry.	97
5.15	$k_{0,0,0}$, $k_{1,0,0}$ and $\frac{k_{1,0,0}}{k_{0,0,0}}$ as a function of the assembly separation for the UOX-MOX case. *: assumed	100
5.16	k_{ij} coupling coefficients for the 20.16 cm UOX-MOX case.	102
5.17	β_{ij} for the 20.16 cm UOX-MOX case.	103
5.18	ℓ_i for different levels of assembly separation for the UOX-MOX case. Results are given in μs .	104
5.19	β_i for different levels of assembly separation for the UOX-MOX case. Results are given in pcm .	104
6.1	k_0 , λ_1 , dominance ratio (DR), eigenvalue separation (EVS), for different discretization schemes, calculated with ERANOS.	115
6.2	k_0 , k_1 , dominance ratio (DR), eigenvalue separation (EVS) and main kinetic parameters, calculated with TFM.	124
6.3	k_0 , k_1 , dominance ratio (DR), eigenvalue separation (EVS), calculated with ERANOS.	127
6.4	Radial k_{ij} coupling coefficients for Design 1.	127
6.5	Radial k_{ij} coupling coefficients for Design 2.	128
6.6	k_0 , k_1 , dominance ratio (DR), eigenvalue separation (EVS), importance and flux fractions for the two azimuthal halves of the core.	131
A.1	Parallelepiped data and dominance ratio results.	137
A.2	PWR geometry azimuthal and axial dominance ratio, calculated with TFM.	137

B.1	Serpent 2 settings.	138
D.1	k_{ij} coupling coefficients matrix for the full square geometry.	145
E.1	Radial design of the different types of pins used in the geometry. Based on the BEAVRS benchmark.	147
E.2	UOX fuel isotopic composition.	148
E.3	MOX fuel isotopic composition.	148
E.4	B_4C control rod material isotopic composition.	148
E.5	Zircaloy cladding isotopic composition.	149
E.6	Steel isotopic composition. Used in the guide tubes and the structure base.	150
F.1	Azimuthal k_{ij} coupling coefficients for the VENUS-F core in the CR0* configuration.	153
F.2	ℓ_i and β_i for the VENUS-F core in the CR0* configuration.	154
F.3	Azimuthal k_{ij} coupling coefficients for Design 1.	157
F.4	ℓ_i and β_i for Design 1.	157
F.5	Azimuthal k_{ij} coupling coefficients for Design 2.	161
F.6	ℓ_i and β_i for Design 2.	161

Acronyms

AOA - Axial Offset Anomaly

BEAVRS - Benchmark for Evaluation and Validation of Reactor Simulations

BWR - Boiling Water Reactor

CEA - Commissariat à l'énergie atomique et aux énergies alternatives

DR - Dominance Ratio

EPR - European Pressurized Reactor

EVS - Eigenvalue Separation

KUCA - Kyoto University Critical Assembly

PWR - Pressurized Water Reactor

MOX - Mixed Oxide (fuel)

SCK CEN - Studiecentrum voor Kernenergie - Centre d'Étude de l'énergie Nucléaire

TFM - Transient Fission Matrix

UOX - Uranium Oxide (fuel)

XS - Cross Section

ZEPHYR - Zero power Experimental PHYsics Reactor

ZPR - Zero Power Reactor

Chapter 1

Introduction

1.1 Context and incentive

In the field of nuclear reactor physics, experimental facilities play a key role. Depending on their intended purpose, they can either consist of specialized cores, centered around a certain class of experiments, or they can be designed with versatility in mind, allowing for a wide array of applications. Zero power reactors or ZPRs, often fall in the second category, aiming to provide diverse testing environments. Alongside computational analyses, these facilities are used to both expand our understanding of the complex nature of reactor phenomena and support the nuclear industry.

In the context of the latter point, experimental reactors are often used to simulate the behavior of larger cores, allowing the study of phenomena related to power reactor operation, in a safe environment. However, there are limits to the extent that these smaller cores can exhibit the same effects and one particular difference between them and larger cores is their dominance ratio (DR). It is a quantity that describes the magnitude of the effect that the so-called flux harmonics have on the neutron flux and how coupled the various parts of a system are with each other. The flux harmonics are eigen-modes of the transport equation and in the general case, are perturbed differently than the fundamental mode, with the neutron flux shape being the weighted sum of the fundamental (steady-state) and harmonics modes. A high dominance ratio means that the fundamental and first harmonic modes are close to one another and the latter has a significant contribution to the overall flux behavior. Systems with a high DR will typically exhibit a large degree of neutronic decoupling, meaning that a local perturbation is likely to lead to oscillations [1]. Inversely, a low DR means that the contribution of the harmonics decreases rapidly and the fundamental mode will be established faster after a perturbation.

Large power cores are typically decoupled and characterized by particularly high dominance ratio values, leading to often quite prominent power tilts. The issue is exacerbated in typical light water reactor designs due to axial heterogeneities resulting from normal operation, where it is commonly referred to as axial offset anomaly (AOA) [2]. AOA can affect full power shutdown margins and thus mandates operation at lower power levels, presenting a significant issue for fuel cycle economics. Similarly to the axial case, studies have shown [3–5] that large cores exhibit similar power tilt issues on the azimuthal plane, especially if it is characterized by heterogeneities or a heavy reflector is used, such as in the case of the European Pressurized Reactor (EPR) design.

Consequently, the dominance ratio and flux harmonics behavior are of great interest to reactor physics research. While work has been done on the subject [6, 7] Unfortunately, it is not possible to compute them directly using the tools available during the thesis, except for cases where the geometry respects certain symmetries [8, 9]. For the general case however, another approach must be used to reconstruct the harmonic fluxes. This is where multipoint kinetics models come into play. They expand the commonly known point kinetics model into multiple regions, with each region described by the usual point kinetics, plus contributions from all other regions. It provides good results regarding the kinetic behavior of a system, while at the same time being relatively inexpensive when compared to full kinetics modeling approaches. The model introduces the notion of neutronic coupling, describing the region-wise interactions that take place in the system, which in turn allows one to study its spatial behavior.

It is therefore of great interest to develop a methodology of designing zero power reactor cores that are characterized by a high dominance ratio. Such designs will be able to exhibit spatial kinetics effects in a similar fashion to large cores, allowing the investigation of such issues in both safe and efficient ways. The versatility and relative ease of use of several ZPRs, makes them ideal testbeds for a variety of studies and scenarios. However, their small size means that they are also, typically, far more coupled than their large counterparts and are characterized by low dominance ratio values. Certain designs overcome this limitation in innovative ways, one such example being the ZEPHYR fast-thermal coupled core concept [10–12], developed by the French Alternative Energies and Atomic Energy Commission (CEA). ZEPHYR manages to increase the decoupling between different regions of the system by incorporating a radial design comprised of various fissile, fertile and absorber regions of highly different neutron spectra.

The aim of the thesis is to develop a simulation-based methodology of analyzing the kinetic and coupling behavior of nuclear systems by using multipoint kinetics approaches and finally use said methodology to produce zero power reactor designs that exhibit a high dominance ratio. The thesis explores the use of two multipoint kinetics models -

the Transient Fission Matrix model [13–19], running in the Serpent 2 Monte Carlo code [20] and Kobayashi’s multipoint kinetics model [21–24], running in the ECCO/ERANOS system of deterministic codes [25]. The advantages, limitations and applications of each model are explored throughout a part of the thesis, with the models first being used to analyze the ZEPHYR coupled core design. Unfortunately, a little over one year after the start of the PhD, the ZEPHYR program was indefinitely suspended due to budgetary concerns and will be revisited at a later date. As such it is used as a numerical benchmark in this context. At this point, the focus of the work is shifted, to encompass a larger study on the dependency of the dominance ratio on various factors, in more general geometries [26]. Finally, the developed methodology is applied in creating high dominance ratio configurations in the VENUS-F zero power reactor of the SCK CEN [27, 28].

The simulation-based methodology consists of using the dominance ratio as an evaluation criterion of produced designs. With the tools used in this thesis, it can be determined by three different ways, two of them based on coupling coefficient matrices generated via multipoint kinetics models (TFM in Serpent 2 and Kobayashi in ERANOS) and one of them based on symmetry properties of the system (if possible). The different approaches complement each other and allow the analysis of a geometry in various ways, ranging from a single-axis, highly detailed analysis with TFM, to full 3D coupling study with a limited number of regions, with Kobayashi’s model.

- One approach that is used to produce high DR configurations is the "small large core" idea, where small geometries, such as those present in this thesis, are optimized in order to reduce the neutron migration area in respect to the overall geometry size - effectively increasing decoupling across the system.
- Another approach utilizes the concept of zoning, which can be seen in geometries such as ZEPHYR and relies on decoupling parts of the core by using absorbing and/or fertile elements.
- And yet another way of achieving decoupling, with the possibility of dynamically controlling it as well, is to use systems with movable parts, where the decoupling is controlled by modifying the distance between two reactors.

After high dominance ratio configurations are produced, their response to perturbation by the use of control rods is studied, in terms of changes in the kinetic behavior and the manifestation of tilts in the source distribution.

1.2 Layout of the thesis

Chapter 2 establishes a theoretical basis of the two main multipoint kinetics approaches, starting with Avery's model [29], developed in the 50's. Avery based his model on an intuitive process, introducing the concept of the "coupling coefficients", quantities that describe the neutronic coupling or connection between different regions of a system, be it a single core or multiple reactors interacting with each other. Next, the focus shifts to Kobayashi's work from the 90's, where he saw the need for and subsequently developed a more rigorously derived multipoint kinetics model A short comparison between the two approaches is included, as well as a section describing the implementation of Kobayashi's model in the ERANOS code [25]. Finally, the Transient Fission Matrix (TFM) model, recently developed by A. Laureau, is presented. It describes a hybrid stochastic-deterministic approach, based on using information gathered from a Monte Carlo calculation, as input for deterministic multipoint kinetics equations, and offers a detailed look into the kinetic behavior of a system.

Chapter 3 introduces the notions of flux harmonics, dominance ratio and eigenvalue separation. It describes the behaviors connected to high dominance ratio cores and connects the dominance ratio to power tilts, using a simple, two-region model. It is discussed how the coupling coefficients can be used to access the harmonics of the system, by virtue of reconstructing the fission source distributions. A reduced order model for connecting the dominance ratio to intrinsic characteristics of the system is also presented, allowing its estimation as well as showing ways of affecting it by altering said characteristics. It is shown that the dominance ratio is largely determined by the relative ability of neutrons to travel within a geometry - systems where the migration area is small compared to the overall size of the geometry, are largely decoupled and characterized by high dominance ratios.

Chapter 4 describes how the Transient Fission Matrix model and Kobayashi's multipoint kinetics model, are used to analyze the kinetic behavior of the ZEPHYR fast-thermal coupled core geometry. It serves as an introductory chapter to the methodology developed during the thesis, describing the process, as well interpreting the various results that these two multipoint implementations produce. The TFM model is used to analyze a staggered control rod insertion scenario and discuss the resulting changes in coupling behavior. Some of the ways that the two codes complement each other are also mentioned, with more remarks on that given in the following chapter. It also discusses the possibility of accessing the first flux harmonic directly, by taking advantage of the system's symmetries.

Chapter 5 briefly addresses the need to open up the topic of the thesis, following the postponement of ZEPHYR and showcases how the previously developed analysis methodology

is used to investigate how the coupling behavior is affected by both geometry and material changes. A calculation benchmark was produced, consisting of a coupled system of two PWR type fuel assemblies placed in light water. The assemblies are free to move along a single geometry axis, starting from right next to each other and ending 20 cm apart, increasing the decoupling both due to distance itself, as well as the developing water blade between them. Material changes consist of changing the fuel type, inserting control rods to various parts of the geometry and introducing varying amounts of diluted boron in the moderator. Additionally, this chapter provides extensive comparison data between the TFM and Kobayashi's model. The simplicity of the studied geometry also allows a more in-depth conversation regarding the use of higher order harmonics in detecting or predicting flux tilts.

Chapter 6 describes how the experience gained thus far was applied in producing high dominance ratio configurations in the VENUS-F core of the SCK CEN, serving as a proof of concept of the developed methodology. This is done in the context of a possible collaboration between CEA and SCK CEN and as such, the VENUS-F zero power reactor represents an ideal candidate for testing high dominance ratio configurations and investigate space-time kinetics issues related to large cores. After an initial analysis of the coupling behavior of the core in the CR0* configuration, a progressive optimization process is followed, culminating in two candidate designs. A discussion regarding their feasibility and safety margins follows, followed by a description of their coupling behavior and their response to a perturbation.

Finally, Chapter 7 presents the conclusions of the thesis and offers some ideas for future prospects.

1.3 Publications

- P. Blaise, A. Laureau, P. Ros, P. Leconte, and K. Routsonis. Transient Fission Matrix approach for assessing complex kinetics behavior in the ZEPHYR ZPR coupled core configurations. *Ann. Nucl. Energy*, 128:390–397, 2018.
- K. Routsonis, P. Blaise, J. Tommasi and G. Valocchi. Transient fission matrix analysis of rod drop experiments in coupled cores for addressing high dominance ratio configurations. *Proc. International Conference on Mathematics and Computational Methods Applied to Nuclear Science & Engineering (M&C 2019), Portland, OR, United States*, 2019.
- K. Routsonis, P. Blaise, and J. Tommasi. Numerical Benchmark of Strongly to Loosely Coupled Assemblies using the Transient Fission Matrix method. *Proc. PHYSOR 2020: Transition to a Scalable Nuclear Future*, 2020.
- K. Routsonis, P. Blaise, and J. Tommasi. A twin assemblies benchmark for coupling behavior and kinetics parameters calculations. *Ann. Nucl. Energy*, 2021.
- K. Routsonis, P. Blaise, and J. Tommasi. Coupling coefficient and dominance ratio calculations for a strongly to loosely coupled fuel assembly problem. To be submitted to *Ann. Nucl. Energy*.

Chapter 2

Multipoint kinetics theory

This chapter presents the theoretical basis of the concepts explored in this thesis. To successfully analyze and predict the response of a nuclear system to a perturbation or change, it is necessary to understand how different parts of the system are connected to one another. This is especially true if one is interested in local changes, instead of only looking at the system as a whole. On one end of the spectrum, there is the full reactor kinetics modeling, offering the best quality in terms of accuracy at a very heavy computational cost. On the other end, there is the Point Kinetics model, which is easy to work with, but generally fails to give good results (or any results), depending on the question at hand. Multipoint kinetics are between these two extremes, expanding upon the point kinetics model and treating a reactor as a collection of different regions that interact with each other.

The first section will present R. Avery's approach, since he was the pioneer of the subject. His work will be given in some detail, to help familiarize the reader with the concepts explored, as Avery takes an approach that is quite intuitive and can be easily followed.

The second section will showcase K. Kobayashi's approach, where he expanded upon Avery's work and derived more rigorous expressions in a simple manner, starting from well understood concepts. Kobayashi's models are used in the deterministic part of the calculation performed in the context of the thesis, in the ERANOS code.

The third section will present the Transient Fission Matrix model, developed by A. Laureau. It is a hybrid model, using data generated with the Serpent 2 Monte Carlo code as input for deterministic calculations, allowing for a relatively inexpensive way to analyze the kinetics of a system (currently in one dimension), while taking advantage of the precision offered by stochastic calculations. This model was used extensively during the thesis and was the primary tool for designing high dominance ratio configurations.

2.1 Avery's multipoint kinetics

2.1.1 Introduction to coupled systems

Robert Avery, in his 1958 paper titled "Theory of Coupled Reactors" [29], set the foundations of multipoint kinetics. The premise was simple; the Boltzmann equation can technically be applied to any system. Avery sought to discretize an arbitrary system and separate it into different "reactors" and study how these individual regions behaved and affected each other. From this point onward in this chapter, the terms reactor and region can be considered interchangeable. A coupled reactor system is one where some of the neutrons born in different reactors will be emitted during fissions caused by neutrons born in other reactors. Each region can be associated with a source and the sum of all the partial sources gives the total system source.

Avery introduces the quantity k_{ij} and defines it as "the expectation value that a fission neutron in reactor j gives rise to a next generation fission neutron in reactor i ". Another name widely adopted for this quantity is *coupling coefficient*. The average prompt neutron lifetime for this process is defined as ℓ_{ij} . k_{ij} is a measure of the cross coupling between reactors i and j and in the general case, $k_{ij} \neq k_{ji}$. However, the two coupling coefficients are expected to be equal if the two reactors are identical and no other factors come into play. It follows that k_{ii} is the region's own contribution to its population of fission neutrons.

The quantity $\Delta_i = 1 - k_{ii}$ is defined and it is a measure of the subcriticality of a region or reactor i .

S_i is the total fission source in reactor i and S_{ij} is the total fission source in reactor i which results from fission by neutrons coming from reactor j . For a system of N reactors, it stands that

$$S_i = \sum_{j=1}^N S_{ij} \quad (2.1)$$

and

$$\frac{S_{ii}}{S_i} = k_{ii} \quad (2.2)$$

Avery uses a two-region geometry to illustrate some concepts and derive their expressions. This decision is likely related to the fact that the author had a real design in mind, namely a Coupled fast-thermal power breeder reactor concept that was patented in 1957 [30, 31].

The source terms are,

$$\frac{S_{11}}{S_1} = k_{11} \quad (2.3)$$

$$\frac{S_{12}}{S_2} = k_{12} \quad (2.4)$$

$$\frac{S_{21}}{S_1} = k_{21} \quad (2.5)$$

$$\frac{S_{22}}{S_2} = k_{22} \quad (2.6)$$

and from 2.1,

$$S_{11} + S_{12} = S_1 \quad (2.7)$$

$$S_{22} + S_{21} = S_2 \quad (2.8)$$

Combining the above, expressions for the quantity S_i can be written as

$$k_{11}S_1 + k_{12}S_2 = S_1 \quad (2.9)$$

$$k_{21}S_1 + k_{22}S_2 = S_2 \quad (2.10)$$

The criticality condition is

$$\begin{vmatrix} (k_{11} - 1) & k_{12} \\ k_{21} & (k_{22} - 1) \end{vmatrix} = 0 \quad (2.11)$$

or

$$k_{12}k_{21} = \Delta_1\Delta_2 \quad (2.12)$$

This condition stems from the fact that the system of Eq. (2.9) and Eq. (2.10) needs to have a self-consistent solution and that this solution does not yield a negative value for the source terms, since the latter would mean that at least one reactor would be supercritical by itself. Thus, for this expression, both reactors have to be either subcritical on their own with the total system being critical or simply critical on their own, without contributions from the other reactor.

Solving for relative values of S_i ,

$$\frac{S_1}{S_2} = \frac{k_{12}}{\Delta_1} = \frac{\Delta_2}{k_{21}} \quad (2.13)$$

if the coupling vanishes in one direction, the above expression is valid, but one of the two expressions will be indeterminate. If both couplings vanish, then both expressions become indeterminate and any power ratio between the two (necessarily self-critical) reactors can exist.

Considering the reactivity, the number of neutrons needed to maintain criticality in the system is defined as ν_c and $\nu \neq \nu_c$ when a system is non-critical. Small deviations from

criticality can be written as $k_{ex} \approx \rho$, where $k_{ex} = k - 1$ and $\rho = (\nu - \nu_c)/\nu$. For the case of the two reactors,

$$\begin{pmatrix} k_{11} & k_{12} \\ k_{21} & k_{22} \end{pmatrix} \begin{pmatrix} S_1 \\ S_2 \end{pmatrix} = k \begin{pmatrix} S_1 \\ S_2 \end{pmatrix} \quad (2.14)$$

where k is the criticality value of the system. Using $k = 1 + k_{ex}$

$$\Delta_1 \Delta_2 + k_{ex} (\Delta_1 + \Delta_2) + k_{ex}^2 = k_{12} k_{21} \quad (2.15)$$

Equation (2.15) is valid even if one of the reactors is supercritical by itself and in cases where the reactivity change is small compared to the subcriticality of both reactors, the square term can be omitted and the reactivity is given by

$$k_{ex} \approx \rho \approx \frac{k_{12} k_{21} - \Delta_1 \Delta_2}{\Delta_1 + \Delta_2} \quad (2.16)$$

The reactivity can also be expressed as a deviation from the critical values, as

$$\rho \approx \frac{\Delta_1 \Delta_2}{\Delta_1 + \Delta_2} \left(-\frac{\delta \Delta_1}{\Delta_1} - \frac{\delta \Delta_2}{\Delta_2} + \frac{\delta k_{12}}{k_{12}} + \frac{\delta k_{21}}{k_{21}} \right) \quad (2.17)$$

In the simple scenario of a change of ν by an amount of $\delta\nu$ in each reactor, recalling that $\rho = (\nu - \nu_c)/\nu$, the resulting reactivity change in the system is

$$\rho \approx \frac{\frac{1}{\Delta_1}}{\frac{1}{\Delta_1} + \frac{1}{\Delta_2}} \frac{\delta \nu_1}{\nu_1} + \frac{\frac{1}{\Delta_2}}{\frac{1}{\Delta_1} + \frac{1}{\Delta_2}} \frac{\delta \nu_2}{\nu_2} \quad (2.18)$$

Generalizing for N reactors, Eq. (2.14) becomes

$$\begin{pmatrix} k_{11} & k_{12} & \dots & k_{1N} \\ k_{21} & k_{22} & \dots & k_{2N} \\ \vdots & \vdots & & \vdots \\ k_{N1} & k_{N2} & \dots & k_{NN} \end{pmatrix} \begin{pmatrix} S_1 \\ S_2 \\ \vdots \\ S_N \end{pmatrix} = k \begin{pmatrix} S_1 \\ S_2 \\ \vdots \\ S_N \end{pmatrix} \quad (2.19)$$

and the criticality condition is given by

$$|k_{ij} - \delta_{ij}| = 0, \quad \delta_{ij} = \begin{cases} 1, & i = j \\ 0, & i \neq j \end{cases} \quad (2.20)$$

Equation (2.18) becomes

$$\rho \approx \sum_{i=1}^N \alpha_i \frac{\delta \nu_i}{\nu_i} \quad (2.21)$$

where

$$\alpha_i = \frac{\frac{1}{\Delta_i}}{\sum_{j=1}^N \frac{1}{\Delta_j}} \quad (2.22)$$

2.1.2 Direct kinetics equations

The kinetic behavior of a coupled system can be described by the following equations,

$$\ell_{ij} \frac{dS_{ij}}{dt} = k_{ij}(1 - \beta) \sum_{h=1}^N S_{jh} - S_{ij} + k_{ij} \sum_m \lambda_m C_{m,j} \quad (2.23)$$

$$\frac{dC_{m,i}}{dt} = \beta_{m,i} \sum_{h=1}^N S_{jh} - \lambda_m C_{m,i}, \quad \sum_m \beta_{m,i} = \beta_i \quad (2.24)$$

where $C_{m,i}$ is a weighted measure of the number of delayed neutron emitters for family m for reactor i , $\beta = \beta_{eff}$ is the total delayed neutron fraction for the system, $\beta_{m,i}$ is the delayed neutron fraction for reactor i and delayed neutron family m and β_i is the delayed neutron fraction for reactor i , summed over all delayed neutron families. For simplicity, it is assumed that k_{ij} and the lifetime ℓ_{ij} are the same for both prompt and delayed neutrons. While this is a significant simplification, it does not subtract from the process at hand, the only loss being in the number of variables handled; the end result remains indicative of the logic displayed here.

At this point, Avery inserts the notion of the redundant variables R_{ij} , defined as

$$S_{ij} = \frac{R_{ij}}{\ell_{ij}} \quad (2.25)$$

The reasoning behind this is that it allows the multipoint kinetic equations to be put into a more usual form, as

$$\frac{dR_{ij}}{dt} = k_{ij}(1 - \beta) \sum_{h=1}^N \frac{R_{jh}}{\ell_{jh}} - \frac{R_{ij}}{\ell_{ij}} + k_{ij} \sum_m \lambda_m C_{m,j} \quad (2.26)$$

$$\frac{dC_{m,i}}{dt} = \beta_{m,i} \sum_{h=1}^N \frac{R_{jh}}{\ell_{jh}} - \lambda_m C_{m,i}, \quad \sum_m \beta_{m,i} = \beta_i \quad (2.27)$$

N_{ij} can be considered as a metric akin to neutron density and it serves as a measure of the weighted number of neutrons in the system that were born in reactor j and will proceed to produce next generation neutrons in reactor i . dR_{ij}/dt is given by the difference in production and loss rates for the aforementioned type of these coupling neutrons. The production rate consists of the prompt production term and the delayed production term. $S_j = \sum_h \frac{R_{jh}}{\ell_{jh}}$ is the total number of source neutrons in reactor j , of which the prompt neutrons are $(1 - \beta) S_j$.

The prompt production rate is given by

$$k_{ij} (1 - \beta) S_j \quad (2.28)$$

while the delayed production rate, by

$$k_{ij} \sum_m \lambda_m C_{m,j} \quad (2.29)$$

The term R_{ij}/ℓ_{ij} represents the loss rate of R_{ij} type neutrons. Avery states that the inclusion of the above is because of the lack of correlation between the k_{ij} coupling coefficients themselves and the related average prompt neutron lifetimes, ℓ_{ij} . To solve the direct problem, the k_{ij} is considered time-dependent, but the ℓ_{ij} is constant with time. Then, one solves for the time dependence of the N_{ij} and $C_{m,j}$ variables.

2.1.3 Adjoint kinetics equations

For the adjoint formulation, Avery assumes only prompt neutrons, for the sake of simplicity. While this is a significant assumption, it does not affect the extracted conclusions. Equation (2.26) is then written as

$$\frac{dR_{ij}}{dt} = k_{ij} \sum_{h=1}^N \frac{R_{jh}}{\ell_{jh}} - \frac{R_{ij}}{\ell_{ij}} \quad (2.30)$$

and its adjoint is

$$\frac{dR_{ij}^\dagger}{dt} = \sum_{h=1}^N k_{hi} \frac{R_{hi}^\dagger}{\ell_{ij}} - \frac{R_{ij}^\dagger}{\ell_{ij}} \quad (2.31)$$

For the example of the two reactor case, dR_{12}^\dagger/dt would be written as

$$\frac{dR_{12}^\dagger}{dt} = k_{11} \frac{R_{11}^\dagger}{\ell_{12}} + k_{21} \frac{R_{21}^\dagger}{\ell_{12}} - \frac{R_{12}^\dagger}{\ell_{12}} \quad (2.32)$$

and by solving for the ratio of the steady-state values of R_{ij}^\dagger it stands that

$$R_{ij}^\dagger = R_{ih}^\dagger = R_i^\dagger \quad (2.33)$$

Regarding the reactivity, the parameter α_i of Eq. (2.22) can be expressed as

$$\alpha_i = \frac{R_i^\dagger S_i}{\sum_{h=1}^N R_h^\dagger S_h} \quad (2.34)$$

The quantity α_i is equal to the fraction of the importance production rate of the system, from all fission source neutrons born in reactor i . In turn, the average importance of a fission neutron born in reactor i is defined by R_i^\dagger .

Regarding the rate that the importance changes, the rate of removal from the i, j^{th} region is

$$R_{ij}^\dagger S_{ij} = R_i^\dagger S_{ij} \quad (2.35)$$

and from the entire system

$$\sum_{i,j} R_{ij}^\dagger S_{ij} = \sum_i R_i^\dagger S_i \quad (2.36)$$

As for the rate that importance is born into i , j^{th} region, it is

$$k_{ij} R_{ij}^\dagger S_j = k_{ij} R_i^\dagger S_j \quad (2.37)$$

and into the entire system

$$\sum_{i,j} k_{ij} R_{ij}^\dagger S_j = \sum_{i,j} k_{ij} R_i^\dagger S_i \quad (2.38)$$

Looking at Eq. (2.33) and considering a steady-state, one can see that the resulting values from Eq. (2.37) and Eq. (2.38) are the same as for Eq. (2.35) and Eq. (2.36), meaning that the rate of importance removal to productions is unity and the total importance remains stable. The amount of importance in the i , j^{th} region is given by the product of the importance change rate and the neutron lifetime for that region.

Using the definition for the redundant variables from Eq. (2.25), the importance of the i , j^{th} region is

$$R_i^\dagger R_{ij} \quad (2.39)$$

and the entire system

$$\sum_{i,j} R_i^\dagger R_{ij} \quad (2.40)$$

2.1.4 Prompt neutron lifetime

The prompt neutron lifetime ℓ is the time it takes for a prompt neutron that was just born, to either be absorbed or escape and is heavily dependent on the material composition in the system, its geometry and its size. It can be defined as the ratio of the total neutron importance in the system to the rate of the importance removal. It can be written as

$$\ell = \frac{\sum_{i,j} R_{ij}^\dagger R_{ij}}{\sum_{i,j} R_{ij}^\dagger S_{ij}} = \frac{\sum_{i,j} R_{ij}^\dagger S_{ij} \ell_{ij}}{\sum_{i,j} R_{ij}^\dagger S_{ij}} \quad (2.41)$$

At steady-state, both the relative R_{ij}^\dagger and S_{ij} values do not involve ℓ_{ij} and thus, Eq. (2.41) gives the prompt neutron lifetime as a linear combination of the region-wise partial lifetimes.

The two reactor case gives

$$\ell = \frac{\Delta_2 k_{11}}{\Delta_1 + \Delta_2} \ell_{11} + \frac{\Delta_1 k_{22}}{\Delta_1 + \Delta_2} \ell_{22} + \frac{\Delta_1 \Delta_2}{\Delta_1 + \Delta_2} (\ell_{12} + \ell_{21}) \quad (2.42)$$

Since there exists a weighting factor attached to intervals between fissions and it depends on the region-wise importance, ℓ is not the average time between prompt fissions. The weighting factor for ℓ_{ij} is

$$\frac{S_{ij}}{\sum_{i,j} S_{ij}} \quad (2.43)$$

and finally the average time between fissions is,

$$\bar{\ell} = \frac{\Delta_2 k_{11}}{\Delta_2 + k_{21}} \ell_{11} + \frac{\Delta_1 \Delta_2}{\Delta_1 + k_{12}} \ell_{21} + \frac{\Delta_1 \Delta_2}{\Delta_2 + k_{21}} \ell_{12} + \frac{\Delta_1 k_{22}}{\Delta_1 + k_{12}} \ell_{22} \quad (2.44)$$

One notable point is that the cross lifetimes ℓ_{12} and ℓ_{21} initially have the same weighting factor in Eq. (2.42) and end up having different ones in Eq. (2.44). The latter makes sense if one considers the fact that they are associated with different numbers of fissions. The term in 2.42 is a consequence of the fact that the relative importance for each event is such as to maintain an equal total importance production between neutrons going from reactor 1 to reactor 2 and neutrons going from reactor 2 to 1.

2.2 Kobayashi's Multipoint Kinetics

Between 1958 and the 90's, a series of works had been developed that expanded upon Avery's theory. However, they are either based on physical considerations, are complicated or include approximations. Seeking to develop a nodal model for coupled reactors that was rigorously derived from well understood concepts, Keisuke Kobayashi released a series of papers [21–24] in the 90's that described this process and he describes his approach as an expansion upon the single point reactor kinetics problem.

2.2.1 Static problem

The starting point is the static multigroup transport equation, with the fission source of every reactor (or region) as an unknown. Consider a multiple reactor system V and its boundary L . The assumed boundary condition is that the incoming neutron flux at the boundary is zero. This can be written as

$$\psi = \psi_g(\mathbf{r}, \boldsymbol{\Omega}) = 0, \text{ for } \boldsymbol{\Omega} \cdot \mathbf{n} < 0 \text{ at } \mathbf{r} \in L \quad (2.45)$$

ψ_g denotes the total angular flux of the energy group g for direction $\boldsymbol{\Omega}$, \mathbf{n} is the outward unit vector normal to surface L .

The system can be described by

$$A\psi_g(\mathbf{r}, \boldsymbol{\Omega}) = \frac{1}{k} B\psi_g(\mathbf{r}, \boldsymbol{\Omega}) \quad (2.46)$$

where $k = k_{eff}$ is the balancing eigenvalue that guarantees a steady-state system. The operators A and B are given by

$$A\psi_g(\mathbf{r}, \boldsymbol{\Omega}) = (\boldsymbol{\Omega}\nabla + \Sigma_{t,g})\psi_g(\mathbf{r}, \boldsymbol{\Omega}) - \sum_{g'} \int_{4\pi} d\boldsymbol{\Omega}' \Sigma_s(g, \boldsymbol{\Omega} \leftarrow g', \boldsymbol{\Omega}') \psi_{g'}(\mathbf{r}, \boldsymbol{\Omega}') \quad (2.47)$$

and

$$B\psi_g(\mathbf{r}, \boldsymbol{\Omega}) = \frac{\chi_g}{4\pi} \sum_{g'} \nu \Sigma_{f,g'}(\mathbf{r}) \int_{4\pi} d\boldsymbol{\Omega} \psi_{g'}(\mathbf{r}, \boldsymbol{\Omega}) = \frac{\chi_g}{4\pi} F\psi_g(\mathbf{r}, \boldsymbol{\Omega}) \quad (2.48)$$

The fission operator F is defined via

$$F\psi_g(\mathbf{r}, \boldsymbol{\Omega}) = \sum_{g'} \nu \Sigma_{f,g'}(\mathbf{r}) \int_{4\pi} d\boldsymbol{\Omega} \psi_{g'}(\mathbf{r}, \boldsymbol{\Omega}) \quad (2.49)$$

The notations $\Sigma_{t,g}$, $\nu \Sigma_{f,g}$ and χ_g are the total cross section, average neutron production through fission and average fission neutron spectrum for group g , respectively. $\Sigma_s(g, \boldsymbol{\Omega} \leftarrow g', \boldsymbol{\Omega}')$ denotes the scattering cross section from group g' and direction $\boldsymbol{\Omega}'$ to group g and direction $\boldsymbol{\Omega}$.

The adjoint of operator A is

$$A^\dagger = -\boldsymbol{\Omega}\nabla + \Sigma_{t,g} - \sum_{g'} \int_{4\pi} d\boldsymbol{\Omega}' \Sigma_s(g, \boldsymbol{\Omega} \rightarrow g', \boldsymbol{\Omega}') \quad (2.50)$$

A Green's function is defined through

$$A^\dagger G(\mathbf{r}, \boldsymbol{\Omega}, g; \mathbf{r}', g') = \delta(\mathbf{r} - \mathbf{r}') \delta_{gg'} \quad (2.51)$$

and must satisfy the boundary condition

$$G(\mathbf{r}, \boldsymbol{\Omega}, g; \mathbf{r}', g') = 0, \text{ for } \boldsymbol{\Omega} \cdot \mathbf{n} > 0 \text{ at } \mathbf{r} \in L \quad (2.52)$$

If Eq. (2.46) is multiplied by Eq. (2.52), Eq. (2.51) is multiplied by $\psi_g(\mathbf{r}, \boldsymbol{\Omega})$ and their difference is integrated over the system V , the solid angle and summed over the energy groups, the resulting expression is

$$\int_{4\pi} d\boldsymbol{\Omega} \psi_{g'}(\mathbf{r}', \boldsymbol{\Omega}) = \frac{1}{4\pi k} \int_V d\mathbf{r} \int_{4\pi} d\boldsymbol{\Omega} \sum_g G(\mathbf{r}, \boldsymbol{\Omega}, g; \mathbf{r}', g') \chi_g S(\mathbf{r}) \quad (2.53)$$

where $S(\mathbf{r})$ is the number of neutrons produced per unit volume in a unit time and is defined by

$$S(\mathbf{r}) = \sum_{g'} \nu \Sigma_{f,g'}(\mathbf{r}) \int_{4\pi} d\boldsymbol{\Omega} \psi_{g'}(\mathbf{r}, \boldsymbol{\Omega}) = F\psi_g(\mathbf{r}, \boldsymbol{\Omega}) \quad (2.54)$$

An integral equation for the fission source can be written as

$$S(\mathbf{r}) = \frac{1}{4\pi k} \sum_g \nu \Sigma_{f,g}(\mathbf{r}) \int_V d\mathbf{r}' \int_{4\pi} d\boldsymbol{\Omega}' \sum_{g'} G(\mathbf{r}', \boldsymbol{\Omega}', g'; \mathbf{r}, g) \chi_{g'} S(\mathbf{r}') \quad (2.55)$$

and can be solved if the corresponding Green's function is known. This expression for $S(\mathbf{r})$ enables the reader to understand the physical meaning of $G(\mathbf{r}', \Omega', g'; \mathbf{r}, g)$; it expresses the total flux integrated over angle at \mathbf{r} with energy g , induced by a neutron generated at \mathbf{r}' , with energy g' and direction Ω' .

For a region in the system V , denoted as V_i , that has a non zero fission cross section, the following importance function is introduced

$$G_i(\mathbf{r}, \Omega, g) = \int_{V_i} d\mathbf{r}' \sum_{g'} \nu \Sigma_{f,g'}(\mathbf{r}') G(\mathbf{r}, \Omega', g; \mathbf{r}', g') \quad (2.56)$$

If Eq. (2.51) is multiplied by $\nu \Sigma_{f,g'}(\mathbf{r}')$, integrated over the region V_i and summed over the energy groups, the following expression is obtained

$$A^\dagger G_i(\mathbf{r}, \Omega, g) = \nu \Sigma_{f,g}(\mathbf{r}) \delta_i(\mathbf{r}), \quad \delta_i(\mathbf{r}) = \begin{cases} 1, & r \in V_i \\ 0, & r \notin V_i \end{cases} \quad (2.57)$$

The advantage of this expression is that $G_i(\mathbf{r}, \Omega, g)$ can be solved with relative ease if one takes the adjoint multigroup equation without a system-wide fission term, with only a fixed fission term in region V_i .

S_i is the fission source corresponding to the fission neutrons produced in V_i in a unit time,

$$S_i = \int_{V_i} d\mathbf{r} S(\mathbf{r}) = \int_{V_i} d\mathbf{r} \sum_g \nu \Sigma_{f,g}(\mathbf{r}) \int_{4\pi} d\Omega \psi_g(\mathbf{r}, \Omega) \quad (2.58)$$

With the help of 2.57, the region-wise source is written as

$$S_i = \frac{1}{4\pi k} \int_V d\mathbf{r}' \int_{4\pi} d\Omega' \sum_{g'} G_i(\mathbf{r}', \Omega', g'; \mathbf{r}, g) \chi_{g'} S(\mathbf{r}') \quad (2.59)$$

and is potentially easier to solve than Eq. (2.58), because of the $G_i(\mathbf{r}', \Omega', g'; \mathbf{r}, g)$ term. The function G_i expresses the expected number of fission neutrons born in V_i by a neutron born at position \mathbf{r} , with direction Ω and its energy within group g . The solution of G_i can be obtained by solving the adjoint multigroup equation with the fixed term $\nu \Sigma_{f,g}(\mathbf{r})$ in the region V_i . For a two-region system, where V_i and V_j are the two regions, the coupling coefficient is calculated as

$$k_{ij} = \frac{\frac{1}{4\pi} \int_{V_j} d\mathbf{r}' \int_{4\pi} d\Omega' \sum_{g'} G_i(\mathbf{r}', \Omega', g') \chi_{g'} S(\mathbf{r}')}{\int_{V_j} d\mathbf{r}' S(\mathbf{r}')} \quad (2.60)$$

where χ is the average fission neutron spectrum. Using (2.60) on (2.59), one obtains the nodal equation for N coupled systems,

$$S_i = \frac{1}{k} \sum_{j=1}^N k_{ij} S_j \quad (2.61)$$

2.2.2 Time-dependent problem

If one considers time dependence, (2.46) becomes

$$\frac{1}{v_g} \frac{\partial \psi_g(\mathbf{r}, \boldsymbol{\Omega}, t)}{\partial t} = -[A - (1 - \beta) B^p] \psi_g(\mathbf{r}, \boldsymbol{\Omega}, t) + \frac{1}{4\pi} \sum_m \chi_{m,g}^d \lambda_m C_m(\mathbf{r}, t) \quad (2.62)$$

C_m , λ_m and $\chi_{m,g}^d$ are the precursor density, decay constant and delayed neutron energy for the respective precursor/delayed neutron group, $m = 1, 2, 3, \dots$, while χ_g^p , v_g and β denote the prompt neutron spectrum for energy group g , neutron velocity for group g and the delayed neutron fraction. The global precursor density for the delayed neutron group m , $m = 1, 2, 3, \dots$ is given by

$$\frac{\partial C_m(\mathbf{r}, t)}{\partial t} = \beta_m F \psi_g(\mathbf{r}, \boldsymbol{\Omega}, t) - \lambda_m C_m(\mathbf{r}, t), \quad \sum_m \beta_m = \beta \quad (2.63)$$

The region-wise coupling coefficient can now be broken down in a prompt and a delayed part. The two parts are

$$k_{ij}^p(t) = \frac{\frac{1}{4\pi} \int_{V_j} d\mathbf{r} \int_{4\pi} d\boldsymbol{\Omega} \sum_g G_i(\mathbf{r}, \boldsymbol{\Omega}, g) \chi_g^p S(\mathbf{r}, t)}{\int_{V_j} d\mathbf{r} S(\mathbf{r}, t)} \quad (2.64)$$

and

$$k_{m,ij}^d(t) = \frac{\frac{1}{4\pi} \int_{V_j} d\mathbf{r} \int_{4\pi} d\boldsymbol{\Omega} \sum_g G_i(\mathbf{r}, \boldsymbol{\Omega}, g) \chi_{m,g}^d \lambda_m C_m(\mathbf{r}, t)}{\int_{V_j} d\mathbf{r} C_m(\mathbf{r}, t)} \quad (2.65)$$

Consequently, the region-dependent neutron lifetime for region i (Kobayashi defines this parameter's physical meaning for the one-point model as the mean neutron production time [32]) and coupled delayed neutron fraction (the part of the fissions at next generation in i due to only the delayed neutrons born in j , with respect to the total number of fissions at next generation in i due to all neutrons produced in j) are written as,

$$\ell_i(t) = \frac{\int_V d\mathbf{r} \int_{4\pi} d\boldsymbol{\Omega} \sum_g G_i(\mathbf{r}, \boldsymbol{\Omega}, g) \frac{1}{v_g} \frac{\partial \psi_g(\mathbf{r}, \boldsymbol{\Omega}, t)}{\partial t}}{\int_{V_i} d\mathbf{r} \frac{\partial S(\mathbf{r}, t)}{\partial t}} \quad (2.66)$$

and

$$\beta_{ij}(t) = \frac{\frac{1}{4\pi} \int_{V_j} d\mathbf{r} \int_{4\pi} d\boldsymbol{\Omega} \sum_g G_i(\mathbf{r}, \boldsymbol{\Omega}, g) \beta \chi_g^d S(\mathbf{r}, t)}{k_{ij}^p(t) \int_{V_j} d\mathbf{r} S(\mathbf{r}, t)} \quad (2.67)$$

The equation for the partial precursor density for region i is

$$\frac{dC_{m,i}(t)}{dt} = \beta_{m,i} S_i(t) - \lambda_m C_{m,i}(t) \quad (2.68)$$

And finally, the region-wise delayed neutron fraction for region i and delayed neutron family m is

$$\beta_{m,i} = \frac{\int_{V_i} d\mathbf{r} \int_{4\pi} d\boldsymbol{\Omega} \beta_m F \psi_g(\mathbf{r}, \boldsymbol{\Omega}, t)}{\int_{V_i} d\mathbf{r} S(\mathbf{r}, t)}, \quad \sum_m \beta_{m,i} = \beta_i \quad (2.69)$$

2.2.3 Diffusion problem

Similar to the above approach to the multipoint kinetics problem starting from the transport equation, a diffusion based approach is also possible and sometimes more useful, depending on the computational capabilities of the solver used. In the general, time-dependent case, the expression that describes the system is now,

$$\frac{1}{v_g} \frac{\partial \phi_g(\mathbf{r}, t)}{\partial t} = (\nabla D_g \nabla + \Sigma_{a,g}) \phi_g(\mathbf{r}, t) + \sum_{g'} \Sigma_s(g \leftarrow g') \phi_{g'}(\mathbf{r}, t) + \chi_g^p(1 - \beta) \sum_{g'} \nu \Sigma_{f,g'} \phi_{g'}(\mathbf{r}, t) + \chi_g^d \sum_m \lambda_m C_m(\mathbf{r}, t) \quad (2.70)$$

with

$$\frac{dC_m(\mathbf{r}, t)}{dt} = \beta_m \sum_{g'} \nu \Sigma_{f,g'}(\mathbf{r}) \phi_{g'}(\mathbf{r}, t) - \lambda_m C_m(\mathbf{r}, t), \quad \sum_m \beta_m = \beta \quad (2.71)$$

The scalar neutron flux of energy group g and position \mathbf{r} is represented by $\phi_g(\mathbf{r})$, D_g is the diffusion coefficient, $\Sigma_{a,g}$ is the absorption cross section, $\Sigma_s(g \leftarrow g')$ is the scattering cross section from group g' to g , $\nu \Sigma_{f,g}$ is the neutron multiplicity and the fission cross section and finally, χ_g^p and χ_g^d are the average prompt and delayed fission neutron spectra.

Following the same process as before, the time dependent coupling coefficients for prompt and delayed neutrons are given by

$$k_{ij}^p(t) = \frac{\int_{V_j} d\mathbf{r} \sum_g G_i(\mathbf{r}, g) \chi_g^p S(\mathbf{r}, t)}{\int_{V_j} d\mathbf{r} S(\mathbf{r}, t)} \quad (2.72)$$

and

$$k_{m,ij}^d(t) = \frac{\int_{V_j} d\mathbf{r} \sum_g G_i(\mathbf{r}, g) \chi_{m,g}^d C_m(\mathbf{r}, t)}{\int_{V_j} d\mathbf{r} C_m(\mathbf{r}, t)} \quad (2.73)$$

The region dependent neutron lifetime is calculated as

$$l_i(t) = \frac{\int_V d\mathbf{r} \sum_g G_i(\mathbf{r}, g) \frac{1}{v_g} \frac{\partial \phi_g(\mathbf{r}, t)}{\partial t}}{\int_{V_i} d\mathbf{r} \frac{\partial S(\mathbf{r}, t)}{\partial t}} \quad (2.74)$$

while the region dependent delayed neutron fraction is given by

$$\beta_{ij} = \frac{\int_{V_j} d\mathbf{r} \sum_g G_i(\mathbf{r}, g) \beta \chi_g^d S(\mathbf{r}, t)}{k_{ij}^p(t) \int_{V_j} d\mathbf{r} S(\mathbf{r}, t)} = \frac{\int_{V_j} d\mathbf{r} \sum_g G_i(\mathbf{r}, g) \beta \chi_g^d S(\mathbf{r}, t)}{\int_{V_j} d\mathbf{r} \sum_g G_i(\mathbf{r}, g) \chi_g^p S(\mathbf{r}, t)} \quad (2.75)$$

where $G_i(\mathbf{r}, g)$ is the region-wise importance function.

The partial delayed neutron fraction is given by

$$\beta_{m,i}(t) = \frac{\int_{V_i} d\mathbf{r} \beta_m F' \phi_g(\mathbf{r}, t)}{\int_{V_i} F' \phi_g(\mathbf{r}, t)} = \frac{\int_{V_i} d\mathbf{r} \beta_m S(\mathbf{r}, t)}{\int_{V_i} S(\mathbf{r}, t)}, \quad \sum_m \beta_{m,i} = \beta_i \quad (2.76)$$

Lastly, for the steady-state case, the k_{ij} coupling coefficients are given by

$$k_{ij} = \frac{\sum_g \chi_g \int_{V_j} d\mathbf{r} G_i(\mathbf{r}) S(\mathbf{r})}{\int_{V_j} d\mathbf{r} S(\mathbf{r})} \quad (2.77)$$

A comparison between Avery's and Kobayashi's multipoint kinetics models can be found in [33].

2.2.4 Implementation in ERANOS

Kobayashi's approach was implemented in the ERANOS code externally, with all calculation steps written directly in the input file.

The first part of the process consists of the region homogenization and cross section calculation part in the ECCO module. The pin-wise structure is defined and a homogenization scheme in ECCO produced self-shielded cross sections and homogenized media. At this stage, the different media that will make up the volumes corresponding to the aforementioned i, j, \dots regions are defined, alongside all other necessary media. Next the geometry is constructed and the method allows to define a coupling region comprised by multiple homogenized media, allowing any kind of region shape to be used for coupling and/or discretization. The only current limitation here is that it is not possible to have a zone with no multiplying media at all, since the region-wise source term cannot be zero.

In summary, the process in ERANOS starts with a forward and adjoint flux calculation in 33 groups, the purpose of which is to produce forward and adjoint flux sets. For 2D geometries, the BISTRO Sn transport solver [34] can be used. However, it was determined that a diffusion calculation is a necessary compromise, as the transport solver's discretization scheme produced inconsistencies related to mesh selection when coupled with the discretization of the coupled regions (the transport solver takes the middle of each mesh, while the multipoint scheme and the diffusion solver take the edges of each mesh) in the 2D case and the solver is unavailable in the 3D case. All results shown in this work were obtained with steady-state 3D diffusion calculations.

The next step calculates the effective delayed neutron fraction for 8 delayed neutron families and the average prompt and delayed neutron lifetimes. Required precursor decay constants and delayed neutron yields and energy spectra are taken from the JEFF-3.1 library.

After that, the partial sources are calculated for each region participating in the multipoint calculation. What follows is another adjoint diffusion calculation without fission source for each region, calculating the region-wise importances G_i , as described by Eq.

(2.57).

At this point, the coupling coefficients can be calculated for the next generation, both in the k_{ij} and in the $k_{m,ij}^d$ forms, as well as the region-wise neutron lifetime ℓ_i , the partial delayed neutron fraction β_i , partial neutron fraction per delayed neutron family $\beta_{m,i}$ and coupled delayed neutron fraction β_{ij} .

The k_{ij} matrix is then treated within the GNU Octave software, at which point the eigenvalues and eigenvectors can be extracted. Following that, the dominance ratio $DR = k_1/k_0$ and eigenvalue separation $EVS = (k_0k_1)/(k_0 - k_1)$ are computed.

Multipoint kinetics models have been similarly implemented in other codes and solvers [35–37].

2.3 The Transient Fission Matrix method

A general fission matrix is a tool designed to characterize the neutron propagation after one generation, with the Green function being the response to a neutron pulse and the fission matrices correspond to the discretization of the Green functions. By design, the multiplication applied on the generation q source neutron vector (\mathbf{N}_q) corresponds to the propagation of this source neutron over one generation ($\mathbf{N}_{q+1} = \underline{G}\mathbf{N}_q$). The fission matrix eigenvector is the solution of the equation

$$\underline{G}\mathbf{N} = k_{eff}\mathbf{N} \quad (2.78)$$

Since the method tracks the neutron propagation in the system, the eigenvector of a matrix corresponds to the source distribution at equilibrium. As it will be seen later, the eigenvector shape can be used to study the behavior of the system by representing the fission source shape. More specifically, the right eigenvectors access forward source modes [38] and if the fission matrix discretization is good enough, left eigenvectors access adjoint flux modes [39].

The Transient Fission Matrix (TFM) model [13–19], allows for the spatial kinetic modeling of a nuclear system by pre-calculating the time dependent transport characteristics. The information contained in a fission matrix is the probability that a neutron born in volume j (or V_j) produces a new fission neutron in a volume i (or V_i), where V_i and V_j are volumes of a discretized geometry (propagation probability). During a Monte Carlo calculation, for each neutron emitted in j , its fission neutron production $\nu\Sigma_f\psi$ is estimated in each volume i . k_{ij} matrices are constructed, that condense the whole transport neutron information during one generation. The information is presented in four matrices (line i , column j), according to the neutron emission spectrum χ and the neutron multiplicity ν ,

differentiating between prompt p and delayed d cases. Thus, four different matrices have to be calculated: $\underline{G}_{\chi_p \nu_p}$, $\underline{G}_{\chi_p \nu_d}$, $\underline{G}_{\chi_d \nu_p}$ and $\underline{G}_{\chi_d \nu_d}$, where χ refers to the origin volume and ν refers to the target volume. Delayed neutron information is condensed and presented in one delayed group. Prompt and delayed neutrons differ greatly in both emission spectra and thus in their behavior in the reactor. Their multiplicities also differ greatly, due to the very different way they are produced. The above make the distinction in the four aforementioned matrices necessary, if one is to perform kinetics calculations. The \underline{G} matrices take into account the type of neutron at its birth, as well as the type of neutron it creates after one generation. To take into account coupled effects between prompt and delayed neutron, a block matrix is constructed,

$$\underline{G}_{all} = \begin{pmatrix} \underline{G}_{\chi_p \nu_p} & \underline{G}_{\chi_d \nu_p} \\ \underline{G}_{\chi_p \nu_d} & \underline{G}_{\chi_d \nu_d} \end{pmatrix} \quad (2.79)$$

The \underline{G}_{all} operates on the eigenvector $N_{eq,all} = (N_{eq,p}, N_{eq,d})$, which corresponds to the prompt and delayed neutron distribution at equilibrium. The \underline{G}_{all} matrix is associated to the eigenvalues of the system. Additionally, the eigenvector of the $\underline{G}_{\chi_p \nu_p}$ matrix gives the shape of the neutron source [16].

The temporal aspect, a requirement to deal in kinetics with fission matrices, is covered by obtaining the average prompt neutron fission-to-fission time (generation time) from j to i , stored in the $\underline{T}_{\chi_p \nu_p}$ matrix. Due to the difference between the precursor lifetime and the neutron transport time, this matrix is enough for the calculation.

All the matrices discussed below are calculated with a modified version of the Serpent 2 neutron transport code (specifically the 2.1.21 version). The process does introduce a geometrical systemic bias in the calculation of the fission source shape due to the discretization of the fission matrix [17] (same as other multipoint methods), which decreases with the number of nodes.

This approach allows the estimation of reactor kinetic parameters as well [17]. The $\underline{T}_{\chi_p \nu_p}$ matrix in conjunction with the original fission matrices, can produce β , the effective delayed neutron fraction and Λ , the effective neutron generation time in the system. In the case of an infinite lattice, the latter is governed solely by absorption, while in a finite system, leakage must also be considered.

The term $G_{\chi_p \nu_p}(t - t', \mathbf{r}', \mathbf{r})$ represents the probability that a prompt neutron will be created at \mathbf{r} , from a prompt neutron created at \mathbf{r}' , after time $t'' = t' - t$. $\underline{T}_{\chi_p \nu_p}$ here denotes the discretized version of the operator $T_{\chi_p \nu_p}(\mathbf{r}', \mathbf{r})$.

$$T_{\chi_p \nu_p}(\mathbf{r}', \mathbf{r}) = \frac{\int_{t''} dt'' G_{\chi_p \nu_p}(t'', \mathbf{r}', \mathbf{r}) t''}{\int_{t''} dt'' G_{\chi_p \nu_p}(t'', \mathbf{r}', \mathbf{r})}, \text{ for } t'' > 0 \quad (2.80)$$

$$\underline{T}_{\chi_p \nu_p, ij} = \frac{\sum_{\Delta t_k} q_{\chi_p \nu_p, ij} (\Delta t_k)^{\frac{t_k + t_{k+1}}{2}}}{\sum_{\Delta t_k} q_{\chi_p \nu_p, ij} (\Delta t_k)} \quad (2.81)$$

Time is discretized and Δt_k is the interval between t_k and t_{k+1} , while g denotes the current generation. The terms and the process of calculating the rest of the quantities appearing here are explained in [17].

Continuing, the operator $\tilde{G}_{\chi_x \nu_x}(\mathbf{r}', \mathbf{r}) = \int_{-\infty} dt' G_{\chi_x \nu_x}(t - t', \mathbf{r}', \mathbf{r})$, its discretized version $\underline{G}_{\chi_x \nu_x}$ and the prompt fission neutron production shape that corresponds to it, \mathbf{S} , are defined. To obtain the effective neutron lifetime $\ell = \ell_{eff}$, importance must be taken into account. This is done with the adjoint operator $\tilde{G}_{\chi_x \nu_x}^\dagger$ and its eigenvector is defined as $N_p^*(\mathbf{r})$. ℓ can be calculated by

$$\ell = \frac{\int \int_{\mathbf{r}, \mathbf{r}'} d\mathbf{r}' d\mathbf{r} N_p^*(\mathbf{r}) \left[T_{\chi_p \nu_p}(\mathbf{r}', \mathbf{r}) \tilde{G}_{\chi_p \nu_p}(\mathbf{r}', \mathbf{r}) \right] N_p(\mathbf{r}')}{\int \int_{\mathbf{r}, \mathbf{r}'} d\mathbf{r}' d\mathbf{r} N_p^*(\mathbf{r}) \tilde{G}_{\chi_p \nu_p}(\mathbf{r}', \mathbf{r}) N_p(\mathbf{r}')} \quad (2.82)$$

Note that in the context of the TFM model, ℓ corresponds only to fission-to-fission lifetime, since (n, γ) and other non-fission reactions carry no importance.

β is calculated directly as $\beta = 1 - k_p$, under the condition that the system is critical with $k_{eff} = 1$. The value of k_p is calculated by verifying equilibrium conditions, either by specifying the total neutron population of the system or making sure that precursor population is stable over time. The fission matrices have to be adjusted iteratively in order to obtain this equilibrium condition.

Three terms are introduced. $N_p(t)$, the prompt neutron production at time t , $\sum_m \lambda_m C_m(t)$, the delayed neutron production by precursor decay, with $C_m(t)$ being the precursor density and λ_m the decay constant, and subsequently $\underline{G}_{\chi_d \nu_p} \sum_m \lambda_m C_m(t)$, that enables to account for the importance of delayed neutrons by expressing the probability for delayed neutrons to produce new prompt neutrons. The subscript $m = 1, 2, 3, \dots$ denotes the corresponding delayed neutron group.

Using these new terms, the following balance equations are constructed [14, 17]:

$$\frac{dN_p(t)}{dt} = \underline{G}_{\chi_p \nu_p} \frac{1}{\ell} N_p(t) + \underline{G}_{\chi_d \nu_p} \sum_m \lambda_m C_m(t) - \frac{1}{\ell} N_p(t) \quad (2.83)$$

$$\frac{dC_m(t)}{dt} = \frac{\beta_m}{\beta} \left(\underline{G}_{\chi_p \nu_d} \frac{1}{\ell} N_p(t) + \underline{G}_{\chi_d \nu_d} \sum_m \lambda_m C_m(t) \right) - \lambda_m C_m(t), \quad \sum_m \beta_m = \beta \quad (2.84)$$

with the constraint that ℓ is relatively small compared to the time scale of the transient in question. Finally, the generation time $\Lambda = \Lambda_{eff}$ can be calculated as $\Lambda = \frac{\ell}{k_p}$.

Note that the above formulation does not take into account the different energy spectra corresponding to the different delayed neutrons groups. A more accurate approach would involve computing an m number of matrices. Also, it stands that $\frac{1}{\lambda_m} \approx \frac{1}{\lambda_m} + \ell$ if $\lambda_m \ell \ll 1$ but [13, 15] have shown that the approximations made here still end up with a good agreement of the results.

Comparing the above to Kobayashi's multipoint approach [22–24], one thing to note is that Kobayashi's importance function, $G_i(\mathbf{r}, \Omega, g)$, is akin to a fission matrix, based on its description. Apart from that, a few differences are apparent, starting with the fact that TFM uses a Monte Carlo calculation as its initial input. They mostly have to do with the TFM method's approximations, with Kobayashi's method going into more detail regarding the separate treatment of precursor groups, where each group has its own energy spectrum and also gives a way of getting β_{ij} values. Although not a real limitation, the information on neutron lifetime and delayed neutron fraction is presented differently, with Kobayashi outputting β_i values, while the TFM method outputs a global delayed neutron fraction. The same goes for ℓ . The latter are merely by the choice in the calculation scheme and not inherent limitations of TFM.

The TFM method utilizes a number of approximations in order to offer a lower running time and that's what its main purpose is. It inherently does suffer from errors related to Fission Matrix methods in Monte Carlo. Despite that, there appears to be good agreement with reference calculations, within a reasonable margin as shown in [13]. In Chapter 5, a comparison of results obtained with the TFM model versus results obtained directly with Serpent 2 and versus results obtained with Kobayashi's model in ERANOS, is given. The differences between the methods vary, with simpler geometries showing better agreement, but in all cases, they are on the order of a few percent, meaning that the two methods can complement each other in order to both analyze and design systems.

Chapter 3

Flux harmonics, dominance ratio and eigenvalue separation

Let a nuclear system be described by the following short formulation of the Boltzmann equation

$$\psi = \frac{1}{k_{eff}} B\psi , \quad B = (L + T - S)^{-1} F \quad (3.1)$$

where $\psi = \psi(\mathbf{r}, \Omega, E)$ is the neutron flux, k_{eff} is the effective neutron multiplication factor used to balance the production and loss terms and L , T , S , F are the leakage, collision, scattering and neutron production by fission operators, respectively. The B operator has several solutions y_n for the flux ψ , corresponding to different eigenvalues k_n , with

$$y_n = \frac{1}{k_n} B y_n , \quad k_0 > k_1 > k_2 > \dots \quad (3.2)$$

where $k_0 = k_{eff}$. The higher order solutions correspond to the so called flux harmonics, higher eigen-modes of the transport equation.

The dominance ratio (DR) of a nuclear system is defined as the ratio between the fundamental and first mode eigenvalues [40, 41],

$$DR = \frac{k_1}{k_0} \leq 1 \quad (3.3)$$

and the eigenvalue separation (EVS) is defined as [42],

$$EVS = \frac{k_0 k_1}{k_0 - k_1} \quad (3.4)$$

It has been shown that the higher the dominance ratio or eigenvalue separation, the higher the contribution of the first harmonic mode is to the overall behavior of the system. This translates to a higher degree of neutronic decoupling [43], which in turn leads to an

increased system response to perturbations [3, 4, 42, 44, 45]. A high dominance ratio or EVS is commonly associated with large, thermal power cores, such as PWRs and BWRs (values close to or in excess of 0.99 are typical [40]), typically increases with irradiation time, especially at the beginning of the irradiation cycle [40] and is responsible for issues related to core stability [42, 43, 45, 46]. This can be shown if the perturbed flux is expressed as a sum of the fundamental flux and the flux harmonics, as [42],

$$\psi_{pert} = \psi_0 + \sum_{n=1}^N a_n \psi_n, \quad a_n = -\frac{k_0 k_n}{k_0 - k_n} \frac{\langle \psi_n^\dagger, (\delta A - \frac{\delta F}{k_0}) \psi_0 \rangle}{\langle \psi_n^\dagger, F \psi_n \rangle} \quad (3.5)$$

The EVS from Eq. (3.4) appears naturally in this expression. Furthermore, a high dominance ratio has been shown to create convergence issues in the power iteration method of calculation codes [41], with the error associated with the flux convergence improving as the term k_1/k_0 reduces. Experimentally, the eigenvalue separation has been measured for a few systems [47, 48].

The coupling coefficients that are obtained with any of the methods discussed thus far, form a matrix that describes the neutronic coupling of the system at hand, in terms of the probability that a neutron born in region j will create a next generation neutron in region i . The eigenvector of a k_{ij} matrix can give the shape of the fission source and solving for the eigenvalues of the matrix is similar to solving for the eigenvalues of the neutron transport problem [49]. Thus, the coupling coefficients can be associated with the dominance ratio or eigenvalue separation [50]. The amount of coupling regions determines how many fission source modes can be accessed [51] and how accurate their shapes will be [42], with the first matrix eigenvector corresponding to the fundamental mode. At minimum, two coupling regions are required to access the first source harmonic mode, three coupling regions are required for the second mode etc. While the fission source distribution modes are different from the actual flux harmonic modes, the first eigenvalue of the k_{ij} matrix corresponds to the fundamental eigenvalue k_0 of the transport problem. Higher order eigenvalues of the matrix can approach the eigenvalues corresponding to the flux harmonics and the accuracy improves with discretization [43]. Thus, especially for heterogeneous geometries, a higher number of coupling regions is desirable and this is explored in Chapters 4 and 5. Furthermore, the discretization scheme determines what kind of harmonics are accessed - azimuthal, radial or axial [52, 53].

The dominance ratio can also be associated to the flux or power tilt in a reactor core [45, 54]. For a core separated into two regions (or a system comprised of two reactors), the coupling coefficients matrix becomes,

$$k_{ij} = \begin{pmatrix} k_{11} & k_{12} \\ k_{21} & k_{22} \end{pmatrix} \quad (3.6)$$

Regions that are tightly coupled, typically display a low dominance ratio and as a consequence, will exhibit at least one significant coefficient for $i \neq j$ and at least one region will display considerable subcriticality. On the contrary, loosely coupled regions, with a high system dominance ratio, typically exhibit small coupling coefficients, will both be closer to criticality on their own and are expected to display significant tendencies for power shape tilts. This can be shown better if one expresses the fractional power in the two regions as [29, 55],

$$f_1 = \frac{k_{12}}{1 - k_{11} + k_{12}} \quad (3.7)$$

and

$$f_2 = \frac{k_{21}}{1 - k_{22} + k_{21}} = \frac{1 - k_{11}}{1 - k_{11} + k_{12}} \quad (3.8)$$

When the terms $k_{11} - k_{12}$ or $k_{22} - k_{21}$ become close to one, the relative power distribution becomes sensitive to small changes and thus power tilts become an issue for loosely coupled cores.

From the above, one can see how loosely coupled cores, such as those found in PWRs and BWRs, suffer from power tilt issues and how tightly coupled cores, do not. It is thus interesting to design small cores that exhibit high dominance ratios, or convert existing ones to do so, as they can then be used to study large core effects and a number of studies on representativity of both thermal and fast cores have been carried out on the subject [56–58].

3.1 Reduced order model for the dominance ratio

It is useful to connect the dominance ratio to simple reactor quantities, as a means to predict its behavior when changes occur in the system. Starting from the one-speed diffusion theory, the general form of the static diffusion equation is [59]

$$-D\nabla^2\phi(\mathbf{r}) + \Sigma_a\phi(\mathbf{r}) = \nu\Sigma_f\phi(\mathbf{r}), \quad \phi(\tilde{\mathbf{r}}_s) = 0 \quad (3.9)$$

where ϕ is the scalar flux, D is the diffusion coefficient, $\Sigma_a\phi(\mathbf{r})$ is the absorption term, $\Sigma_f\phi(\mathbf{r})$ is the neutron production through fission and $\tilde{\mathbf{r}}_s$ is the extrapolated boundary of the system. With the introduction of the buckling term B , Eq. (3.9) can be written as

$$\nabla^2\phi(\mathbf{r}) + B^2\phi(\mathbf{r}) = 0 \quad (3.10)$$

where $B = B_g$ is the geometric buckling of the system. For a critical reactor, $B_g = B_m$, where B_m is the materials buckling,

$$B_m^2 = \frac{\nu\Sigma_f - \Sigma_a}{D} \quad (3.11)$$

The eigenvalues of the system can be determined by

$$k_n = \frac{\nu \Sigma_f}{B_n^2 D + \Sigma_a} \quad (3.12)$$

Consequently, the dominance ratio can be written as

$$DR = \frac{k_1}{k_0} = \frac{B_0^2 \frac{D}{\Sigma_a} + 1}{B_1^2 \frac{D}{\Sigma_a} + 1} \quad (3.13)$$

and if one uses $M^2 = D/\Sigma_a$, Eq. (3.13) becomes

$$DR = \frac{k_1}{k_0} = \frac{B_0^2 M^2 + 1}{B_1^2 M^2 + 1} \quad (3.14)$$

Equation (3.14) connects the dominance ratio of the system to its geometric characteristics via the B_g terms and to its materials via the migration length. What this effectively means is that the dominance ratio for the same geometry becomes larger, as the size of the geometry increases with respect to M (as in, how many migration lengths can fit inside) and this is termed as "apparent size". In terms of coupling, this means that in systems with a large apparent size, neutrons don't travel a lot, compared to the actual size of the geometry and thus, the system is loosely coupled. Inversely, a small apparent size means that neutrons can travel far in the geometry and the system is more tightly coupled as a result.

Using Eq. (3.13) or Eq. (3.14), one can estimate the dominance ratio of a given system with ease, assuming the required quantities are known. In all cases, this is a bounded problem; the dominance ratio is always between unity and a lower limit, determined by the geometry of the system. Take the case of a 1D bare, homogeneous, finite slab reactor of length L . For the condition that the flux vanishes at the boundary, the buckling is given by

$$B_n^2 = \left[(n+1) \frac{\pi}{\tilde{L}} \right]^2 \quad (3.15)$$

where \tilde{L} is the extrapolated length. Based on that, for the current geometry, Eq. (3.14) is bounded between $\frac{1}{4} \leq DR < 1$.

In a parallelepiped with sides a , b and c , the flux is given by

$$\phi_{n,m,l} = \phi_0 \cos\left(\frac{(n+1)\pi x}{\tilde{a}}\right) \cos\left(\frac{(m+1)\pi y}{\tilde{b}}\right) \cos\left(\frac{(l+1)\pi z}{\tilde{c}}\right) \quad (3.16)$$

and the geometric buckling is given by

$$B_{n,m,l}^2 = \pi^2 \left(\frac{(n+1)^2}{\tilde{a}^2} + \frac{(m+1)^2}{\tilde{b}^2} + \frac{(l+1)^2}{\tilde{c}^2} \right) \quad (3.17)$$

with

$$n = 0, 1, 2, \dots, m = 0, 1, 2, \dots, l = 0, 1, 2, \dots \quad (3.18)$$

In a 2D or 3D system, every dimension has its own harmonics development. In the general case, $B_{1,0,0}^2 \neq B_{0,1,0}^2 \neq B_{0,0,1}^2$, but in certain cases, the equality relationship is true for some or all terms (e.g. a parallelepiped core with $a = b$ has $B_{1,0,0}^2 = B_{0,1,0}^2$). For certain geometries, that might change and the first harmonic mode might be axial and associated with $B_{0,0,1}^2$, such as in the case of a PWR core with an active height larger than its diameter (Table A.2). As mentioned before, the discretization determines which harmonics will become visible during a calculation. Out of the resulting $k_{1,0,0}, k_{0,1,0}, k_{0,0,1}$ eigenvalues, the largest one encountered will correspond to the first harmonic mode. Subsequent modes can be given by any combination of the n, m, l indexes and will be ordered in descending order. A fuel pin would have several axial harmonics being larger than the first azimuthal or radial ones.

This work focuses mostly on azimuthal harmonics associated with $B_{1,0,0}^2$ and the relationship between $k_{1,0,0}$ and $k_{0,0,0}$, unless otherwise stated. Since the dominance ratio is a global parameter, $k_{1,0,0}$ will be shortened to k_1 when it is associated with the first harmonic of the system and the $\frac{k_{1,0,0}}{k_{0,0,0}}$ ratio will be referred to simply as dominance ratio or DR in that case. As for k_{eff} , it stands that $k_{eff} \equiv k_0 \equiv k_{0,0,0}$.

For a reactor with fixed dimensions, the dominance ratio becomes dependent solely on the materials of the system. In the case of a parallelepiped with $a = b = c = 200$ cm, Fig. 3.1 shows its dependence on the migration length, diffusion coefficient and macroscopic absorption cross section. Breaking the material part down to these intrinsic system quantities allows to track the behavior of the dominance ratio on the surface shown in Fig. 3.1d. For a fixed geometry, such as an existing reactor, this analysis enables one to place a system on that surface and then decide on potential material changes in order to move towards the top of the surface, dominated by red color, and achieve a desired dominance ratio value. The selection of available materials and other constraints will of course complicate the process, but nevertheless, a graph similar to Fig. 3.1d can be used to help with choosing the best and/or easiest way of affecting the dominance ratio in a large scale, by moving along the path of least resistance. The actual surface itself is of course dependent on the geometry of the system, through the buckling terms.

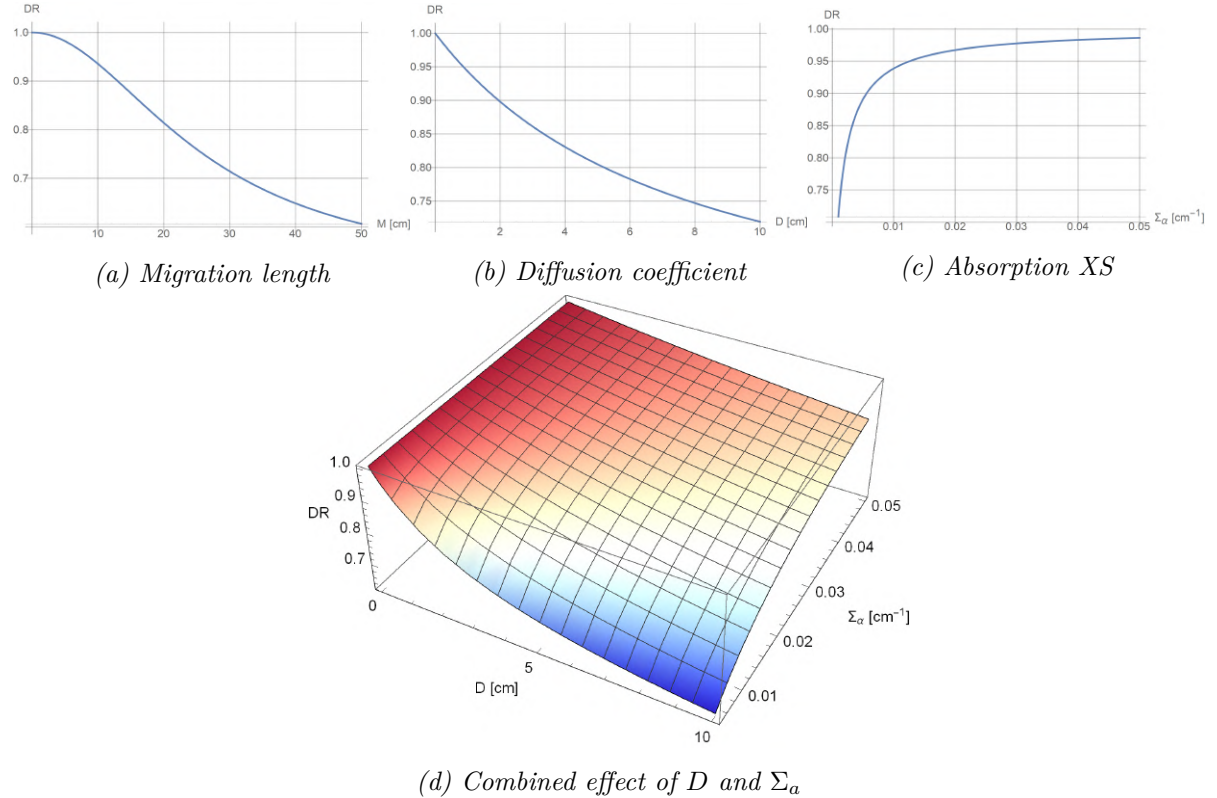
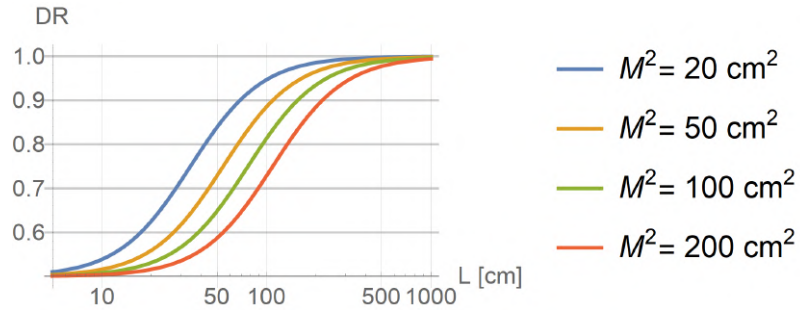


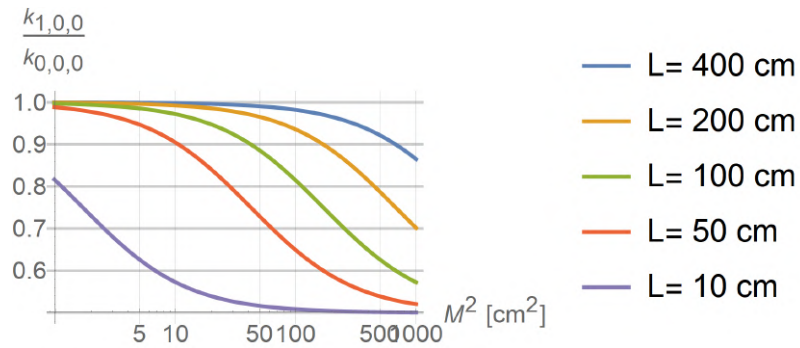
Figure 3.1: Dominance ratio versus material properties of the system.

The addition of any material will induce changes to both D and Σ_a . If one wishes to increase the decoupling via this approach, enough absorbing material needs to be added for the D/Σ_a quantity to decrease. However, in a lot of real applications, the material balance of the core is altered locally, by using reactivity devices or zoning, in a way that separates parts of the core from each other, such as in the case of the ZEPHYR design. The effective use of such methods however, requires knowledge of the shape of the fundamental mode and ideally, the first harmonic mode as well.

On the other hand, if the material composition is fixed, the dominance ratio can be controlled by altering the system size. Figure 3.2 shows both sides of the same coin, with Fig. 3.2a giving the dominance ratio versus side length L , for a parallelepiped with $a = b = c = L$, for different values of the migration area. A small M^2 enables a high dominance ratio to be achieved with small systems, while for high values of M^2 , even large systems remain relatively tightly coupled. On the other hand, Fig. 3.2b shows that large geometries will remain loosely coupled even for particularly high migration length values.



(a) Dependency on size, for different values of the migration area



(b) Effect of size, for different values of the migration area

Figure 3.2: The effect of geometry size.

Finally, Fig. 3.3 gives the dependency on both the geometry size and the migration length, for a parallelepiped with $a = b = c = L$, serving as a combined picture of everything that was discussed before.

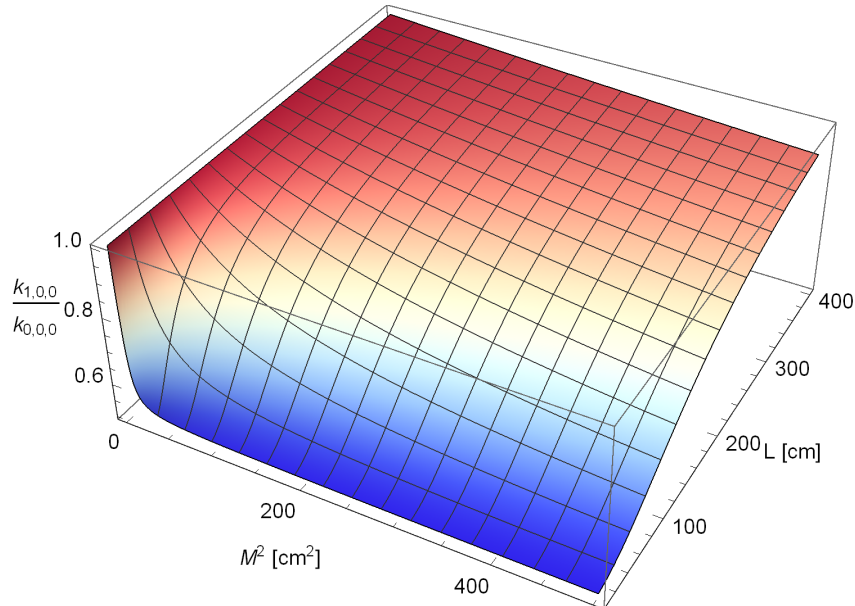


Figure 3.3: Dependency on migration length and geometry size.

3.2 Experimental results of eigenvalue separation measurements in the KUCA reactor

The dominance ratio or eigenvalue separation have been studied in relatively few experiments. It is quite a challenging process to connect the EVS and/or DR to measured data. This section will briefly describe some of the experiments carried out in the KUCA reactor (Kyoto University Critical Assembly) in the 90's. This will connect relevant conclusions to the work carried out within the thesis and give an insight on the expected agreement between simulation and experiment. It is worth noting that the authors define the EVS as $\frac{1}{k_1} - \frac{1}{k_0}$, which is the inverse of how it is defined in this thesis. The relevant expressions have been adjusted accordingly, so they will differ slightly from the ones found in the source material.

Measurement of eigenvalue separation by using position sensitive proportional counter [60]

The first experiment used a long, position sensitive proportional counter (PSPC) to measure the axial flux profile of the active core at different levels of subcriticality and subsequently calculate the flux integral $R_{m,z}$ along the z axis. This integral for an axial mode m can be expressed as

$$R_{m,z} = \int \psi_{m,z}^\dagger(z) F \Phi(x_0, y_0, z) dz = S \sum_{n_x}^{\infty} \sum_{n_y}^{\infty} \frac{\lambda_{n_x, n_y, m_z}}{1 - \lambda_{n_x, n_y, n_z}} C_{n_x, n_y, m_z} \quad (3.19)$$

where F is the production operator, S is the source, $\psi_{m,z}^\dagger$ is the m_{th} adjoint function and $\Phi(x_0, y_0, z)$ is the measured flux along the z axis, with the PSPC positioned at (x_0, y_0) and

$$C_{n_x, n_y, m_z} = \frac{\psi_{n,x}^\dagger(x_s) \psi_{n,y}^\dagger(y_s) \psi_{m,z}^\dagger(z_s)}{\langle \psi_{n,x}^\dagger \psi_{n,x} \rangle \langle \psi_{n,y}^\dagger \psi_{n,y} \rangle} \psi_{n,x}(x_0) \psi_{n,y}(y_0) \quad (3.20)$$

with (x_s, y_s, z_s) referring to the neutron source position. A fuel element with a source of Cf^{252} was used to induce tilts and excite higher modes.

Any eigenvalue of the system can be expressed like in the previous chapter,

$$\lambda_{n_x, n_y, m_z} = \frac{k_\infty}{1 + B_{n_x, n_y, m_z}^2 M^2} \quad (3.21)$$

and a tilt is defined as

$$f_z = \frac{R_1}{R_0} \quad (3.22)$$

It is possible to connect the flux tilt with the eigenvalue separation, through the subcriticality δ_0 , as

$$f_z = \frac{R_1}{R_0} = \frac{\delta_0}{EVS^{-1} + \delta_0} \frac{\langle \psi_{1,z}^\dagger S \rangle}{\langle \psi_{0,z}^\dagger S \rangle} \quad (3.23)$$

It was found that, while there were differences between the measured and calculated eigenvalue separations, they fell within the 2.6% error margin of the measured data. The simple expression of Eq. (3.21) allows for a good estimation of the EVS, if the investigated core is considered as the equivalent bare core. The experimental method proposed serves as a handy tool for EVS monitoring.

Measurement of Flux Tilt and Eigenvalue Separation in Axially Decoupled Core [61]

The second experiment dealt with two axially decoupled cores. The upper and lower cores consist of 93.2% enriched uranium, separated by a blanket of natural uranium and polyethylene. The entire system is using polyethylene as top and bottom reflector. The eigenvalue separation was introduced by an expression similar to Eq. (3.5),

$$\phi_{pert} = \phi_0 + \sum_{n=i} EVS_n \frac{\langle \psi_n^\dagger, (\frac{\delta F}{k_0} - \delta A) \phi_0 \rangle}{\langle \psi_n^\dagger, F \psi_n \rangle} \psi_n \quad (3.24)$$

where ϕ_{pert} and ϕ_0 are the perturbed and unperturbed neutron flux, respectively. It was shown that the first mode reactivity worth can be approximated by the difference between the perturbation reactivities added to the lower and upper cores due to the fundamental mode,

$$\left| \frac{\langle \psi_1^\dagger, (\delta F - \delta A) \psi_0 \rangle}{\langle \psi_1^\dagger, F \psi_1 \rangle} \right| = \left| \frac{\langle \psi_0^\dagger, (\delta F - \delta A) \psi_0 \rangle_L}{\langle \psi_0^\dagger, F \psi_0 \rangle_{L+U}} - \frac{\langle \psi_0^\dagger, (\delta F - \delta A) \psi_0 \rangle_U}{\langle \psi_0^\dagger, F \psi_0 \rangle_{L+U}} \right| = |\rho_L - \rho_U| \quad (3.25)$$

The first mode EVS is connected to the flux tilt through

$$f = EVS |\rho_L - \rho_U| \quad (3.26)$$

Control rod worth measurements were made and the flux tilt was determined by the reaction rate distribution. The relevant conclusions were two. The first one states that "the measured differential reactivity worth of a control rod was asymmetric over the two core regions and that the interference effect on the control rod worth was stronger in an axially decoupled core than in a single core. The flux distribution was tilted by the insertion of rods and the magnitude of the flux tilt varied considerably, depending on the

position of each rod". This conclusion is very interesting in the context of large, decoupled power cores, since their control rod banks operate in the axial direction. BWR cores are likely more affected than PWRs, due to the higher heterogeneity. It is also relevant to axially heterogeneous fast core designs.

The second conclusion has to do with the agreement between the measured (0.282 ± 0.006) versus calculated (0.299) EVS, with the two values agreeing with each other within 6%.

Analysis of First-Harmonic Eigenvalue Separation Experiments on KUCA Coupled-Core [47]

The last experiment that will be discussed is on a system consisting of two cores placed in light water, with the ability to change the distance between them. This geometry served as inspiration for the fuel storage benchmark of Chapter 5. The two cores are controlled by one pilot rod each and it is possible to induce flux tilts by manipulating the former. The authors connect the EVS to the tilt as

$$f = EVSw_{diff} + f_0 \quad (3.27)$$

where w_{diff} is the difference in rod worths between the two pilot rods and f_0 is the initial tilt, if present. Another method to measure the EVS is through drops of an additional rod on a single core.

Besides the experimental part, this work features some interesting conclusions regarding calculation schemes, with the authors using the measured EVS values as a reference. Three things are studied:

The effect of doing a 3D calculation versus a 2D one, with a supplied axial buckling based on the axial fundamental mode calculation. It was found that, in the case of this geometry (active height of 570mm), the produced errors were on the order of 0.1%-0.2% in both the fundamental and first mode. This is a very useful conclusion that can help reduce calculation requirements if the full 3D behavior is not needed and the geometry is axially uniform, requiring a single 3D fundamental mode calculation. A similar conclusion was reached during this thesis, near the beginning of the ERANOS calculations using Kobayashi's multipoint model. However, the calculations were kept 3D, for consistency between all geometries and with the Serpent 2 TFM calculations.

The effect of reducing the energy group structure for the calculation, where it was determined that a particularly small number of groups (11 groups) introduces significant errors, especially for the first mode. The error goes away when a higher group count is used (26). A 41-group structure was used as reference.

The third conclusion is significant and it deals with the errors introduced as a result of choosing a 2D diffusion calculation versus a 2D Sn transport one. The paper presents a thorough discussion on the matter that is briefly summarized by saying that the difference in the leakage calculation affects the fundamental and first mode differently, at least in this geometry, due to the changes in reflection behavior as the two assemblies move closer together. The diffusion approach, when compared to reference results, is found to calculate the EVS with much larger errors than the transport approach. This last conclusion is relevant to this thesis, since the mesh discretization of the transport solver that was used in ERANOS produced incompatibilities with the region discretization for Kobayashi's multipoint model and in the end, diffusion was used. However, the calculated DR and EVS results in this thesis were in good agreement with values generated through the TFM calculation.

Chapter 4

The ZEPHYR fast-thermal coupled core

4.1 General characteristics and flux profiles

As the EOLE and MINERVE [62] experimental reactors were reaching their end of life at CEA Cadarache, a new facility was considered as their replacement. Part of its planned features was the capability to host a coupled core configuration. The CEA started the design of a new zero power reactor under the ZEPHYR (Zero power Experimental PHYSics Reactor) program, with the aim of building a versatile experimental facility [10–12]. The design was called to meet the capabilities of a thermal and a fast system at the same time. Through an optimization process incorporating lessons taken from the MASURCA fast zero power reactor and its available fuel stockpile, the study aimed at answering various reactor physics questions for heterogeneous systems. Questions such as whether or not the neutronics conditions of a fast core can be reproduced at the center of a fast-thermal coupled core, or if the surrounding adaptation and thermal zones exert a spectral influence on the center of the fast zone. The main goal of fast-thermal experimental programs is to measure integral total cross-sections of several isotopes of interest in a targeted fast spectrum through accurate reactivity effects measurements. Therefore, the neutronics characteristics of this spectrum have to be reproduced in the center of the fast-thermal coupled configuration. The fast core geometry presented here is based on a PHENIX-like fast unit cell, called ZONA1, from the ZONA1 core of the ERMINE V program [63]. The materials are coming from the existing inventory of CEA, specifically the stockpile of the MASURCA reactor. A ZONA1 cell is made of six MOX rodlets, two natural UOX rodlets and eight square sodium rodlets. A single ZONA1 cell itself is 12 inches tall and is shown in Fig. 4.1. The neutron spectrum of the cell rests between the spectra of the two cores of

the PHENIX reactor. Unfortunately, the ZEPHYR program was indefinitely suspended in late 2018, due to budgetary concerns and will be revisited after the completion of the JHR, at CEA Cadarache. This took place about a year into this PhD. As such, the focus of the doctoral work turned into other projects, yet the analyses performed up to that point yielded interesting results.

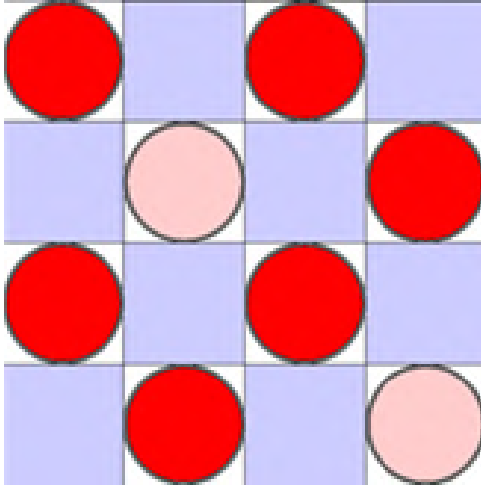


Figure 4.1: Top-down view of a ZEPHYR ZONA1 cell.

The coupled core is divided into three main zones, themselves separated by rings of certain materials. The central fast zone (ZONA1) is surrounded by an adaptation zone comprised of natural UOX (ZONA2), itself contained inside a thermal lattice ring of 3.7% enriched PWR-grade UOX fuel pins, submerged in light water (ZONA3). Despite its highly heterogeneous nature, the core's effective delayed neutron fraction β_{eff} is largely controlled by the thermal lattice. Calculated at 739 pcm with Serpent 2 Monte Carlo code, this brings additional safety margins during operation and experiments.

The fast and thermal zone are separated by two rings. The ring separating the adaptation zone from the thermal zone is comprised of 30.2% enriched metallic uranium fuel rods. Its purpose is to utilize the thermal neutrons produced by the 3.7% enriched UOX lattice, in order to produce a high number of fast fission neutrons.

The ring separating the fast central zone from the adaptation zone consists of natural B₄C absorber rods. Its role is to absorb any thermal neutrons in the vicinity, effectively screening the central fast zone from incoming thermal neutrons, allowing only incoming fast neutrons to enter it and contributing to the decoupling of the core. At the same time, it serves as a safety measure in case of water ingress in the central zone, by absorbing possible outgoing thermal neutrons.

A top-down view of the geometry, created in Serpent 2, is presented in Fig. 4.2 and Fig.

4.3. Figure 4.4 gives radial flux profiles of the geometry as calculated in Serpent 2, while Fig. 4.5 gives the radial adjoint total flux, as calculated in the ERANOS deterministic code. The adjoint flux profile of the core is quite interesting, as it can give a visual depiction of the importance of different regions [19]. Finally, Fig. 4.6 gives the neutron flux spectra of the various regions.

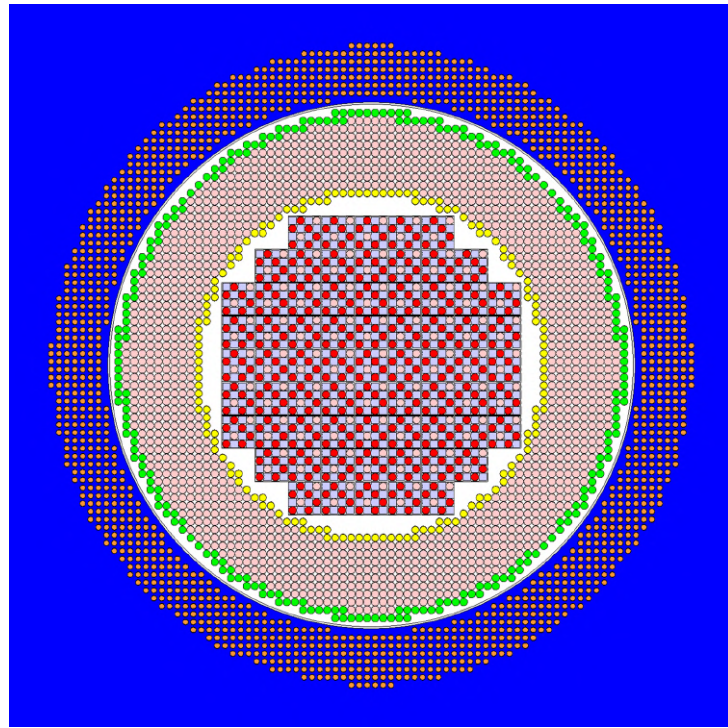


Figure 4.2: X-Y representation of the Serpent 2 modeling of the ZEPHYR fast-thermal coupled core configuration. Blue: light water, Orange: UO_2 3.7% enrichment, Green: metallic U 30.2% enrichment, Pink: natural UO_2 , Yellow: B_4C absorber, White: air. The central cell design is the one presented in Fig. 4.1.

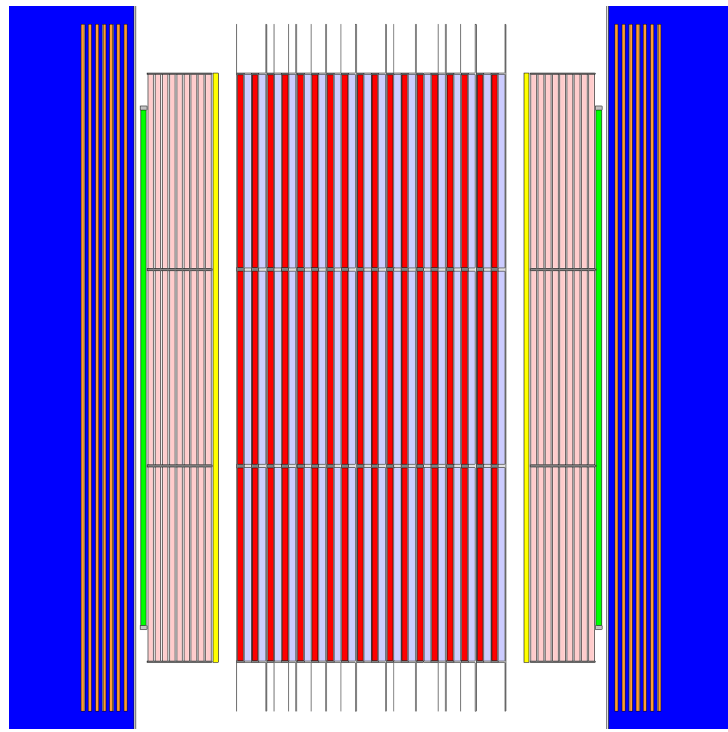


Figure 4.3: X-Z representation of the Serpent 2 modeling of the ZEPHYR fast-thermal coupled core configuration.

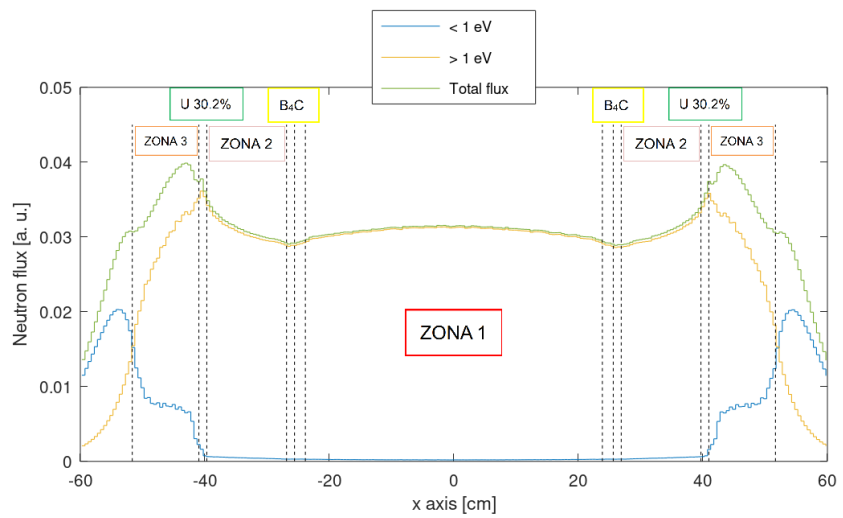


Figure 4.4: Flux profiles in the ZEPHYR fast-thermal coupled core configuration, calculated in Serpent 2. The geometry zones are marked on the figure.

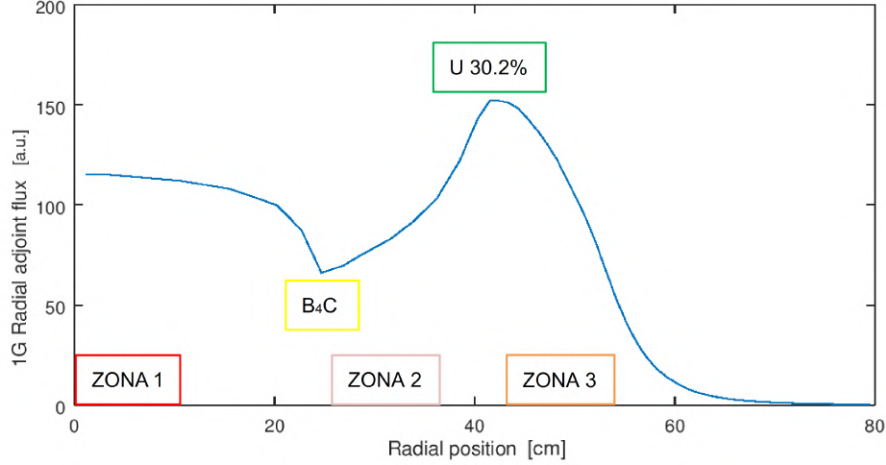


Figure 4.5: 1G radial adjoint flux in the ZEPHYR fast-thermal coupled core, calculated in ERANOS.

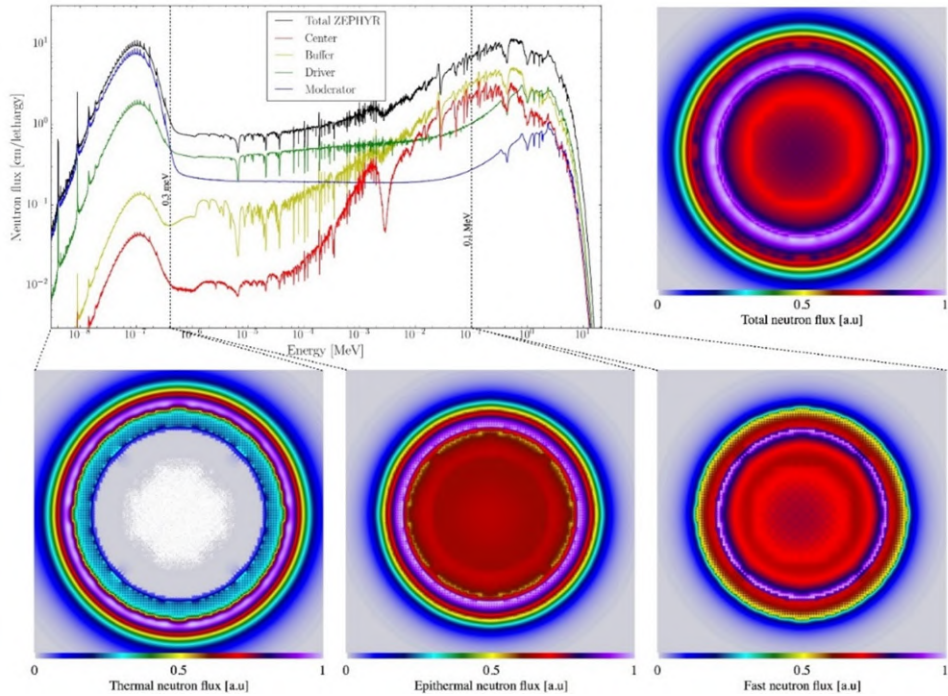


Figure 4.6: Neutron spectra in the different areas of the fast-thermal coupled core (upper left) together with the neutron flux maps calculated with the Serpent 2 code: total flux (upper-right), and thermal/epithermal/fast flux (bottom).

In Fig. 4.5, one can see the importance of the 30.2% enriched uranium ring and the decoupling effect that the natural UO₂ (ZONA2) causes. Overall, the core is fairly complicated and its analysis presents certain challenges, as a lot of quantities change along

the core mid-plane, such as the diffusion length and the various cross sections. The same goes for several kinetic parameters, such as the local neutron generation time and effective delayed neutron fraction. The above makes the use of simplified models particularly difficult.

4.1.1 Development of the control rod assemblies

One part of the design that had to be developed, was a control system capable of providing multiple positions for negative reactivity injections, with the dual purpose of safety and inducing power tilts to the geometry. CEA has both B_4C and Hf rod material in its inventory and thus, both materials were investigated. The selection process for the material was based on its overall effectiveness. In all design cases, the B_4C inserted more negative reactivity and thus was selected.

Case	1	2	3	4
ZONA1	B_4C	B_4C	Hf	Hf
ZONA3	B_4C	Hf	Hf	B_4C
$\Delta\rho$ [pcm]	-6357	-5305	-3920	-4979
$\Delta\rho$ [\$]	-8.60	-7.18	-5.30	-6.74

Table 4.1: Control rod material selection results.

The second part consisted of coming up with an actual design, based on the desired specifications. Control rod followers (absorber elements are placed above/below regular fuel assemblies and as they enter the core, they displace the latter) were used, since this would yield a uniform flux profile when the control elements were withdrawn, would not end up altering the original design and provide the most control rod worth, due to the removal of fuel. For the ZONA1 central fast zone, the idea was to replace four fuel assemblies with control assemblies. Initially, the full sixteen positions were used for B_4C rods, but this yielded diminishing returns after a point due to the shadowing effect, so a maximum of twelve rods were used.

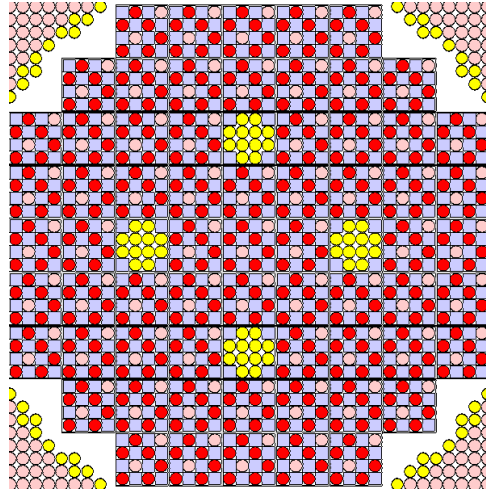


Figure 4.7: ZEPHYR ZONA1 control assemblies (marked with yellow).

For the ZONA3 thermal zone, while there were no fuel assemblies used originally (the lattice was comprised of individual pins), a follower system required that a number of pins were placed on a moving assembly. Keeping in mind that the main goal of the approach was to come up with a system that can perturb the core and induce tilts, four positions were selected again, with twelve pins each. Given the lower coupling in thermal lattices, the control elements were spread out a little more, which helped reduce the shadowing effect and aimed at partially splitting ZONA3 into four quarters. The resulting design is given in Fig. 4.8

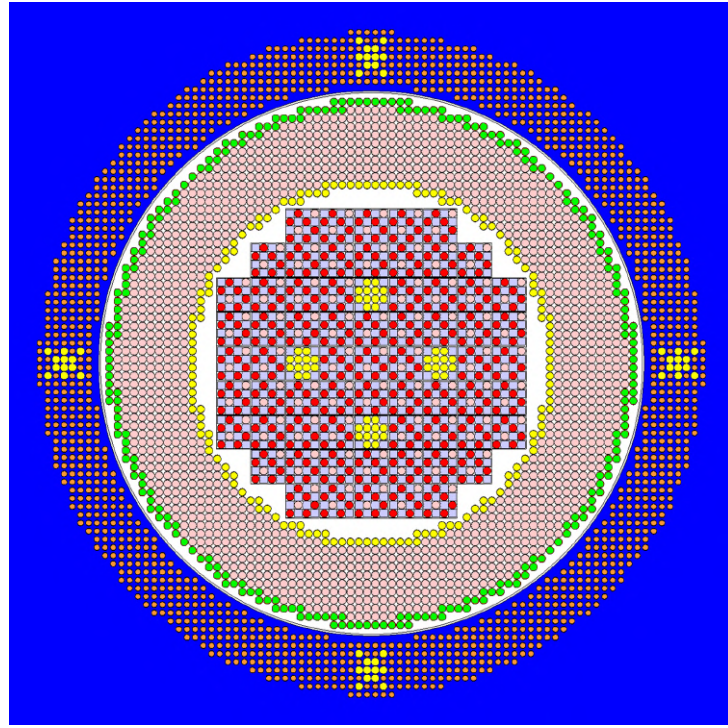


Figure 4.8: ZEPHYR final design in shutdown configuration, with control assemblies in ZONA1 and ZONA3 (marked with yellow).

The effect of the control elements on the total neutron flux can be seen in Fig. 4.9. Partial insertion of these control assemblies is later used to observe the change in coupling behavior of the system.

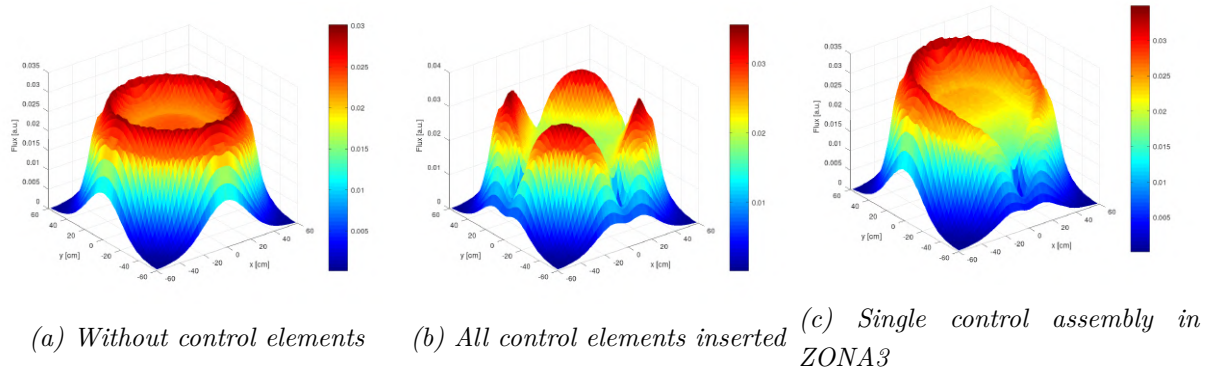


Figure 4.9: Total flux map of the ZEPHYR core, with and without inserted control elements. Normalized to one source neutron.

4.2 Analysis with the TFM model in Serpent 2

The ZEPHYR coupled core was analyzed with the TFM model, in the Serpent 2 Monte Carlo code. This was the first time the model was used in this PhD work and as such, the primary point was to gain familiarity with the model, perform calculations and develop a data analysis workflow for the TFM results. The next part was supposed to focus on using the previous results to alter the configuration in order to achieve a higher dominance ratio, but as mentioned before, the entire ZEPHYR program was suspended in 2018. Thus, the analysis of the design with the TFM model (and later Kobayashi's approach) is limited to the existing geometry.

This part will also serve to familiarize the reader with the transient fission matrices, placing emphasis on explaining them as well as their eigenvalues and eigenvectors and looking at the conclusions one can obtain with this information. Other aspects of the model will be explored in Chapter 5. To avoid confusion when talking about parts of the geometry versus specific TFM discretized nodes, the following nomenclature is used:

- Zone: refers to a general part of the geometry; used in descriptions.
- Region, node: refer to a specific discretized node, such as a TFM node or a region referring to a coupling coefficient calculation.

Furthermore, taking examples from existing literature [40,41,43], Monte Carlo simulations were run with 5×10^5 neutrons for 2000 cycles (10^9 neutron histories in total), with 50 discarded cycles in the beginning, to ensure good fission source convergence. These settings were used for all calculations presented in this document.

The uncertainty on the extracted eigenvalues is not a straightforward matter. One option is to run independent calculation using different seeds. However, this can be a very time-consuming option. If an estimation needs to be made based on a single calculation, an assumption is necessary, since the uncertainties of both the raw Monte Carlo input and of the TFM coupling coefficients are not directly known. Assuming that the coupling coefficients (the elements of a TFM matrix) carry the same relative uncertainty as the k_{eff} that is calculated by Serpent 2, each TFM matrix \underline{G} , comes with an error matrix $\underline{\varepsilon}$. The norm of the $\underline{\varepsilon}$ matrix can give an estimation of the uncertainty associated with the eigenvalues of the \underline{G} matrix, under this assumption. The number of nodes also affects this value [64]. Considering that for all applications in this work, the k_{eff} uncertainty was on the order of 3 pcm, the resulting eigenvalue uncertainty is between 32-37 pcm for all geometries analyzed in this work.

Both the independent calculation method and the assumption method were tested on several scenarios, with the k_{ij} uncertainty results for all geometries in this work varying by below 10 pcm between the two methods. Thus, this assumption, while contestable (the local k_{ij} and global k_{eff} quantities could have different uncertainties), yielded good results in this work and can be used as an empirical method, when multiple independent calculations are not feasible. Ideally, it should be compared against the results of at least two independent calculations, for geometries differing significantly.

Since the current implementation of the TFM model allows one-dimensional analysis, in order to get a good idea for the behavior of ZEPHYR at the core center plane, the first step was to move away from the ZEPHYR inspired RZ-type geometry and convert it to a square Cartesian one, maintaining the relative volume of all zones. This square geometry was previously calculated [19] and is presented in Fig 4.10. The TFM model was applied to a traverse of the geometry, taken at the core mid-plane.

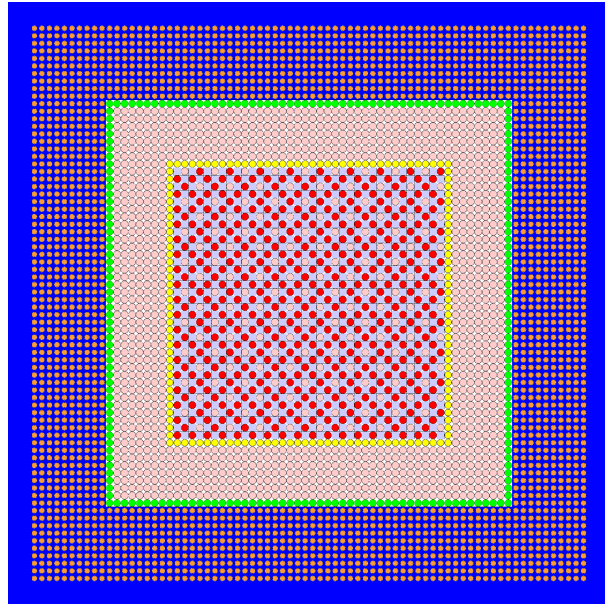


Figure 4.10: Square representation of the ZEPHYR core. Blue: light water, Orange: UO_2 3.7% enrichment, Green: metallic U 30.2% enrichment, Pink: natural UO_2 , Yellow: B_4C absorber, White: air. The central cell design is the one presented in Fig. 4.1.

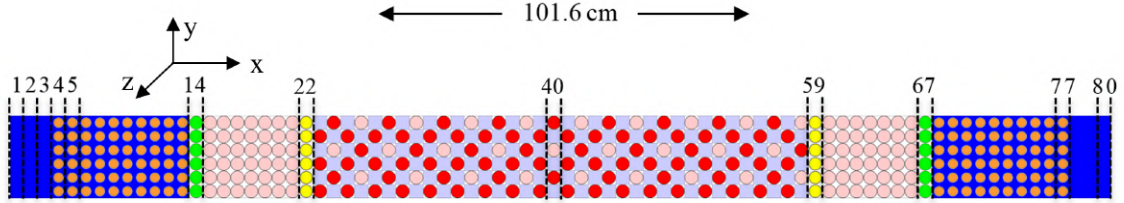


Figure 4.11: Top-down view of the traverse of the square geometry used in the TFM calculation. The region discretization is also shown.

The fission rate plot of the traverse is given in Fig. 4.12.

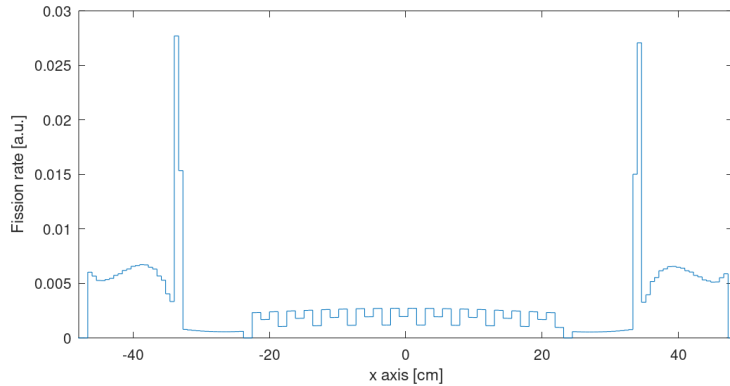


Figure 4.12: Fission rate, for the traverse of the square geometry. The error is on the order of 10^{-4} . Normalized to one source neutron.

In order to help with understanding how to read the matrices, an example is given in Fig. 4.13. The figure depicts the $G_{\chi_p \nu_p}$ matrix for the traverse geometry. The superimposed geometry shown at the top represents the Origin bins j , while the geometry shown to the left represents the Target bins i . In this example, the marked intersection point gives the probability that a prompt neutron born in the middle of the fast zone will generate a prompt neutron in the row of 30.2% enriched rodlets in node 67. The TFM matrices are essentially k_{ij} coupling coefficients matrices, but they differentiate between prompt and delayed neutrons and are color coded, because of the large number of values.

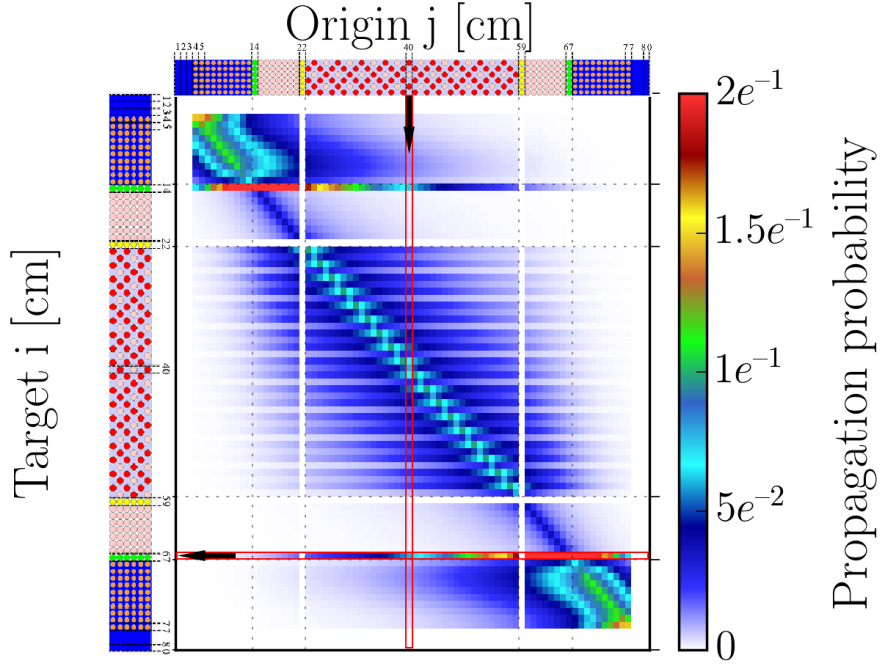


Figure 4.13: TFM example of a $G_{\chi_p \nu_p}$ matrix.

The TFM matrices for the reference case are given below. The different regions of the geometry are marked with origin and target axis ticks and with dashed lines. Figures 4.14 and 4.15 give the kinetics picture of the system or otherwise its response to a neutron pulse for one generation. From the diagonal of the matrix, it's clear that in the fast zone (nodes 23-58), most neutrons born through fission cause a high number of fissions close to their origin point and a lower number, further away. Fission neutrons propagate quite a bit due to the increased migration area of the fast lattice, as shown by the length of the blue lines and the zone is characterized by relatively low but stable fission rates, as shown in Fig. 4.12. The thermal regions (4-13, 68-77) display higher propagation probabilities, essentially meaning that an incoming neutron is more likely to cause a fission event there. Furthermore, the reduced migration area in the thermal lattice means that neutrons are even more likely to produce more neutrons in their immediate vicinity, as indicated by the elevated propagation probability in the diagonal there. The nodes containing the 30.2% enriched metallic uranium fuel (14, 67) display very high propagation probabilities and fission rates, since most neutrons coming to these nodes will induce fission. Additionally, observation of the adjacent rows of PWR fuel (13, 68) shows a sharp drop in propagation probability. Fig. 4.12 shows diminished local fission rates, indicating that thermal neutrons in the immediate zone of the 30.2% enriched fuel are absorbed by it due to the amount of ^{235}U and its high thermal fission cross section, leaving very few neutrons for fissions in the nearby 3.7% enriched UOX. Indeed, this zone utilizes most of the neutrons

incoming from the thermal lattice, leaving very few of them to move towards the center of the core. Finally, the natural uranium (15-21, 60-66) and B₄C (22, 59) regions display low and zero propagation probabilities and fission rates, respectively, with the B₄C zone serving to isolate ZONA1 from thermal neutrons coming from the outside.

In the end, the comparison of the fission rate plot from Fig. 4.12 with the TFM matrices shows that areas with high fission rates and especially high fission cross sections are associated with high neutron propagation probabilities, something very logical, since these materials will utilize most incoming neutrons to produce new ones, instead of, for example, capturing them. In addition to the above, the $\underline{G}_{\chi_p \nu_p}$ matrix in Fig. 4.14b shows that the delayed-to-prompt propagation probability is much higher in the thermal lattice zone, since it is characterized by an increase in delayed neutron production.

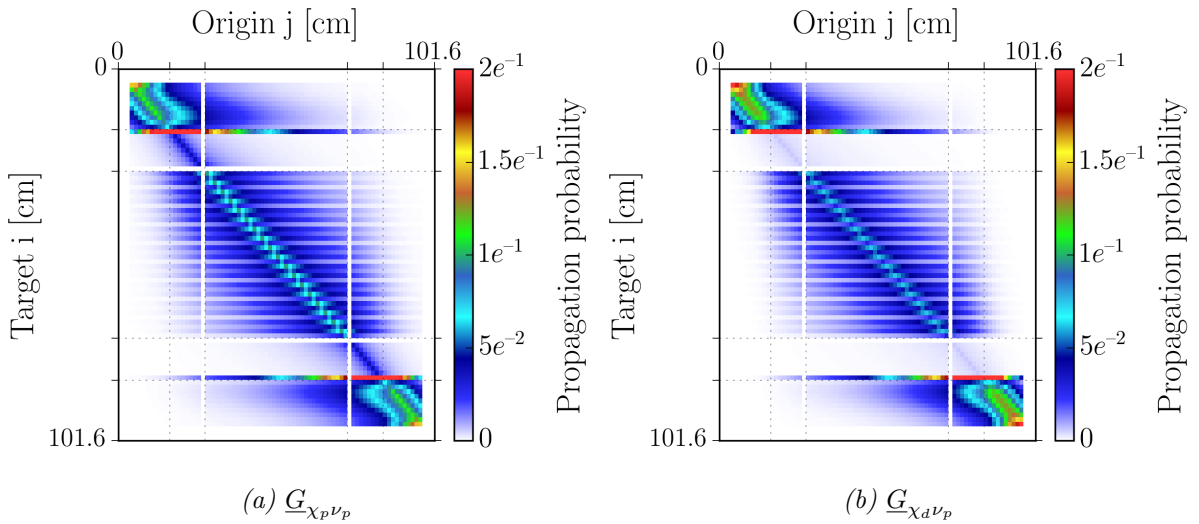


Figure 4.14: Prompt production matrices for 0% rod insertion.

Moving to the $\underline{G}_{\chi_p \nu_d}$ and $\underline{G}_{\chi_d \nu_d}$ matrices describing the propagation probability for delayed neutron production and taking a look at the scale, on the side, one will observe that the probability values are two orders of magnitude lower than for the prompt matrices. It is significantly higher in the thermal lattice (4-13, 68-77) zone and somewhat lower in the natural uranium (15-21, 60-66) zone. The uranium isotopes in these zones, especially the ²³⁸U, yield the highest delayed neutron fractions. Moving to the ZONA1 fast (nodes 23-58) zone, the overall ²³⁸U is much lower and this causes the significant drop in delayed neutron production.

This becomes even more pronounced in the $\underline{G}_{\chi_d \nu_d}$ matrix, where delayed neutron production drops notably in the central fast zone. This is due to the absence of enriched uranium isotopes. Unlike prompt neutrons, whose emission energies are given by the Watt spectrum, delayed neutrons are mainly produced at lower energies, on the order of

a few hundred keV. This, coupled with the fact that the (n, f) reaction for ^{238}U starts opening up after 1 MeV (the cross section for the competing (n, γ) reaction is much higher than (n, f) before that point), means that most delayed neutrons will go on to cause fissions in the plutonium isotopes instead, which in turn exhibit lower delayed neutron production. A similar effect (minus the plutonium part) is observed in the natural uranium zone.

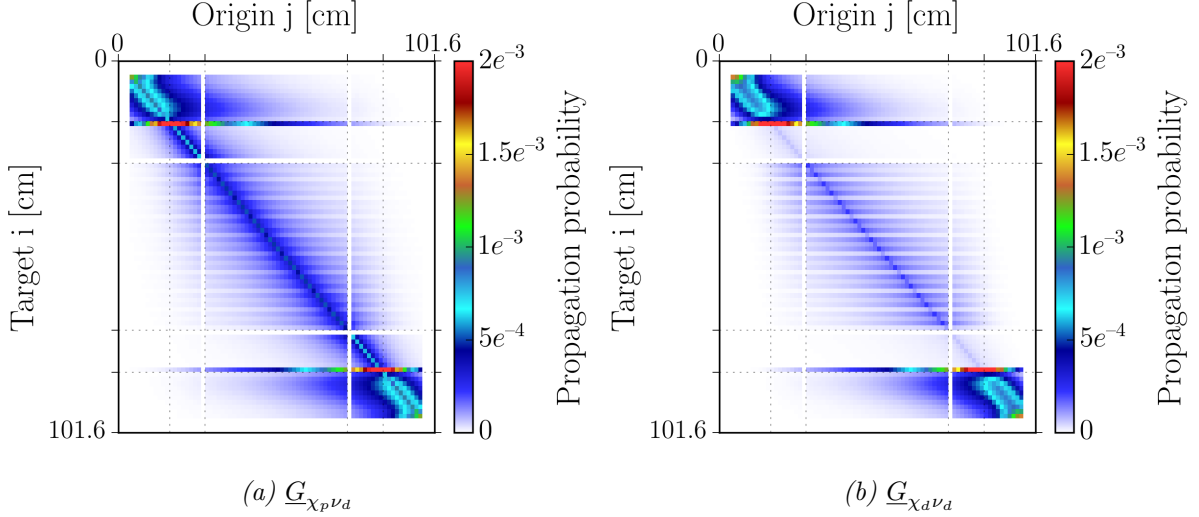


Figure 4.15: Delayed production matrices for 0% rod insertion.

The $T_{\chi_p \nu_p}$ matrix gives the average prompt-to-prompt generation time for each TFM node. The system displays vastly varying generation times, due to the different regions being characterized by very dissimilar spectra. More specifically, nodes 4-13 and 68-77 show that all neutrons that cause fissions in the thermal zone (ZONA3), do so after taking time to be thermalized. Inversely, ZONA1 shows low propagation times, since most neutrons cause fissions while still being fast. Comparing the $T_{\chi_p \nu_p}$ with the G matrices, one understands that neutrons entering ZONA1 from ZONA3 are still fast, after having crossed the natural uranium zone. The 30.2% enriched uranium zone has relatively high propagation times, since most fissions are caused by neutrons coming from the adjacent thermal zone or by neutrons that arrived from the other side of the geometry, having to cross the natural uranium zone in the process. The natural uranium zone itself is characterized by low times, except for nodes corresponding to origins in the thermal zone.

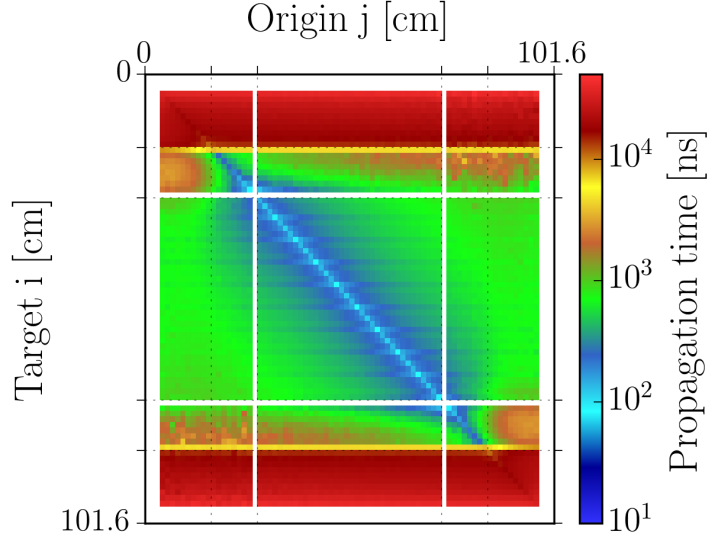


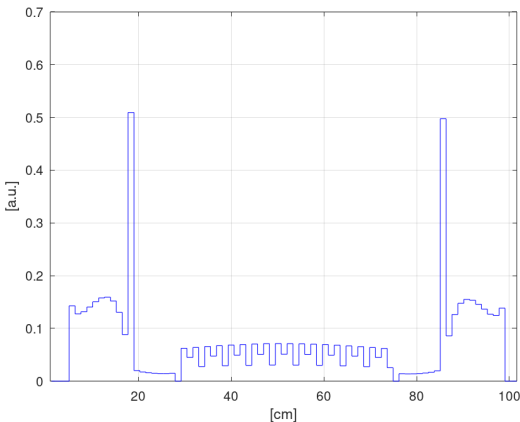
Figure 4.16: $T_{\chi_p \nu_p}$ matrix.

Finally, it is also possible to obtain the matrix eigenvalues and eigenvectors and receive additional information. It should be noted that due to the fact that the matrices present the raw probability for neutron production for one generation, it is not possible to obtain fully accurate results for the overall behavior. Instead, the system can be studied with respect to the different $p \rightarrow p$, $d \rightarrow p$, $p \rightarrow d$ and $d \rightarrow d$ pairs. Since the prompt-to-prompt events constitute the vast majority of the total events, the $G_{\chi_p \nu_p}$ can be used to give a reasonably accurate picture of the system. The fundamental and first mode eigenvectors are given in Figures 4.17a and 4.17b respectively. The fundamental eigenvector is always positive (the real source distribution cannot have negative points) and gives direct information regarding the region-wise importance and since the prompt-to-prompt case offers a very good approximation of the geometry, it closely follows the fission rate. The first mode eigenvector on the other hand is connected to the stability of the system and gives a picture of how the node importance would be affected in the event of a perturbation. Thus, the maxima and minima of the first mode eigenvector can be used to determine the optimal safety or pilot rod positions in a core, for example. In this particular geometry, it is easy to see that the positions with the potential to affect the greatest change, correspond to the 30.2% enriched uranium fuel region, since it provides much of the reactivity and neutron production in the system.

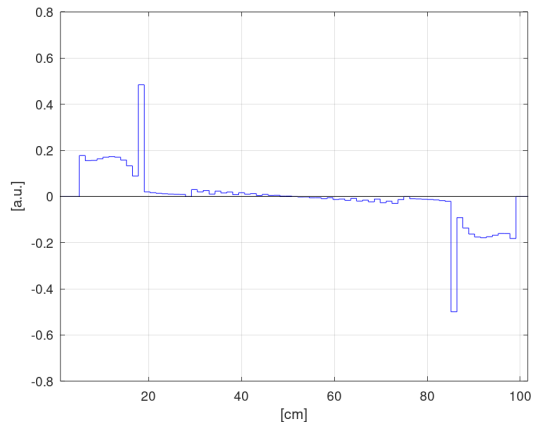
Furthermore, it is interesting to note the overlap of the first mode with the fundamental one, in the thermal lattice zone. Although both the dominance ratio and the eigenvalue separation refer to the entire system, in a heterogeneous geometry like that, the fundamental and first mode are going to be closer to each other in zones whose characteristics favor it. In this case, the thermal lattice part is characterized by a lower average neutron

energy (see Fig. 4.6) and a smaller migration length than the rest of the geometry.

In the thermal lattice zone, the fundamental eigenvector has a shape that corresponds to a thermal flux curve, followed immediately by a peak for the 30.2% enriched uranium part. After that, the natural uranium in ZONA2 is characterized by low importance. The center of the geometry, containing the fast ZONA1 part, has a flat cosine shape overall, with the highs and lows owing to how the ZONA1 cells are designed. Looking at Fig. 4.11, a TFM node in that part could contain one, two or three MOX positions. The same effect is observed in the fission rate plot.



(a) Fundamental eigenvector.



(b) first mode eigenvector.

Figure 4.17: Eigenvectors of the $G_{\chi_p \nu_p}$ matrix.

As in other multipoint models, the number of accessed eigenvalues and eigenvectors equals the amount of nodes used in the TFM discretization. The eigenvalues of the \underline{G}_{all} block matrix give accurate results regarding the prompt and delayed neutron interactions. In this case, a discretization of 80 nodes will yield 80 eigenvalues. A certain number of them are zero (8), degenerate (9) or complex (9), with small imaginary parts of (the latter being several orders of magnitude smaller than the real parts, where applicable). Complex eigenvalues are associated with rotational symmetry [8, 65], while zero eigenvalues refer to non-multiplying parts of the geometry. The real parts of the first 72 eigenvalues of the system are presented in Fig. 4.18 and given in Table 4.2. The fundamental eigenvalue $k_0 \equiv k_{0,0,0}$ is given with index 0 and the following indexes correspond to $k_{n,0,0}$ eigenvalues.

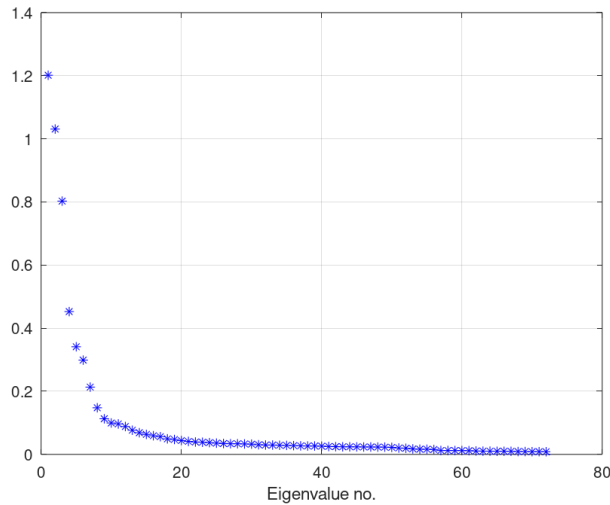


Figure 4.18: G_{all} block matrix first 72 eigenvalues (real parts).

0	1.20162	15	0.05912	30	0.03052	45	0.02350	60	0.01177
1	1.03104	16	0.05603	31	0.02969	46	0.02350	61	0.01073
2	0.80279	17	0.04930	32	0.02963	47	0.02323	62	0.01023
3	0.45258	18	0.04719	33	0.02892	48	0.02305	63	0.01023
4	0.34105	19	0.04386	34	0.02851	49	0.02225	64	0.00981
5	0.29877	20	0.04114	35	0.02778	50	0.02023	65	0.00981
6	0.21323	21	0.03927	36	0.02700	51	0.01937	66	0.00981
7	0.14772	22	0.03852	37	0.02652	52	0.01733	67	0.00901
8	0.11286	23	0.03732	38	0.02652	53	0.01632	68	0.00899
9	0.09953	24	0.03565	39	0.02604	54	0.01630	69	0.00863
10	0.09650	25	0.03442	40	0.02497	55	0.01551	70	0.00863
11	0.08832	26	0.03367	41	0.02445	56	0.01234	71	0.00845
12	0.07656	27	0.03367	42	0.02398	57	0.01234		
13	0.06869	28	0.03307	43	0.02398	58	0.01216		
14	0.06332	29	0.03251	44	0.02383	59	0.01216		

Table 4.2: G_{all} block matrix first 72 eigenvalues (real parts), calculated with the TFM model.

Using the fundamental and first higher mode eigenvalues, it is possible to determine the

dominance ratio or eigenvalue separation of the system. While these values are lower than for typical fully water-moderated systems, they are significant for this type of zero power reactor, due to the decoupling zones.

$$DR = \frac{k_1}{k_0} \equiv \frac{k_{1,0,0}}{k_{0,0,0}} = 0.86$$

$$EVS = \frac{k_0 k_1}{k_0 - k_1} = 7.12$$

4.2.1 TFM analysis of a control rod insertion scenario

The scenario involves the gradual insertion of control rods in the two positions shown in Figures 4.19 and 4.20. The system response is investigated at 25%, 50% , 75% and 100% rod insertion and compared with the "clean" geometry (0% rod insertion), which corresponds to the one analyzed in [19]. The total neutron flux for all cases is given in the Appendix, Fig. D.1. This work was presented in the M&C2019 international conference [66].

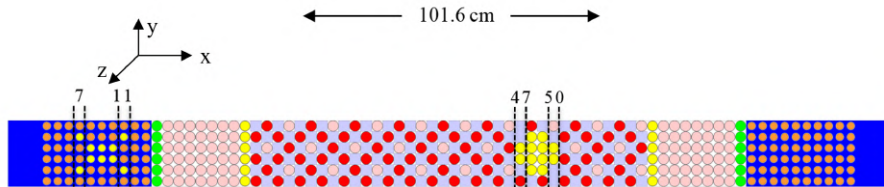


Figure 4.19: Top-down view of the "1D" geometry used in the TFM calculation, with control rods inserted. The TFM discretization is also shown.

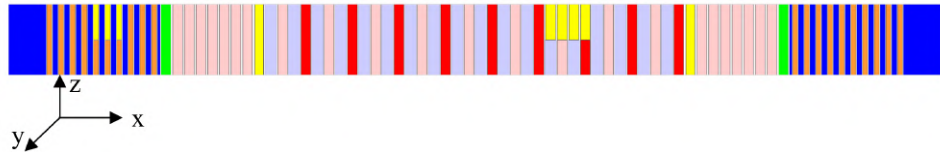


Figure 4.20: Side view of the "1D" geometry used in the TFM calculation, at 50% control rod insertion.

First, like before, the fission rate graph is given in Fig. 4.21, this time for all cases.

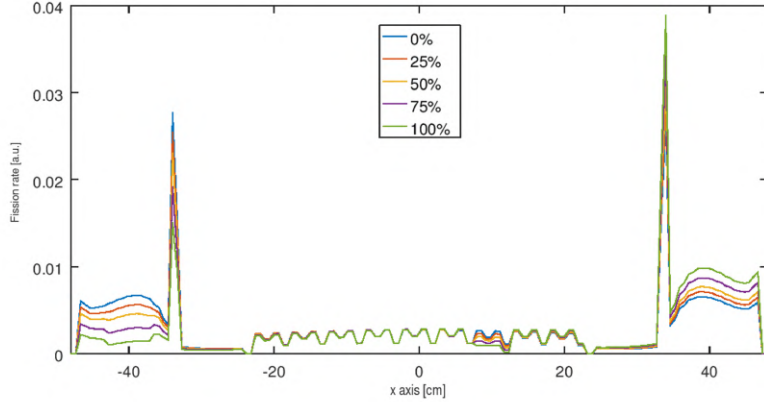


Figure 4.21: Fission rate, for the traverse of the square geometry, for all rod insertion cases.

Looking at the $G_{\chi_p \nu_p}$ matrix, it is interesting to note the gradual shift and then its abrupt change in the 100% insertion case. The latter takes place due to the eventual complete lack of fuel in the corresponding pin-cells, thus dropping their neutron propagation probability to zero, since incoming neutrons do not induce fission events. This cannot be immediately corroborated by the fission rate graph, but one needs to merely realize that the fuel elements around the control rods continue their fission events in the particular node, albeit at a reduced rate. Consequently, the propagation probability of the entire node is significantly lowered, but no node drops to zero. The insertion in the fast part is also better understood if one looks at the $T_{\chi_p \nu_p}$, explained below. A similar behavior is observed on all other matrices as well. Note that additional axis ticks and dashed lines indicate the positions of control element insertion.

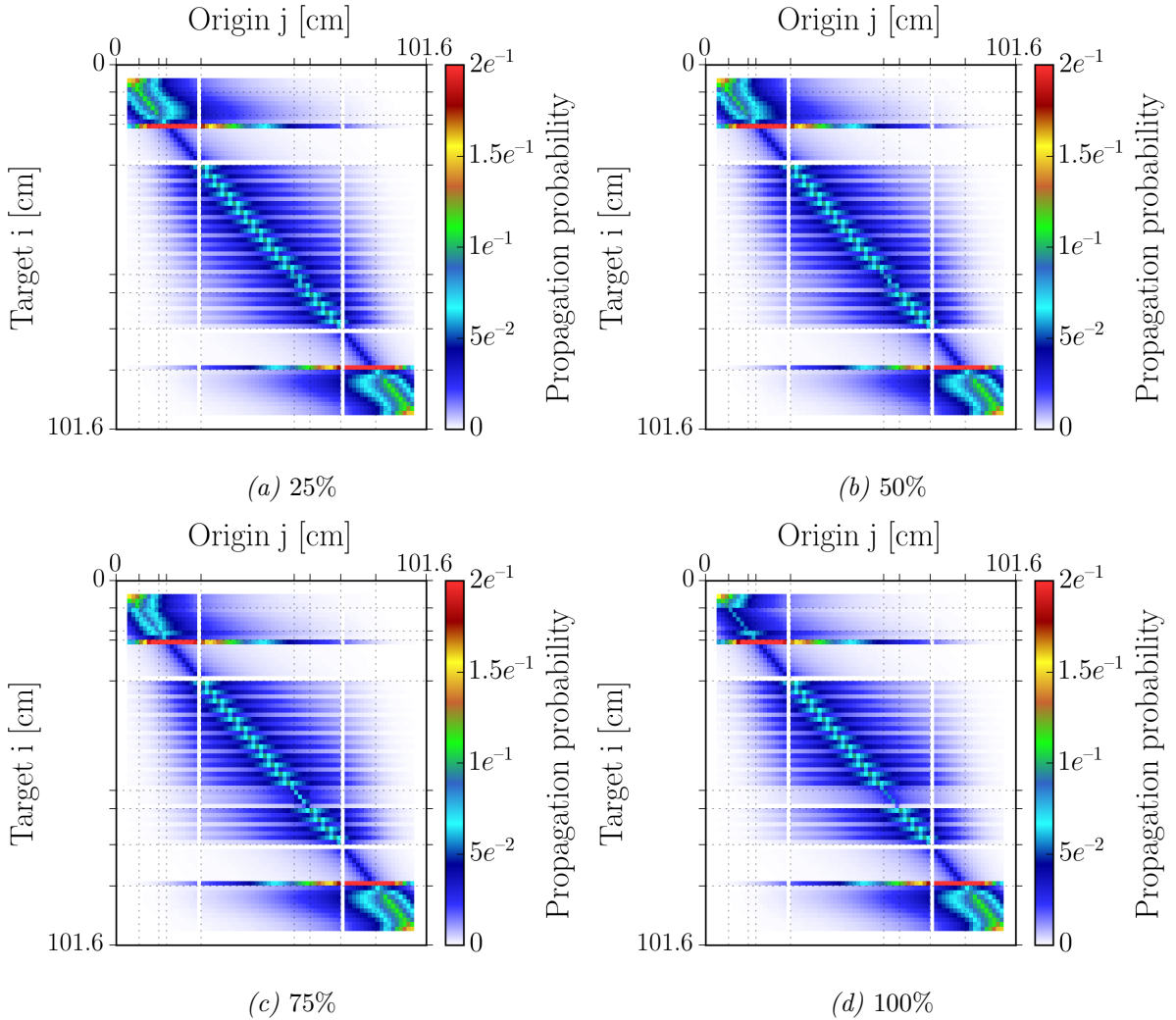


Figure 4.22: $\underline{G}_{\chi_p \nu_p}$ matrices for various levels of control rod insertion.

Fig. 4.23 shows that the propagation time of prompt neutrons at nodes 4-14 is decreased significantly. This is attributed to local spectrum hardening close to the absorber rods; the B_4C thermalizes nearby neutrons and consequently absorbs them, effectively leaving only the fast neutrons that did not interact, to propagate. A similar thing occurs in the fast zone, albeit it is only clearly visible for node 50. Looking at Fig 4.19, nodes 47, 48 and 49 still have at least one MOX fuel rod, while node 50 does not. This translates to a significant loss of reactivity in this node and one can see why, if one recalls the conversation about the $^{238}U(n,f)$ reaction opening above 1 MeV. The only neutrons that can cause fission in this node are fast neutrons and this can be seen by the low propagation time that characterizes the node. In addition to that, these neutrons have to avoid being thermalized and absorbed by the B_4C when they reach the node.

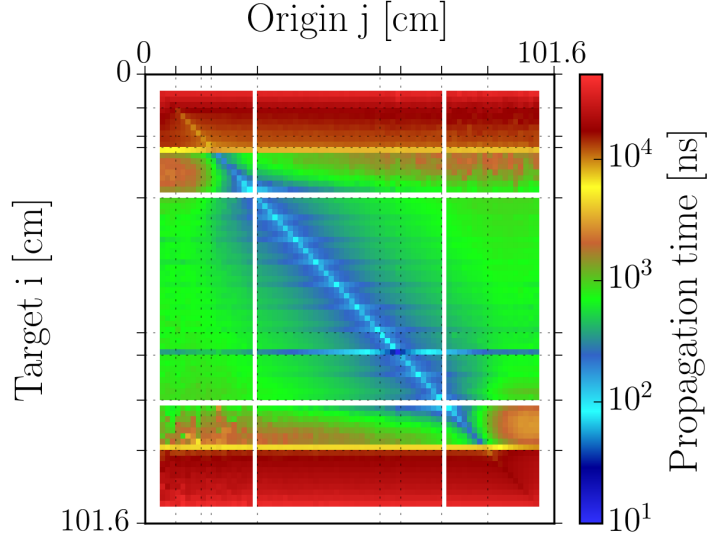
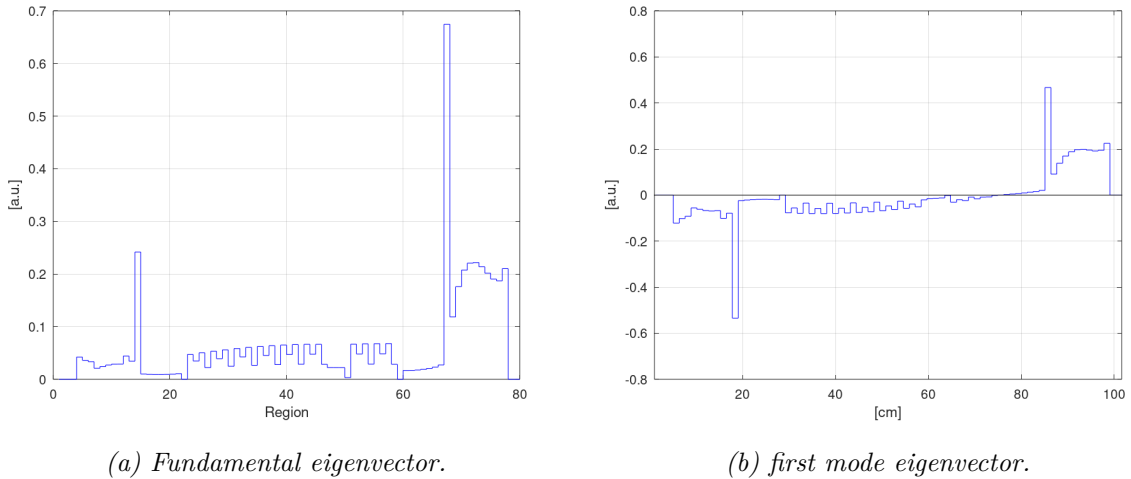


Figure 4.23: $T_{\chi_p \nu_p}$ matrix, for 100% rod insertion.

The effects of the control element insertion to fission events are mostly localized and this is clearer when looking at Fig. 4.24a, which presents the $G_{\chi_p \nu_p}$ matrix eigenvector for the case of 100% control element insertion. The shift in the distribution of the fundamental eigenvector is because the leftmost thermal regions exhibit a much lower neutron production, which in turn lowers the fission rates in the adjacent metallic U mesh. This lowers the importance of the leftmost part and thus increases the importance of the unaffected rightmost part, which now supplies a greater percentage of the systems fission neutrons. The central fast zone remains mostly unaffected away from the inserted absorber elements, with only localized distortions to the eigenvector being visible. The last observation is in line with the fact that according to the diagonals of all the G matrices, neutrons in the fast zone produce fission events close to their birth point. As for the first mode eigenvector, is it notable that the leftmost 30.2% enriched uranium part displays lower a higher potential for perturbation than its rightmost counterpart, likely due to the nearby presence of strong absorber elements, indicating that this part of the core can potentially experience higher reactivity variations, starting from the present configuration.



(a) Fundamental eigenvector.

(b) first mode eigenvector.

Figure 4.24: Eigenvectors of the $G_{\chi_p \nu_p}$ matrix, for 100% rod insertion.

4.3 Analysis with Kobayashi's multipoint kinetics model in ERANOS

The ERANOS platform was used to also analyze both the square geometry of Fig. 4.10 and its central traverse, in Fig. 4.11. The implementation of Kobayashi's multipoint kinetics model in the code allows full three-dimensional coupling analysis and to observe how zones in completely different parts of the core - in any direction - communicate with each other. Similarly to the TFM model, Kobayashi's k_{ij} coupling coefficients are used to track the neutron production in the geometry.

Converting the aforementioned geometries for use within the ECCO/ERANOS code, one has to account for the limitations of the code. The highest amount of memory the code could use in a single session was 1.5 GB (software limit), which often limited the amount of mesh detail one could achieve with it. In addition, the creation of the partial, region-wise importance and region-wise source only adds to the memory requirement. All in all, the maximum number of meshes was limited to below 500,000. In most cases dealing with complicated geometries, the process would need to be broken in three separate calculation parts, described in broad terms as:

1. The ECCO code was used to generate self-shielded, homogenized cross sections and store them in an archive.
2. The geometry was generated, using homogenized media. The 3D diffusion calculation would run and store the forward and adjoint fluxes in an archive.

- The coupling coefficients calculation would run using the forward and adjoint fluxes, whereupon the partial source and importance would be calculated, before generating the k_{ij} matrix, β_{ij} matrix, $k_{m,ij}^d$ matrices and the ℓ_i and β_i partial quantities.

The geometry mesh needs to be chosen smartly, in order to maximize accuracy where it matters and work within the limitations of the code. In general, the mesh size should correspond to the neutron mean free path in that zone and finer discretization should be used in regions characterized by significant flux changes, in order to reliably reproduce the reference flux. For the coupling calculation, separate homogenized media can be listed to form a coupling region. At this time in development, the maximum number of coupling regions was eight, before the calculation would run out of memory. Figure 4.25 shows the regions used for the squared ZEPHYR geometry, as well as the central traverse that was used.

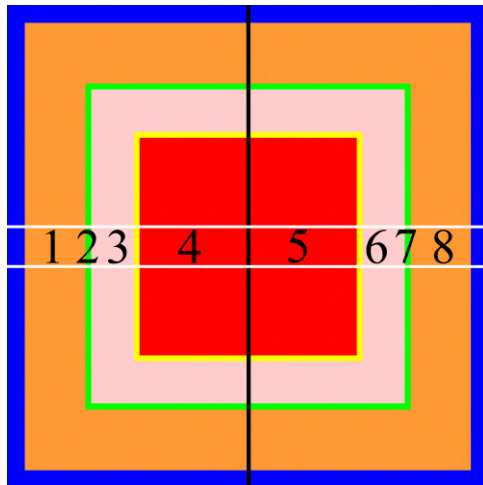


Figure 4.25: Homogenized squared geometry in ERANOS. The coupling zones and the center traverse are marked. Blue: light water, Orange: UO_2 3.7% enrichment, Green: metallic U 30.2% enrichment, Pink: natural UO_2 , Yellow: B_4C absorber, Red: ZONA1 homogenized cell (4.1).

4.3.1 Traverse geometry

Looking at the traverse first, the following coupling coefficients matrix was produced. It is not perfectly symmetric, but this is merely due to the convergence criteria used in the calculation (Appendix B). Increasing the convergence requirements would often lead to the calculation running out of memory before completion. Despite that, the differences are only a few pcm for the most part and the coupling behavior is well described.

$$k_{ij} = \begin{pmatrix} 0.81419 & 0.60589 & 0.44484 & 0.12996 & 0.03811 & 0.00825 & 0.00330 & 0.00107 \\ 0.20103 & 0.34949 & 0.28600 & 0.11728 & 0.03011 & 0.00724 & 0.00317 & 0.00100 \\ 0.02908 & 0.08366 & 0.11815 & 0.04631 & 0.00743 & 0.00131 & 0.00054 & 0.00017 \\ 0.06063 & 0.17851 & 0.29081 & 0.57920 & 0.25859 & 0.06920 & 0.04519 & 0.01132 \\ 0.01130 & 0.04522 & 0.06913 & 0.25867 & 0.57926 & 0.29084 & 0.17852 & 0.06064 \\ 0.00018 & 0.00055 & 0.00130 & 0.00747 & 0.04628 & 0.11812 & 0.08363 & 0.02913 \\ 0.00101 & 0.00320 & 0.00722 & 0.03009 & 0.11730 & 0.28596 & 0.34951 & 0.20103 \\ 0.00106 & 0.00324 & 0.00826 & 0.03812 & 0.13000 & 0.44483 & 0.60591 & 0.81411 \end{pmatrix}$$

Table 4.3: k_{ij} coupling coefficients matrix for the traverse.

Visualizing the k_{ij} matrix yields a picture similar to the TFM \underline{G} matrices, but for all neutrons, prompt and delayed.

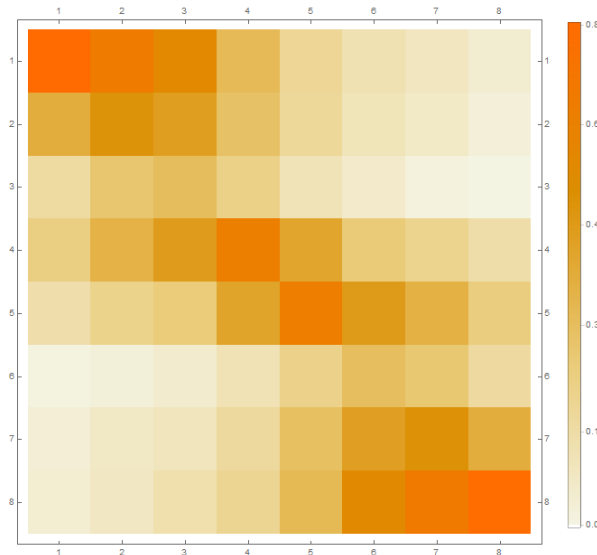


Figure 4.26: Coupling matrix for the traverse geometry, generated with ERANOS.

The matrix fundamental eigenvalue correctly yields the k_{eff} of the system, as it is independently calculated by the ERANOS diffusion solver, which serves as a further indicator that the coupling coefficients are accurate and that the method works reasonably well. Table 4.4 gives the first eight eigenvalues of the system.

0	1.17556	4	0.18061
1	1.05272	5	0.15671
2	0.73512	6	0.03391
3	0.35469	7	0.03265

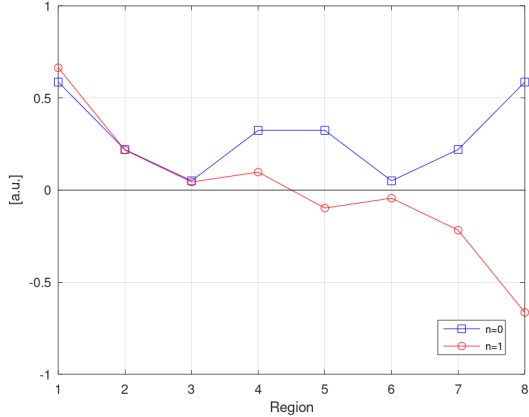
Table 4.4: First eight eigenvalues of the ZEPHYR traverse geometry, calculated in ERANOS.

The dominance ratio and eigenvalue separation are thus calculated as

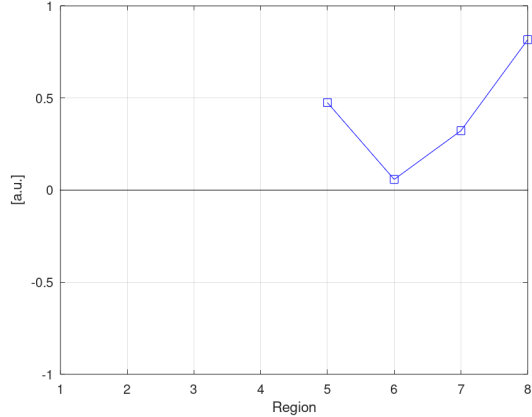
$$DR = \frac{k_1}{k_0} = 0.90$$

$$EVS = \frac{k_0 k_1}{k_0 - k_1} = 10.07$$

The fundamental and first higher mode are also given in Fig. 4.27. At this point, any comparison with the much more detailed eigenvectors in Fig. 4.17 obtained with the TFM model, should keep in mind that the k_{ij} matrix in ERANOS only has one node per fissile/fertile zone and uses diffusion. As such, all importances for a specific region (ZONA1, ZONA2, 30.2%U, ZONA3) are lumped together and as such, the eigenvector shape will not be the same as the one obtained with TFM. In this case, because only the traverse is studied, ZONA1 has significantly more relative volume than the other regions, something that would not happen if the entire geometry was taken. It is also possible to observe the overlap of the fundamental and the first mode in the thermal part, the same as with the TFM-generated eigenvectors. The eigenvector shape was also compared to results of Kobayashi's model developed independently [35] for the APOLLO3® platform [67] and applied to the same type of geometry, albeit only on the right half. The two shapes are in quite good agreement, and differences can be attributed to slight variations in geometry and the use of diffusion in ERANOS versus transport in APOLLO3.



(a) ERANOS 2.4



(b) APOLLO3® in [35]

Figure 4.27: k_{ij} matrix eigenvectors for the traverse geometry, as calculated in ERANOS in this work and in APOLLO3®.

Flux harmonic

ERANOS is also able to reproduce the fundamental (Fig. D.2) and first harmonic fluxes of the system. There is a built-in subroutine that utilizes the user-supplied fundamental forward and adjoint flux profiles of the system as inputs for a higher order flux calculation, solving the system for the first harmonic solution. While this works well for an RZ cylindrical geometry (where it can only access radial or axial modes), it was found that it cannot converge for Cartesian XY(Z) geometries, producing results such as the one below.

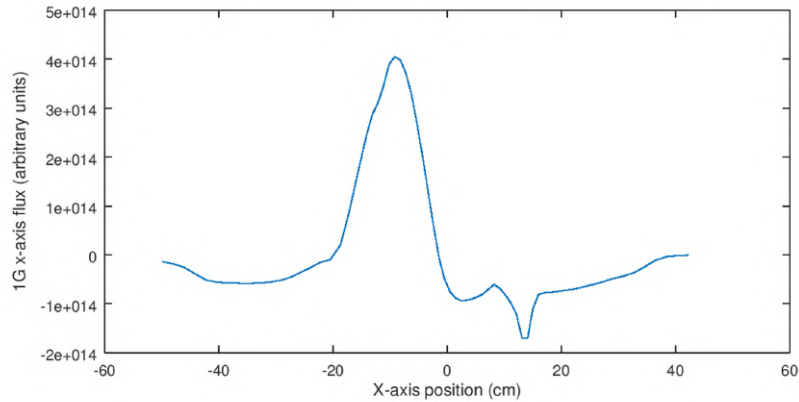


Figure 4.28: Non-converged forward first harmonic flux, before system symmetries were used.

However, if one takes advantage of certain symmetries of the system in question and runs a diffusion calculation with a zero flux boundary condition on the symmetry boundary,

it is possible to reproduce the correct harmonic fluxes [8, 9]. At this point, it is possible to extract similar conclusions about the system, this time based on the first harmonic flux mode shape, rather than the source shape. A notable example is the forward harmonic flux maximum at the ~ 40 cm point, corresponding to the 30.2% enriched uranium zone, indicating that this part of the geometry is characterized by high local importance. The k_1 eigenvalue calculated with this method has a value of 1.07533, differing 2.10% from the one calculated with the k_{ij} matrix. This difference is likely related to the heterogeneity of the geometry and the presence of the single row of highly reactive fuel. In Chapter 5, that deals with much simpler geometries, the same difference is reduced by a factor of 10.

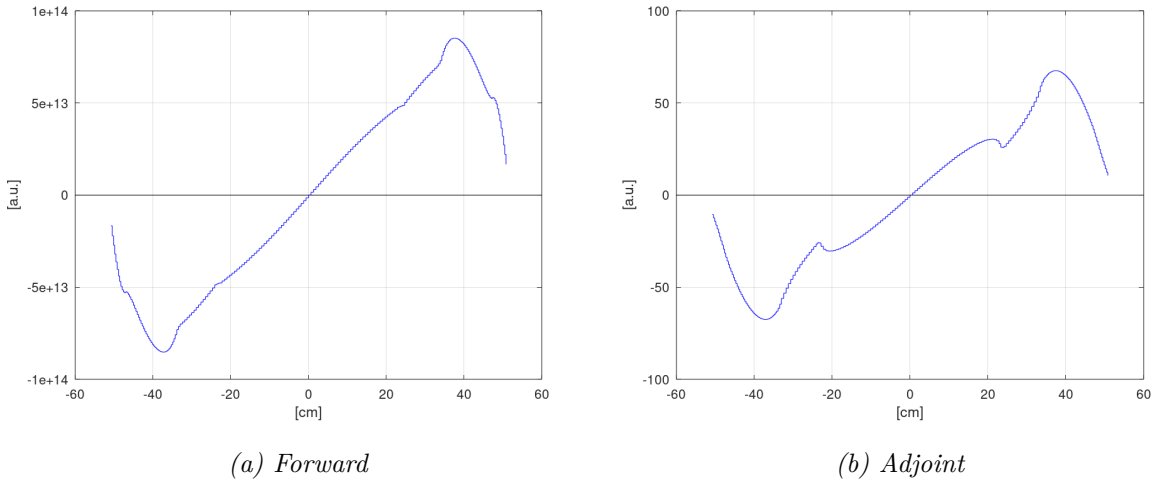


Figure 4.29: First harmonic total flux profiles for the square ZEPHYR traverse, calculated in ERANOS.

4.3.2 Full square geometry

The same analysis was performed, this time in the square geometry of Fig. 4.10. Looking at the coupling region discretization, the main difference between this and the traverse is that now, all regions have their correct volumes. However, the discretization now is not limited to the x axis, since the outer zones now go around the inner ones. As such, it is now possible to explore the system in more ways. This approach permits the selection of any region in the 3D geometry. The reader needs to keep in mind though, that the eigenvalues accessed this way are not necessarily the same ones that are accessed with the traverse geometry (azimuthal ones) and as such, it is not always possible to be confident about the calculated dominance ratio. For example, in power reactor cores, it is desirable to access axial eigenvalues and investigate associated eigenvalues separation problems [45]. It also goes without saying that the eigenvalues themselves will not remain

the same with different discretization, unless a sufficient number of zones is selected, so that the entire geometry is covered.

The first eight eigenvalues, dominance ratio and eigenvalue separation are given below, while the coupling coefficients matrix is given in the Appendix, in Table D.1.

0	0.99887	4	0.17677
1	0.87559	5	0.16390
2	0.53516	6	0.02932
3	0.35871	7	0.02838

Table 4.5: First eight eigenvalues of the full square geometry, calculated in ERANOS.

$$DR = \frac{k_1}{k_0} = 0.88$$

$$EVS = \frac{k_0 k_1}{k_0 - k_1} = 7.09$$

Purely from an eigenvalue standpoint, the traverse and the full square are quite close, with similar dominance ratios. However, the difference in the two approaches becomes apparent if one looks at the matrix eigenvectors. Now that all regions have their original volume ratios, ZONA1 no longer shows up with increased importance.

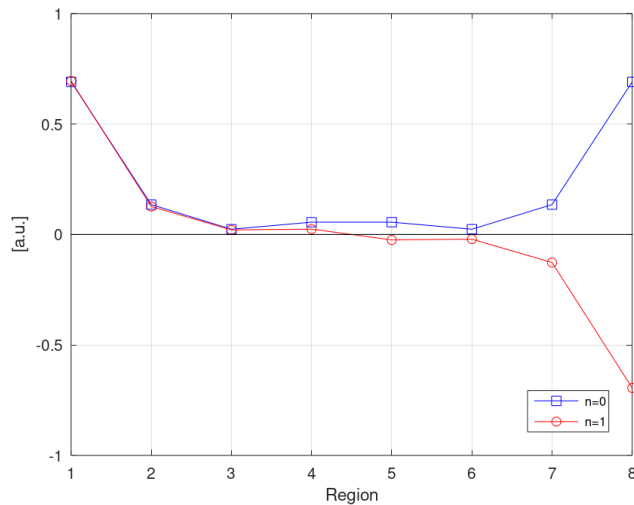


Figure 4.30: First two eigenvectors of the square geometry, obtained with the k_{ij} model implemented in ERANOS.

4.4 Remarks

This chapter showcases the application of the calculation tools and data processing flow that were used throughout the thesis. The geometry analyzed is the ZEPHYR fast-thermal coupled core concept, developed internally in CEA, as a versatile zero power reactor and a candidate for the replacement of the now decommissioned EOLE and MINERVE experimental reactors. The Transient Fission Matrix model in Serpent 2 works on Cartesian geometries and as such, an equal-volume square geometry of the ZEPHYR core was used for most calculations. It allows one to receive accurate information for the system in question, along one of its axes and as a consequence, gain information regarding the fundamental and higher modes along this axis, leading to conclusions about the dominance ratio and the eigenvalue separation. Kobayashi's coupling coefficients method in ERANOS, while capable of a similar analysis, allows for the selection of any region inside a full 3D geometry, albeit at the cost of a reduced number of coupling nodes and the limitation of relying on a diffusion calculation. The two methods reliably complement each other, each offering a different level of detail, features and of course, computational requirements. In the case of TFM, the entirety of the calculations had to be performed locally, which was one of the reasons it was limited to the 1D case. Serpent has relatively high memory requirements and from the context of CPU time, a calculation of reasonably good accuracy could take more than 24 hours on a 12 thread CPU.

Chapter 5

Coupled assemblies benchmark

After the ZEPHYR project was indefinitely postponed by the CEA, a new focus area needed to be found for a practical application of the PhD. During the first year of the thesis, literature review of papers related to multipoint kinetics and coupling coefficient generation in neutronic codes revealed that most of these investigations lacked a common testing ground. It is customary for neutronic codes to be tested against either well-established benchmarks or real world data and yet when it comes to the aforementioned topics, all tests are made on different geometries and the testing methodology is often developed in-house. To that end, there was an opportunity to propose a benchmark to be used for testing and validation of future relevant calculation schemes. Part of this work is available in the proceeding of the PHYSOR2020 international conference [26].

Inspired by experiments performed in the KUCA (Kyoto University Critical Assembly) reactor [68,69] in the 90's [47,61], the geometry chosen here is a light water tank containing two fuel assemblies that can freely move in the tank, forming a water blade between them. The water blade length ranges from 0 cm to 20.16 cm. For each step of separation, TFM and region-wise coupling coefficients matrices together with kinetic parameters are presented. Similarly to the previous chapter, eigenvalues and eigenvectors are extracted and the $\frac{k_{1,0,0}}{k_{0,0,0}}$ eigenvalue ratio is calculated. A thorough comparison takes place, between results obtained with the Transient Fission Matrix model implemented in the Serpent 2 Monte Carlo code and results obtained with Kobayashi's k_{ij} method, implemented in ERANOS. Considering the two approaches are completely separate in terms of development, the comparison serves as a discussion on validation, as well as comparing the limitations of the two approaches.

5.1 Calculation setup

The geometry consists of a light water tank with two fresh PWR-type fuel assemblies placed inside. There is a single fuel material used per assembly and two scenarios are investigated - one where both assemblies contain UOX fuel of the same enrichment and one where one assembly contains UOX, while the other contains MOX. The fuel pin pitch is 1.26 cm. The y axis uses periodic boundary conditions, while the x and z axes use void boundary conditions. The two assemblies are separated by an adaptive water blade and are free to move along the x axis, with the width of the blade (separation) ranging from 0 cm to 20.16 cm (from 0 to 16 times the lattice pitch). The analysis of the geometry took place along the axis and both the TFM and the detector discretization meshes are based on the lattice pitch (1.26cm), with the former utilizing one node per pitch length (62) and the latter, four nodes per pitch length (248). This allows the results to be expressed in both absolute length values and in relation to the lattice pitch of the system. Whenever the latter occurs, it is given as a number times the pitch, i.e. 20.16 cm (16x).

Fig. 5.1 gives a top-down view of the UOX-UOX geometry, showing the typical characteristics of two PWR assemblies, designed with the standard spider-type control rod assembly guide tubes and central instrumentation tube in the middle. Note that the assemblies essentially continue along the y axis, because of the boundary conditions used. The radial design of the fuel pins, guide tubes and instrumentation tubes are taken based on the BEAVRS benchmark [70] are given in Table E.1, while the axial design is simplified compared to that of a real, full size assembly, as it would exceed the available active height of typical experimental reactors, especially zero power setups. The vertical design is shown in Fig. 5.2. The total height of the geometry is 130 cm, while the fuel active height is 80 cm.

As for the material selection, the UOX fuel has an enrichment of 3.71 w.t.-% and the control rod absorbing material is enriched B_4C , with a $^{10}B/B_{total}$ ratio of 90%. Detailed compositions are given in Tables E.2 and E.4 respectively, in Appendix E.

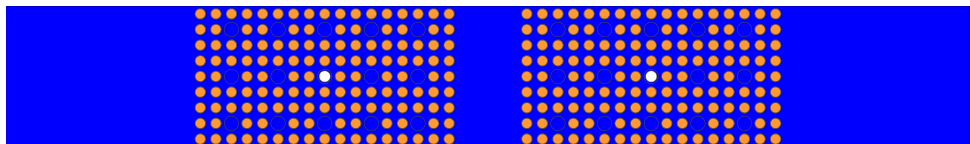


Figure 5.1: X - Y view of the UOX-UOX geometry, with a separation of 5.04 cm (4x). The total length of the geometry is 78.12 cm (62x).

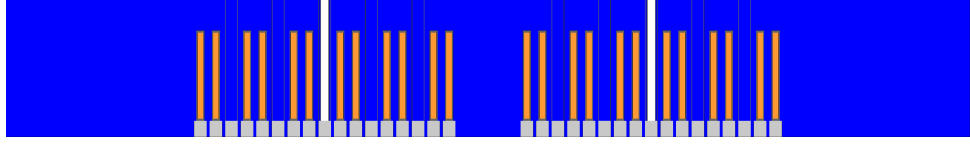


Figure 5.2: X-Z view of the UOX-UOX geometry. The pins and guide tubes are on top of steel supports placed at the bottom of the geometry.

For the UOX-MOX case below, the fuel of the right assembly was replaced with reactor grade MOX fuel, whose composition is given in Table E.3 and comes from burned UO₂ fuel with a burnup value of 35 GWd/t, that was used in the MISTRAL experiment [71]. Everything else is kept the same. The choice to include a MOX fuel of lower reactivity offers insight into the effects of having fuels of both different reactivities and isotopic compositions. The same scenario would present itself when mixing fresh and burnt fuel assemblies or burnt assemblies with different irradiation times (once or twice cycled), something that is very common in power reactor core loading strategies.



Figure 5.3: X-Y view of the UOX-MOX geometry, with a separation of 20.16 cm (16x). The total length of the geometry is 78.12 cm (62x).

Finally, it should be noted that the change in the azimuthal coupling behavior is the x axis is studied here and thus the $\frac{k_{1,0,0}}{k_{0,0,0}}$ eigenvalue ratio is used throughout this chapter, even though there are cases where $k_{1,0,0}$ is not the highest eigenvalue after the fundamental one. Since the analysis is limited to one axis, this does not affect the conclusions made here.

5.2 TFM calculations

5.2.1 Results for the UOX-UOX case

This part focuses on the results obtained with Transient Fission Matrix model, in the Serpent 2 code. in the UOX-UOX case, for a water blade width 0 cm, 2.52 cm, 5.04 cm, and 20.16 cm (0, 2, 4 and 16 pitch lengths, respectively). Figure 5.4 showcases the $\underline{G}_{\chi_p \nu_p}$ prompt-to-prompt propagation probability matrices for all cases. Initially focusing on the first matrix (0 cm), it gives the system's response to a neutron pulse for one generation. From the diagonal of the matrix, it's clear that there is a high probability for a produced neutron to induce fission in a nearby node and that probability drops for target nodes away from the origin one, due to the relatively short mean free path of neutrons in a thermal lattice. It is apparent that with a separation of 0 cm, the two assemblies behave essentially as a single core and there is a great deal of contributed prompt-to-prompt events from one assembly to the other. The two ends of the geometry display higher localized fission-to-fission probabilities, due to the moderator reflection effect. This reflection effect also appears on the edge fuel pins as the assemblies are separated, pinpointing a local increase of moderation.

As the separation between the two assemblies increases, the system transitions from a single fissile geometry to two partially independent ones, the coupling between the two assemblies decreasing at each step. It is interesting to note that for the small separation value of 2.52 cm (2x), the moderator excess between the two assemblies serves as a thermal flux trap and actually increases the number of both local and contributed fission events that take place, leading to an increase in the overall k_{eff} of the system (Table 5.1). Neutrons enter the moderator zone and due to the lack of strongly absorbing elements (namely fuel), eventually experience more scattering events and drop to lower average energies before scattering back inside the fuel lattices to be absorbed by the fuel elements. Due to the lower average energy, the local average fission cross section is higher. The reactivity increase, albeit safe, is not negligible, at 200 pcm (or 0.276\$) and in a potential experiment, this behavior should be taken into account for both control and accuracy purposes. On a similar note, the β_{eff} of the system in Table 5.2 (calculated with the TFM model) shows a slight drop before increasing at the end. Values corresponding to a single UOX assembly are given at the end of each table. Comparing the data for the single assembly and the 20.16 cm case, it can be seen that while the system is not completely decoupled at that separation level, it is very close to being so.

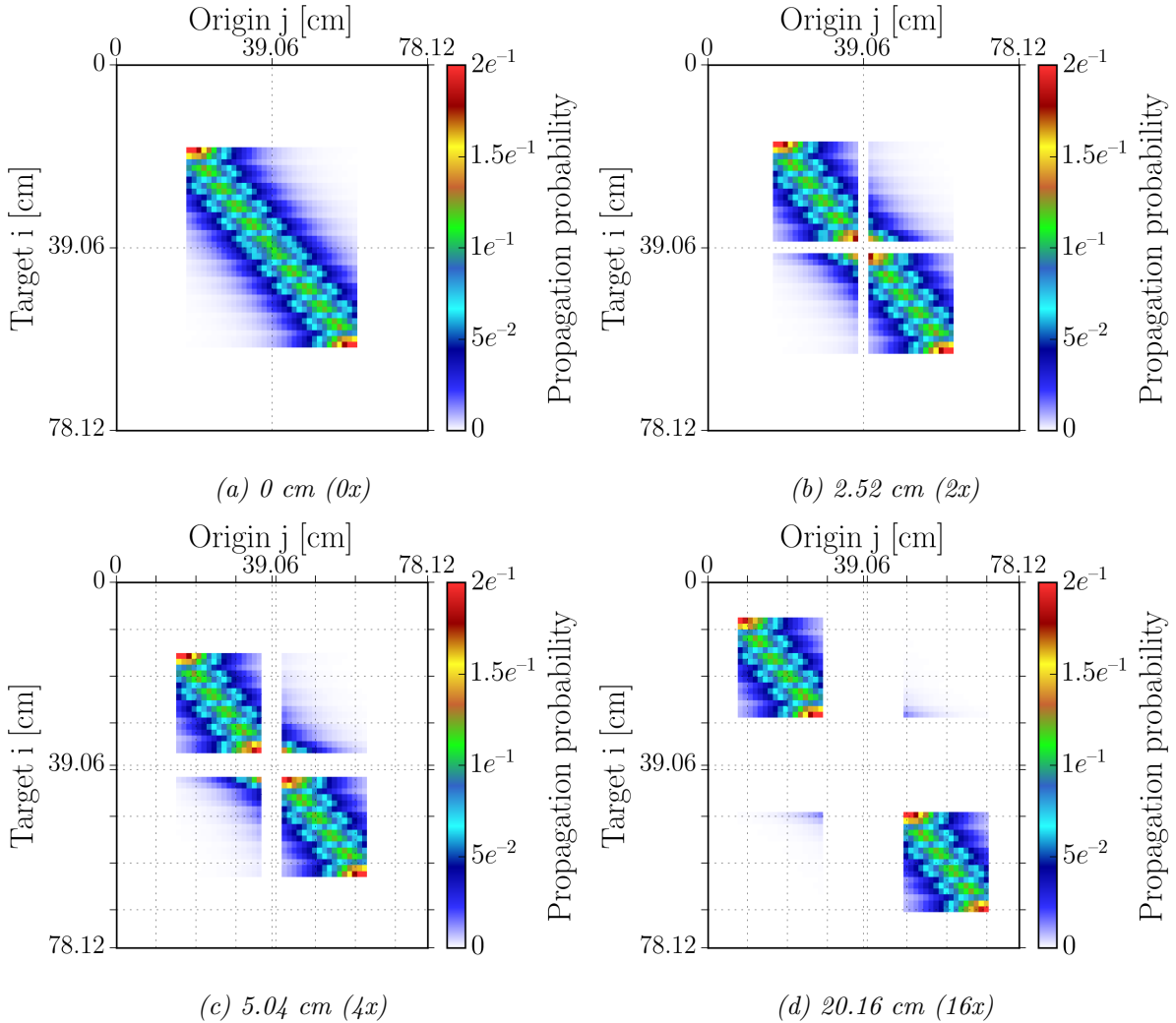


Figure 5.4: $G_{\chi_p \nu_p}$ matrices for the UOX-UOX geometry, for different levels of assembly separation.

The next figure shows the prompt-to-prompt matrix eigenvector, corresponding to the fundamental mode and denoting the importance of each node. It follows an expected evolution and supports the previous observations, including the one regarding the local increase in fission events at the inner assembly boundaries because of the thermal flux trap phenomenon. It is also a good way to view the coupling (or decoupling) between the two assemblies.

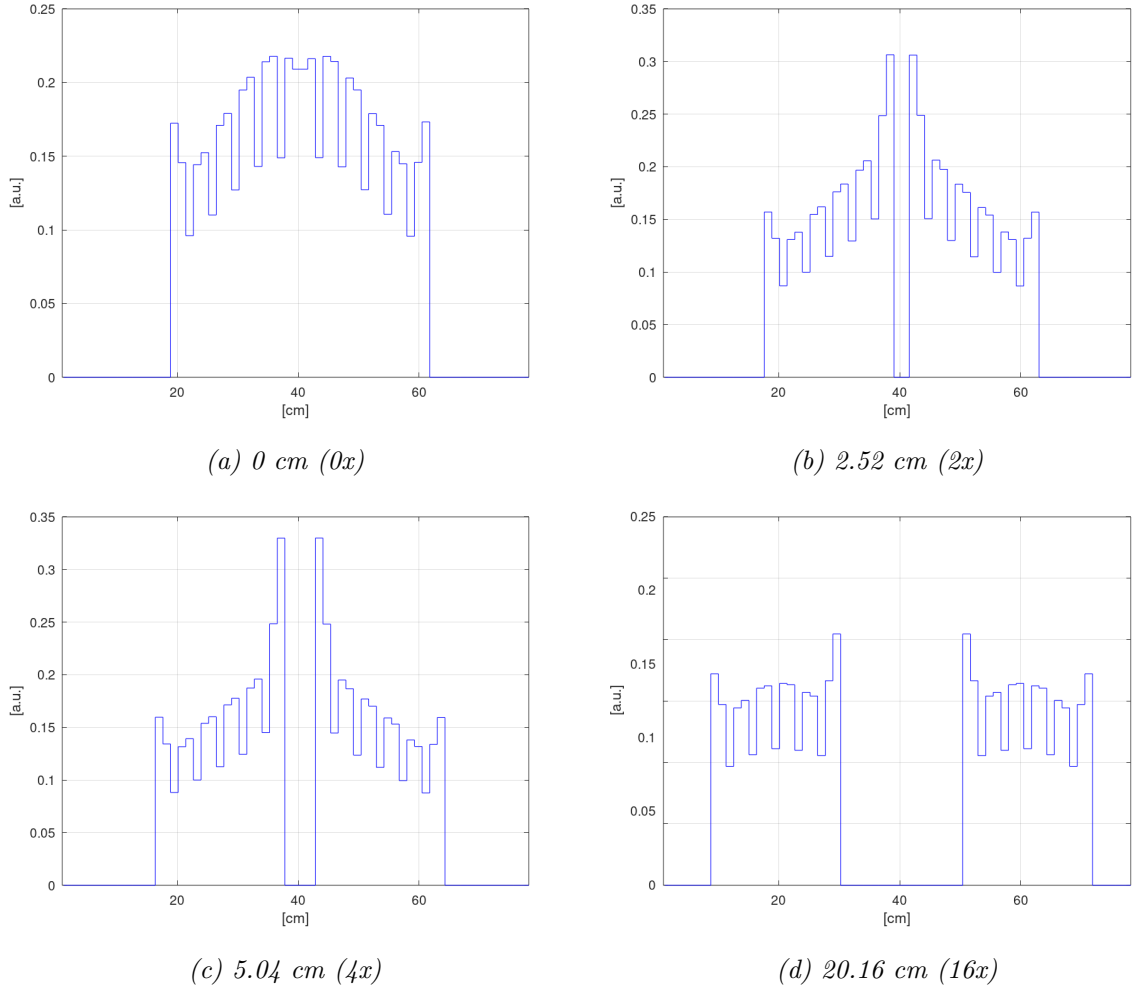


Figure 5.5: $G_{\chi_p \nu_p}$ matrix eigenvector for the UOX-UOX geometry, for different levels of assembly separation.

Figure 5.6 shows the $G_{\chi_p \nu_p}$ matrix eigenvector for a single UOX assembly. For the lone assembly, the eigenvector shape is completely symmetrical. Comparing Figures 5.5 and 5.6 reinforces the previous statement regarding the decoupling of the two assemblies at 20.16 cm. They are indeed quite decoupled, but not completely.

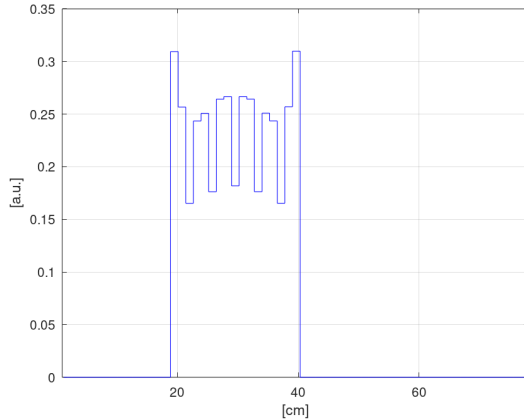


Figure 5.6: Prompt-to-prompt matrix eigenvector for a single UOX fuel assembly.

After that point, the reflection effect becomes significant and propagation probability increases locally at the assembly boundaries, since any neutrons with emission angles towards the moderator either do not contribute to fissions at all (and so the information is lost) or are reflected and induce fissions at the lattice boundary. The two assemblies start to behave like two separate systems more and more, ending up as two reflected and mostly decoupled cores, with minimal contributions to each other. The above observations are consistent between all fission matrices, $G_{\chi_p \nu_p}$, $G_{\chi_p \nu_d}$, $G_{\chi_d \nu_p}$ and $G_{\chi_d \nu_d}$. Figure 5.7 shows all of the G matrices for the case of 2.52 cm (2x) separation. In general, what can be seen is that no matter if the neutron is prompt or delayed, it has a high chance of creating a prompt neutron in the next generation, something that is expected, given the values of the delayed neutron fraction. This can be seen very well in the $G_{\chi_d \nu_p}$ matrix. In the case of the UOX-MOX system shown later, the matrices containing delayed neutron data are notably different from the UOX-UOX case, due to the presence of the several different Pu isotopes.

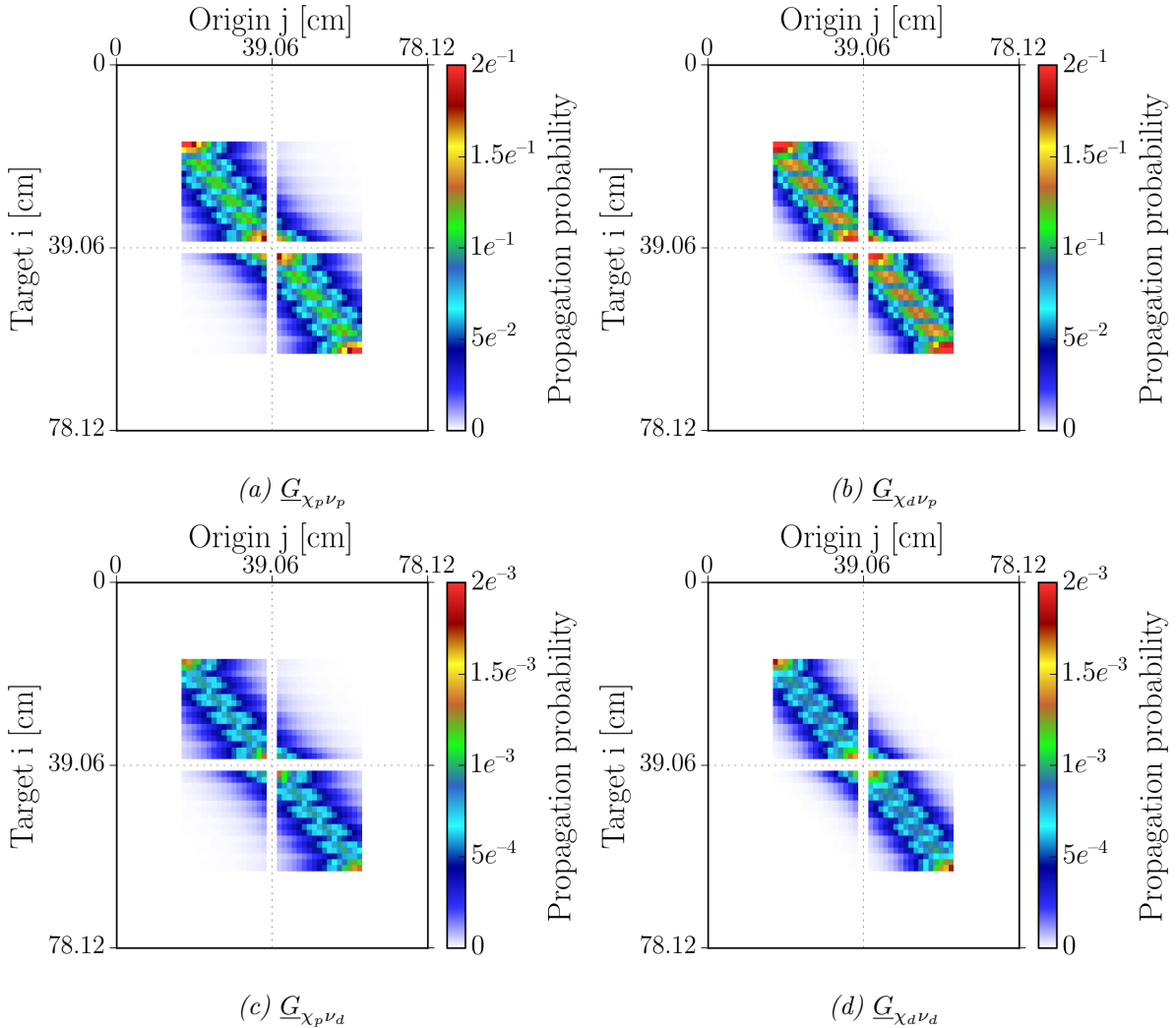


Figure 5.7: \underline{G} matrices for the UOX-UOX geometry, for a separation of 2.52 cm (2x).

The $T_{\chi_p \nu_p}$ matrix shown in Fig. 5.8 paints a similar picture as the previous ones, with the most apparent feature being that increased moderation and reflection effects at the inner boundaries become apparent very easily. The look of the contribution parts (top right and bottom left) in the separated cases is due to the fact that the scale is bounded on both ends. Any node where the average generation time is below 20 μs will show up as blue, while if it exceeds 80 μs , it will show up as red. Especially in the 20.16 cm (16x) case, the statistics for these parts are quite bad, since very few fission events occur from neutron contributions from the other assembly and thus the cross-contribution parts look quite non-uniform. The results of the matrix also correlate well with the evolution of the average generation time values that were independently calculated with Serpent 2 with Nauchi's method, given in Table 5.2.

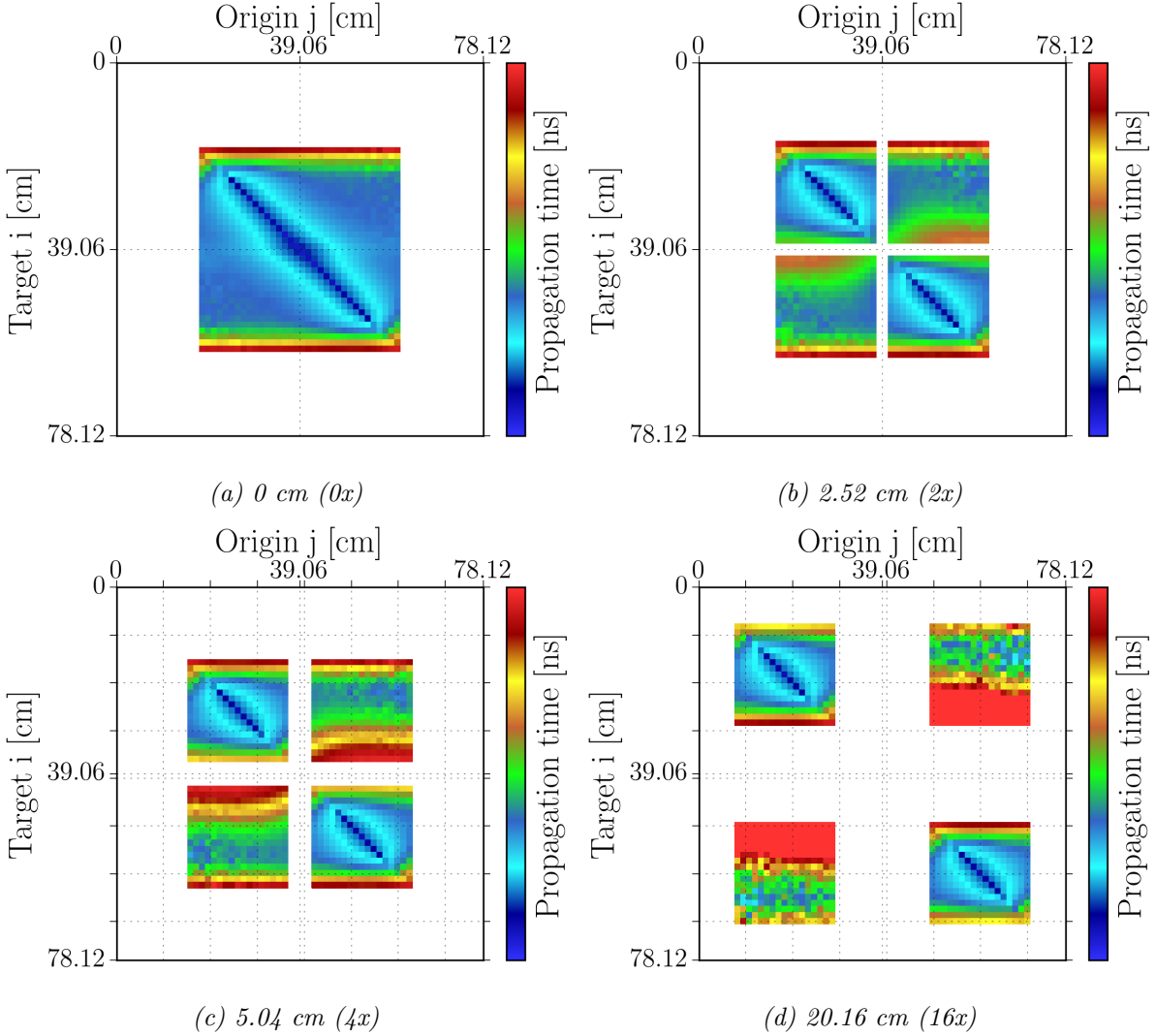


Figure 5.8: $T_{\chi_p \nu_p}$ matrices for the UOX-UOX geometry, for different levels of assembly separation.

Finally, the following tables are compiled, with all quantities referring to the entire system. All values shown are calculated with the TFM model. Although the validity of the TFM model is not the subject of this paper, in all cases, the k_{eff} , β_{eff} , ℓ and Λ_{eff} results were compared with reference data calculated natively in Serpent 2 with Nauchi's method. All values are either close to or below 1% from the reference. A comparison table is provided for the 0 cm and 15 cm cases. The eigenvalues of the system were computed by using the G_{all} block matrix. The uncertainty associated with the eigenvalues is on the order of 32 pcm (see the beginning of section 4.2), with the first $\frac{k_{1,0,0}}{k_{0,0,0}}$ ratio value being $DR = 0.76278(32)$. However, only two digits are kept for the eigenvalue ratio, so the uncertainty is omitted. The same is true for all TFM cases that follow in this chapter.

Separation (cm)	Separation (pitch)	$k_{0,0,0}$	$k_{1,0,0}$	$\frac{k_{1,0,0}}{k_{0,0,0}}$
0	0	1.26644	0.96602	0.76
2.52	2	1.26897	0.99457	0.78
5.04	4	1.23610	1.02076	0.83
10.08	8	1.16272	1.06167	0.91
15.12	12	1.12617	1.08417	0.96
20.16	16	1.10831	1.09103	0.98
Single UOX assembly	N/A	1.10688	0.59717	0.54

Table 5.1: $k_{0,0,0}$, $k_{1,0,0}$ and $\frac{k_{1,0,0}}{k_{0,0,0}}$ as a function of the assembly separation for the UOX-UOX case.

Separation (cm)	Separation (pitch)	β_{eff} (pcm)	Λ_{eff} (μ s)
0	0	729	24.7
2.52	2	725	27.1
5.04	4	725	31.7
10.08	8	738	36.2
15.12	12	751	35.7
20.16	16	760	34.3
Single UOX assembly	N/A	762	34.7

Table 5.2: β_{eff} and Λ_{eff} as a function of the assembly separation for the the UOX-UOX case.

Separation (cm)	Quantity	TFM value	Reference	Difference
0	k_{eff}	1.26644	1.26632(2)	0.009%
	β_{eff} (pcm)	729	732	-0.425%
	ℓ_{eff} (μ s)	31.1	30.7	1.088%
	Λ_{eff} (μ s)	24.7	24.5	0.571%
15	k_{eff}	1.12617	1.12625(3)	-0.007%
	β_{eff} (pcm)	751	756	-0.506%
	ℓ_{eff} (μ s)	39.9	40.3	-0.706%
	Λ_{eff} (μ s)	35.7	36.1	-1.036%

Table 5.3: Comparison between values calculated with the TFM model versus reference data calculated natively in Serpent 2.

From the data in Table 5.1, the eigenvalue ratio can be plotted versus the assembly separation. Considering that $\frac{k_{1,0,0}}{k_{0,0,0}}$ is an indicator of the amount of the decoupling (or coupling) on the x axis, Fig. 5.9 also indicates that the decoupling increases with separation and supports the fact that at the last point, the assemblies are almost fully decoupled (full decoupling would be indicated by a $\frac{k_{1,0,0}}{k_{0,0,0}} = 1$ and β_{eff} and Λ_{eff} values that correspond to the single assembly case).

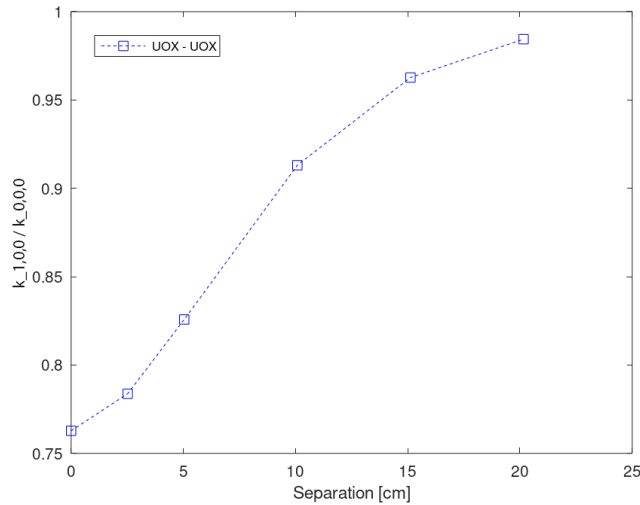


Figure 5.9: $\frac{k_{1,0,0}}{k_{0,0,0}}$ value versus assembly separation, for the UOX-UOX case.

Lastly, the $G_{\chi_p \nu_p}$ matrix eigenvector was plotted for the first five modes, for the 5.04

cm separation case. This simple geometry makes it easy to understand the connection between the fundamental and the higher modes and how the latter contribute to the shape of the former one. As was stated before, the degree that the higher azimuthal modes contribute to the fundamental one can be expressed via the $\frac{k_{1,0,0}}{k_{0,0,0}}$ ratio.

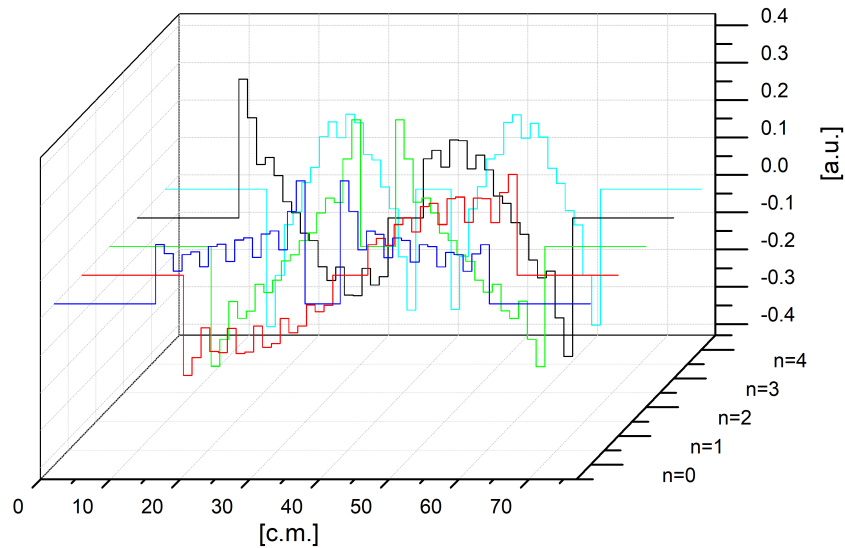


Figure 5.10: $G_{\chi_p \nu_p}$ matrix eigenvector for the first five modes, for the UOX-UOX 5.04 cm case.

Results of control rod insertion

The effect of control rod insertion on the system's decoupling is now analyzed. The ultimate aim of the static approach presented here is to exhibit amplified effects due to the control rod that could lead to measurable transient phenomena or signatures of eigenvalue ratio modification. In this case, the effect of inserting B_4C control rods into the guide tubes of the right assembly is studied. The top-down view of the geometry can be seen in Fig. 5.11. The control rod height is equal to the active height of the fuel.

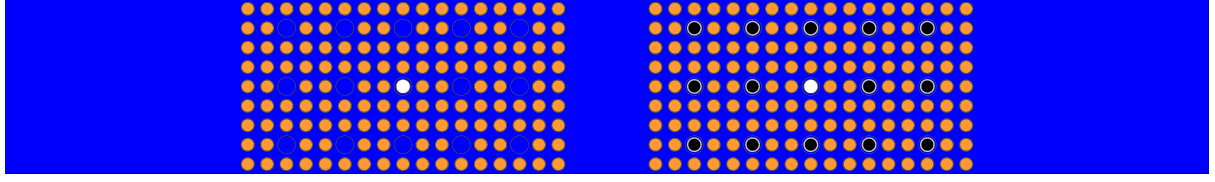


Figure 5.11: X-Y view of the UOX-UOX geometry, with a separation of 5.04 cm (4x) and B_4C control rods inserted into the right assembly.

Figure 5.12 displays the $G_{\chi_p \nu_p}$ matrix. The insertion of negative reactivity causes the affected assembly to display a significant drop in propagation probability across all nodes, as expected, with the distinct detail that the boundary nodes do not appear particularly affected in absolute terms, due to the moderator reflection effect and because the small neutron mean free path in thermal lattices causes the effect of the closest control rods to be partially shielded by the in-between row of fuel.

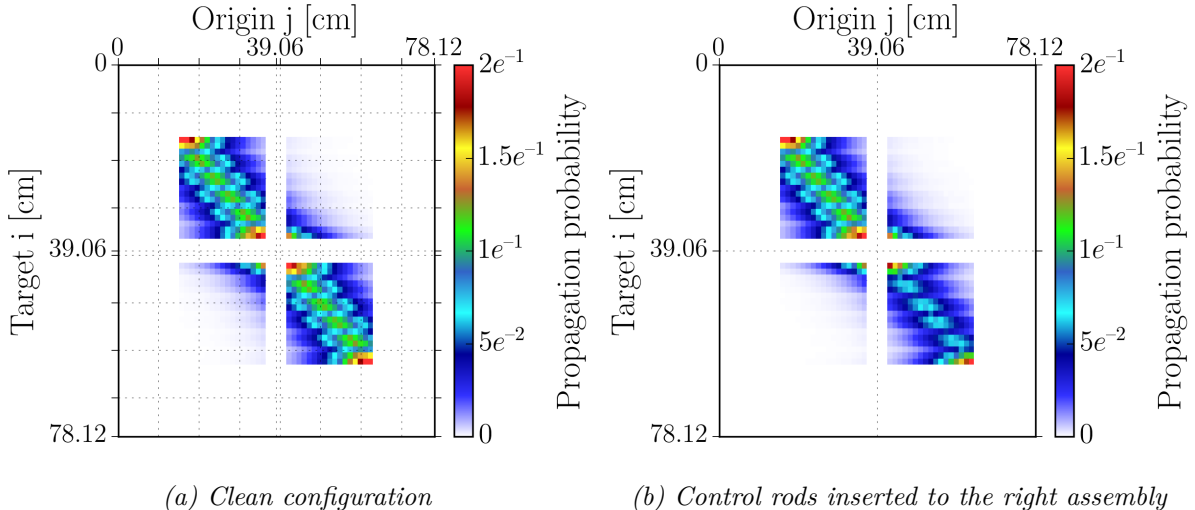


Figure 5.12: $G_{\chi_p \nu_p}$ matrices for the UOX-UOX geometry, for a separation of 5.04 cm (4x), showing the effects of control rod insertion.

Comparing Fig. 5.5 for 5.04 cm with Fig. 5.13, it can be seen that the insertion of control rods has a notable effect on the left assembly, at this level of coupling. The left assembly, because of its higher reactivity and relative importance, starts dominating the system. Because the rodded assembly acts as very weak neutron source now, the eigenvector of the left one changes and takes a shape closer to that of a single UOX assembly in water. The inner boundary of the right assembly still emits neutrons into the water blade, since the local prompt-to-prompt propagation probability at the boundary node is not particularly affected. This is responsible for the left assembly's elevated importance at the inner boundary node, which however is much lower than the same node for the case without

control rods of Fig. 5.5.

Furthermore, looking at Table 5.4, the $\frac{k_{1,0,0}}{k_{0,0,0}}$ value was reduced, despite the introduction of absorber elements. This is because the change was localized. A short analysis follows in the next part, where absorber is introduced to the entire system. The same table shows that when it comes to the Λ_{eff} value of the combined system, the left UOX assembly dominates the entire geometry, because of its higher importance.

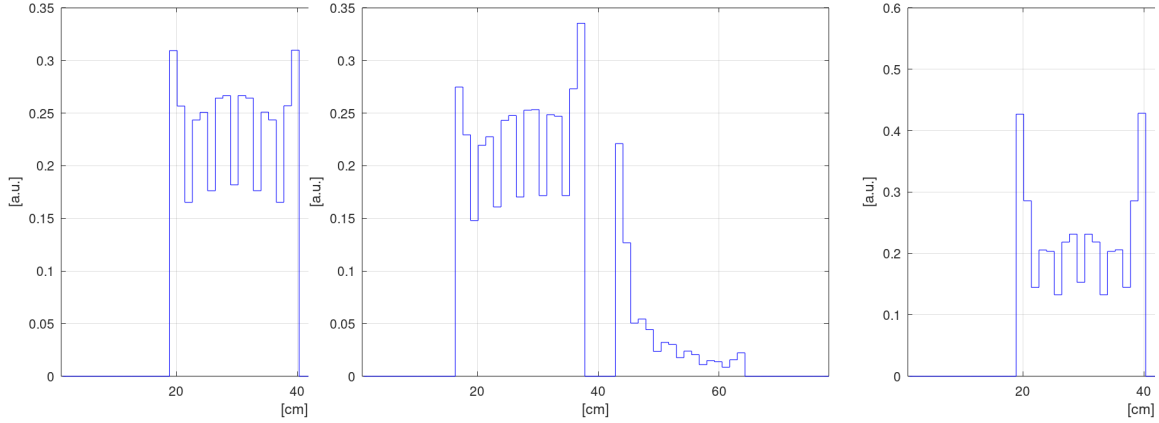
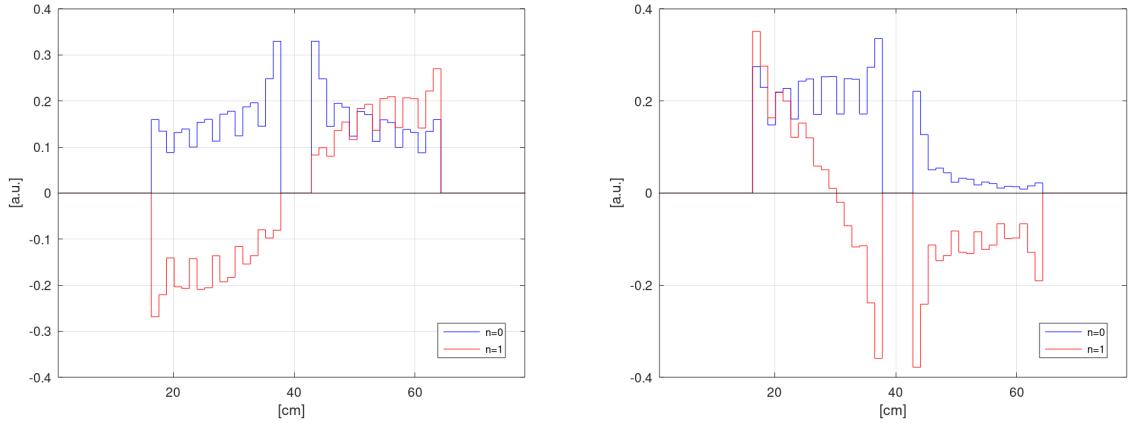


Figure 5.13: Prompt-to-prompt matrix eigenvector for a single UOX assembly (left), the system of Fig. 5.11 (middle) and a single UOX assembly with control rods inserted (right).

The first mode results are also given in Fig. 5.14, overlayed on top of the fundamental mode, and they are quite interesting. While for all symmetrical cases, the first mode eigenvector becomes zero on the symmetry axis (as expected), in the case of rod insertion, it is heavily displaced towards the middle of the clean (non-rodded) assembly and is clearly connected to shape changes of the fundamental mode (this is discussed more thoroughly in the next section). This indicates that the first mode eigenvector becomes zero at the system's center of importance.



(a) Clean configuration

(b) Control rods inserted to the right assembly

Figure 5.14: $G_{\chi_p \nu_p}$ matrices for the UOX-UOX geometry, for a separation of 5.04 cm (4x), showing the effects of control rod insertion.

Setup	$k_{0,0,0}$	$k_{1,0,0}$	$\frac{k_{1,0,0}}{k_{0,0,0}}$
UOX - Rodded UOX at 5 cm	1.13963	0.72353	0.64
Unrodded UOX-UOX at 5 cm	1.23610	1.02076	0.83
Single UOX assembly	1.10688	0.59717	0.54
Single UOX Rodded assembly	0.65811	N/A	N/A

Table 5.4: $k_{0,0,0}$, $k_{1,0,0}$ and $\frac{k_{1,0,0}}{k_{0,0,0}}$ as a function of the assembly separation for the rod insertion case.

Setup	β_{eff} (pcm)	Λ_{eff} (μs)
UOX - Rodded UOX at 5 cm	735	33.4
Unrodded UOX-UOX at 5 cm	725	31.7
Single UOX assembly	762	34.7
Single UOX Rodded assembly	759	57.8

Table 5.5: β_{eff} and Λ_{eff} as a function of the assembly separation for the rod insertion case.

Figure 5.15 depicts the thermal flux (< 1 eV) of the system for all the different cases studied above. Of note is the sharp increase of the flux between the two assemblies at the beginning of separation (2.52 cm), leading to the increase in the total reactivity of

the system. Of particular interest is the flux shape difference between the “5.04 cm” and “5.04 cm CR” cases. With control rods inserted, the right assembly acts as a very weak neutron source and so the left’s flux is not affected by it in a significant way, its flux shape going from sloped to noticeably more symmetrical and indicative of a single assembly. At the same time, the right assembly’s flux shape is also not heavily affected by incoming flux from the left, with the exception of the first two rows of fuel pins, since the control rods absorb most of the incoming flux after that point. The latter also explains the fairly symmetrical part of the $\underline{G}_{\chi_p \nu_p}$ matrix of Fig. 5.12, corresponding to the right assembly. The thermal flux shape for both assemblies corresponds closely to the shape of the $\underline{G}_{\chi_p \nu_p}$ eigenvector shown in Fig. 5.13, as expected in this thermal system. The flux detector setup in Serpent 2 was discretized to 248 bins along the x axis.

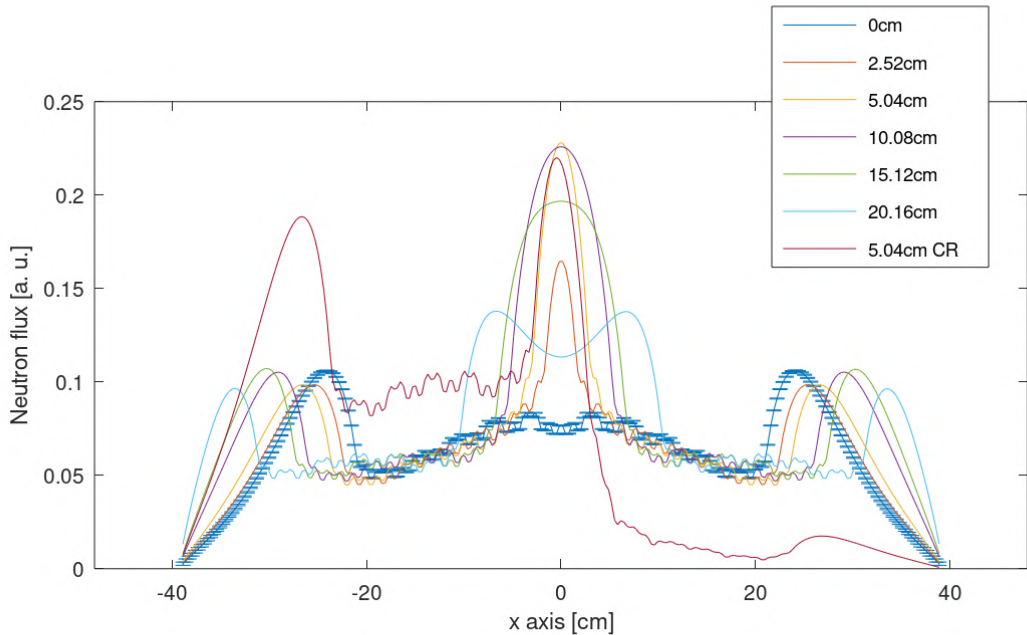


Figure 5.15: 1D thermal flux for the UOX-UOX geometry, including the case of control rod insertion (5.04cm CR), for the entire system size. Error bars are shown only for the 0 cm case, to avoid cluttering the graph. Normalized to one source neutron.

Results for boron in the moderator

The effect of boron diluted in the moderator was also studied, since this is a common way of managing reactivity both in experimental and power reactors. Based on the dependence of $\frac{k_{1,0,0}}{k_{0,0,0}}$ on the geometric buckling and the migration length of the system,

$$\frac{k_{1,0,0}}{k_{0,0,0}} = \frac{B_{0,0,0}^2 M^2 + 1}{B_{1,0,0}^2 M^2 + 1}$$

and considering the latter is given by $M^2 = D/\Sigma_a$, increasing the total absorption cross section will reduce the migration length and increase $\frac{k_{1,0,0}}{k_{0,0,0}}$. The UOX-UOX 5 cm separation case was taken and boron was gradually added in the moderator. Table 5.6 shows the results and Fig. 5.16 gives a linear fit model of the data collected, from which one can see that each ppm of Boron increases $\frac{k_{1,0,0}}{k_{0,0,0}}$ by about $5.2E - 5$. Of course, the result is relevant to this geometry, since in this case, there is a water blade between the two assemblies that operate in a soft neutron spectrum and the boron will greatly reduce the available number of thermal neutrons that go from one assembly to the other. Testing on different geometries and less thermal systems will likely produce different results, albeit the eigenvalue ratio should increase in all cases, by virtue of the increased absorption cross section.

Recalling section 3.1, it should be noted that $\frac{k_{1,0,0}}{k_{0,0,0}}$ increased with the addition of absorber at a system-wide level. However, the ratio decreased when control rods were added only on one of the two assemblies, before. The latter is a clear case of a localized absorber actually decreasing $\frac{k_{1,0,0}}{k_{0,0,0}}$, since the rodded assembly, now producing and containing a very small percentage of the total neutrons, actually becomes "irrelevant" for most of the system neutrons. The majority of neutrons do not see the right assembly and thus, for this majority, the "apparent size" of the system becomes smaller, namely consisting of the left assembly, mostly. Thus, the overall coupling increases for most neutrons, while it decreases for a few, yielding a net decrease in the eigenvalue ratio.

Boron (ppm)	$k_{0,0,0}$	$k_{1,0,0}$	$\frac{k_{1,0,0}}{k_{0,0,0}}$
0	1.23610	1.02076	0.82579
100	1.17928	0.98126	0.83208
220	1.11488	0.93368	0.83747
350	1.06856	0.90236	0.84446
500	1.01523	0.86409	0.85213

Table 5.6: $k_{0,0,0}$, $k_{1,0,0}$ and $\frac{k_{1,0,0}}{k_{0,0,0}}$ as a function of boron concentration in the moderator.

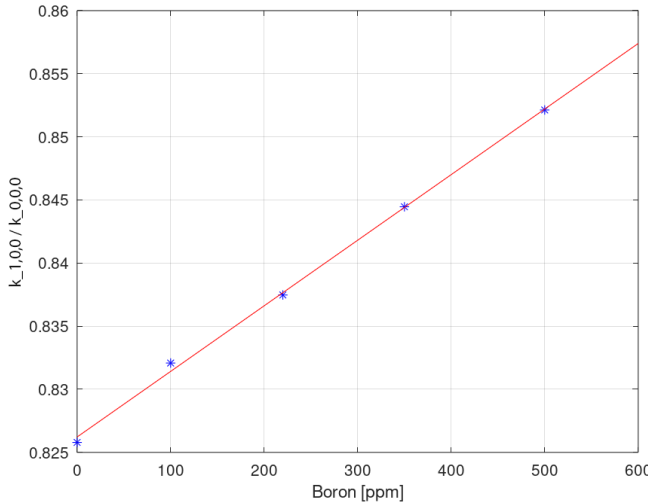


Figure 5.16: Boron dilution effect on the $\frac{k_{1,0,0}}{k_{0,0,0}}$ value. The linear fit is $\frac{k_{1,0,0}}{k_{0,0,0}} = (5.19716 \times 10^{-5})\text{ppm} + 0.82622$, with $R^2 = 0.99791$.

5.2.2 Results for the UOX-MOX case

In a similar fashion, the two assemblies were moved apart the same way. This section primarily focuses on the differences between the UOX-UOX and UOX-MOX cases, as opposed to directly explaining the observed phenomena. The MOX fuel is less reactive than the UOX one and the presence of the Pu isotopes affects both the multiplicity ν and introduces changes to the cross sections of the involved reactions (the most prominent one occurring at the 0.3 eV peak for the (n, f) reaction of ^{239}Pu which serve to harden the neutron spectrum inside and in the vicinity of the MOX assembly).

Figures 5.17, 5.18, 5.19 and 5.20 describe the coupling behavior in a similar way as for the UOX-UOX case, with notable differences when it comes to the MOX part. One interesting detail in Fig. 5.17 is that the MOX assembly seems to be affected more by the presence of high thermal flux, either incoming from the UOX assembly or moderator reflection. The ends of the MOX assembly show higher neutron propagation probability, compared to the ends of the UOX one and this behavior remains the same regardless of the separation.

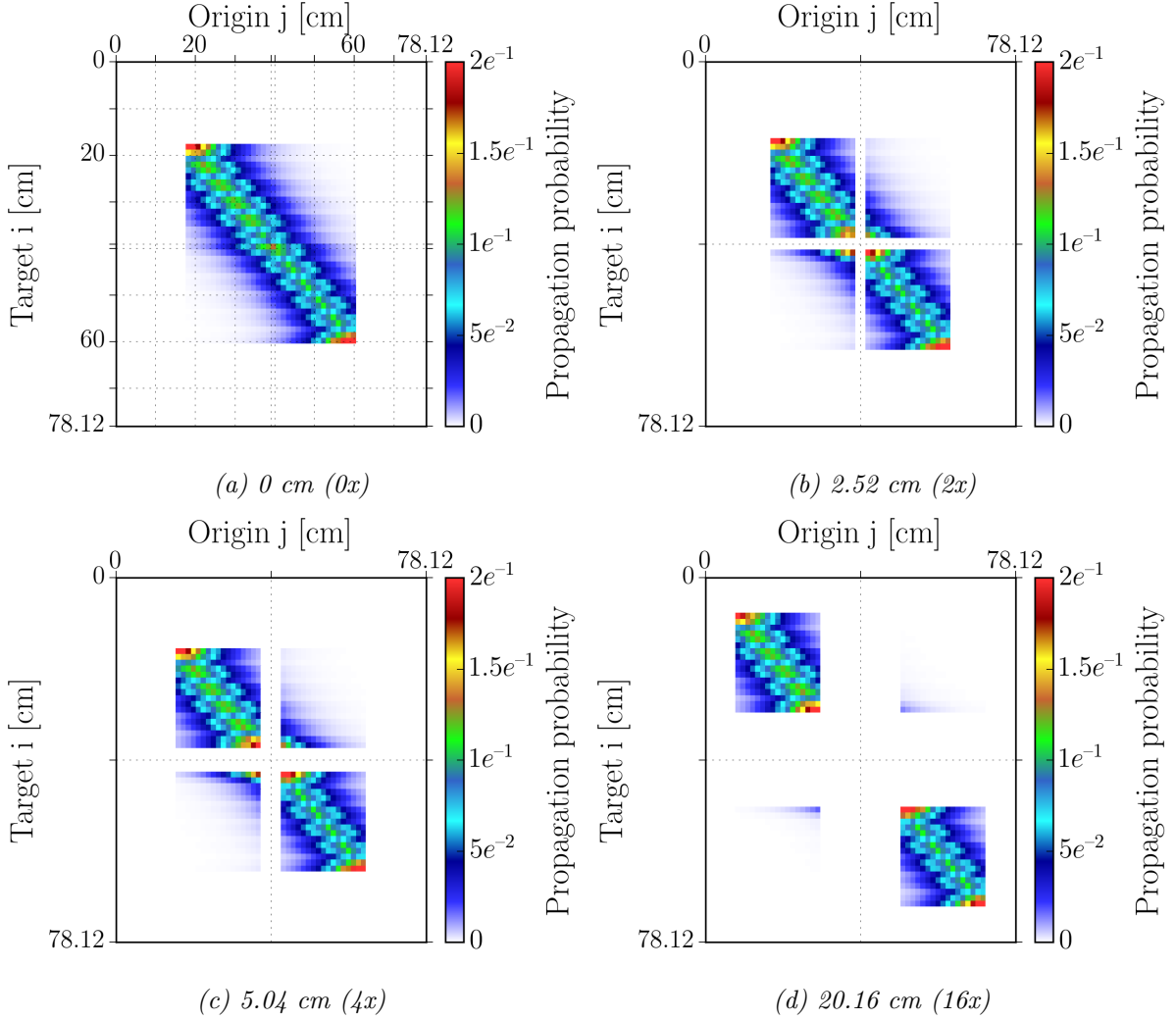


Figure 5.17: $\underline{G}_{\chi_p \nu_p}$ matrices for the UOX-MOX geometry, for different levels of assembly separation.

While the $\underline{G}_{\chi_p \nu_p}$ matrices do not differ much between the UOX-UOX and UOX-MOX cases, the $\underline{G}_{\chi_p \nu_d}$ and $\underline{G}_{\chi_d \nu_d}$ matrices display significant changes. Notably, delayed neutron production is significantly lower in the MOX part, both from neutrons coming from within the assembly itself and from contributed ones. This is expected, given the lower delayed neutron fraction present in fuels containing plutonium and the symmetrical shape of the MOX part merely shows that the delayed neutron production in the MOX fuel benefits little from the increased thermal flux available between the two assemblies.

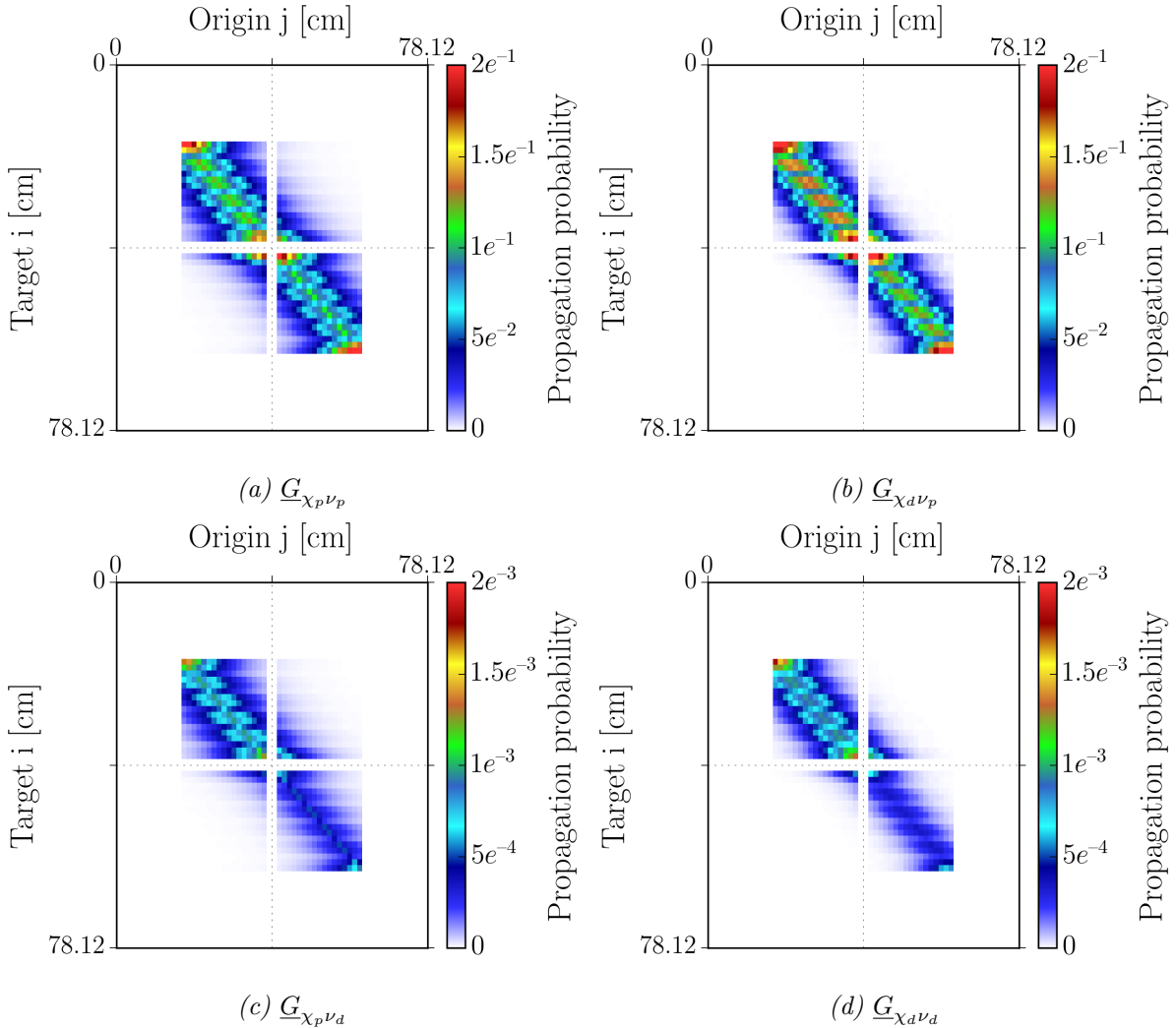


Figure 5.18: \underline{G} matrices for the UOX-MOX geometry, for a separation of 2.52 cm (2x).

Both Fig. 5.19 and Table 5.8 show significant differences in average generation time between the two assemblies. The MOX fuel is characterized by much lower generation times across the entire assembly, attributed to the harder flux spectrum (see Figures 5.22 and 5.23). The intra-assembly behavior does not change significantly with separation.

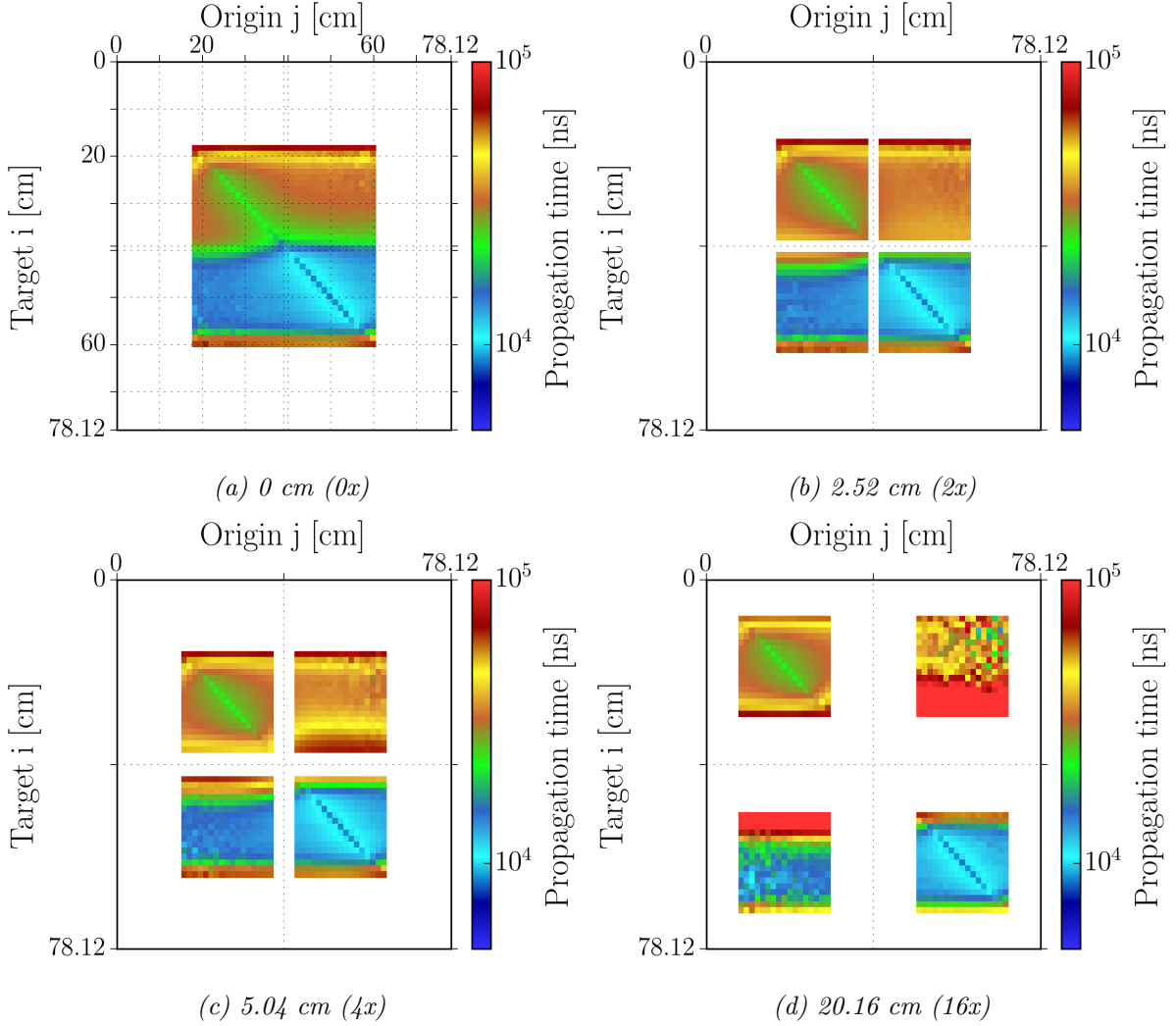


Figure 5.19: $T_{\chi_p \nu_p}$ matrices for the UOX-MOX geometry, for different levels of assembly separation.

The eigenvector in Fig. 5.20 tells an interesting story. The UOX part follows a similar evolution as in the UOX-UOX case. The MOX part, however, undergoes some very significant changes. These two findings indicate that the thermal neutron flux between the two assemblies (flux trap) is more important than any neutrons directly going from one assembly to the other without being thermalized in the flux trap. The two assemblies create a common pool of thermal neutrons. The ^{239}Pu isotope in MOX fuel has a higher (n, γ) reaction cross section than the ^{235}U in UOX, taking better advantage of the available thermal neutrons and leading to a higher importance of the first MOX fuel row, when the assemblies are close and the UOX assembly contributes a lot of thermal neutrons to the common flux trap. However, the presence of the rest of Pu and ^{238}U isotopes creates a strong shielding effect for the rest of the MOX assembly, as can be clearly seen

by the importance shape. As the assemblies move apart, the increased thermal neutron availability to the MOX assembly drops significantly and the MOX assembly by itself, massively decreases in fission rate and importance.

The shape of the eigenvector for the UOX assembly, however similar to that of Fig. 5.5, displays one significant difference, as it is much more symmetrical now, indicating that the degree of decoupling between the two assemblies is higher now, since the UOX assembly's shape appears to be almost unaffected by the MOX assembly. This is a clear indication that less reactive fuels produce a lesser degree of coupling between them and other fuels in their vicinity. On a side note, considering that the core is comprised either by the same type of fuel everywhere or has uniform different parts, the eigenvector can give a good estimate of the fission rate (see Figures E.1 and E.2).

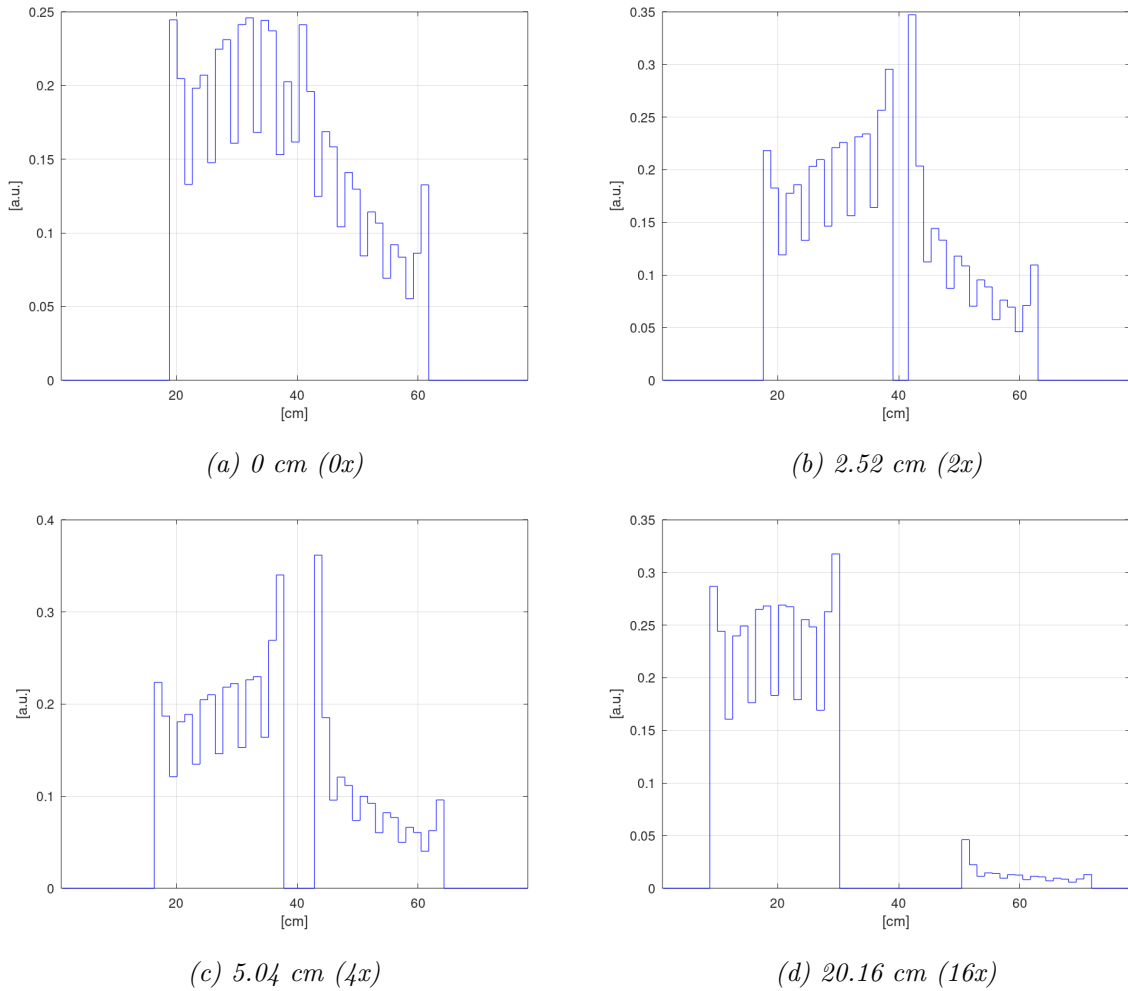


Figure 5.20: $G_{\chi_p \nu_p}$ matrix eigenvector for the UOX-MOX geometry, for different levels of assembly separation.

Lastly, k_{eff} , β_{eff} and Λ_{eff} results are also given for the UOX-MOX case, together with the values corresponding to single UOX and MOX assemblies, in Table 5.7 and 5.8. The main point to notice here is that as the decoupling increases, the more reactive UOX assembly starts dominating the system, with β_{eff} rapidly increasing past the 5.04 cm point, finally reaching a value close to that of the single UOX assembly. Still, the MOX assembly maintains some influence, with the k_{eff} dropping quite a bit at the end and β_{eff} and Λ_{eff} being lower from the UOX-UOX case. It is important to note that the reactivity increase upon assembly separation occurs here in a much more pronounced and potentially dangerous manner, in the form of a 1424 pcm (or 2.408\$) increase. This can be seen in Fig. 5.20 for the 2.52 cm case, if one compares the relative shape and bin heights of the MOX compared to the UOX one. This is again explained by the higher reaction rate of the first two rows of the MOX assembly to the increased thermal flux present in the water blade. Ultimately, the system ends up with a significantly lower $\frac{k_{1,0,0}}{k_{0,0,0}}$ value than the UOX-UOX case, because the weakly reactive MOX assembly remains coupled to the UOX one, even at the end, due to its subcriticality.

Separation (cm)	Separation (pitch)	$k_{0,0,0}$	$k_{1,0,0}$	$\frac{k_{1,0,0}}{k_{0,0,0}}$
0	0	1.18000	0.88635	0.75
2.52	2	1.19694	0.91003	0.76
5.04	4	1.17826	0.92730	0.79
10.08	8	1.12704	0.94518	0.84
15.12	12	1.10834	0.94923	0.86
20.16	16	1.10008	0.94428	0.86
Single UOX assembly	N/A	1.10688	0.59717	0.54
Single MOX assembly	N/A	0.95290	0.56422	0.59

Table 5.7: $k_{0,0,0}$, $k_{1,0,0}$ and $\frac{k_{1,0,0}}{k_{0,0,0}}$ as a function of the assembly separation for the UOX-MOX case.

Separation (cm)	Separation (pitch)	β_{eff} (pcm)	Λ_{eff} (μ s)
0	0	591	22.1
2.52	2	591	24.1
5.04	4	603	28.7
10.08	8	657	34.3
15.12	12	711	34.6
20.16	16	741	33.6
Single UOX assembly	N/A	762	34.6
Single MOX assembly	N/A	349	23.7

Table 5.8: β_{eff} and Λ_{eff} as a function of the assembly separation for the the UOX-MOX case.

Comparing the evolution of the $\frac{k_{1,0,0}}{k_{0,0,0}}$ value for the UOX-UOX and UOX-MOX cases, the latter both ends at a lower value and plateaus much sooner. This can be attributed to the lower reactivity of the MOX part, especially since a lone MOX assembly is subcritical by itself, as seen in Table 5.7. It is thus likely that the MOX part is locally very subcritical in the 15 cm and 20 cm cases and thus the eigenvalue ratio stabilizes, since the geometry is strongly dominated by the UOX assembly.

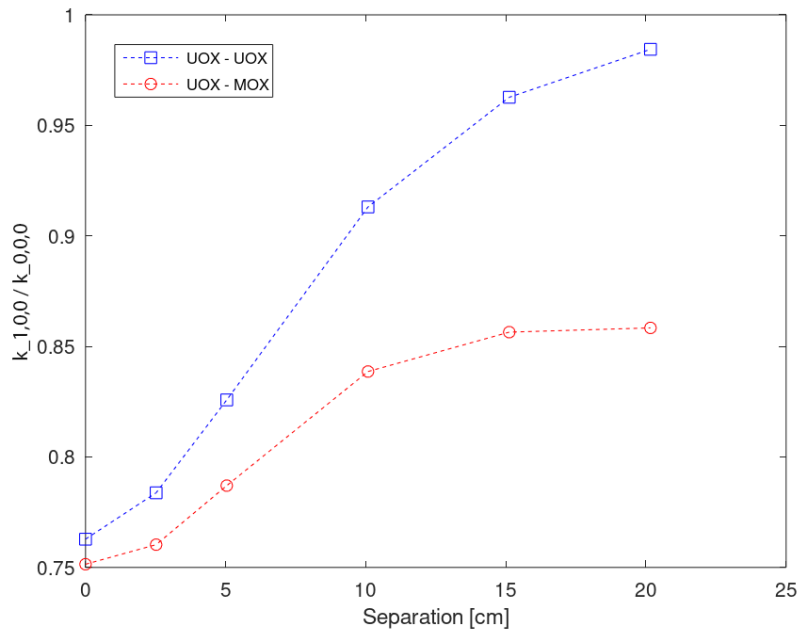


Figure 5.21: $\frac{k_{1,0,0}}{k_{0,0,0}}$ versus assembly separation, compared between the UOX-UOX and UOX-MOX cases.

Flux results for the UOX-MOX case are given in Figures 5.22 and 5.23. Similarly to the previous case of the UOX-UOX system, the thermal ($< 1 \text{ eV}$) flux shape has a close relationship with the $G_{\chi_p \nu_p}$ matrix eigenvector plots, indicating that the thermal flux behavior of the system is clearly dictated by the assembly with the higher reactivity and neutron production, as expected. It is interesting to note that the differences in flux above 1 eV are not nearly as significant between the UOX and the MOX assemblies, due to the harder flux spectrum commonly associated with MOX fuels.

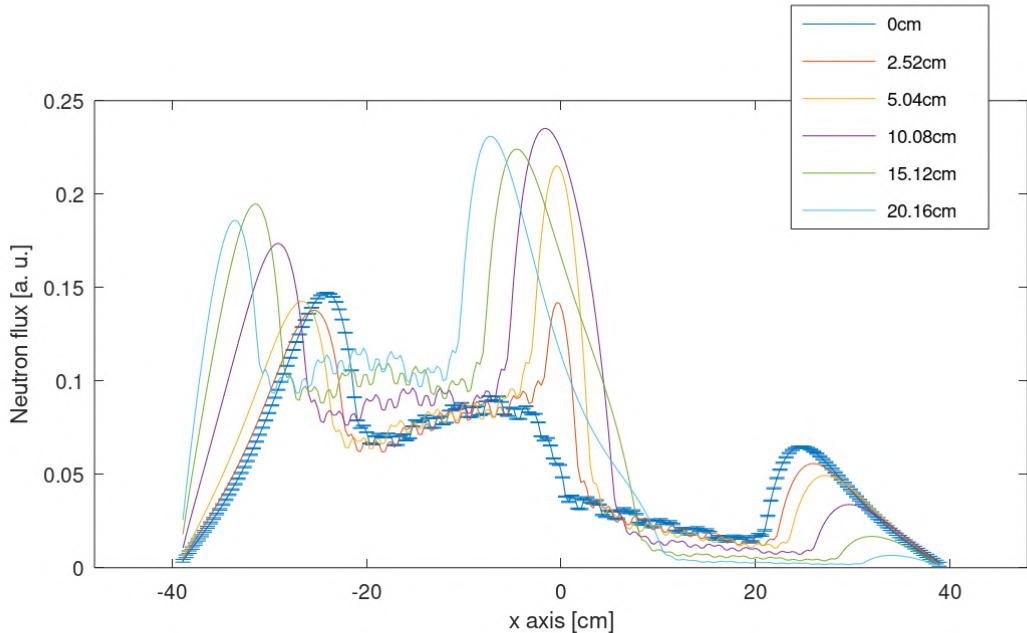


Figure 5.22: 1D flux below 1 eV for the UOX-MOX geometry, for the entire system size. Error bars are shown only for the 0 cm case, to avoid cluttering the graph. Normalized to one source neutron.

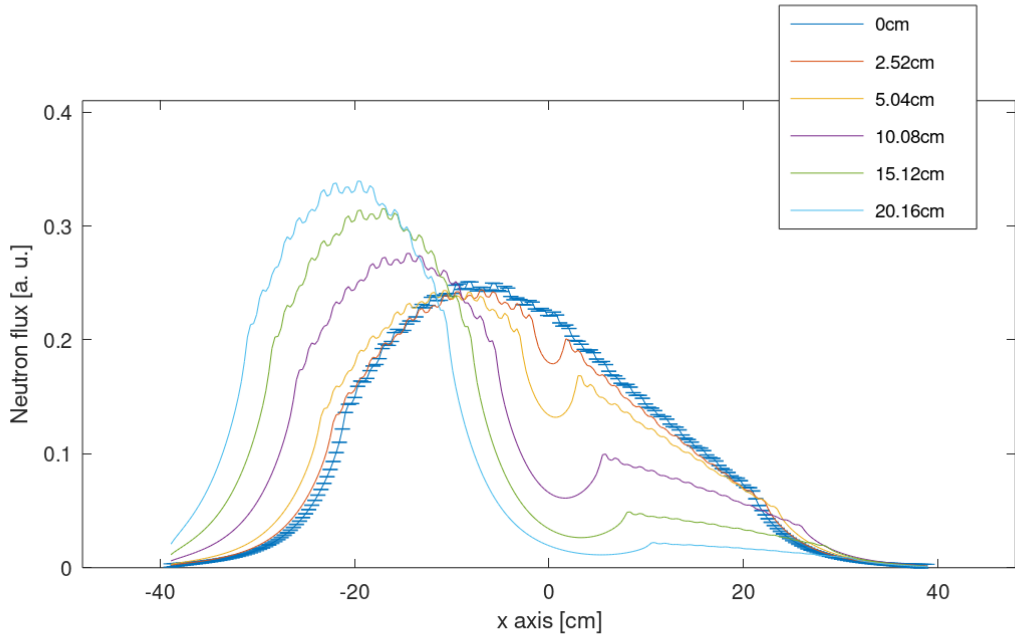


Figure 5.23: 1D flux above 1 eV for the UOX–MOX geometry, for the entire system size. Error bars are shown only for the 0 cm case, to avoid cluttering the graph. Normalized to one source neutron.

5.3 ERANOS k_{ij} calculations

The two assemblies were separated into three regions each and these six regions make up the coupled system. Indexes 1, 2, 3 refer to the left assembly and indexes 4, 5, 6, to the right. To accommodate the fact that each assembly has 17 rows of fuel, regions 1 and 6 each contain 5 rows, while 2, 3, 4, 5 each contain 6 rows. Thus, the outermost regions are smaller. It should be noted that the order of the regions in the k_{ij} matrix has no effect on the eigenvalues of the system.

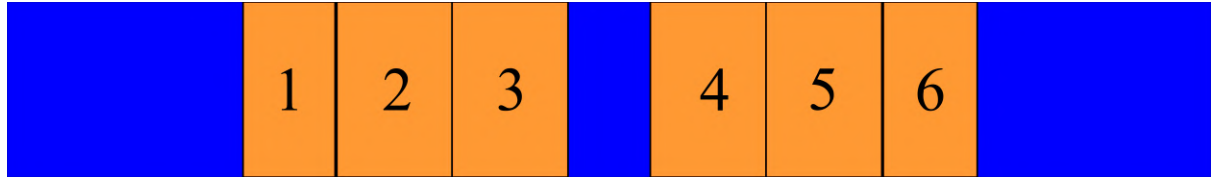


Figure 5.24: *X-Y view of the UOX-UOX geometry, with the homogenized coupling regions marked.*

5.3.1 Results for the UOX-UOX case

Table 5.9 gives the $k_{0,0,0}$ and $k_{1,0,0}$ results obtained with Kobayashi's multipoint model, implemented in the ERANOS code. The $\frac{k_{1,0,0}}{k_{0,0,0}}$ value is compared with the one computed by the TFM model in Serpent 2. The two models are in good agreement and considering that they were independently developed, this serves to validate the model and the approach presented here. Figure 5.25 shows the eigenvalue ratio versus separation, as calculated with both methods. Note that due to the differences in the calculation schemes between the two codes and the fact that ERANOS is limited to diffusion for 3D analysis, the comparison focuses only on the relation between $k_{0,0,0}$ and $k_{1,0,0}$ and does not extend to the direct comparison of the eigenvalues themselves.

Separation (cm)	(pitch)	$k_{0,0,0}$	$k_{1,0,0}$	$\frac{k_{1,0,0}}{k_{0,0,0}}$ (ERANOS)	$\frac{k_{1,0,0}}{k_{0,0,0}}$ (TFM)	% Difference
0	0	1.21874	0.91857	0.75	0.76	-1.20%
2.52	2	1.22672	0.94241	0.76	0.78	-2.02%
5.04	4	1.17771	0.96732	0.82	0.83	-0.54%
10.08	8	1.08614	0.98795	0.90	0.91	-0.38%
15.12	12	1.06265	1.01854	0.95	0.96	-0.44%
20.16	16	1.03737	1.02262	0.98	0.98	0.14%

Table 5.9: $k_{0,0,0}$, $k_{1,0,0}$ and $\frac{k_{1,0,0}}{k_{0,0,0}}$ as a function of the assembly separation for the UOX-UOX case, calculated in ERANOS.

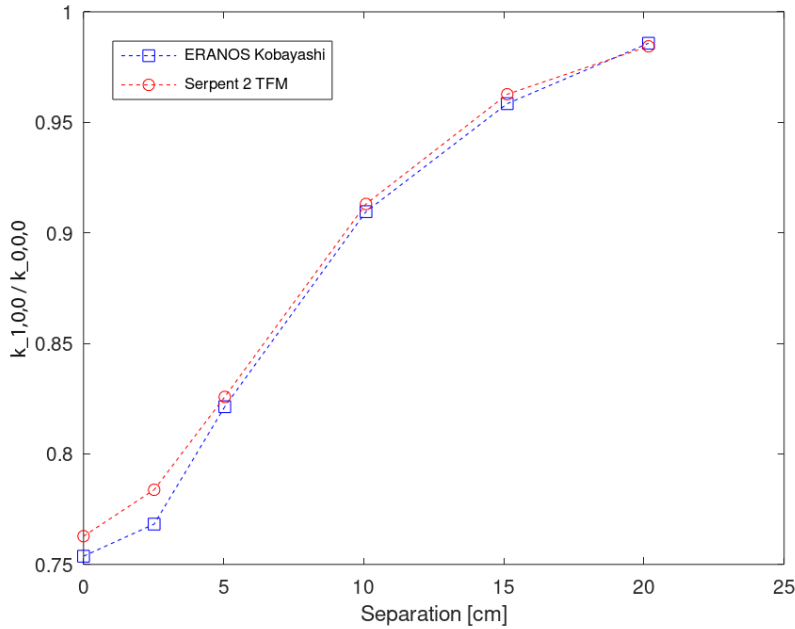


Figure 5.25: $\frac{k_{1,0,0}}{k_{0,0,0}}$ versus separation for the UOX-UOX case, as calculated with ERANOS and with the TFM model.

The full coupling coefficients matrix is given for the 20.16 cm case, in Table 5.10. The 20.16 cm was selected, to showcase effects related to decoupling, but it is compared to the 0 cm case below. The first eigenvalue of the matrix reproduces the k_{eff} calculated by ERANOS with good accuracy (the differences across all cases were on the order of a few pcm from the TFM results), serving as yet another validating point. Additionally, the diagonal elements of the matrix (k_{ii} cases) are characterized by significantly higher values, owing to the fact that a significant number of fissions are induced by neutrons originating from within the region itself. Adjacent regions are also tightly coupled, as shown by the index couples for the left assembly (k_{12}, k_{23}, k_{32} for example) and for the right assembly (k_{45}, k_{46}, k_{65} for example). Furthermore, the matrix cells corresponding to symmetric regions indeed reflect that property quite well, with the corresponding matrix elements being almost equal in most cases ($k_{13} \approx k_{64}$ and $k_{25} = k_{52}$ for example). The difference between k_{33} and k_{11} are due to the fact that region 1 has a lower volume than region 3 and the same goes for the k_{44} and k_{66} pair.

$$k_{ij}^{20.16} = \begin{pmatrix} 0.52858 & 0.31457 & 0.09334 & 0.00081 & 0.00021 & 0.00006 \\ 0.30762 & 0.49820 & 0.28649 & 0.00250 & 0.00064 & 0.00018 \\ 0.10871 & 0.34199 & 0.59325 & 0.01322 & 0.00323 & 0.00088 \\ 0.00088 & 0.00323 & 0.01322 & 0.59338 & 0.34208 & 0.10874 \\ 0.00018 & 0.00064 & 0.00250 & 0.28645 & 0.49819 & 0.30764 \\ 0.00006 & 0.00021 & 0.00081 & 0.09332 & 0.31451 & 0.52856 \end{pmatrix}$$

Table 5.10: k_{ij} coupling coefficients for the 20.16 cm UOX-UOX case.

Next, extracting the eigenvectors of the k_{ij} matrix allows to visualize the various source distribution modes. The number of accessed modes is determined by the number of discretized regions - in this case, six. They can be seen in Figures 5.26a and 5.26b. Due to the complicated shapes of higher modes, it was decided that they will only be presented for the simple geometries of this problem, to keep the graphs clear, uncluttered and easily explainable. And while the higher modes can also be accessed with the TFM model, the increased number of nodes and the inclusion of non-multiplying regions makes the graphs complicated.

The source harmonics give information on how the fission source will be redistributed in the event of a perturbation. A $\frac{k_{1,0,0}}{k_{0,0,0}}$ value close to unity means that the fundamental and first harmonic modes are going to be very close and the shape of the real source distribution (or neutron flux in the case of flux harmonics) will be greatly influenced by the behavior of its first harmonic. The maxima of the first mode give information about the regions that will affect the geometry the most, if perturbed (in this case, the middle of the two assemblies, with the inner parts coming close second) and essentially correspond to the regions with the highest importance. Figure 5.26a belongs to a system with $\frac{k_{1,0,0}}{k_{0,0,0}} = 0.98579$ (comparable to a PWR at the beginning of the irradiation cycle [40]) and the shapes of the positive parts of the fundamental and the first harmonic mode match almost perfectly.

Additionally, when the fundamental mode is compared to the one generated with the TFM model, from Fig. 5.5d, it is possible to extract similar conclusions. The combination of the cosine shape and the importance peaks of Fig. 5.5d are "bundled" together here, leading to the importance of Regions 3 and 4 being just a little bit higher than in Regions 2 and 5.

Of course, the eigenvector shapes given here are fairly basic, because of the limited number of regions. As more regions are used, the shapes will become more detailed. However,

at this point in development, the model was limited to a maximum of six regions for the coupling coefficient calculation (the multipoint model in ERANOS was first applied to the coupled assemblies case, as it was a simple system). In the 3D geometry, this allowed for reasonably good results (when compared to the TFM approach), while minimizing issues related to calculations regularly running out of memory. Also, keep in mind that all coupled regions here are taken in the assemblies themselves and not in the moderator zone in-between. Thus the source shapes given here only refer to the assembly regions, and the entire geometry is not visible.

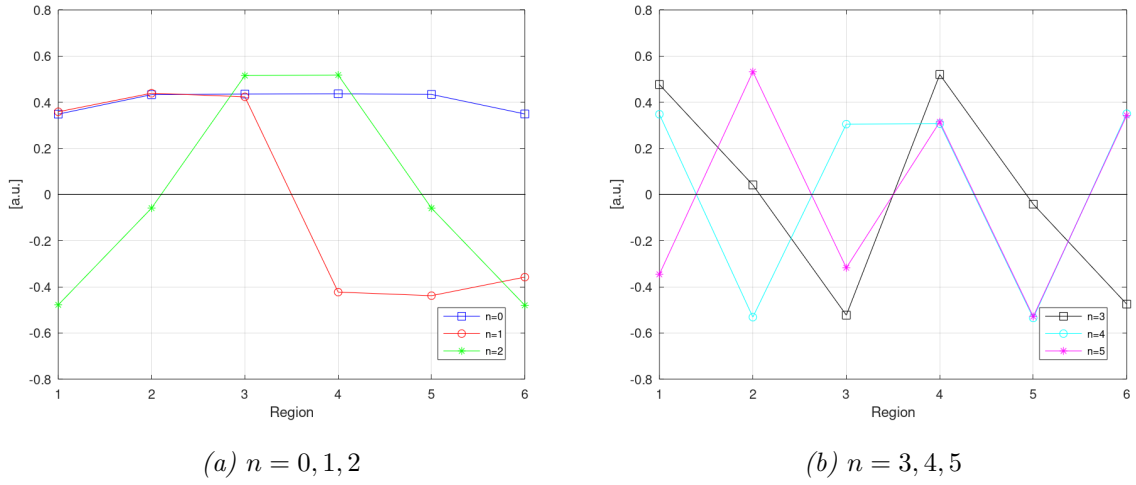


Figure 5.26: First six eigenvectors for the 20.16 cm UOX-UOX case.

Presenting the same result for the 0 cm separation case yields source modes that are easier to understand, since they better describe the entire geometry (with the exception of the left and right moderator regions), since there is no break between the coupled zones. The first mode is noticeably smoother, since there is no gap through a non-multiplying medium, leading to the abrupt step observed in Fig. 5.26b for the 20.16 cm case. The 0 cm case also presents a better opportunity to see how the higher modes are related to the fundamental one. As the first ($n = 1$) mode decreases, the fundamental ($n = 0$) one stops increasing, becoming flatter. When it becomes negative, the fundamental starts dropping. The second ($n = 2$) mode is also related to the fundamental ($n = 0$) one; it decreases as the latter increases, remains unchanged when the fundamental mode does the same and goes up, when the the fundamental decreases. This inverse relationship is the opposite of what is observed for the 20.16 cm case, in Fig. 5.26a, but one simply needs to remember that only one eigenvector for each mode is plotted. Higher modes have higher multiplicities and can manifest in any of them during an experiment.

Looking at Fig. 5.27b, one will notice that the line connecting regions 3 and 4 for $n = 4$

is not straight. However, this being a symmetrical geometry, the values corresponding to these regions should be the same. The difference is due to a slightly asymmetric k_{ij} matrix, likely the result of the calculation convergence process. Such asymmetries can be seen more clearly in certain $2n$, $n = 1, 2, 3 \dots$ higher modes. Additionally, for a symmetrical system with respect to the coupling axis, $2n + 1$, $n = 1, 2, 3 \dots$ eigenvectors are normally always zero in the middle of the geometry, which indicates the center of importance, as discussed before. This behavior was verified by testing on all the geometries investigated during this PhD. Such an analysis can be used to detect slight source asymmetries that might otherwise be hard to spot or detect. Of course, these observations are specific to the case analyzed here, but similar results can be obtained for any configuration, assuming a correct coupling region discretization is used. Taking the same system, but this time with a forced perfectly symmetric k_{ij} matrix, all even eigenvectors, given in Fig. 5.28 are completely flat between regions 3 and 4.

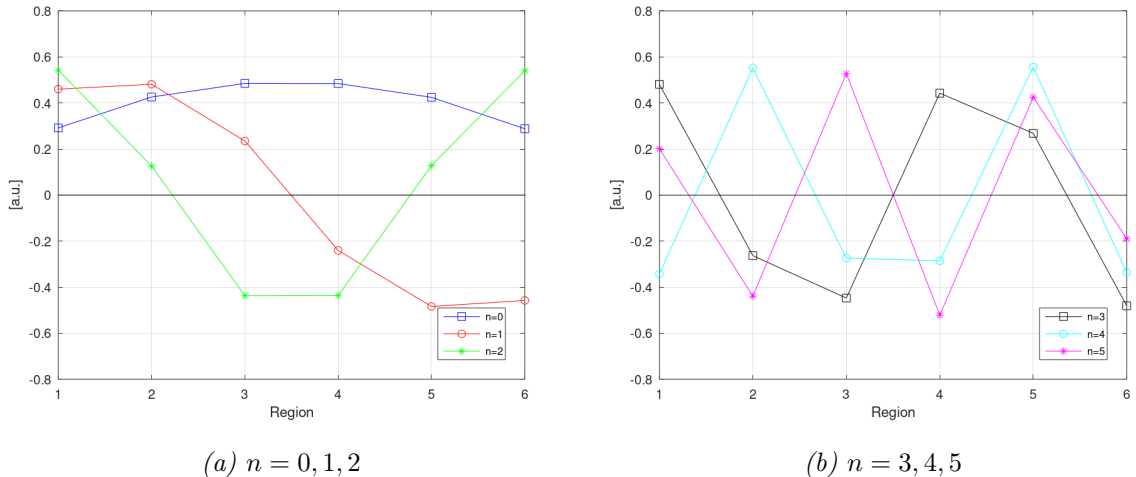


Figure 5.27: First six eigenvectors for the 0 cm UOX-UOX case.

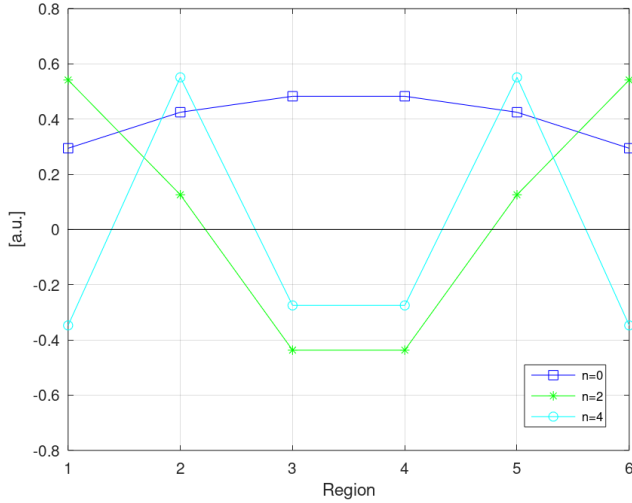


Figure 5.28: Even modes ($n = 0, 2, 4$) for a perfectly symmetric k_{ij} matrix. Observe that the second ($n = 2$) and fourth ($n = 4$) modes are completely flat between regions 3 and 4, indicating a perfectly even source distribution.

Table 5.11 gives the β_{ij} matrix for the 20.16 cm case, while Tables 5.12 and 5.13 give the partial delayed neutron fraction and region-wise neutron lifetime ℓ_i respectively, for all separation levels. Looking at the behavior of the β_{ij} matrix given in Table 5.11, the previous symmetry statement regarding mirroring indexes is also true here. Furthermore, the high variation per index pair suggests that the delayed neutron fraction associated with neutrons incoming from other nodes, depends on the origin node (remember that k_{ij} and β_{ij} matrix columns represent each region's reaction to neutrons incoming from other nodes). The β_i table indicates that zones with better moderation enjoy a higher delayed neutron fraction and generally, the overall delayed neutron fraction increases with separation and additional moderation.

$$\beta_{ij}^{20.16}(\text{pcm}) = \begin{pmatrix} 900 & 740 & 417 & 11 & 6 & 2 \\ 760 & 903 & 743 & 19 & 11 & 5 \\ 417 & 725 & 887 & 59 & 29 & 15 \\ 15 & 29 & 59 & 887 & 725 & 417 \\ 5 & 11 & 19 & 743 & 903 & 760 \\ 2 & 6 & 11 & 417 & 740 & 900 \end{pmatrix}$$

Table 5.11: β_{ij} for the 20.16 cm UOX-UOX case.

Separation (cm)	Region 1	Region 2	Region 3	Region 4	Region 5	Region 6
0	729	761	760	760	761	729
2.52	726	758	748	748	758	727
5.04	740	772	735	735	772	740
10.08	767	803	745	745	803	767
15.12	777	813	762	766	810	777
20.16	784	820	781	781	820	784

Table 5.12: β_i for different levels of assembly separation for the UOX-UOX case. Results are given in pcm.

Looking at ℓ_i , and considering that it is a kinetic parameter that is influenced by the local neutron spectrum, it is possible to extract information about said neutron spectrum across the geometry. Take the example of 0 cm, where the outer regions (1, 6) exhibit an ℓ of $\sim 30.4 \mu s$, while the mid-assembly regions (2, 5) have $\sim 18.3 \mu s$ and the inner regions (3, 4) have an even smaller value of $\sim 18.2 \mu s$, indicating that the spectrum gets harder in the middle of the geometry, since there is no water gap between the two assemblies now. On the other hand, in the case of 20.16 cm separation, the outer regions (1, 6) have a slightly lower ℓ than before, since they moved closer to the vacuum boundary of the geometry, while the inner regions (2,5) now exhibit a much higher ℓ than before, because of the increased thermalization that takes place in the large water gap between the assemblies. In fact, at that level of separation, the inner and outer assembly regions have very similar ℓ values, indicating that they are characterized by the same average neutron energy.

Separation (cm)	Region 1	Region 2	Region 3	Region 4	Region 5	Region 6
0	30.3	18.3	18.2	18.2	18.3	30.4
2.52	30.5	18.4	24.5	24.5	18.7	30.8
5.04	30.6	18.4	31.3	31.3	18.4	30.6
10.08	30.7	18.2	33.1	33.1	18.2	30.7
15.12	30.6	18.2	31.3	29.9	18.1	28.8
20.16	29.4	18.1	29.6	29.6	18.1	29.4

Table 5.13: ℓ_i for different levels of assembly separation for the UOX-UOX case. Results are given in μs .

Finally, applying the zero flux condition on the symmetry boundary of the system ($x = 0$) and running in diffusion, the actual first mode harmonic flux was calculated for some cases and is shown in Fig. 5.29. This gives a much more detailed picture of the first mode behavior, including the behavior in non-multiplying regions. There are distinct points that the first harmonic's tangent changes, that correspond to the assembly boundaries (an assembly has a total length of 21.42 cm). The same conclusions can be extracted as with the TFM in Serpent 2 or Kobayashi's model in ERANOS, with respect to the system's stability. The calculated first mode eigenvalues are given in Table 5.14 and they are within 0.02% from the values calculated with the k_{ij} matrix. This agreement represents a tenfold improvement over the more complicated ZEPHYR geometry. A case can therefore be made that for symmetrical, simple geometries and material compositions, this is a viable way to accurately access higher harmonic modes without the need to calculate the coupling coefficients. However, care must be taken to avoid using this method inappropriately and so a more extended study, aimed at finding its limits, is a good idea.

Separation (cm)	$k_{1,0,0}$ (harmonic)	$k_{1,0,0}$ (k_{ij})	% Difference
0	0.91835	0.91857	-0.024
2.52	0.94222	0.94241	-0.020
20.16	1.02239	1.02262	-0.022

Table 5.14: $k_{1,0,0}$ eigenvalues calculated via a harmonic flux calculation on one half of the symmetric geometry.

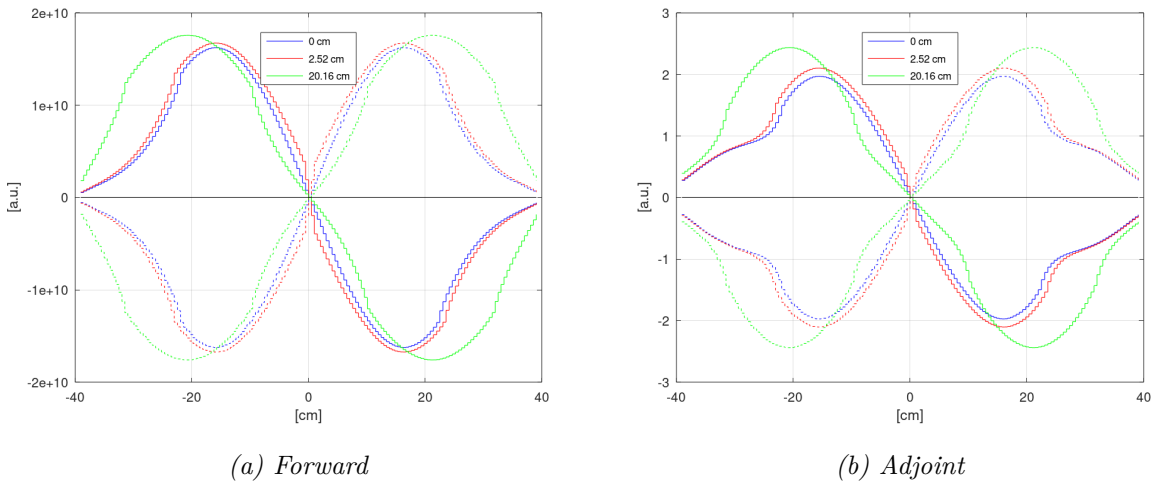


Figure 5.29: First mode azimuthal flux harmonics for the 0 cm, 2.52 cm and 20.16 cm cases.

Results of control rod insertion

In a similar fashion to the control rod insertion scenario that was explored with TFM, rods were inserted in one part of the left assembly. The number of regions was increased to twelve (this calculation was performed later during the thesis) and one of the twelve segments, the third from the left (3/12), was changed to a medium corresponding to a rodded assembly. The 0 cm separation case was used, since the eigenvector shape is more intuitively understood there. The fundamental and first mode eigenvectors are presented in Fig. 5.30. Contrary to the TFM case, where rods were inserted in an entire assembly, leading to a severe deformation of the eigenvector shape, the present change, represented in just 1/6th of one assembly, is producing a smaller, but still noticeable effect.

The first mode eigenvector also indicates that due to the reduced neutron production, this node is less able to affect the system behavior. Also, similarly to the TFM case, the system's center of importance has shifted to the right - towards the un-rodded assembly and the eigenvector displays that, by virtue of the displaced axis intersection point ($y = 0$ for $x \approx 6.9$, instead of $x = 6.5$).

Furthermore, looking at the comparisons, the fundamental eigenvector is perturbed more than the first mode one. This is an interesting behavior, that can be utilized in high dominance ratio configurations, where the neutron flux is largely controlled by the first harmonic. Depending on the method of perturbation, this could leave the flux only mildly disturbed, while perturbing the fundamental mode, for example.

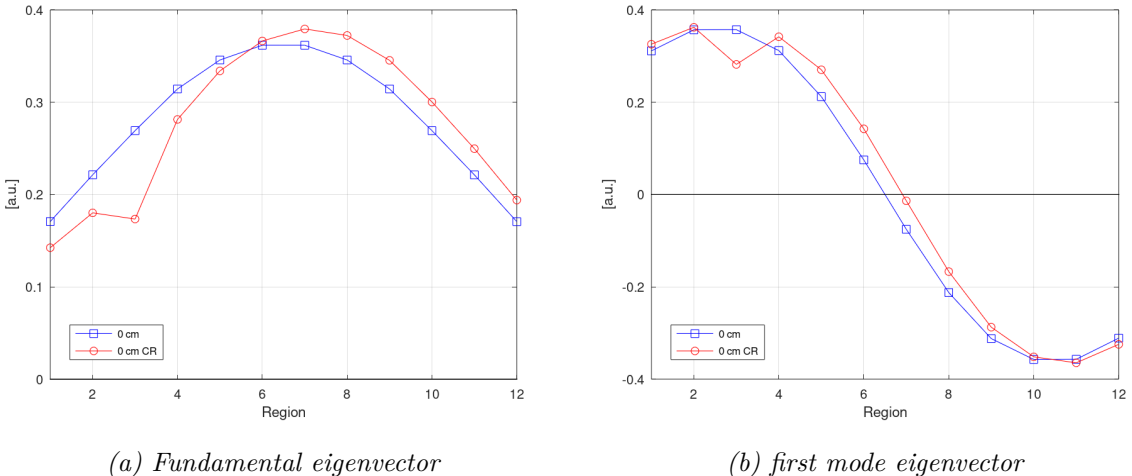


Figure 5.30: Fundamental and first mode eigenvectors of the 12 region, 0 cm separation case, before and after control rods were inserted in the (3/12) region.

5.3.2 Results for the UOX-MOX case

The process was repeated for the UOX-MOX geometry, shown in Fig. 5.3. The same results as above are given in Tables 5.15, 5.16, 5.17, 5.18 and 5.19. The homogenization and region discretization remains the same as before, with the MOX assembly regions on the left side, as shown in Fig. 5.31. The calculated $\frac{k_{1,0,0}}{k_{0,0,0}}$ values are again compared between ERANOS and TFM and the percent differences, while marginally larger than in the UOX-UOX case, are still pretty low and below 3%. Since this calculation involves a higher number of fissile and fertile isotopes because of the MOX fuel, the slight increase in discrepancy between ERANOS and TFM is not unreasonable.

There is one additional point that was investigated here though and it involves the fact that, for the 20.16 cm UOX-UOX case, the dominance ratio calculated with ERANOS exceeds the TFM one. It was investigated whether the same would happen with the UOX-MOX case or not. For the latter, the last TFM value was treated as a local plateau, at a value of 0.85837. Two additional UOX-MOX cases were run in ERANOS, for separations of 25.20 cm and 30.24 cm, and it was determined that a local plateau does indeed exist here, but both resulting values remain below the assumed TFM plateau. It is also notable that for the new separation values, the dominance ratio kept increasing, albeit very slowly, indicating that the plateau assumption is correct for the geometry at hand. As separation increases beyond a certain point, the dominance ratio value will surely asymptotically reach unity, but the plateau assumption is correct for the scale of the current problem.

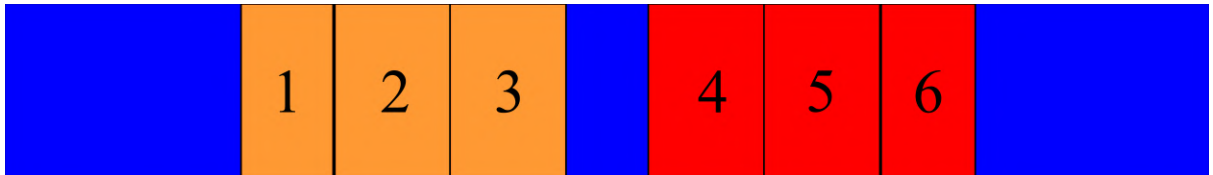


Figure 5.31: *X-Y view of the UOX-MOX geometry, with the homogenized coupling regions marked.*

Separation (cm)	(pitch)	$k_{1,0,0}$	$k_{1,0,0}$	$\frac{k_{1,0,0}}{k_{0,0,0}}$ (ERANOS)	$\frac{k_{1,0,0}}{k_{0,0,0}}$ (TFM)	% Difference
0	0	1.05673	0.77815	0.73	0.75	-2.05%
2.52	2	1.07629	0.79741	0.74	0.76	-2.62%
5.04	4	1.04803	0.81366	0.77	0.78	-1.37%
10.08	8	1.03296	0.85673	0.83	0.83	-1.11%
15.12	12	1.01940	0.86616	0.84	0.85	-0.80%
20.16	16	1.01721	0.86726	0.85	0.86	-0.68%
25.20	20	1.01133	0.86232	0.85	0.86*	-0.67%
30.24	24	0.98854	0.84401	0.85	0.86*	-0.54%

Table 5.15: $k_{0,0,0}$, $k_{1,0,0}$ and $\frac{k_{1,0,0}}{k_{0,0,0}}$ as a function of the assembly separation for the UOX-MOX case. *: assumed

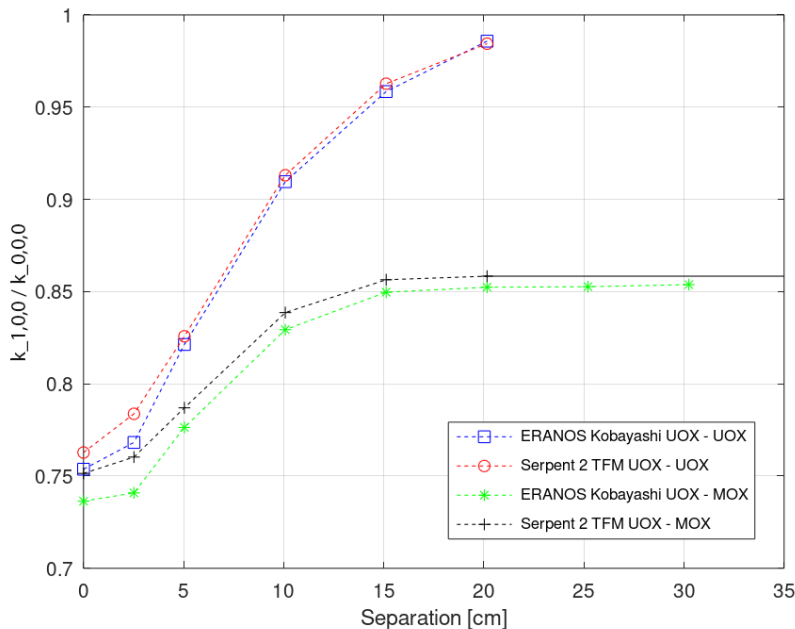


Figure 5.32: $\frac{k_{1,0,0}}{k_{0,0,0}}$ value versus separation for both the UOX-UOX and UOX-MOX cases, as calculated with ERANOS and with the TFM model. A TFM plateau is assumed for UOX-MOX at 0.85837.

The agreement between the two codes also improves with separation, for both the UOX-UOX and UOX-MOX cases. It is possible that as decoupling increases, the smaller contributions from one assembly to the other lead to more accurate k_{ij} coefficients or

that the additional moderator reflection has a similar effect. This is shown in Fig. 5.33. The TFM method was used as reference since it can potentially yield results that describe the system flux more accurately, due to the increased number of coupling regions available [42]. For the particular geometry, the TFM discretization was 62 regions, including non-multiplying media zones.

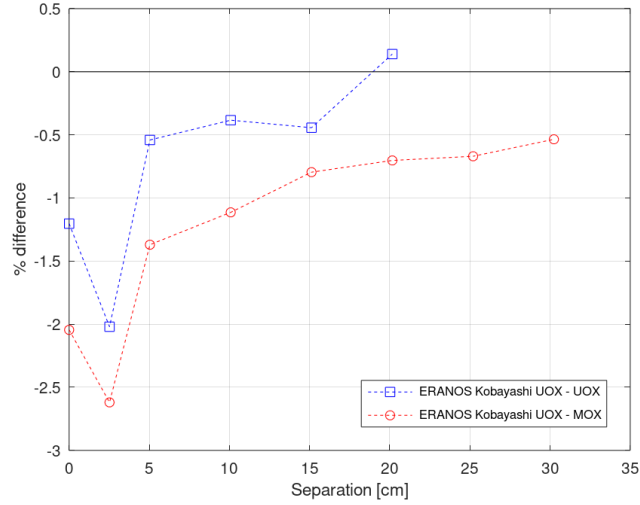


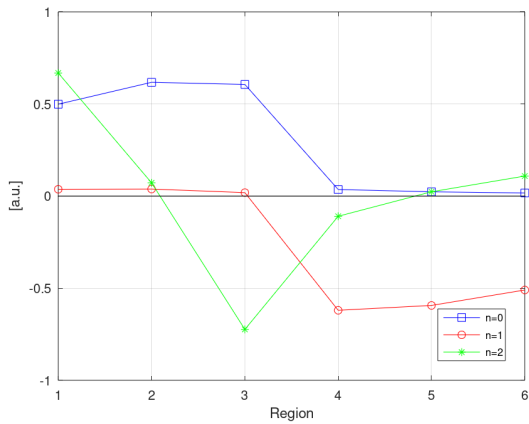
Figure 5.33: $\frac{k_{1,0,0}}{k_{0,0,0}}$ value % difference versus separation for both the UOX-UOX and UOX-MOX cases, of the k_{ij} method in ERANOS, using the TFM method in Serpent 2 as reference. A TFM plateau is assumed for UOX-MOX at 0.85837.

Looking at the k_{ij} matrix in Table 5.16 and comparing it with the one in Table 5.10, it is evident that for the UOX-MOX case, neutrons generated in the UOX assembly produce more neutrons in the MOX assembly than the other way around. The MOX part itself also has lower internal coupling coefficients, indicating that it uses a larger proportion of externally incoming neutrons, to generate fission events. Based on that, one can say that the MOX part is more tightly coupled to the UOX part than the other way around, which is logical, considering the UOX part's higher reactivity, leading to an increased number of fission events and thus fission neutrons. It should be said again that rows correspond to the same origin, while columns correspond to the same target.

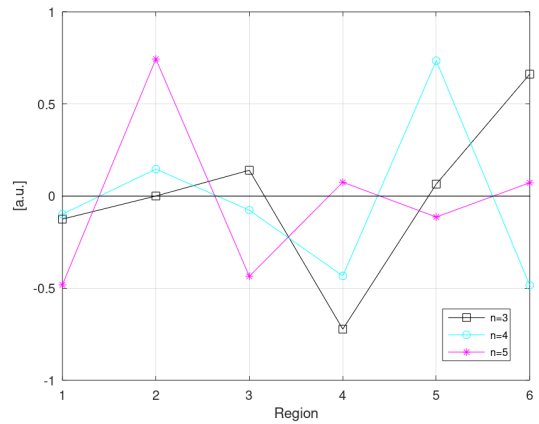
$$k_{ij}^{20.16} = \begin{pmatrix} 0.52020 & 0.30984 & 0.09323 & 0.00092 & 0.00024 & 0.00007 \\ 0.30528 & 0.49062 & 0.28521 & 0.00282 & 0.00071 & 0.00020 \\ 0.10820 & 0.33681 & 0.58389 & 0.01455 & 0.00347 & 0.00093 \\ 0.00082 & 0.00300 & 0.01207 & 0.52416 & 0.28707 & 0.08374 \\ 0.00015 & 0.00052 & 0.00199 & 0.22382 & 0.42456 & 0.24336 \\ 0.00005 & 0.00018 & 0.00066 & 0.07147 & 0.26548 & 0.47129 \end{pmatrix}$$

Table 5.16: k_{ij} coupling coefficients for the 20.16 cm UOX-MOX case.

The eigenvectors were again plotted and show the fundamental and higher mode behavior of the system, for the 20.16 cm and 0 cm cases, respectively. Unlike the UOX-UOX system, this one is not symmetrical and the behavior of all flux modes shows that. The $2n + 1$, $n = 1, 2, 3, \dots$ modes are no longer zero in the middle of the geometry and are obviously not symmetric to the y axis.



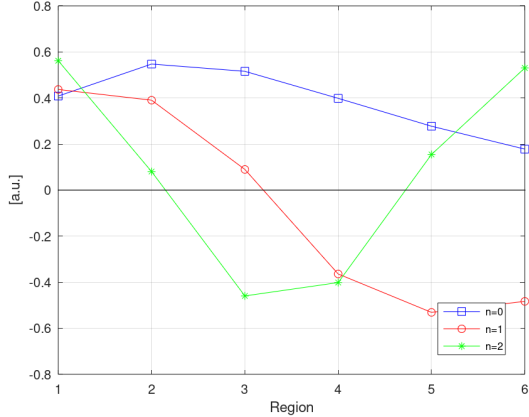
(a) $n = 0, 1, 2$



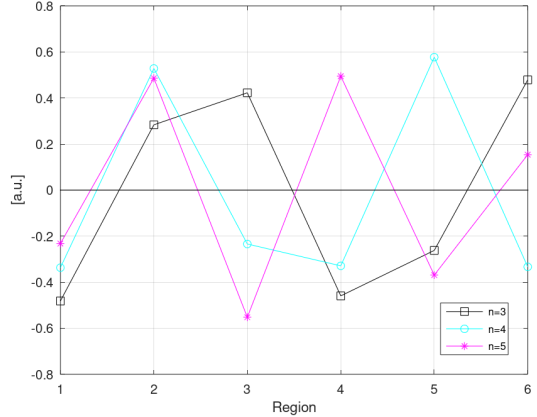
(b) $n = 3, 4, 5$

Figure 5.34: First six modes for the 20.16 cm UOX-MOX case.

The 0 cm UOX-MOX case, with a $\frac{k_{1,0,0}}{k_{0,0,0}}$ value of 0.73638, is again well suited to show how the fundamental mode is related to the higher ones, if one looks at Fig. 5.35a. The fundamental mode starts to decrease at region 3, again when the first mode becomes negative. The second ($n = 2$) mode behavior on the other hand, is again opposite to the fundamental one. Also, the fourth ($n = 4$) mode clearly indicates the asymmetry present in the system, as discussed before.



(a) $n = 0, 1, 2$



(b) $n = 3, 4, 5$

Figure 5.35: First six modes for the 0 cm UOX-MOX case.

Looking at the β_{ij} matrix in Table 5.17, the previous observation that the delayed region-wise neutron fraction depends on the node of origin still stands correct. A notable change compared to the UOX-UOX case is the fact that all values associated with MOX origin nodes have low values (expected), while all values associated with UOX origin nodes remain relatively unchanged. This leads to the conclusion that the UOX part is controlling the β_{eff} of the entire system, as expected, since delayed neutron production is typically higher in UOX fuel than it is in MOX.

$$\beta_{ij}^{20.16}(\text{pcm}) = \begin{pmatrix} 903 & 742 & 421 & 4 & 2 & 1 \\ 766 & 906 & 749 & 8 & 4 & 2 \\ 421 & 727 & 890 & 27 & 13 & 6 \\ 17 & 30 & 61 & 408 & 340 & 176 \\ 6 & 11 & 17 & 337 & 435 & 343 \\ 4 & 7 & 10 & 177 & 347 & 413 \end{pmatrix}$$

Table 5.17: β_{ij} for the 20.16 cm UOX-MOX case.

The ℓ_i matrix below displays significantly shorter values for the MOX parts, attributed to the plutonium isotopes and the resulting harder neutron spectrum. Of interest is the difference in region 4, corresponding to the MOX part's left-most zone, between the 0 cm and all other cases, due to the harder spectrum and initial lower moderation in that part. Upon separation, ℓ_2 increases at a rapid pace, almost reaching values consistent with the UOX assembly, presumably influenced by it. After a point, the amount of moderator

between the two assemblies and the reflection it causes makes region 4 to behave similarly to region 6, since they are now both boundary regions of the MOX assembly, both highly moderated. Region 5, in the middle of the MOX assembly, consistently displays the lowest lifetime, indicating that the spectrum is the hardest there.

Separation (cm)	Region 1	Region 2	Region 3	Region 4	Region 5	Region 6
0	29.8	18.1	17.0	9.6	8.4	21.9
2.52	29.8	18.2	22.8	15.8	8.9	22.6
5.04	29.8	18.2	29.4	24.0	8.5	22.9
10.08	29.4	18.0	30.9	28.2	8.6	24.4
15.12	29.0	18.0	29.3	24.0	8.5	22.1
20.16	28.1	17.9	28.0	23.9	8.6	23.0

Table 5.18: ℓ_i for different levels of assembly separation for the UOX-MOX case. Results are given in μs .

Finally, the β_i matrix in Table 5.19 shows that, as expected, the MOX assembly is characterized by much lower delayed neutron fractions. At low levels of separation, the MOX region closest to UOX (region 4) exhibits a much higher β_i value than the rest of the MOX assembly, because of the softer flux profile in proximity to UOX fuel. As separation increases, like before, region 4 starts to be affected less and less by the UOX part, approaching the values of region 6.

Separation (cm)	Region 1	Region 2	Region 3	Region 4	Region 5	Region 6
0	744	763	679	490	375	336
2.52	740	767	683	464	359	332
5.04	752	785	704	420	357	337
10.08	774	815	758	356	369	352
15.12	781	823	778	352	377	361
20.16	787	828	789	358	381	364

Table 5.19: β_i for different levels of assembly separation for the UOX-MOX case. Results are given in pcm.

5.4 Remarks

This chapter presents a detailed numerical benchmark, aimed at providing a common ground for the testing, comparison and verification of calculation schemes related to space-time kinetics. Assembly separation directly translates to different degrees of azimuthal coupling and subsequent change of the system $\frac{k_{1,0,0}}{k_{0,0,0}}$ value. The two assemblies initially function as a single core and as separation begins and continues, the coupling between them decreases steadily. In the case of both UOX-UOX and UOX-MOX, the difference in reactivity around the 2.52 cm point served to show that for thermal lattices, the flux trapped between assemblies is more important than direct neutron contributions. It would be interesting to investigate the same scenario in the context of a fast neutron lattice.

Chapter 6

High dominance ratio configurations in the VENUS-F zero power reactor

The methodology developed in this work was used in the context of a potential collaboration with SCK CEN, in order to contribute to experimental designs in the VENUS-F reactor [27, 28]. The program will aim at coming up with configurations and relevant experiments that would deal with the following topics:

- Improvement of the nuclear data associated with fuel behavior and effects in fast and epithermal spectra.
- Validation of thermalization laws and scattering cross sections.
- Investigation of temperature effects to the material balance and stability, as a core approaches end of life.
- Accurate generation of delayed neutron parameters for safety during operation and transport.
- Management of subcritical reactivity levels and space-time kinetics effects, including coupling/decoupling effects through high dominant ratio configurations.

The focus of the last year of the thesis concentrated on the latter point, within the context of fast/epithermal configurations. The objective was to support the experimental campaign by designing high dominance ratio configurations. The approach consisted of generating and analyzing fast-epithermal configurations, starting from a reference VENUS-F configuration and studying the effect that moderating the entirety or part of the core will have. There are several options in terms of which materials can be used, from the inventories of both CEA and SCK. Once the candidate materials are selected, the core can

be redesigned and analyzed by both Monte Carlo and deterministic calculations. This work, building on the experience gained during the first two years of the thesis, served as a proof of concept for the developed methodologies.

6.1 Characteristics of the VENUS-F core

For the results to be usable, the first part of this project demanded a detailed modeling of the VENUS-F core. Details were obtained from SCK CEN. VENUS-F is a zero power reactor, featuring a 12×12 lattice and a radial reflector. The geometry used for this work is based on the CR0 critical configuration [27] minus one fuel assembly. The new core, named CR0*, contains 96 fuel assemblies, each with 25 positions (5x5), alongside a number of reflector assemblies, irradiation/instrumentation positions and two pilot rod positions. The assemblies themselves contain nine fuel positions, each of them containing two ~ 30 cm long rodlets of 30.2% enriched metallic uranium from the MASURCA reactor stockpile, same as the ones used in the ZEPHYR concept. The rest of the positions contain square lead blocks. The main reflector material in the core is lead and it is used both in the lattice reflector assemblies and the radial reflector around the core. The reflector assemblies have a lead grid structure. Stainless steel blocks are used for axial reflection, bordering the active core. Six of the core assemblies are equipped with safety rod followers on top. Both the safety and pilot assemblies use B_4C . Also, the flux spectrum of the core in Fig. 6.3 shows that this is a decidedly fast core. Figure 6.1 shows the top down view of the geometry. The core was designed in full, with an active core height of 60.96 cm and all safety and pilot rod positions modeled. The side-view is presented in Fig. 6.2. Out of several possible initial critical configurations, CR0* was chosen, since the high number of assemblies in the core allows for more extensive modification and at the same time, increases the size of the core, which helps in achieving a high dominance ratio.

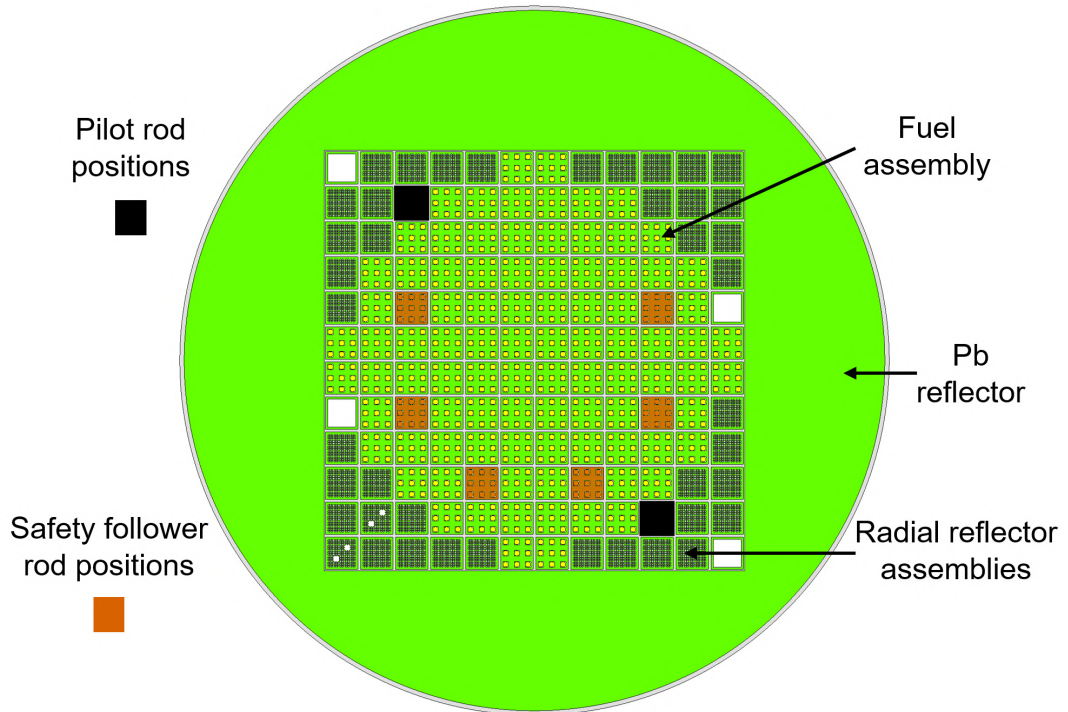


Figure 6.1: Top-down view of the Serpent 2 model of the VENUS-F core. Yellow: metallic U 30.2% enrichment, Orange: B₄C safety rod position, Black: void (B₄C pilot rod position), White: air.

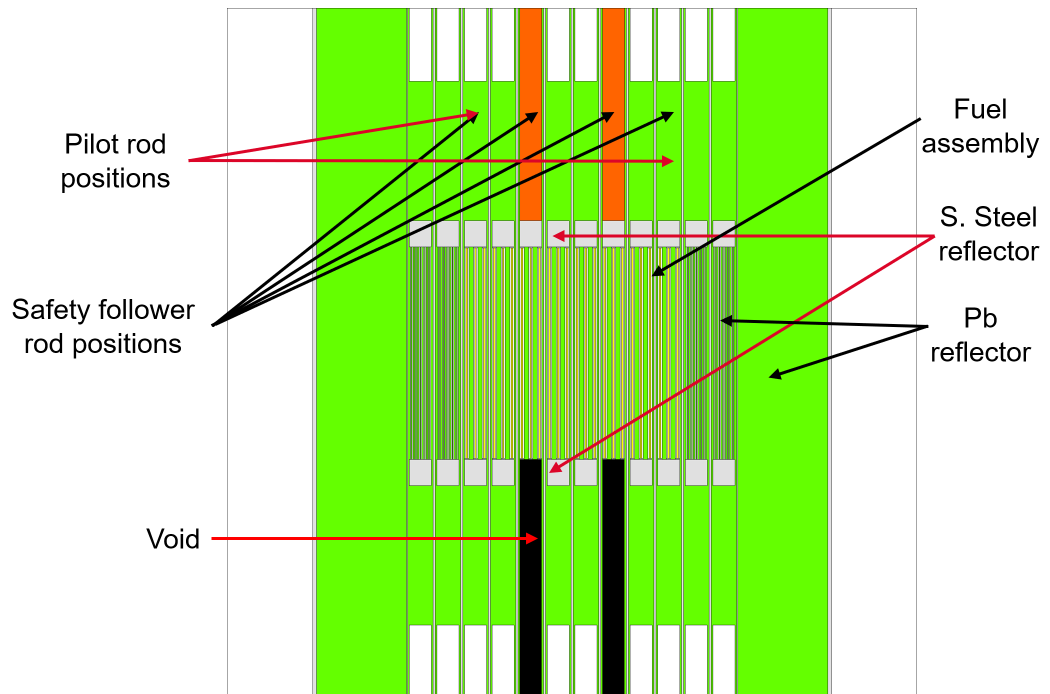


Figure 6.2: Side view of the Serpent 2 model of the VENUS-F core.

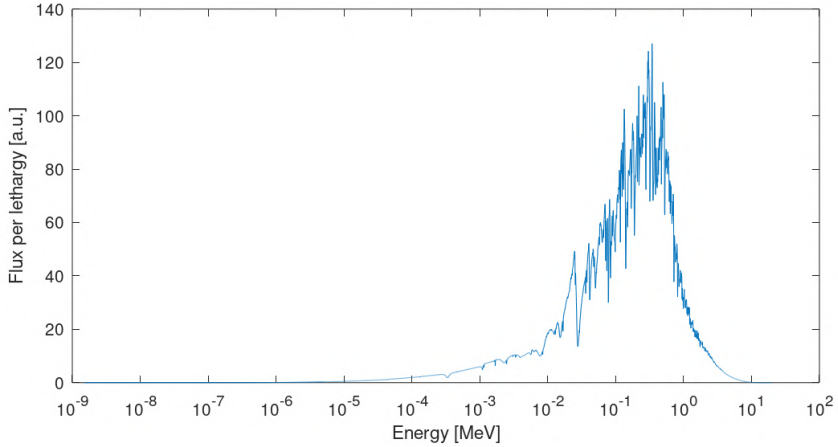


Figure 6.3: Core-wide flux spectrum of the VENUS-F core.

Starting with a 1D TFM analysis of the default core, the two first eigenvalues of the $\underline{G}_{\chi_p \nu_p}$ matrix yield

$$DR_{CR0*}^{TFM} = \frac{k_1}{k_0} = \frac{0.66548}{0.99672} = 0.67$$

$$EVS_{CR0*}^{TFM} = \frac{k_0 k_1}{k_0 - k_1} = 2.00$$

The uncertainty associated with the eigenvalues is on the order of 35 pcm (see the beginning of section 4.2), with the dominance ratio value being $\frac{k_{1,0,0}}{k_{0,0,0}} = 0.66767(45)$. As before, only two digits are kept for the dominance ratio and EVS and so the uncertainty is omitted. The same is true for all TFM cases that follow.

This azimuthal analysis guarantees that the first harmonic mode is correctly accessed. This is discussed later, in section 6.1.2.

In this case, the eigenvector, shown in Fig. 6.4 is quite steep, indicating that the largest portion of the system importance is located at the center of the core. This result is a combination of the node discretization and the core geometry itself. The central nodes contain much more fissile material due to the way the geometry is discretized (x axis) than nodes far from the center and at the same time, the core center itself contains more fissile material than the periphery. If one looks at the core flux and fission rate profiles

(Figures F.1, F.3, F.4), they do agree with the eigenvector shape. Also, notice that the positions of the first mode eigenvector maxima and minima roughly correspond with the positions of the safety rods in the system (remember that the eigenvector plot x axis is no. of region, not cm). This was discussed before, but this is a practical example of how the shape of the first mode eigenvector can identify the optimal positions for control elements. The two positions at the bottom would also be indicated to be at the first eigenvector extremes. The appearance of the eigenvectors (interchanging highs and lows) has to do with the discretization used, which was one node per 2 cm and thus some nodes contain fuel only partially (it is also useful to see Fig. F.4). Given that the core does not contain any rapid material changes (such as in the case of the single row of 30.2% U in ZEPHYR), this scheme is sufficient and allows for good accuracy, without losing any information, while at the same time keeping post-processing fast and single TFM matrix size at around 11 MB.

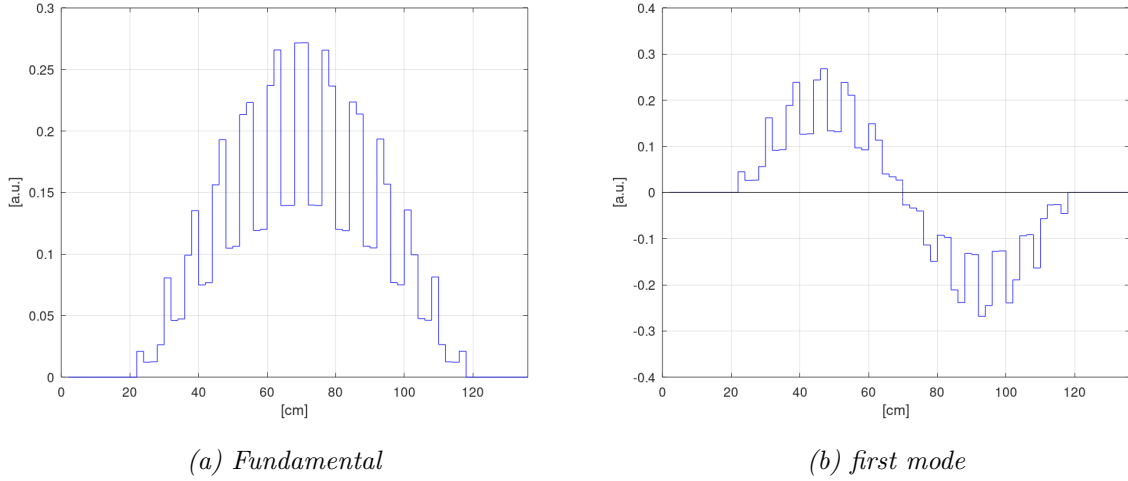


Figure 6.4: $G_{\chi_p \nu_p}$ matrix eigenvectors for the default VENUS-F core configuration.

A full-core coupling coefficient matrix was generated in ERANOS, with 12 nodes along the azimuth, as shown in Fig. 6.5. The treatment produced the region-wise coefficients, generation times and partial delayed neutron fractions. The results are given in Tables F.1 and F.2, in Appendix F. Both the dominance ratio and the eigenvalues separation are quite close to the TFM numbers, indicating good agreement between the two methods with this geometry and discretization.

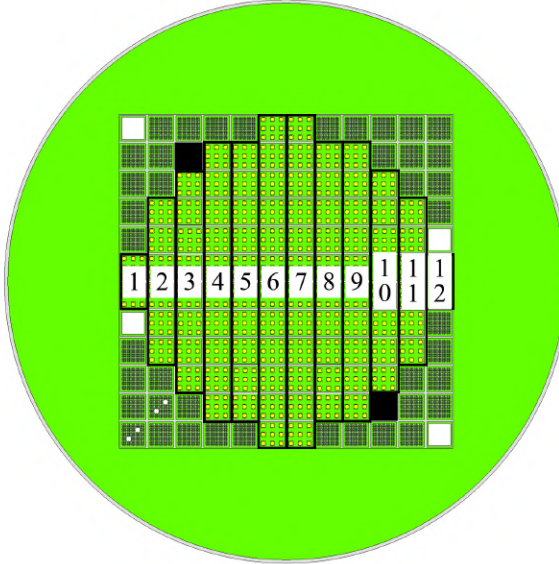


Figure 6.5: Geometry discretization for the k_{ij} model in ERANOS.

$$DR_{CR0*}^{EK} = \frac{k_1}{k_0} = \frac{0.68204}{1.01526} = 0.67$$

$$EVS_{CR0*}^{EK} = \frac{k_0 k_1}{k_0 - k_1} = 2.08$$

Figure 6.6 shows the two first matrix eigenvectors. While less detailed than the ones obtained with TFM, they replicate the shape quite well and allow the same information about the core to be extracted. More specifically, the fundamental eigenvector indicates that the core is characterized by an importance profile typical of such uniform cores. The first mode eigenvector displays maxima and minima in regions 3 and 10, again corresponding to the optimal positions for symmetric control elements.

Finally, Fig. 6.7 was generated by leveraging the technique described in section 4.3 of the thesis, where a diffusion calculation on one half of a symmetrical geometry, with an enforced zero flux boundary condition along the symmetry axis can be used to generate the first mode harmonic flux. The same conclusions can be made, but the behavior can now be visualized over the entire geometry. The figure displays the actual flux harmonic, instead of the coupling matrix eigenvector. It is very useful to be able to visualize the flux harmonic across the entire core mid-plane, however, this approach does not give any information at all about the coupling behavior of the system.

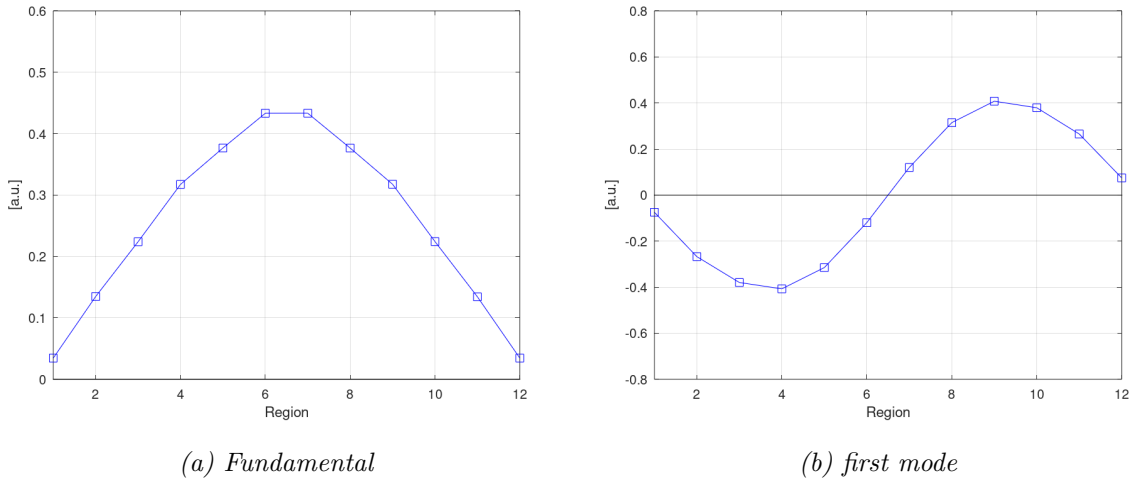


Figure 6.6: k_{ij} matrix eigenvector for the default VENUS-F core configuration.

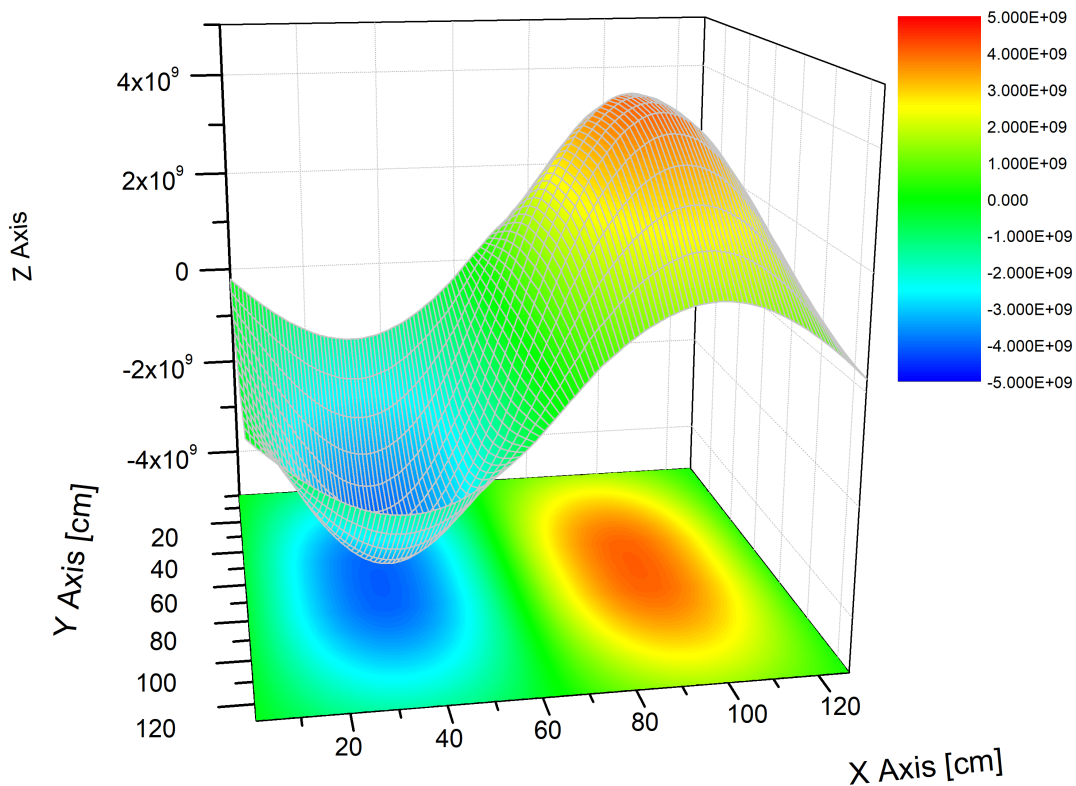


Figure 6.7: First flux harmonic distribution in the core mid-plane, calculated in ERANOS. The z axis represents the harmonic flux in arbitrary units.

6.1.1 k_0 , k_1 and dominance ratio sensitivities

By taking advantage of the symmetry of the geometry, the first order harmonic flux can be calculated, as shown above. ERANOS is able to extract the sensitivities to nuclear data for the calculated flux, so by running a diffusion calculation on the full geometry (both positive and negative parts on the x axis) for the fundamental flux and a calculation on half of the geometry ($+x$ part only), the sensitivity profiles for k_0 and k_1 can be computed. Below, what is shown are the profiles themselves, as well as their ratio and difference, for the fuel and moderator materials present in the core. This type of analysis allows to see how the two modes are perturbed differently and can aid in the design of future experiments aimed at perturbing the modes separately.

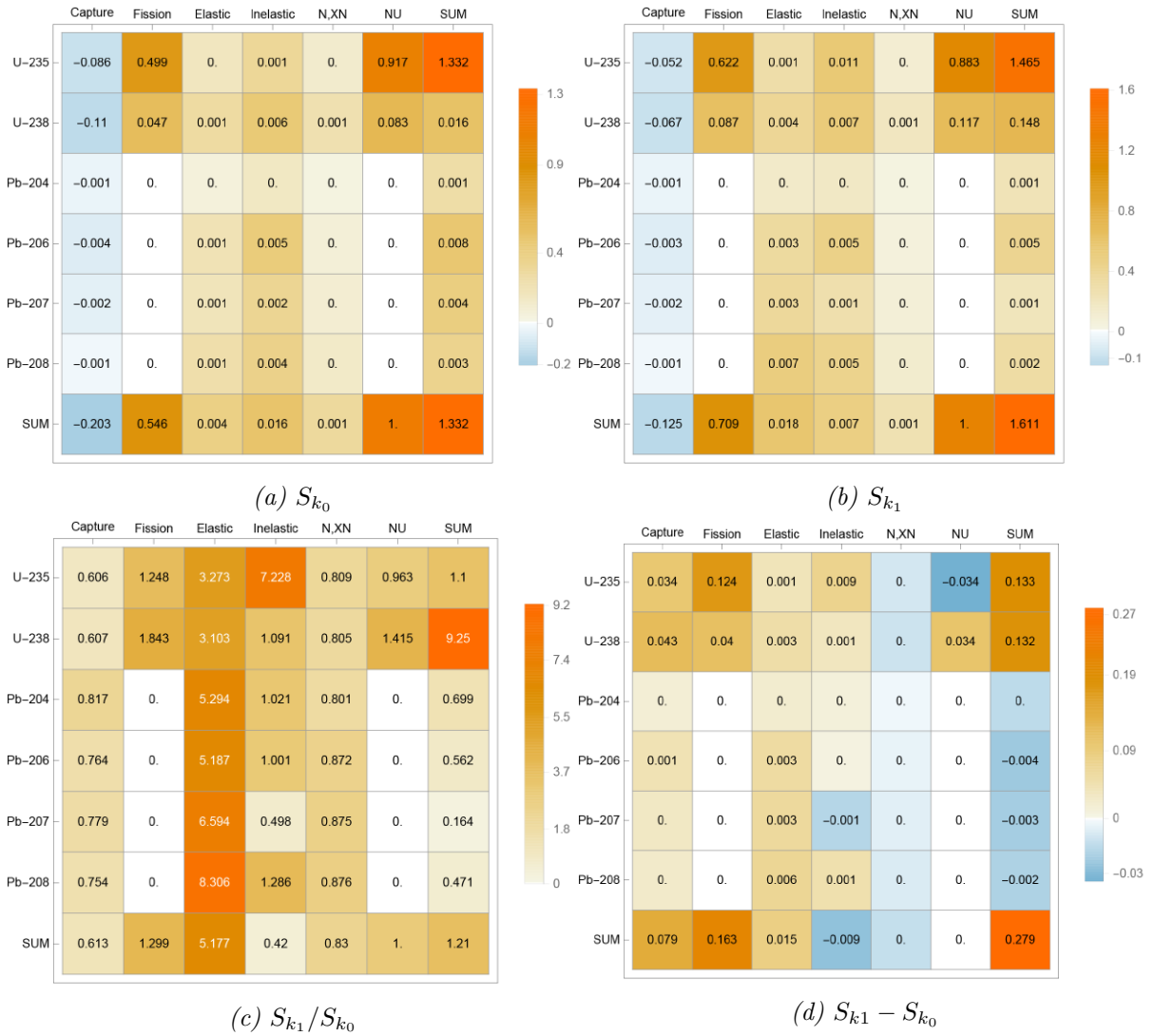


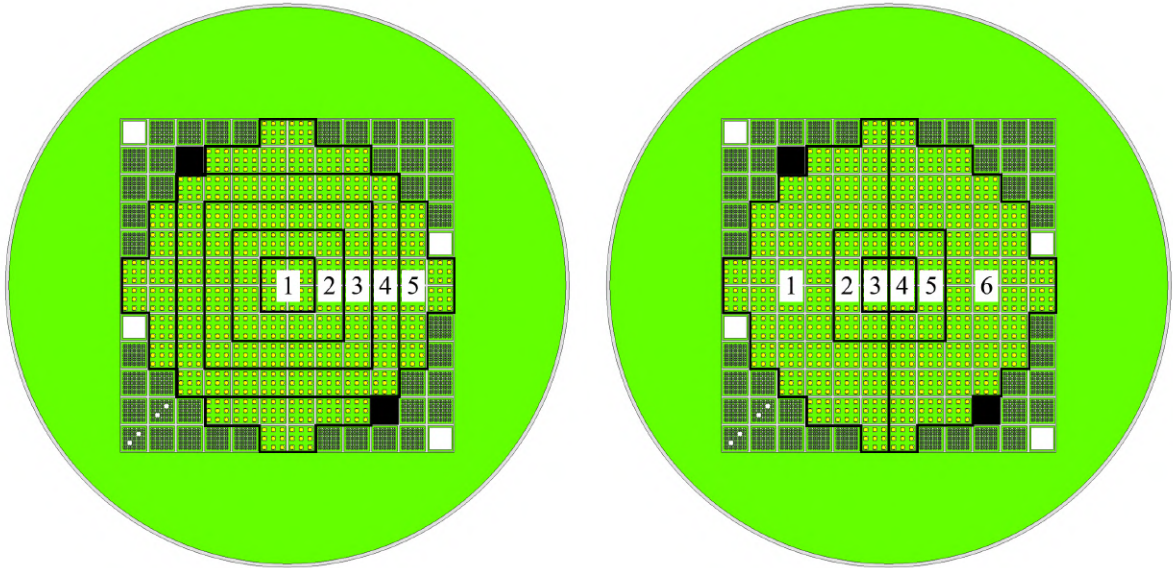
Figure 6.8: Nuclear data sensitivity profiles for the CR0* core.

Figure 6.8c is the most interesting, showing the ratios of the sensitivities of the two modes. The first mode seems to be particularly more influenced by elastic scattering for all isotopes, inelastic scattering in ^{235}U and the concentration of ^{238}U . As such, a perturbation where ^{238}U would be introduced to or removed from the system, would affect the first harmonic mode significantly more than the fundamental one.

6.1.2 Three-dimensional coupling

Since the k_{ij} approach in ERANOS is not limited in its application and discretization scheme, it can be used to study the coupling behavior of two or more arbitrary parts in a geometry, in any combination of (x,y,z) coordinates. It can be used, for example, to observe the neutronic coupling between an assembly where a control rod is dropped in and another one, used for measurements. The only restriction that currently exists in the code is that all coupled regions must contain fissile or fissionable material, as the source term cannot be zero. To illustrate the capability, the VENUS-F active core was discretized in different ways, as shown in Fig. 6.9. Figure 6.9a shows a radial scheme and Fig. 6.9b shows an arbitrary scheme on XY that was split into two axial regions. A 6-region axial scheme was also run. These analyses show how inner and outer parts, as well as how the two axial halves of the reactor are coupled. It is convenient to have 3D coupling information and it can be useful for a multitude of applications, such as experiment planning, core design studies, predicting core-wide behavior or in the design of control devices. At this point in development, the maximum number of coupling regions was increased to twelve.

As always, selecting appropriate discretization schemes allows to access certain harmonics, such as axial or radial. Analyzing the geometry in this manner and comparing the second matrix eigenvalue λ_1 with other discretization schemes, ensures that the eigenvalue corresponding to the actual first harmonic mode is be accessed. In all cases here, the calculated λ_1 is lower than for the azimuthal-only discretization, indicating that the latter's first accessed mode indeed corresponds to the first harmonic mode.



(a) Radial

(b) Radial split

Figure 6.9: Radial discretizations.

	Radial	Axial	3D	Azimuthal
k_0	1.01526	1.01526	1.01526	1.01526
λ_1	0.43588	0.57002	0.65007	0.68204
λ_1/k_0	0.43	0.56	0.64	0.67
EVS	0.76	1.30	1.81	2.08

Table 6.1: k_0 , λ_1 , dominance ratio (DR), eigenvalue separation (EVS), for different discretization schemes, calculated with ERANOS.

The k_{ij} matrix for the 3D coupling case of Fig. 6.9b is visualized in Fig. 6.10. Regions 1-6 refer to the top part and show the source distribution across the core top plane, while regions 7-12 do the same for the bottom plane. The sub-matrices formed by elements $k_{1,7} - k_{1,12}$, $k_{6,7} - k_{6,12}$ and $k_{7,1} - k_{7,6}$, $k_{12,1} - k_{12,6}$ show how the two halves are coupled with each other.

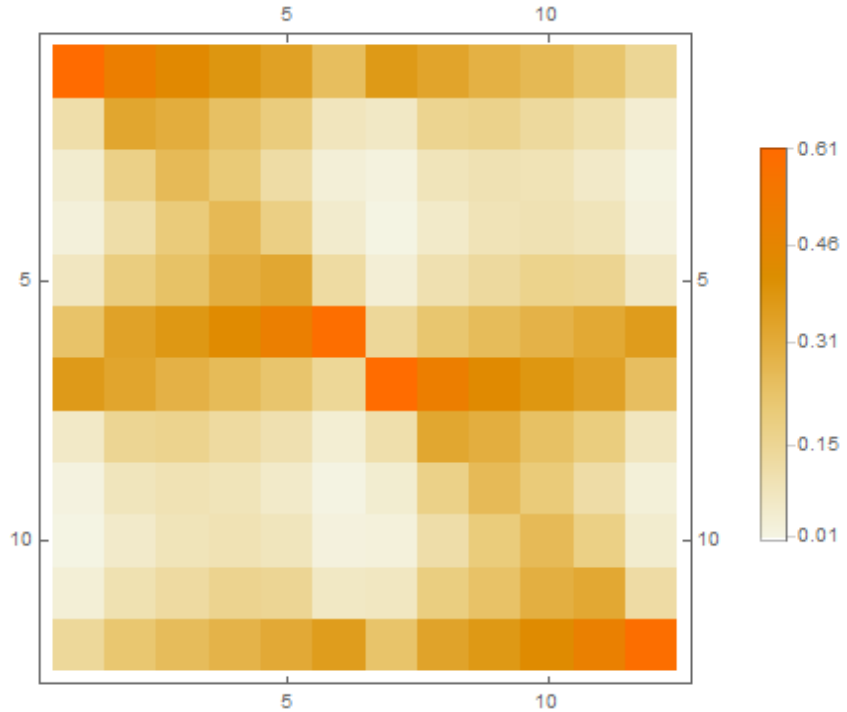


Figure 6.10: 3D coupling for the VENUS-F core in the CR0* configuration. Regions 1-6 refer to the top part and regions 7-12 refer to the bottom part.

6.2 Increasing the dominance ratio

This section describes the iterative approach used to gradually increase the dominance ratio of the core. Each step is presented, explaining to the reader the process that was used, the obstacles encountered and the solutions devised. The material selection was limited to what is available in the inventory of the CEA and/or SCK CEN, as well as adhere to current core loading limitations (as an example, VENUS-F is not rated for a full MOX core and cannot utilize a partial light water region, like ZEPHYR does) and go with a core without light water moderator. Additionally, the decision was taken to limit the designs to solid moderators, as a way of managing the scope of the application. This particular part of the thesis saw heavy use of the TFM model in Serpent 2, mainly due to the code's versatility and most importantly, its ability to run parallel calculations (the ERANOS code is limited to one instance per machine). Serpent 2 was used to design and test configurations, while ERANOS was used to further analyze the most promising candidates.

6.2.1 Moderator changes

Starting with a simple approach, based on the connection of the dominance ratio to core characteristics,

$$DR = \frac{k_1}{k_0} = \frac{B_{0,0,0}^2 M^2 + 1}{B_{1,0,0}^2 M^2 + 1}$$

and considering that the reactor at hand has a fixed physical size, meaning that the geometric buckling is fixed, the only variable left is the migration area, which in turn is given by $M^2 = \frac{D}{\Sigma_a}$, where D is the diffusion coefficient and Σ_a is the macroscopic absorption cross section, it becomes apparent that in order to increase the dominance ratio of a uniform reactor core, one must strive to minimize the migration area. Using this basic approach, it all comes down to how far a neutron can travel in a core, compared to the size of that core. For a fixed core size, the shorter the migration area, the more decoupled the system is and the higher its dominance ratio and eigenvalue separation. Moderator material with good thermalization properties needs to be used, as well as material that will increase the total absorption cross section.

As a first attempt, the lead in the fuel and reflector assemblies was replaced with graphite. This served to reduce the diffusion coefficient D and by extension the migration area M^2 and soften the spectrum to subsequently increase the core reactivity. Of course, it was expected that the k_{eff} would shoot above 1, but as stated before, this was an iterative

process. The softer spectrum meant a local increase in fission rates and at the same time that neutrons, on average, covered smaller distances and induced fewer fissions away from their birth location. The increase in fission rate caused a boost in localized power generation per assembly, with most of these new neutrons causing an elevated number of fissions close to their point of origin. This behavior can easily be seen in the prompt-to-prompt $\underline{G}_{\chi_p \nu_p}$ matrix if one observes the changes between the two matrices and recalling that the diagonal of the TFM matrix describes an $i = j$ scenario, where the origin and target nodes refer to the same zone in the geometry. The one corresponding to the graphite core displays markedly reduced propagation probability values away from the diagonal and increased values on and close to the diagonal. This difference can be seen in Fig. 6.11c; the white space corresponds to non-multiplying regions in the reflector or non-fuel assemblies.

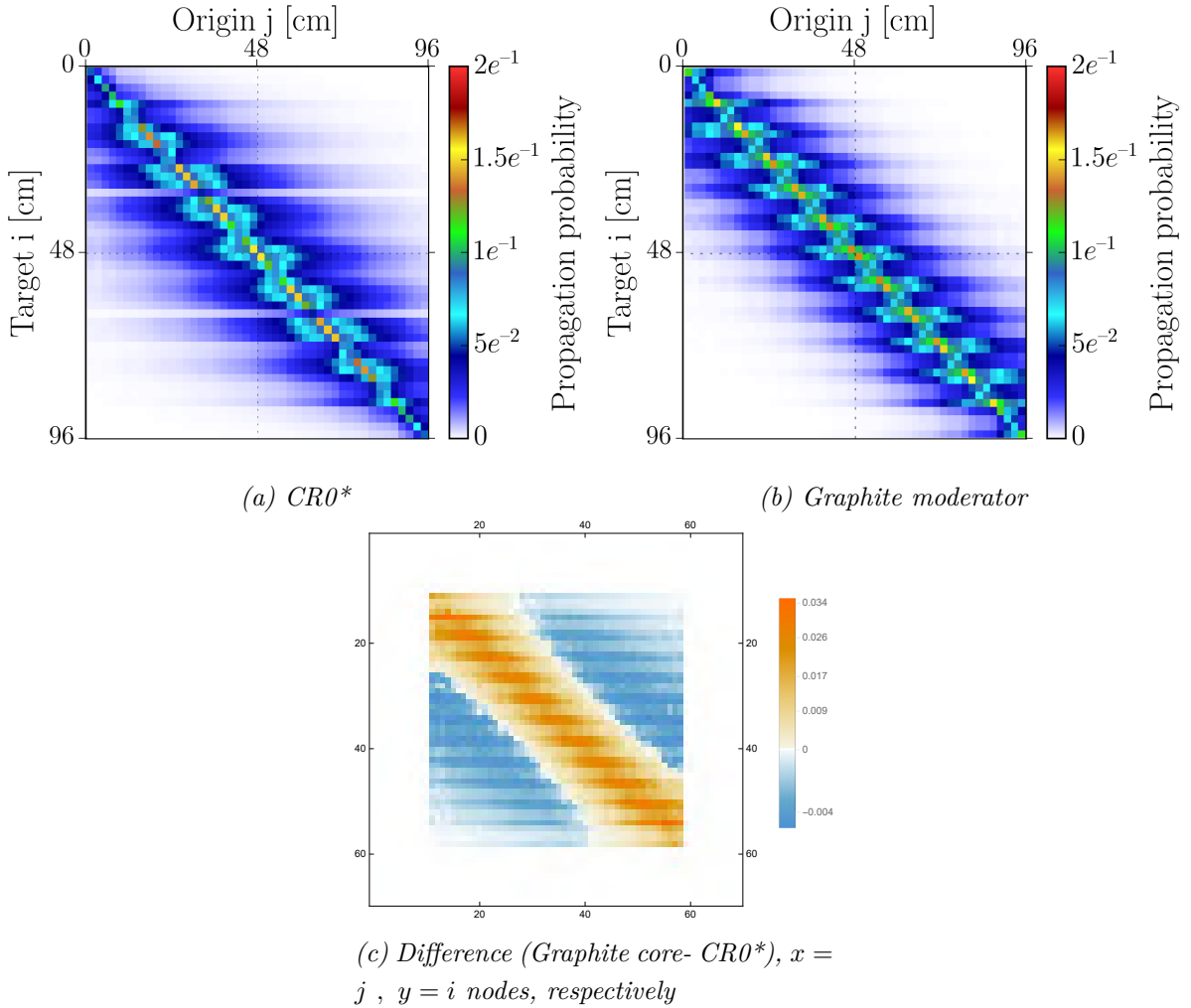


Figure 6.11: $\underline{G}_{\chi_p \nu_p}$ matrices and their difference, for the $CR0^*$ and graphite VENUS-F configurations. The material changes only refer to the 12×12 lattice, not the radial reflector.

The dominance ratio becomes

$$DR_C = \frac{k_1}{k_0} = \frac{0.85901}{1.13498} = 0.76$$

$$EVS_C = \frac{k_0 k_1}{k_0 - k_1} = 3.53$$

and already this simple material change presents a significant improvement over the default configuration. Taking it a step further, the moderator material was changed to high density polyethylene (HDPE), whose molecular formula of CH₂ and density of 0.96 g/cm³ brings it close to light water in terms of hydrogen content and thus helps to further reduce the migration area. This effectively transitions the core to thermal now, with a massive jump in reactivity and a further increase in decoupling. At this point, the dominance ratio of VENUS-F with a polyethylene moderator has matched the one of the ZEPHYR coupled core, although of course the core is not usable in its current state. The $\underline{G}_{\chi_p \nu_p}$ matrix shows an even bigger concentration of propagation probability on the diagonal, while the chance to propagate away from the origin node drops significantly. The $\underline{G}_{\chi_p \nu_p}$ matrix eigenvector is even steeper than before, the importance gathering towards the center even more. At this point, the dominance ratio is comparable to that of the ZEPHYR design. The question is, how to ensure a sufficiently high dominance ratio while bringing the reactivity down to acceptable levels?

$$DR_{HDPE} = \frac{k_1}{k_0} = \frac{1.29510}{1.44765} = 0.89$$

$$EVS_{HDPE} = \frac{k_0 k_1}{k_0 - k_1} = 12.29$$

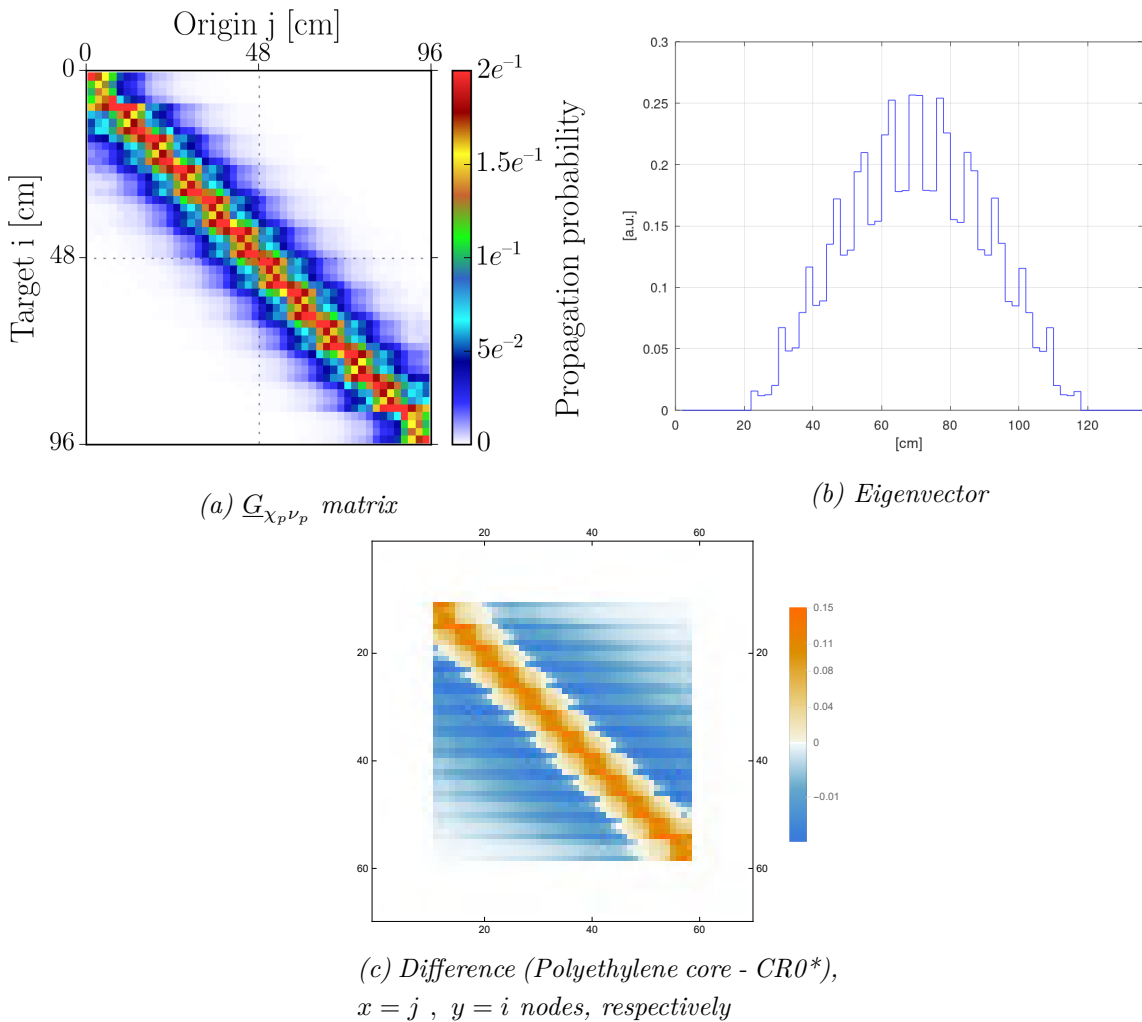


Figure 6.12: $G_{\chi_p \nu_p}$ matrix, its fundamental eigenvector and its difference from CR0*, for the VENUS-F core with polyethylene moderator.

6.2.2 Zones modification

Having exhausted the simple options of moderator material change, if the dominance ratio was going to increase further, the core would need to change in a more meaningful way, incorporating heterogeneous designs. Recalling that decoupling is associated with a high dominance ratio, the next step was to come up with a series of modifications to the core geometry, with the aim of decoupling it further. Several modifications combining polyethylene-moderated and natural uranium assemblies were designed and tested, ultimately settling with a simple one, a ring of assemblies with natural uranium blocks and no enriched fuel elements, placed around the four central assemblies. Seeing as this is now a more thermal core (see Fig. F.6 and Fig. F.10 for less thermalized designs), most neutrons entering the natural uranium zone will be well below the energy threshold

for the (n, f) reaction on ^{238}U and will instead be captured or scattered. Escaping past this assembly ring is possible, but not particularly easy, since the square natural uranium blocks form an essentially large, solid block of fertile and absorbing material. Looking at the difference matrix, one can observe the small break in propagation that the fertile assemblies create, but otherwise, the picture is similar to the one for the previous case.

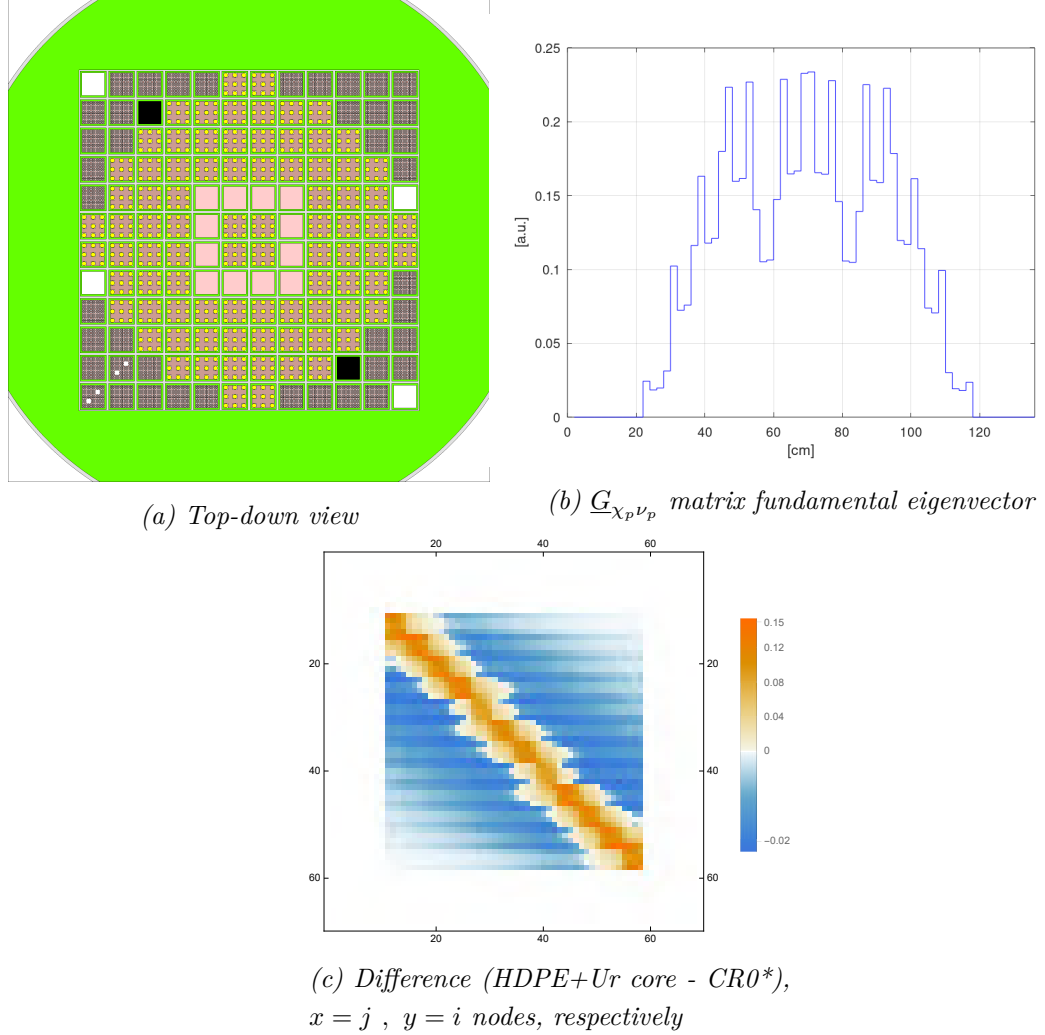


Figure 6.13: VENUS-F configuration with polyethylene moderator and a ring of natural uranium assemblies around the core center. Yellow: metallic U 30.2% enrichment, Brown: CH_2 , Pink: natural UO_2 , Black: void (B_4C pilot rod position), White: air.

$$DR_{\text{HDPE+Ur}} = \frac{k_1}{k_0} = \frac{1.25820}{1.36625} = 0.92$$

$$EV S_{\text{HDPE+Ur}} = \frac{k_0 k_1}{k_0 - k_1} = 15.91$$

The eigenvector clearly shows the decoupling achieved here. The overall shape is much

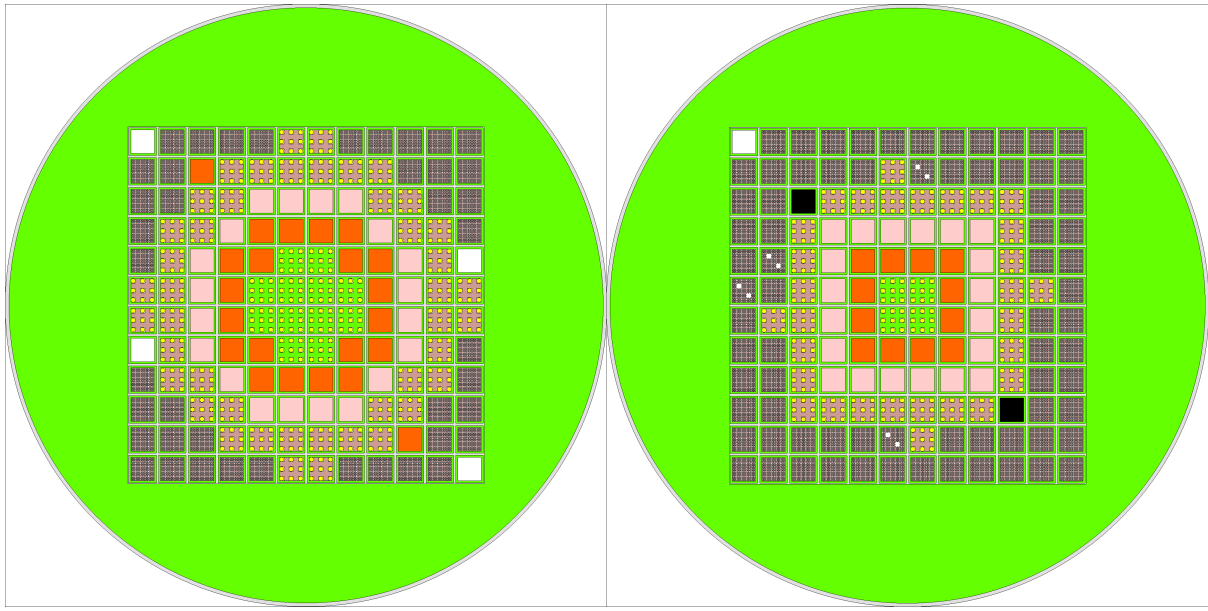
more spread out, meaning that the importance is distributed more equally around the core, instead of being accumulated in the center. This means that different regions of the core become more decoupled from each other and more of their fissions are caused by neutrons born internally, rather by neutrons coming from other nodes, especially the central ones. In terms of coupling, this translates to higher coupling coefficients for nodes that are physically close to each other.

While the configuration now exhibits a good dominance ratio value, due to the hydrogen in the polyethylene, the k_{eff} is unacceptably high. It is clear that a full polyethylene core (at least with 84 fuel positions) is not possible. Two designs were settled upon, both drawing inspiration from the design of the ZEPHYR core. They were made more heterogeneous, replacing the central assemblies for the original ones with lead blocks, while adding a natural B₄C zone and expanding the natural uranium zone outwards. Figure 6.14 gives the geometries themselves, Table 6.2 gives the main information obtained with the TFM model, while Figures 6.15 and 6.16 show the fundamental and first mode $G_{\chi_p \nu_p}$ matrix eigenvectors, respectively. The idea was to reduce the overall reactivity by including more fertile and absorbing materials, while at the same time enhancing the decoupling behavior, which was increased in the process, as the non-fissile elements served to further decouple the different zones of the core. The main difference between the two is the size of the active core and the radial approach of Design 1 versus square approach of Design 2.

Design 1, shown in Fig. 6.14a, utilized the same size of active core as the previous geometries, but that, in conjunction with the number of polyethylene fuel assemblies, made it very difficult to reduce the reactivity past a certain point. Several attempts at a redesign were made, including trying different reflection materials (polyethylene was the best material, because of its higher absorption cross section) but the increasing core geometry complexity and gradual reduction of the dominance ratio, meant that a completely new approach was needed. It is important to note one particular change in the eigenvectors shape in Fig. 6.15a. The maxima (and minima for the first mode) have been displaced closer to the end of the assembly lattice. Referring to the core as a grid, their new position overlaps assembly columns 2 and 11, whereas before it corresponded to columns 3 and 10. This is due to the natural uranium present in columns 3 and 10, reducing both these columns' importance (visible in the fundamental mode), as well as reducing their capacity to affect the reactor behavior if perturbed (visible in the first higher mode). Considering that columns 3 and 10 house the safety rods for the reactor, such a displacement of the first mode eigenvector is not desirable, since the extremes should coincide with the positions of critical control elements, to maximize the latter's effectiveness. An added consideration is that these elements will need to be partially used

to bring the system to criticality. The available negative reactivity of the additional six safety rods is considerably lessened, to just -1141 pcm or -1.50\\$ and that is not nearly enough to induce subcriticality. A number of modifications can be made to alleviate this issue, but at the cost of reducing the dominance ratio. Still, this design is merely a concept, solely focused on exhibiting a high dominance ratio, while simultaneously dealing with some of the excess reactivity introduced by the addition of polyethylene. However, Design 1 approaches dominance ratio values comparable to those of fast neutron power reactors in the 600 MWe class [52] and if other means of controlling its reactivity could be employed, it could allow for interesting experiments. In fact, if doping the polyethylene with low amounts of boron nitride is possible, this can both reduce the excess reactivity and raise the dominance ratio, by increasing the overall absorption cross section. Another option is to use enriched instead of natural B₄C. And yet another one is to experiment with the fuel assembly designs. All of these options are valid, but there was not enough time to explore them.

Design 2, shown in Fig. 6.14b, moved away from the large active core, opting to tackle the reactivity issue by reducing the total amount of fissile material and especially the number of polyethylene fuel assemblies. To allow for a decoupled geometry based on the previous approach, a smaller fast central zone was created, with concentric square zones of B₄C, natural uranium and polyethylene-moderated fuel assemblies. The pilot rods were also moved closer to the active core and a few experimental positions were added, corresponding to the CC5 geometry seen in [27]. This configuration offers several advantages over the previous one, the most notables being that it is much simpler and it brings the excess reactivity down to just 1167 pcm without using any of the control elements, whose combined negative reactivity is -6824 pcm or -8.86\\$, allowing plenty of room for safety. The core can be controlled with the two pilot rods. The fundamental and first mode eigenvectors also show very well defined peaks, corresponding to the single assembly columns of polyethylene-moderated fuel assemblies. The only downside is a slight drop to the dominance ratio, which can be somewhat recovered with use of additional fuel assemblies and partial control rod insertion during operation. Additionally, shifting of the outer fuel assemblies or removal of one of them can bring the excess reactivity down even lower, at the cost of a reduced dominance ratio. The simplicity of this configuration allows it to undergo small modifications, adapting to the needs of the facility, without compromising its characteristics too much. One possible limitation of this geometry is the small size of the central fast zone, but it can be partially increased by using mixed assemblies (part B₄C and part fuel, for example).



(a) Design 1

(b) Design 2

Figure 6.14: VENUS-F high dominance ratio designs. Yellow: metallic U 30.2% enrichment, Brown: CH_2 , Pink: natural UO_2 , Orange: B_4C , Black: void (B_4C pilot rod position), White: air.

	Design 1	Design 2
k_0	1.11381	1.01174
k_1	1.05007	0.93252
DR	0.94	0.92
EVS	18.35	11.91
β_{eff} (pcm)	745	765
ℓ_{eff} (μs)	12.7	13.7
Λ_{eff} (μs)	11.4	13.5

Table 6.2: k_0 , k_1 , dominance ratio (DR), eigenvalue separation (EVS) and main kinetic parameters, calculated with TFM.

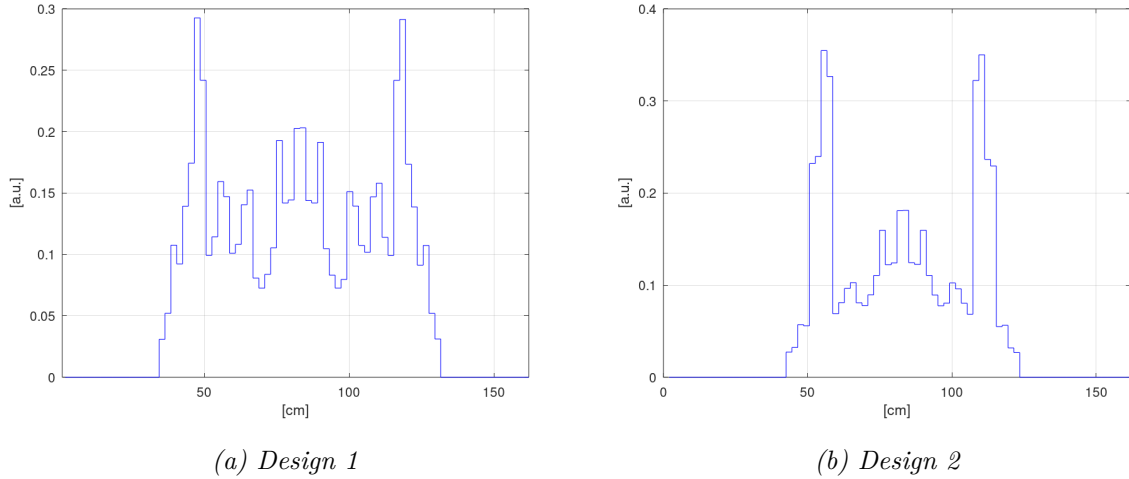


Figure 6.15: $\underline{G}_{\chi_p \nu_p}$ matrix fundamental eigenvector.

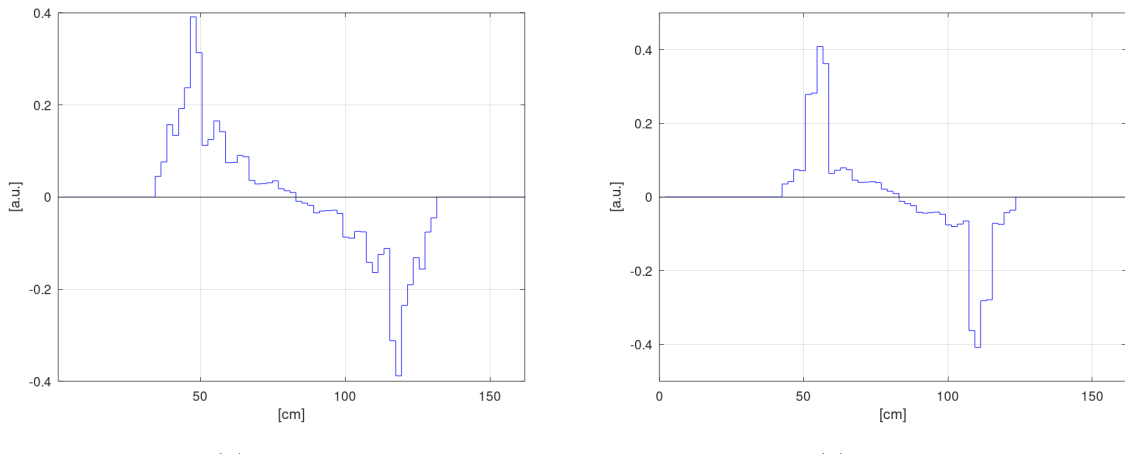


Figure 6.16: $\underline{G}_{\chi_p \nu_p}$ matrix first mode eigenvector.

The $\underline{G}_{\chi_p \nu_p}$ matrices themselves are also presented in Fig. 6.17, as well as their difference. The most notable characteristics are the effect of the external thermal zones on the rest of the geometry and how the B_4C zone changes that, with Design 2 sporting a smaller absorber zone. Furthermore, as far as the azimuthal direction is concerned, thermal fuel assemblies in Design 2 are arranged in longer columns (3rd and 10th columns - 6 assemblies) than in Design 1 (2nd and 11th columns - 5 assemblies), meaning that the corresponding regions carry higher relative importance, something that can be seen in the difference matrix and fundamental eigenvector shapes as well. The positive (beige) line pattern observed in Fig. 6.17c is explained by the increased propagation probability at longer distances, of Design 2 columns 3 and 10 (longer top and bottom lines) and the difference in the B_4C zone placement (shorter two lines).

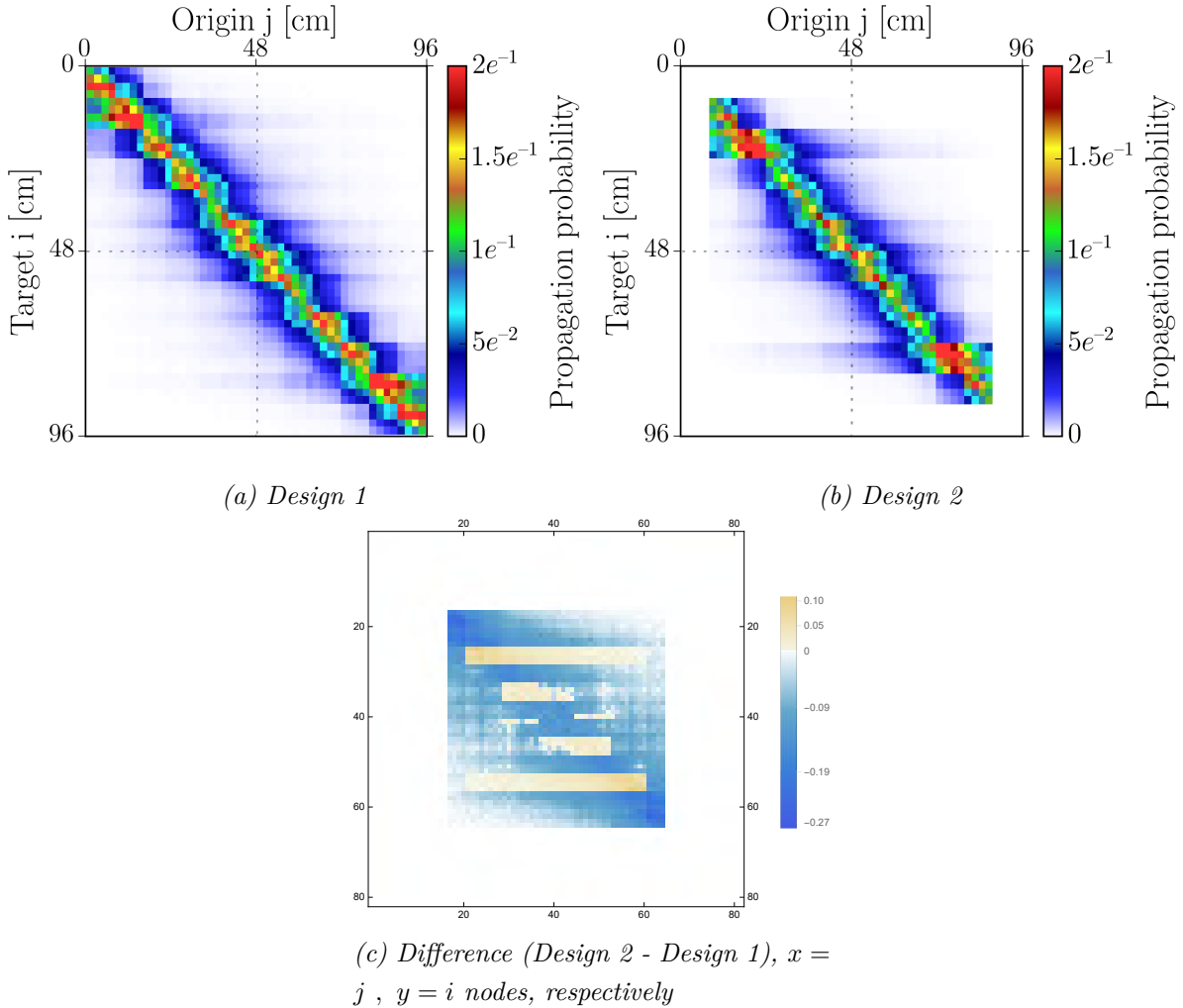
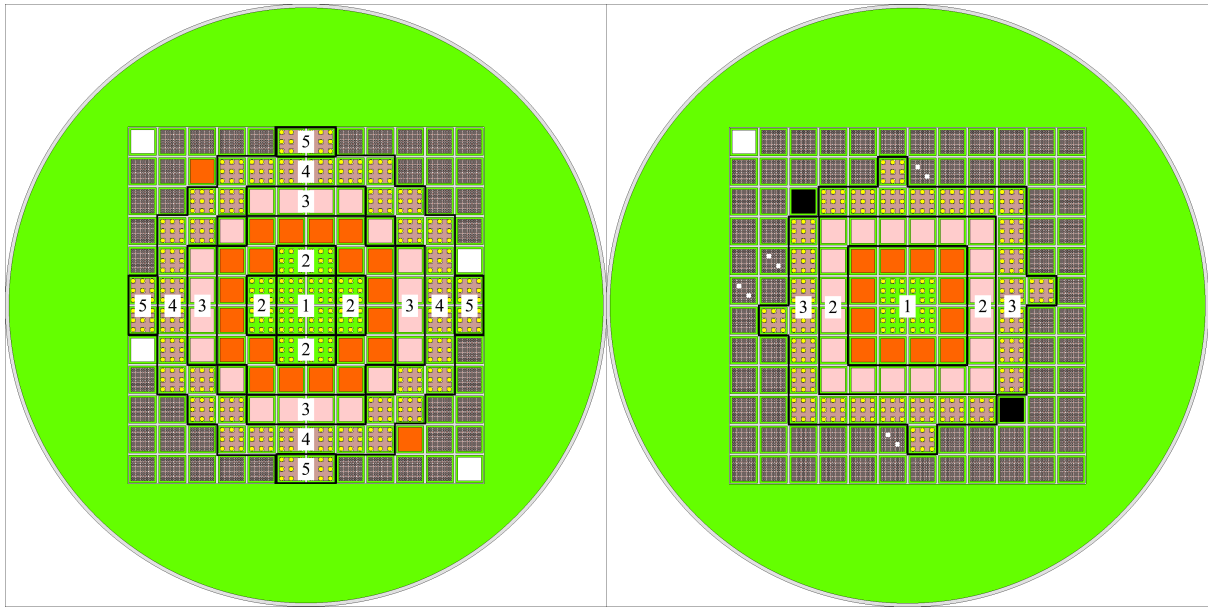


Figure 6.17: $G_{\chi_p \nu_p}$ matrices and their difference.

Having reached a good dominance ratio, the geometries were further analyzed with Kobayashi's coupling coefficients model in ERANOS, in order to obtain more information on the coupling and kinetic parameters of the system. The geometries were both analyzed azimuthally as well as radially, in order to get a picture of the coupling between the central, fertile and thermal zones. The relevant data are given in Appendix F.2. The azimuthal discretization is per fuel assembly column, while the radial is shown below, in Fig. 6.18. Table 6.3 presents the basic eigenvalue data for all cases, with the radial case for Design 2 giving access to radial modes. While the azimuthal fundamental and first mode source distributions are given in the appendix, in Fig. F.16.

Tables 6.4 and 6.5 present the radial coupling coefficients. The fourth and third rows respectively display the high propagation probabilities for the main regions with polyethylene-moderated assemblies.



(a) Design 1

(b) Design 2

Figure 6.18: Radial discretization for the k_{ij} model in ERANOS, for the two high dominance ratio configurations.

	Design 1	Design 1 (radial)	Design 2	Design 2 (radial)
k_0	1.05833	1.05833	0.93661	0.93661
k_1	0.97939	0.39260	0.89962	0.23771
DR	0.93	0.37	0.96	0.26
EVS	13.13	0.62	22.78	0.32

Table 6.3: k_0 , k_1 , dominance ratio (DR), eigenvalue separation (EVS), calculated with ERANOS.

$$k_{ij}^{Design\ 1,\ radial} = \begin{pmatrix} 0.21089 & 0.11119 & 0.02199 & 0.00622 & 0.00270 \\ 0.23212 & 0.23086 & 0.05424 & 0.01562 & 0.00706 \\ 0.05747 & 0.07993 & 0.14533 & 0.05841 & 0.02674 \\ 0.41769 & 0.47863 & 0.80791 & 0.92449 & 0.55355 \\ 0.01730 & 0.02133 & 0.04358 & 0.06217 & 0.42866 \end{pmatrix}$$

Table 6.4: Radial k_{ij} coupling coefficients for Design 1.

$$k_{ij}^{Design\ 2,\ radial} = \begin{pmatrix} 0.22571 & 0.03390 & 0.01046 \\ 0.13772 & 0.22132 & 0.08914 \\ 0.37897 & 0.60909 & 0.85036 \end{pmatrix}$$

Table 6.5: Radial k_{ij} coupling coefficients for Design 2.

6.2.3 Perturbation of the Design 2 configuration

The response to material perturbation was studied, once by inserting the right pilot rod and once by inserting one safety rod, removing the follower fuel assembly in the process. In both cases, the eigenvectors are redistributed in a similar fashion, with the perturbed part losing importance, while another part of the core gaining importance in response. At tilt, in other words. Logical, since the unperturbed part now provides a larger portion of the geometry's fission neutrons. The importance tilts for all cases were also estimated, with f_L referring to the left half-plane and f_R referring to the right. Figure 6.19 shows the differences between the two cases and the original Design 2 geometry. It is notable that for the case of the pilot rod, the entire matrix is close to zero, indicating that, as will be shown below, the effect was minimal. On the other hand, the safety rod case shows a clear effect in the negative scale, with the change being higher by an order of magnitude. Note that both the pilot and the safety rod material is natural B_4C - the results would likely be more pronounced in both cases, if enriched B_4C was used.

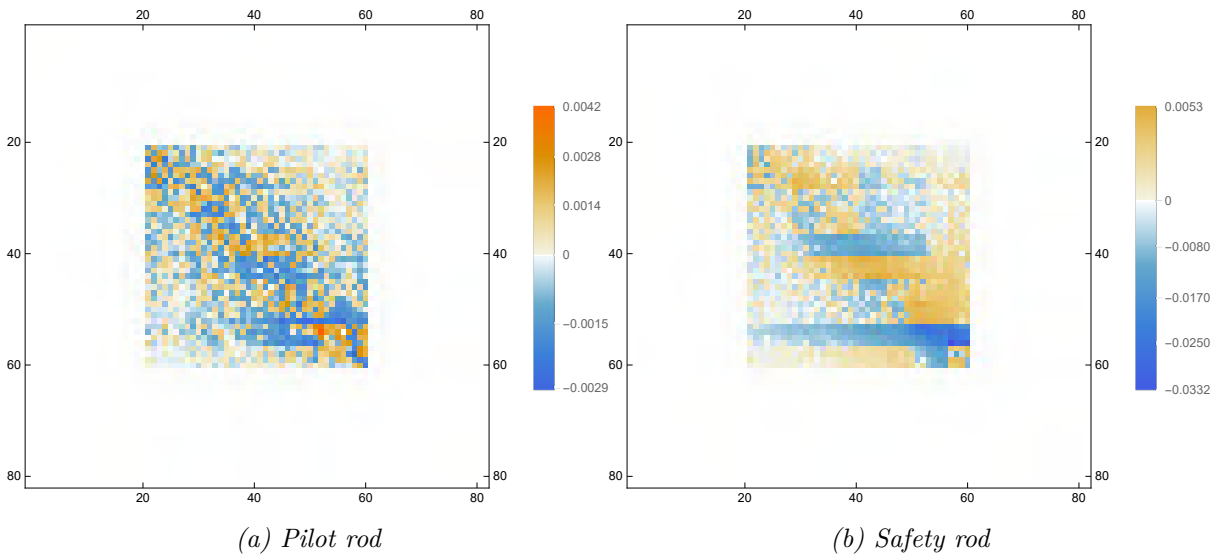


Figure 6.19: $G_{\chi_p \nu_p}$ differences from the default Design 2 geometry, $x = j$, $y = i$ nodes, respectively.

It is interesting to note the differences between the two cases. The changes induced by the pilot rod are minimal, on the order of 0.5-1.5% and the eigenvector shapes barely change (notice that the y axis is double than in Fig. 6.15b). A small redistribution takes place. The slight depression in available neutron flux on one part of the geometry slightly tilts the importance, reducing it locally and raising for the unaffected high-importance part. The slight loss of fission neutrons around the perturbation point causes a drop in the importance of nearby regions as well, as their own ability to produce neutrons is lessened. All in all though, the overall effect is minimal and the measure tilt of only 0.6% confirms that.

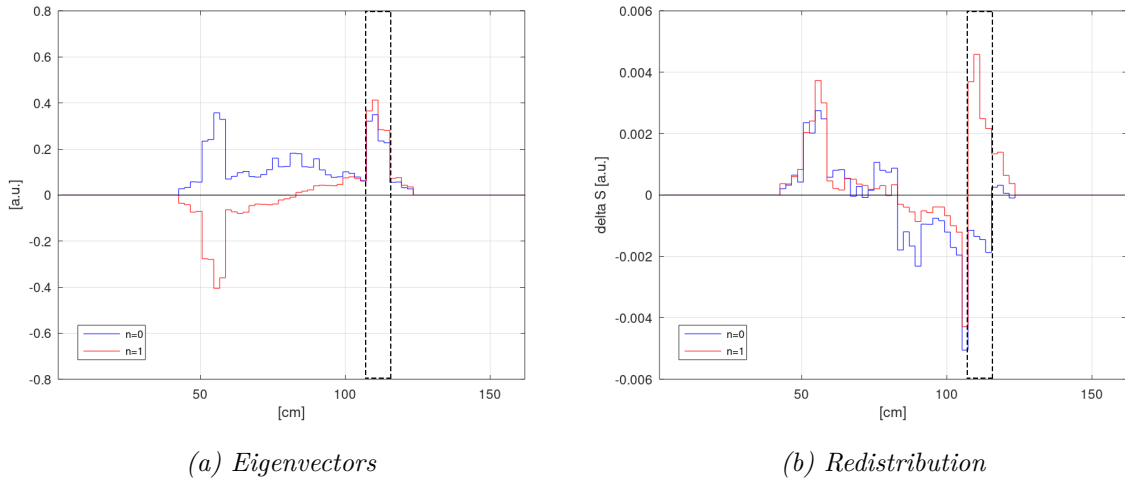


Figure 6.20: $G_{\chi_p \nu_p}$ fundamental and first mode eigenvectors and their redistribution, for the pilot rod insertion in Design 2.

In the case of the safety rod, the results are much more visible. Figure 6.21 shows the flux maps for the Design 2 configuration, with all control elements withdrawn and with the safety rod inserted. Figure F.14 shows the fission rate map. The eigenvector shapes and redistribution in Fig. 6.22, show a very prominent tilt taking place and Table 6.6 shows that the the fist mode is more affected than the fundamental one, hence the drop in dominance ratio. The point of insertion is clearly visible and the local importance is significantly diminished. The first mode eigenvector axis intersection point is displaced towards the system's new center of importance (the fundamental mode integral is the same left and right of that intersection point), causing its increase in the middle of the geometry. The importance tilt is notable, with $f_L=62.2\%$.

Finally, Table 6.6 shows that for the pilot rod case, the fundamental mode was perturbed more, while the safety rod insertion affected the first mode more. Looking at the ratio of the sensitivity profiles for k_0 and k_1 in Fig. 6.23, it becomes apparent that the first mode was perturbed more by the removal of ^{238}U , than by the introduction of additional

B_4C . It is likely that the presence of B_4C in the core in the first place reduces the effect of the safety rod on k_1 . The full sensitivity profiles for Design 2 are given in Fig. F.15, in Appendix F.

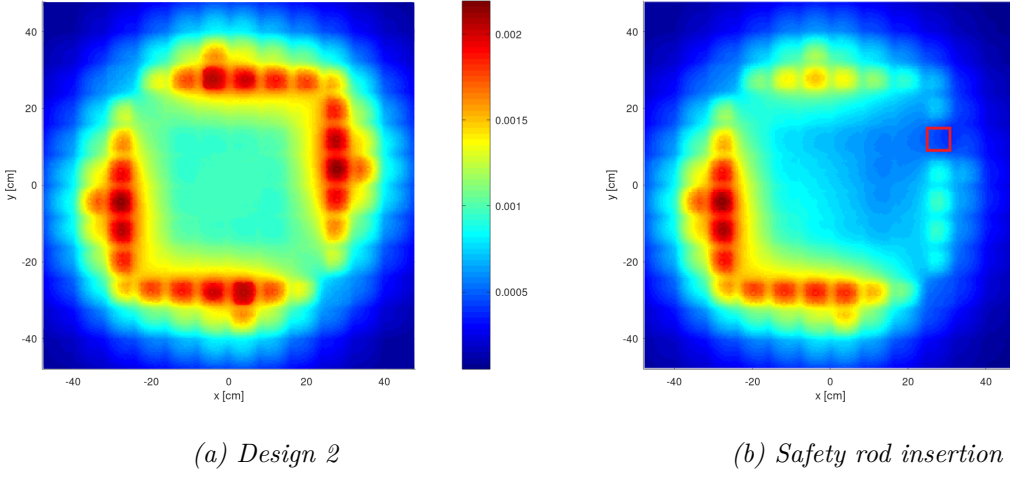


Figure 6.21: Flux maps for the Design 2 configuration, with all control elements withdrawn (left) and with one safety rod inserted (right). A red square marks the point of insertion. Th.

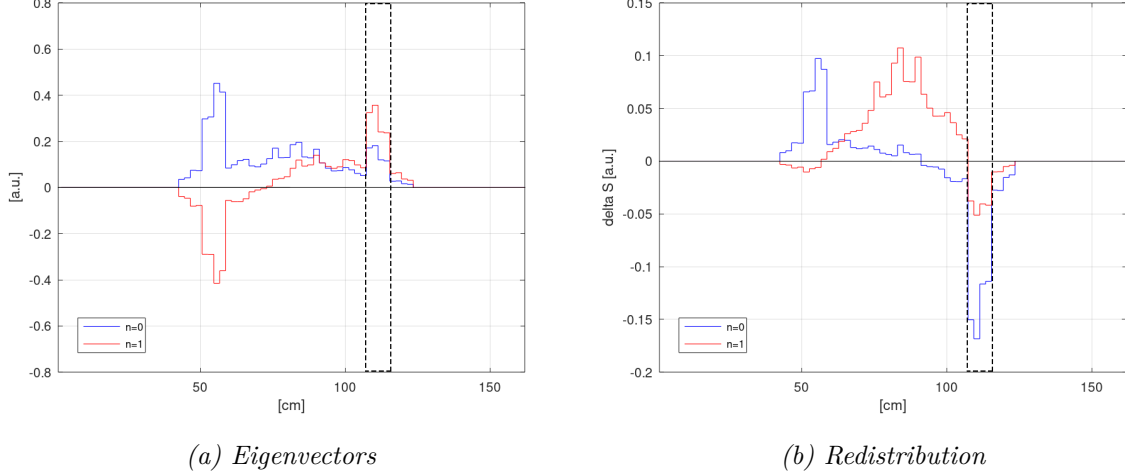


Figure 6.22: $G_{\chi_p \nu_p}$ fundamental and first mode eigenvectors and their redistribution, for the safety rod insertion in Design 2.

	Design 2	Pilot	Safety rod
k_0	1.01174	1.01090	1.00023
k_1	0.93252	0.93223	0.89863
DR	0.92	0.92	0.90
EVS	11.91	11.98	8.84
G_L	50.0%	50.6%	62.2%
G_R	50.0%	49.4%	37.8%
f_L	50.0%	50.6%	60.6%
f_R	50.0%	49.4%	39.4%

Table 6.6: k_0 , k_1 , dominance ratio (DR), eigenvalue separation (EVS), importance and flux fractions for the two azimuthal halves of the core.



Figure 6.23: S_{k_1}/S_{k_0} sensitivities ratio for Design 2.

6.3 Remarks

This chapter presents the process of creating high dominance ratio configurations in the VENUS-F core, using the methodology developed in the course of the thesis. Starting with a simple approach, based on a reduced order model of the dominance ratio, the core scattering/moderating materials are initially changed for ones that display a reduced migration area, replacing the Pb in the assemblies with graphite and finally polyethylene. These changes increased the dominance ratio significantly, but also came with large amounts of positive reactivity as a result of the increased neutron thermalization in the core. Drawing inspiration by the design of ZEPHYR, two designs were produced, that featured a central fast zone screened by a ring of absorber assemblies, an intermediate zone with natural uranium blocks and an outside thermal zone. Design 1 was kept at as a full 96 assembly core, exhibiting the highest dominance ratio, but requiring further reduction of its reactivity. Design 2 features a square core of reduced size that eliminates the reactivity problem, while at the same time maintaining a high dominance ratio. After this point, Design 2 was studied further, being subjected to perturbations by the use of a pilot rod in the first scenario and a safety rod follower in the second, the latter generating a significant tilt in the source distribution of the system and an extensive redistribution of the first mode eigenvector. Sensitivity analysis allows to observe which isotopes affect the geometry more, which can prove useful in experiment design. At the same time, this chapter showcases the use of Kobayashi's model in ERANOS to study the radial, azimuthal and arbitrary 3D coupling behavior of the VENUS-F core.

Chapter 7

Conclusions

The aim of this thesis was to develop a methodology of analyzing and producing high dominance ratio configurations. This was achieved by understanding the issues and motivations for this work, presented in Chapter 1, gathering existing knowledge and approaches in Chapters 2 and 3, followed by a three part process, itself illustrated in the work portion of the thesis, in Chapters 4,5 and 6.

Analysis of the ZEPHYR coupled core

The first part was dedicated to developing an efficient workflow aimed at analyzing existing reactor designs using multipoint kinetics approaches. The geometry of choice is based on the fast-thermal coupled reactor concept that was developed through the ZEPHYR program of CEA. The system is analyzed first using the Transient Fission Matrix model, running on the Serpent 2 Monte Carlo code, which currently implements one-dimensional region discretization. The current 1D implementation, while it introduces limitations, can be used to extract useful data, if a correct discretization is selected. This enables the study of the kinetic behavior of the system via the coupling, pointing out the regions that affect the system the most in terms of importance and importance change, via the fundamental and first mode source distribution modes. Calculating the eigenvalues of the system allows the determination of its dominance ratio and eigenvalue separation. At the same time, the system response to perturbations using reactivity devices is investigated. To remain within the computational resources available for custom calculation schemes, Kobayashi's multipoint kinetics approach was used in the ECCO/ERANOS deterministic code, for XYZ geometries. This enabled a full, three-dimensional analysis of the system, that allows to observe the coupling between arbitrarily selected regions. Depending on the discretization scheme, one can access both azimuthal/axial and radial harmonics,

getting different information than what was possible via a one-dimensional analysis.

Coupled fuel assemblies benchmark

The second part focused on investigating how the kinetic characteristics and coupling behavior of a basic, but realistic coupled system, behave with respect to both geometry and material changes. The analysis included a partial change in the fuel material of the system, with UOX fuel being replaced with less reactive MOX in one of the two assemblies, whereupon the differences in the coupling were noted and explained. The UOX assembly dictated the overall behavior of the system, both due to its higher reactivity (and thus its larger neutron production, leading to higher coupling coefficients towards the less reactive part of the system) and due to the higher ^{238}U content, whose increased delayed neutron production had an effect on the region-wise and coupled delayed neutron fraction terms. The differently reactive parts also helped to illustrate how higher source mode distributions respond to asymmetries in the system. The partial and full introduction of control rods in one of the two assemblies served to illustrate how the source distribution is affected by reactivity devices and helped to further establish a pattern of the first mode eigenvector's zero being shifted towards the parts of the system that displayed the highest importance, effectively indicating that the x axis intersection point follows the system's center of importance. Lastly, the effect of diluting boron to the moderator was studied, finding that added boron increases the dominance ratio in a linear fashion, due to the overall increase in the macroscopic absorption cross section of the system. At the same time, it was shown that for simple geometries that are symmetrical with respect to the discretization axis used for dominance ratio calculations, the latter can also be performed by directly calculating the first flux harmonic in ERANOS. The work done in this chapter led to the production of a stylized benchmark that includes and compares two different multipoint kinetics analysis methods and can be used as a basis for the validation of relevant future calculation schemes.

Producing high dominance ratio configurations in the VENUS-F core

The third part, taking into account the analysis of the dominance ratio behavior given in Chapter 3, aimed at applying the knowledge and experience gained thus far, towards developing high dominance ratio configurations in an existing system. In the wake of the decision of CEA to postpone the ZEPHYR reactor, a potential collaboration between CEA and SCK CEN made the VENUS-F zero power reactor a natural choice for demonstrating the above. It is a versatile facility that can accommodate a number of setups and high dominance ratio configurations and as such can potentially be used to achieve a

part of the experimental program's goals. This real world application was an important part of the thesis process and served as a proof of concept of the methodology developed here. Prioritizing the active core size and starting with 96 fuel assemblies, the problem was initially treated as a fixed geometry approach, whereupon changes in the materials of the system were used to affect the dominance ratio. The main objective remained to increase the apparent size of the core, with respect to the migration area. Thus, a shift towards a more thermal core was considered. While best results were achieved with the use of hydrogen-rich polyethylene moderator, the excess reactivity generated as a result of the thermalization process necessitated a reduction of the core size, to help keep reactivity in check. In the end, the process managed to produce configurations with a higher dominance ratio than the original design of the ZEPHYR coupled core. Additionally, the primary candidate design was perturbed by a pilot rod and a safety rod follower, with the latter scenario generating a significant flux tilt, indicating that the geometry can successfully be used to exhibit large scale spatial effects while ensuring a critical behavior. This chapter also introduces sensitivity analyses for the initial and final core configurations, providing a useful tool for potential experiment design and further optimization.

Future prospects and suggestions

The topic of the thesis can be expanded in several ways. It is of great interest to calculate the dominance ratio and harmonics sensitivity to nuclear data. While this is achieved partially in this thesis, the method is limited in its application, using the ability of the ERANOS code to calculate the first harmonic flux for symmetrical geometries. For the general case, the ability to directly compute harmonic fluxes for general geometries or leverage other workarounds is needed. Another way to approach this is by computing the sensitivities of the coupling coefficients, since they can be used to access higher modes. Nagaya and Kobayashi show [72] how the coupling coefficients can be directly perturbed with respect to the absorption and fission operators and this can be a starting point.

There have been investigations that connect the dominance ratio or eigenvalue separation to characteristics and the propagation of neutron noise in a system [1], via the shape and amplitude of the harmonics. The cited work relates the results to oscillation behavior in BWR cores. It would be interesting for the approach presented in this thesis, to be expanded as to include elements related to this type of dynamic analysis, with an emphasis on detector space-time response. This can allow the study of transients, which has already been successfully demonstrated to be possible via multipoint kinetics [73] and can incorporate feedbacks as well, which is something that has been done before via the coupling of the TFM model in Serpent and OpenFOAM [13, 74].

The expression of the neutron flux via the fundamental and harmonic modes comes with limitations and might not always produce correct results. More work should be done in order to discover such limitations.

In Chapter 6, there are several modifications proposed in order to deal with the excess reactivity of Design 1, which was the geometry that achieved the highest dominance ratio in the VENUS-F core. A further optimization of the design, either by including low amounts of boron nitrate in the polyethylene, using enriched B_4C in the absorber ring or changing the design down to the fuel assembly level, can stand to improve it even further in terms of the achieved dominance ratio and deal with the excess reactivity at the same time. A great starting point would be to use the provided sensitivity profiles.

The present work should prove useful in analyzing and quantifying relevant phenomena related to high dominance ratio systems, in light water power reactors, as well as in finding ways of minimizing oscillations related to the operation of the reactor. Furthermore, suitable, small cores for experimentation can be created through representativity-based analyses, by matching the sensitivities of the large and small cores.

Taking the reduced order model of Chapter 3 as a starting point, the current process, which is currently based on the diffusion analysis of simple geometries, can perhaps either be incorporated or injected in a calculation code, whereupon the importance and source harmonics can be used to iteratively design configurations with the desired kinetic behavior. Once the kinetic profile of the starting system is known, it can be used as a baseline for future iterations, and the routine itself can choose from a predefined selection of materials, to place in certain places in the geometry. The success criterion can either be a predefined dominance ratio value, importance distribution or harmonic mode distribution. The design process can be optimized by feeding data to a deep learning algorithm, such as an artificial neural network (ANN) system that can be coupled with the solver or using a technique such as particle swarm optimization [57].

Appendix A

Dominance ratio model additional data

a=b=c (cm)	200
k_{inf}	1.16188(4)
k_{eff}	1.09698(3)
M^2 (cm 2)	79.92(62)
D (cm)	0.93353(3)
Σ_a (cm $^{-1}$)	0.01168(9)
$k_{1,0,0}/k_{0,0,0}$ (Reduced model)	0.947
$k_{1,0,0}/k_{0,0,0}$ (TFM)	0.952
$k_{1,0,0}/k_{0,0,0}$ (ERANOS)	0.956

Table A.1: Parallelepiped data and dominance ratio results.

R (cm)	185
H (cm)	400
$k_{1,0,0}/k_{0,0,0}$ (azimuthal)	0.985
$k_{0,0,1}/k_{0,0,0}$ (axial)	0.994

Table A.2: PWR geometry azimuthal and axial dominance ratio, calculated with TFM.

Appendix B

Calculation settings

Serpent 2

Particles per cycle	5×10^5
Cycles	2000
Discarded cycles	50
Library	JEFF-3.1.1

Table B.1: Serpent 2 settings.

ERANOS

ZEPHYR ZONA1 (Fig. 4.1) pin-wise geometry in ECCO/ERANOS.

```
CELL 'ZONA1_CELL' !--> 6 MOX + 2 U02NAT + 8 Na + Steel cladding + Air, small changes
COMPOSITION_ORDER 'MOX' 'AIR_MED' 'CLAD_STEEL' 'U02NAT' 'NA'
GEOMETRY DATA
SQUARE 1
5.26 RECTANGULAR LATTICE 4 REP(4,1.2775) 4 REP(4,1.2775)
3
CYLINDRICAL 3
0.60145 REGION 1 'UPU02' COMPOSITION 1 293.16
0.61160 REGION 2 'GAP' COMPOSITION 2 293.16
0.63500 REGION 3 'CLAD' COMPOSITION 3 293.16
INSIDE REGION 4 'AIR' COMPOSITION 2 293.16
CYLINDRICAL 3
0.60005 REGION 5 'U02NAT' COMPOSITION 4 293.16
0.61250 REGION 6 'GAP' COMPOSITION 2 293.16
0.63500 REGION 7 'CLAD' COMPOSITION 3 293.16
INSIDE REGION 8 'AIR' COMPOSITION 2 293.16
REGION 9 'NA' COMPOSITION 5 293.16
1 3 1 3
3 2 3 1
1 3 1 3
3 1 3 2
INSIDE REGION 10 'BUNDLE' COMPOSITION 3 293.16
WHITE
END OF GEOMETRY DATA
```

ECCO ZONA1 cell homogenization scheme.

```
ECCO
MEDIUM (MEDIUM_SET_BEFORE_ECCO)
REFERENCE_UNIT 'BIBREF'
CELL 'ZONA1_CELL' !--> fast fuel cell
EDITION (EDIT_TYPE)
'ZONA1 FUEL SUBASSEMBLY'
TEMPERATURE 1 293.16 2 293.16 3 293.16 4 293.16
           5 293.16 6 293.16 7 293.16 8 293.16
STEPS 5
STEP GEOMETRY ORIGINAL
  GROUP STRUCTURE OTHER (NGCOND)
  INPUT LIBRARY (BIB)
  ELEMENTS ALL
  FLUX SOLUTION CP P1 CONSISTENT ORDER 1
  LEAKAGE NLFACT CELL BENOIST FLUXWT MEAN
  SELF SHIELDING NODBBSH
  BSEARCH 1.0
STEP GEOMETRY ORIGINAL
  GROUP STRUCTURE FINE
  INPUT LIBRARY 'BIB1968'
  FIND_ELEMENTS_IN_LIST
    'U234'   'U235'   'U236'   'U238'
    'Np237'
    'Pu238'  'Pu239'  'Pu240'  'Pu241'  'Pu242'
    'Am241'  'Am243'
    'O16'
    'Fe54'   'Fe56'   'Fe57'   'Fe58'
    'Cr50'   'Cr52'   'Cr53'   'Cr54'
    'Ni58'   'Ni60'   'Ni61'   'Ni62'   'Ni64'
    'Mo92'   'Mo94'   'Mo95'   'Mo96'   'Mo97'   'Mo98'   'Mo100'
    'Si28'   'Si29'   'Si30'
    'Mn55'   'CO'     'H1'     'B10'    'B11'    'N14'    'V0'
    'Na23'
  FLUX SOLUTION CP P1 CONSISTENT ORDER 1
  LEAKAGE NLFACT CELL BENOIST FLUXWT MEAN
  SELF SHIELDING NODBBSH
  (CONDENSE)
  BFROM 1
STEP GEOMETRY ORIGINAL
```

```
GROUP STRUCTURE OTHER (NGCOND)
FLUX SOLUTION CP P1 CONSISTENT ORDER 1
LEAKAGE NLFACT CELL BENOIST FLUXWT MEAN
PRINT DATA FLUXES CROSS SECTIONS MICROSCOPIC VECTORS
BSEARCH 1.0
STEP HOMOGENISE
GEOMETRY HOMOGENEOUS
GROUP STRUCTURE OTHER (NGCOND)
FLUX SOLUTION FM P1 CONSISTENT ORDER 1
BFROM 3
OUTPUT LIBRARY 'Z1_FUEL' CROSS SECTIONS FLUXES
STEP GEOMETRY HOMOGENEOUS
GROUP STRUCTURE OTHER (NGCOND)
FLUX SOLUTION FM P1 CONSISTENT ORDER 1
CONDENSE 1 1
PRINT DATA FLUXES CROSS SECTIONS MICROSCOPIC VECTORS
BFROM 3
ENDSTEPS ;
```

For simpler geometries and/or calculations with 6 or fewer coupling zones, the following settings were used:

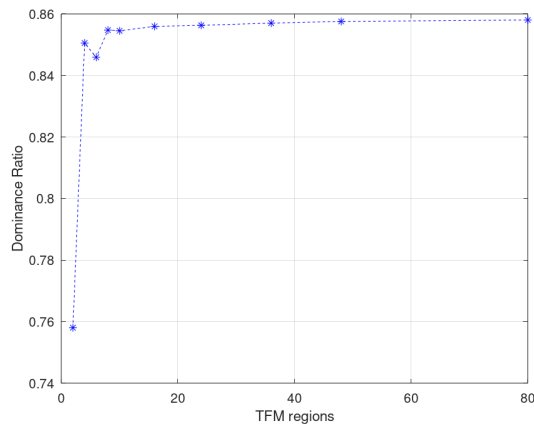
```
->CALC_PARAM
    OUTER_ITERATION
        MAXIMUM_NUMBER 5
        INTEGRAL_CONVERGENCE 1.E-06
        LOCAL_CONVERGENCE 1.E-05
        TCHEBYCHEFF 4
    INNER_ITERATION
        MAXIMUM_NUMBER 200
        LOCAL_CONVERGENCE 1.E-07
    UP_SCATTERING_ITERATION
        MAXIMUM_NUMBER 4
        LOCAL_CONVERGENCE 1.E-05 ;
```

For geometries with finer discretization for the flux calculation and/or calculations with 6 - 12 coupling zones, the following settings were used:

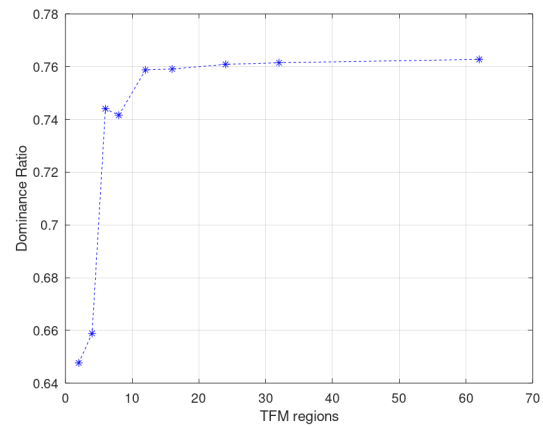
```
->CALC_PARAM
    OUTER_ITERATION
        MAXIMUM_NUMBER 5
        INTEGRAL_CONVERGENCE 1.E-06
        LOCAL_CONVERGENCE 1.E-05
        TCHEBYCHEFF 4
    INNER_ITERATION
        MAXIMUM_NUMBER 40
        LOCAL_CONVERGENCE 1.E-05
    UP_SCATTERING_ITERATION
        MAXIMUM_NUMBER 2
        LOCAL_CONVERGENCE 1.E-05 ;
```

Appendix C

Convergence of $\frac{k_{1,0,0}}{k_{0,0,0}}$ in the TFM model



(a) ZEPHYR traverse



(b) UOX-UOX 0cm

Figure C.1: Convergence of $\frac{k_{1,0,0}}{k_{0,0,0}}$, versus number of regions in the TFM model.

Appendix D

ZEPHYR coupled core additional data

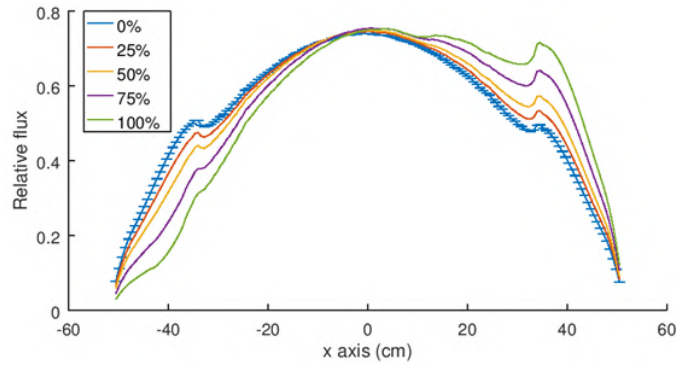


Figure D.1: Total forward flux for the square ZEPHYR traverse, for all rod insertion levels, calculated in Serpent 2.

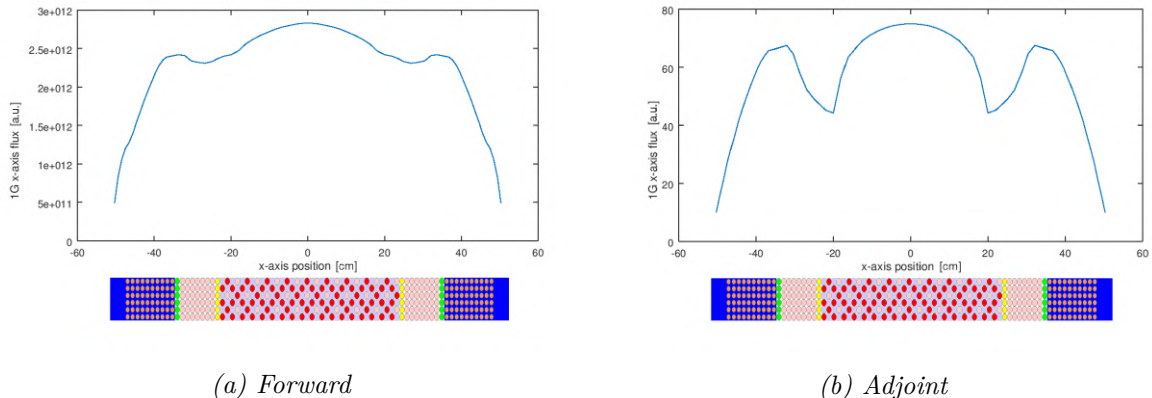


Figure D.2: Total fundamental flux profiles for the square ZEPHYR traverse, calculated in ERANOS.

$$k_{ij} = \begin{pmatrix} 0.81262 & 0.60856 & 0.47629 & 0.20879 & 0.06957 & 0.04979 & 0.04689 & 0.03850 \\ 0.11782 & 0.26513 & 0.20573 & 0.10146 & 0.03537 & 0.02289 & 0.01856 & 0.00753 \\ 0.01527 & 0.05580 & 0.08181 & 0.04201 & 0.00976 & 0.00594 & 0.00369 & 0.00118 \\ 0.01451 & 0.05385 & 0.10258 & 0.45771 & 0.09713 & 0.03238 & 0.01706 & 0.00455 \\ 0.00455 & 0.01706 & 0.03238 & 0.09713 & 0.45771 & 0.10258 & 0.05385 & 0.01451 \\ 0.00118 & 0.00369 & 0.00594 & 0.00976 & 0.04201 & 0.08181 & 0.05580 & 0.01527 \\ 0.00753 & 0.01856 & 0.02289 & 0.03537 & 0.10146 & 0.20573 & 0.26513 & 0.11782 \\ 0.03850 & 0.04689 & 0.04979 & 0.06957 & 0.20879 & 0.47629 & 0.60856 & 0.81262 \end{pmatrix}$$

Table D.1: k_{ij} coupling coefficients matrix for the full square geometry.

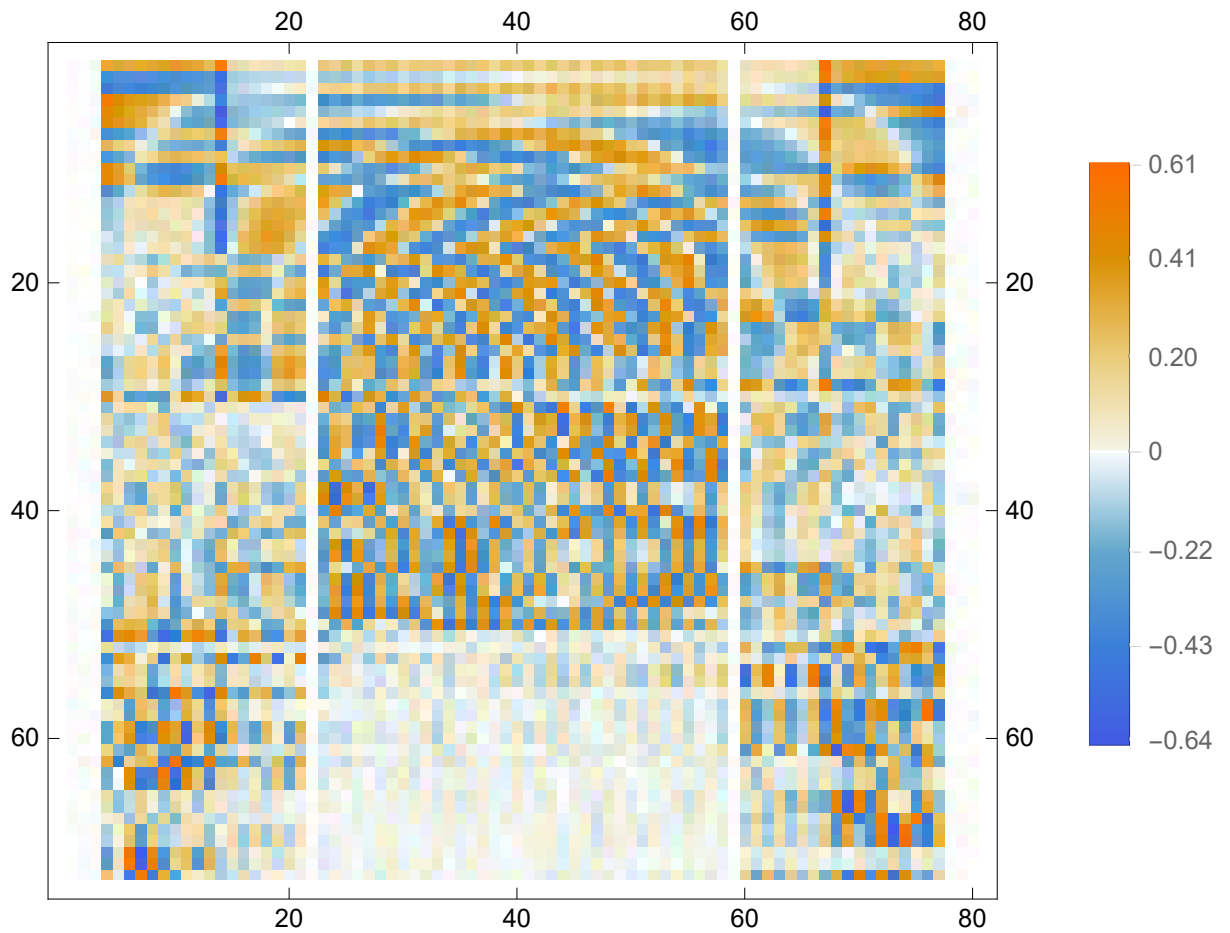


Figure D.3: All accessed $G_{\chi_p \nu_p}$ eigenvectors. Rows indicate the modes and columns indicate the coupling regions.

Appendix E

Coupled assemblies benchmark additional data

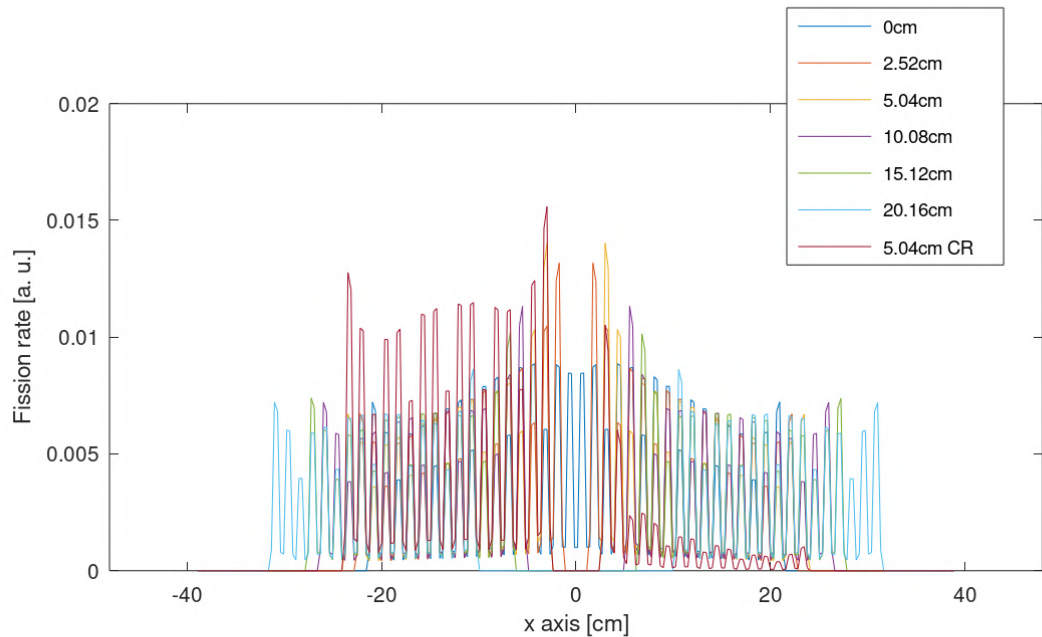


Figure E.1: Normalized fission reaction rate for the UOX-UOX geometry.

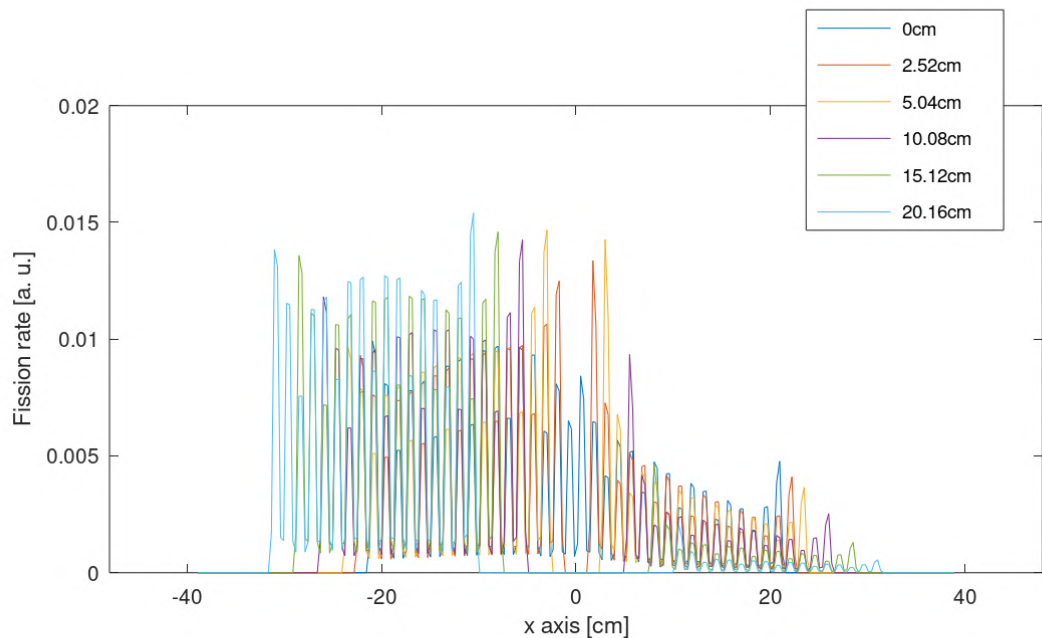


Figure E.2: Normalized fission reaction rate for the UOX-MOX geometry.

	Fuel pin		Empty guide tube		Control rod		Instrumentation tube	
r1 (cm)	0.39218	Fuel	0.56134	Water	0.37338	B ₄ C	0.43688	Air
r2 (cm)	0.40005	He	0.60198	Zircaloy	0.38608	He	0.48387	Zircaloy
r3 (cm)	0.45720	Zircaloy	-	-	0.48387	Steel	0.56134	Water
r4 (cm)	-	-	-	-	0.56134	Water	0.60198	Zircaloy
r5 (cm)	-	-	-	-	0.60198	Zircaloy	-	-
Reflector	Light water		Light water		Light water		Light water	

Table E.1: Radial design of the different types of pins used in the geometry. Based on the BEAVRS benchmark.

Isotope	Atomic density ($10^{24}cm^{-3}$)
U234	7.736440E-06
U235	8.608110E-04
U238	2.205240E-02
O12	4.587230E-02
Np237	1.000000E-12

Table E.2: UOX fuel isotopic composition.

Isotope	Atomic density ($10^{24}cm^{-3}$)
U234	2.77320E-06
U235	5.18830E-05
U236	6.92800E-07
U238	2.11110E-02
Pu238	1.92760E-05
Pu239	9.11410E-04
Pu240	3.85170E-04
Pu241	6.98590E-05
Pu242	8.31300E-05
Am241	1.01110E-04
O12	4.59410E-02
Np237	1.74010E-06

Table E.3: MOX fuel isotopic composition.

Isotope	Atomic density ($10^{24}cm^{-3}$)
B10	9.5910E-02
B11	9.4801E-03
C	2.7853E-02

Table E.4: B_4C control rod material isotopic composition.

Isotope	Atomic density (10^{24}cm^{-3})	Isotope	Atomic density (10^{24}cm^{-3})
Zr90	2.199970E-02	Cr52	6.532980E-05
Zr91	4.797600E-03	Cr53	7.407870E-06
Zr92	7.333240E-03	Cr54	1.843980E-06
Zr94	7.431580E-03	C	4.844710E-05
Zr96	1.197260E-03	Hf174	1.889920E-09
Sn112	4.527330E-06	Hf176	6.073420E-08
Sn114	3.033780E-06	Hf177	2.170610E-07
Sn115	1.586900E-06	Hf178	3.184520E-07
Sn116	6.786330E-05	Hf179	1.589990E-07
Sn117	3.584520E-05	Hf180	4.094840E-07
Sn118	1.130430E-04	N14	6.273680E-06
Sn119	4.004590E-05	N15	2.304600E-08
Sn120	1.521090E-04	Ti46	9.179440E-08
Sn122	2.160980E-05	Ti47	8.278190E-08
Sn124	2.702400E-05	Ti48	8.202530E-07
Fe54	8.565500E-06	Ti49	6.019490E-08
Fe56	1.344600E-04	Ti50	5.763580E-08
Fe57	3.105270E-06	Al27	4.506170E-06
Fe58	4.132540E-07	O16	3.154970E-04
Cr50	3.387770E-06	H1	3.153850E-05

Table E.5: Zircaloy cladding isotopic composition.

Isotope	Atomic density ($10^{24}cm^{-3}$)	Isotope	Atomic density ($10^{24}cm^{-3}$)
Fe54	3.387E-03	Mo94	4.558E-05
Fe56	5.316E-02	Mo95	7.844E-05
Fe57	1.228E-03	Mo96	8.218E-05
Fe58	1.634E-04	Mo97	4.705E-05
Cr50	7.113E-04	Mo98	1.189E-04
Cr52	1.372E-02	Mo100	4.745E-05
Cr53	1.555E-03	Si28	7.766E-04
Cr54	3.872E-04	Si29	3.932E-05
Ni58	6.032E-03	Si30	2.610E-05
Ni60	2.323E-03	Mn55	8.605E-04
Ni61	1.010E-04	P31	3.434E-05
Ni62	3.220E-04	C	5.904E-05
Ni62	8.201E-05	S32	2.099E-05
Mo92	7.312E-05	S34	9.485E-07

Table E.6: Steel isotopic composition. Used in the guide tubes and the structure base.

In Serpent 2, the water in the tank was specified as a light water moderator in the code, using the `therm lwtr lwj3.11t` line and adding the `moder lwtr 1001` string after defining the water composition.

The ${}^4\text{He}$ in the gap between the fuel and the cladding material has an atomic density of 1.0E-10 in units of $10^{24}cm^{-3}$.

Appendix F

VENUS-F additional data

For all graphs containing flux and fission rate results were generated in Serpent 2. The relative error is on the order of 0.001%. All fluxes and rates are normalized to one source neutron.

F.1 CR0* configuration results

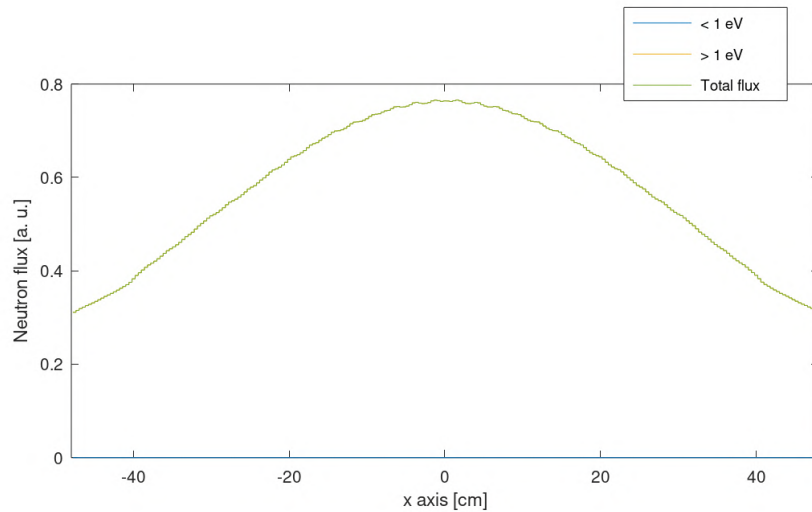


Figure F.1: Flux profiles for the VENUS-F core in the CR0* configuration. The thermal component of the flux is very small and not visible at this scale.

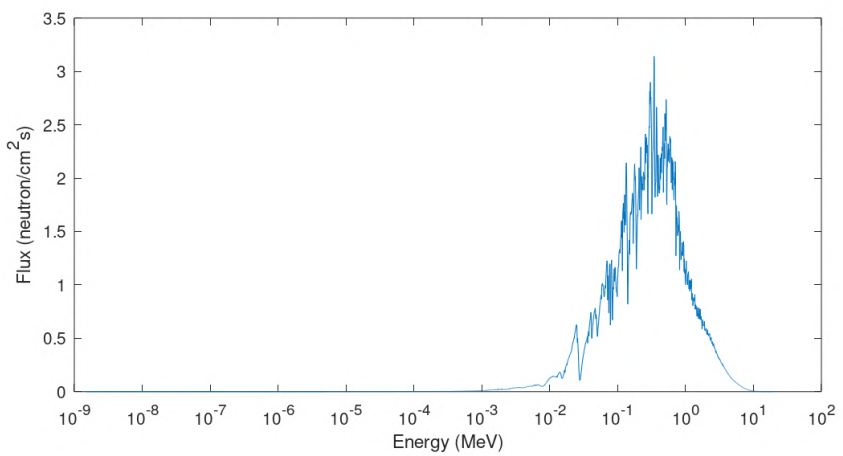


Figure F.2: Flux spectrum for the 4 central assemblies for the VENUS-F core in the CR0* configuration.

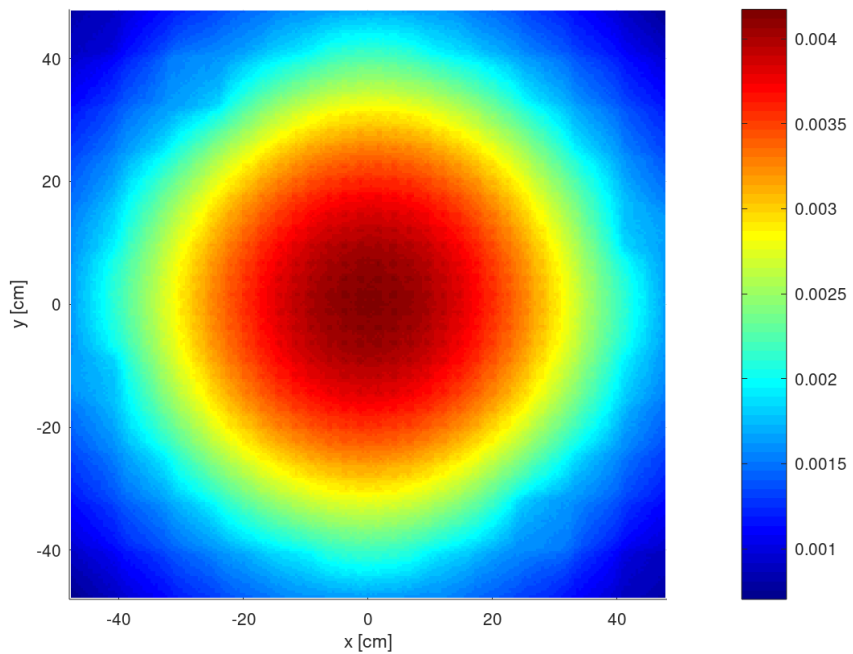


Figure F.3: Total flux map for the VENUS-F core in the CR0* configuration.

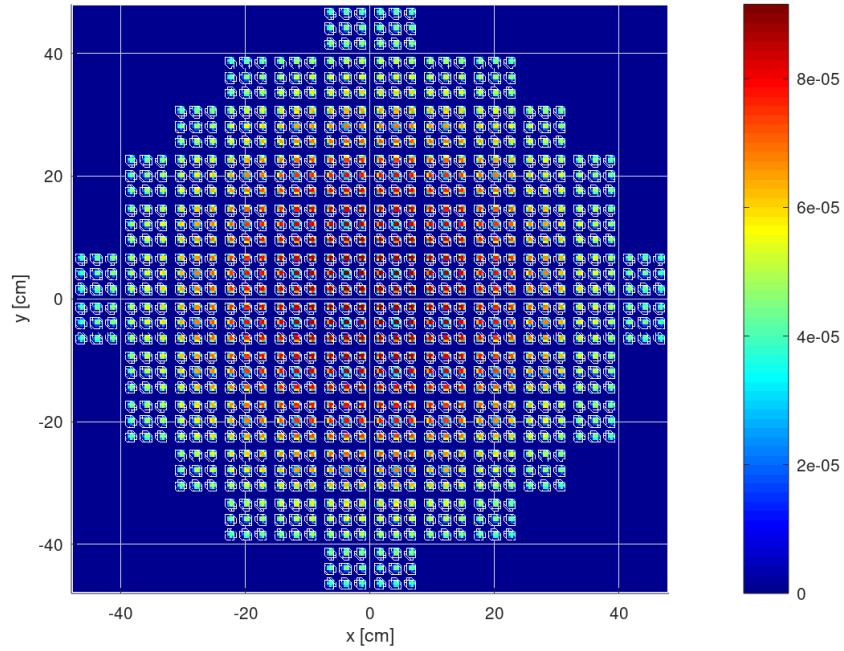


Figure F.4: Fission rate map for the VENUS-F core in the CR0* configuration.

$$k_{ij}^{CR0*} = \begin{pmatrix} 0.13786 & 0.06615 & 0.03479 & 0.01819 & 0.00972 & 0.00486 & 0.00251 & 0.00138 & 0.00080 & 0.00047 & 0.00030 & 0.00021 \\ 0.19853 & 0.23957 & 0.15466 & 0.08301 & 0.04564 & 0.02318 & 0.01199 & 0.00648 & 0.00365 & 0.00211 & 0.00131 & 0.00087 \\ 0.13381 & 0.20300 & 0.26394 & 0.17395 & 0.09907 & 0.05179 & 0.02724 & 0.01469 & 0.00812 & 0.00455 & 0.00273 & 0.00178 \\ 0.08434 & 0.13047 & 0.21032 & 0.27604 & 0.19581 & 0.10763 & 0.05900 & 0.03251 & 0.01785 & 0.00995 & 0.00583 & 0.00371 \\ 0.04799 & 0.07574 & 0.12674 & 0.21798 & 0.28023 & 0.18757 & 0.10666 & 0.06137 & 0.03447 & 0.01874 & 0.01074 & 0.00658 \\ 0.02821 & 0.04523 & 0.07399 & 0.13094 & 0.21124 & 0.28745 & 0.20542 & 0.12244 & 0.07133 & 0.04064 & 0.02357 & 0.01457 \\ 0.01455 & 0.02388 & 0.04085 & 0.07143 & 0.12197 & 0.20534 & 0.28731 & 0.21129 & 0.13129 & 0.07420 & 0.04551 & 0.02849 \\ 0.00657 & 0.01073 & 0.01873 & 0.03458 & 0.06141 & 0.10642 & 0.18781 & 0.27980 & 0.21804 & 0.12692 & 0.07515 & 0.04877 \\ 0.00365 & 0.00573 & 0.00985 & 0.01794 & 0.03245 & 0.05891 & 0.10754 & 0.19585 & 0.27616 & 0.21122 & 0.13079 & 0.08415 \\ 0.00180 & 0.00281 & 0.00450 & 0.00806 & 0.01468 & 0.02733 & 0.05190 & 0.09930 & 0.17407 & 0.26408 & 0.20313 & 0.13401 \\ 0.00088 & 0.00131 & 0.00214 & 0.00368 & 0.00645 & 0.01202 & 0.02325 & 0.04559 & 0.08321 & 0.15411 & 0.23734 & 0.19712 \\ 0.00021 & 0.00030 & 0.00047 & 0.00080 & 0.00139 & 0.00251 & 0.00488 & 0.00965 & 0.01829 & 0.03462 & 0.06632 & 0.13883 \end{pmatrix}$$

Table F.1: Azimuthal k_{ij} coupling coefficients for the VENUS-F core in the CR0* configuration.

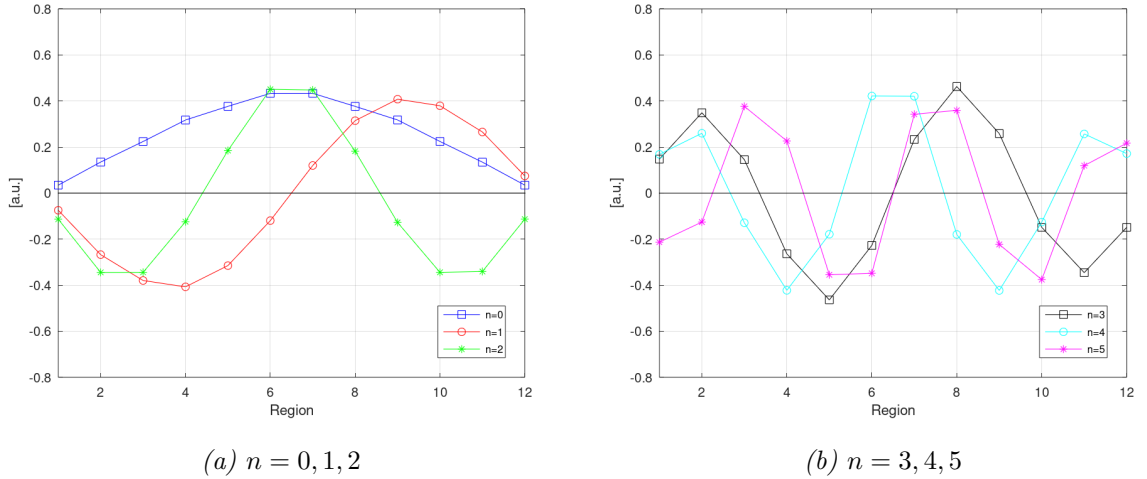


Figure F.5: First six flux modes for the VENUS-F core in the CR0* configuration.

Region	1	2	3	4	5	6
ℓ_i (μs)	1.1739	0.9398	0.7510	0.6957	0.6185	0.6394
β_i (pcm)	739.58	742.26	744.35	745.95	747.11	746.67
Region	7	8	9	10	11	12
ℓ_i (μs)	0.6575	0.7040	0.6329	0.8502	0.9810	1.2021
β_i (pcm)	746.20	746.49	746.32	743.60	740.87	738.55

Table F.2: ℓ_i and β_i for the VENUS-F core in the CR0* configuration.

F.2 Design 1 and Design 2 configurations results

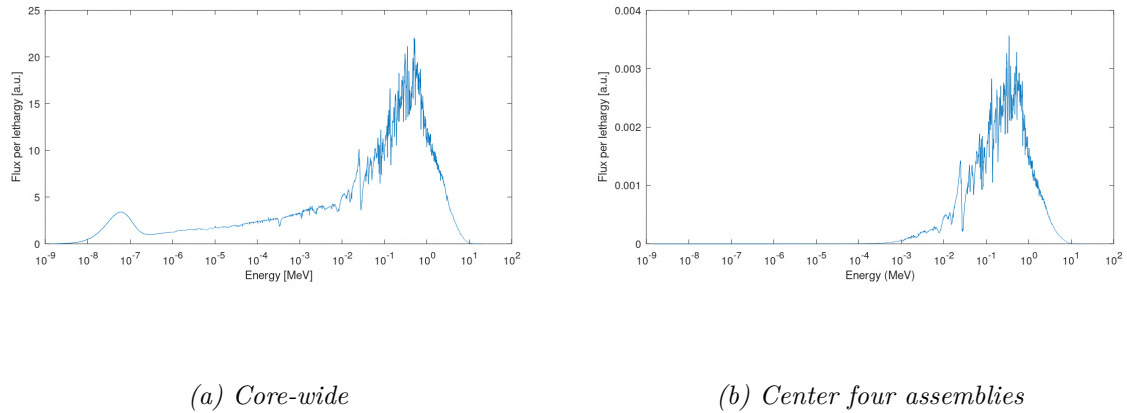


Figure F.6: Flux spectra for Design 1.

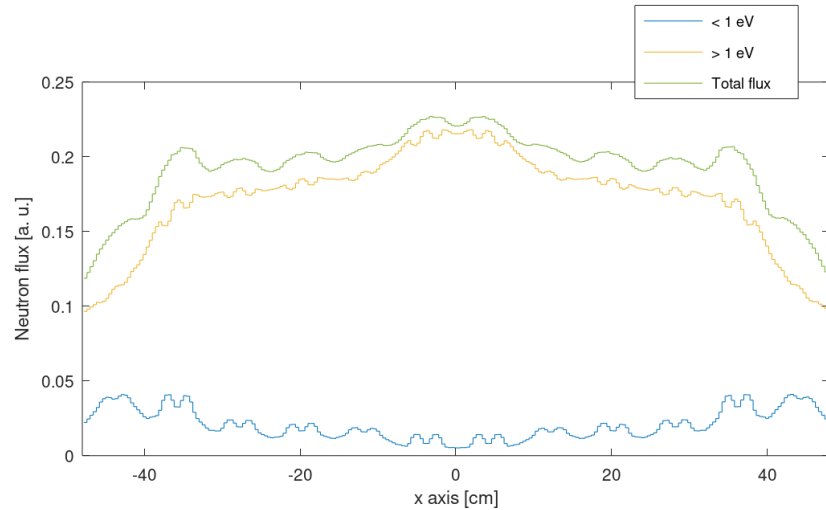


Figure F.7: Flux profiles for Design 1.

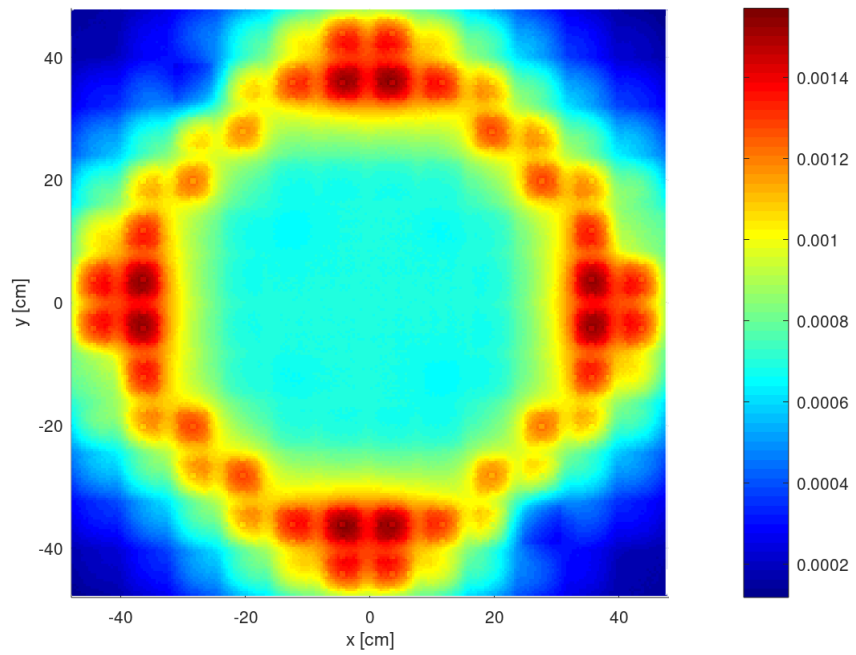


Figure F.8: Total flux map for Design 1.

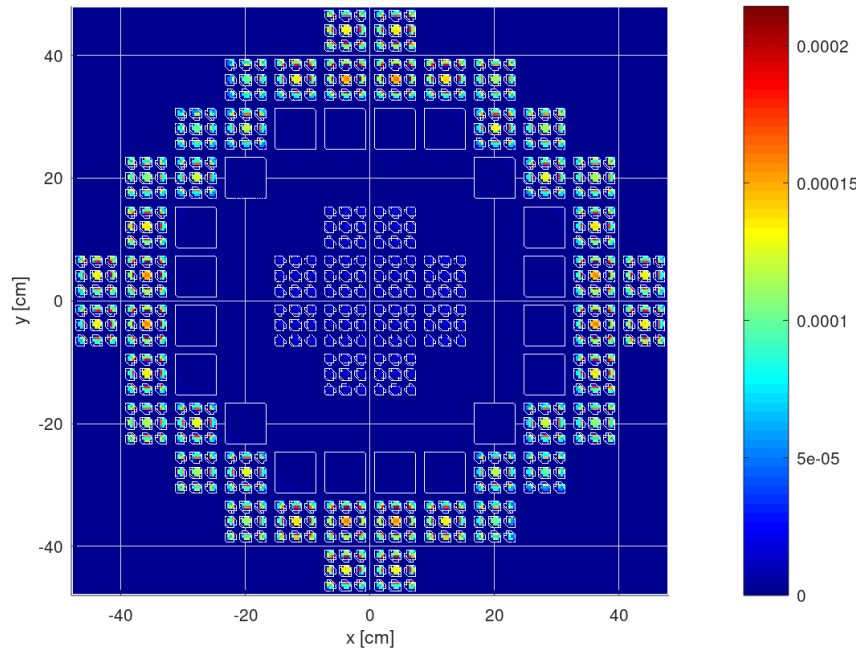


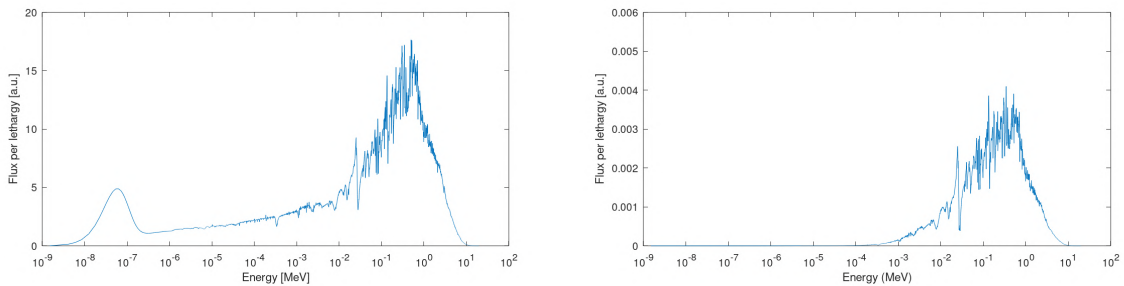
Figure F.9: Fission rate map for Design 1.

$$k_{ij}^{Design\ 1} = \begin{pmatrix} 0.42814 & 0.17045 & 0.03598 & 0.00786 & 0.00613 & 0.00192 & 0.00124 & 0.00090 & 0.00041 & 0.00033 & 0.00019 & 0.00011 \\ 0.49182 & 0.63353 & 0.28671 & 0.06443 & 0.04247 & 0.01263 & 0.00822 & 0.00607 & 0.00257 & 0.00210 & 0.00118 & 0.00062 \\ 0.06777 & 0.19641 & 0.43462 & 0.20609 & 0.07356 & 0.02239 & 0.01145 & 0.00795 & 0.00319 & 0.00232 & 0.00123 & 0.00063 \\ 0.01167 & 0.03630 & 0.18799 & 0.43325 & 0.22289 & 0.07976 & 0.02851 & 0.01551 & 0.00570 & 0.00318 & 0.00152 & 0.00076 \\ 0.00903 & 0.02118 & 0.05394 & 0.16638 & 0.30440 & 0.16058 & 0.05890 & 0.03061 & 0.01078 & 0.00654 & 0.00325 & 0.00156 \\ 0.00438 & 0.00965 & 0.02653 & 0.09133 & 0.25023 & 0.44395 & 0.24939 & 0.09988 & 0.03068 & 0.01170 & 0.00493 & 0.00233 \\ 0.00233 & 0.00493 & 0.01168 & 0.03062 & 0.10008 & 0.24913 & 0.44439 & 0.25074 & 0.09152 & 0.02647 & 0.00966 & 0.00438 \\ 0.00156 & 0.00326 & 0.00653 & 0.01079 & 0.03054 & 0.05896 & 0.16042 & 0.30380 & 0.16671 & 0.05399 & 0.02120 & 0.00906 \\ 0.00076 & 0.00152 & 0.00318 & 0.00570 & 0.01554 & 0.02854 & 0.07961 & 0.22311 & 0.43239 & 0.18780 & 0.03627 & 0.01165 \\ 0.00063 & 0.00123 & 0.00232 & 0.00319 & 0.00793 & 0.01144 & 0.02241 & 0.07371 & 0.20588 & 0.43462 & 0.19621 & 0.06764 \\ 0.00062 & 0.00118 & 0.00210 & 0.00257 & 0.00606 & 0.00821 & 0.01261 & 0.04247 & 0.06450 & 0.28614 & 0.63417 & 0.49084 \\ 0.00011 & 0.00019 & 0.00033 & 0.00041 & 0.00090 & 0.00124 & 0.00192 & 0.00612 & 0.00787 & 0.03590 & 0.17028 & 0.42772 \end{pmatrix}$$

Table F.3: Azimuthal k_{ij} coupling coefficients for Design 1.

Region	1	2	3	4	5	6
ℓ_i (μs)	1.5	1.1	1.0	1.0	0.9	1.0
β_i (pcm)	800	807	749	766	714	792
Region	7	8	9	10	11	12
ℓ_i (μs)	1.0	0.84	1.0	1.0	1.1	1.4
β_i (pcm)	782	730	767	751	808	800

Table F.4: ℓ_i and β_i for Design 1.



(a) Core-wide

(b) Center four assemblies

Figure F.10: Flux spectra for Design 2.

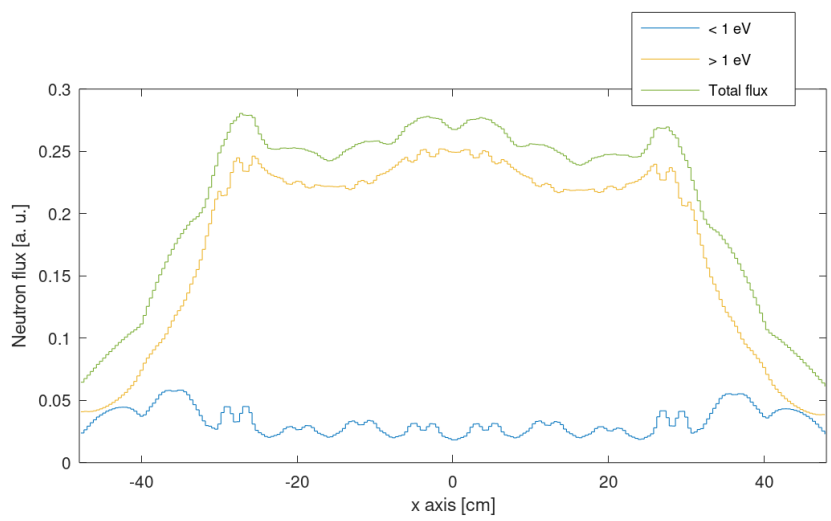


Figure F.11: Flux profiles for Design 2.

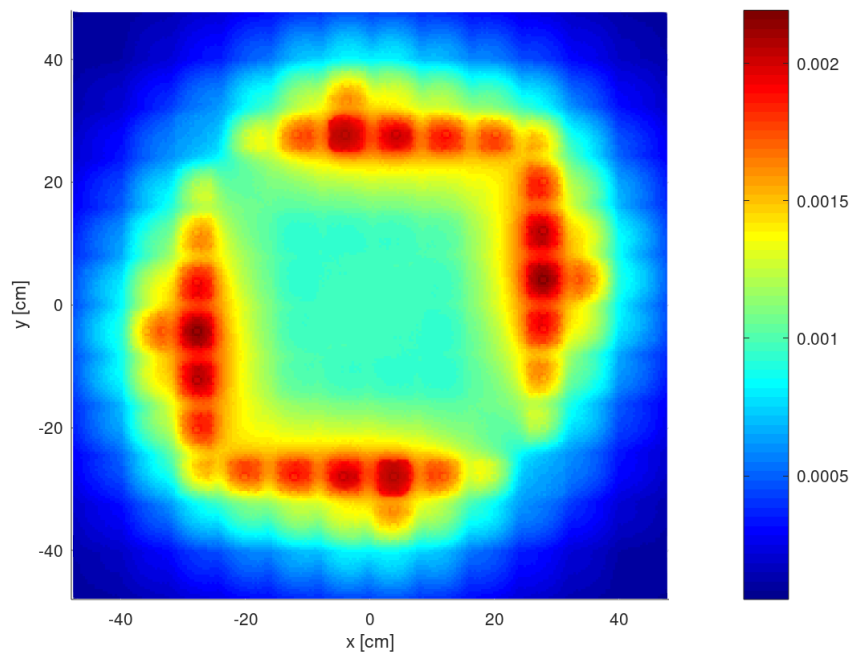


Figure F.12: Total flux map for Design 2.

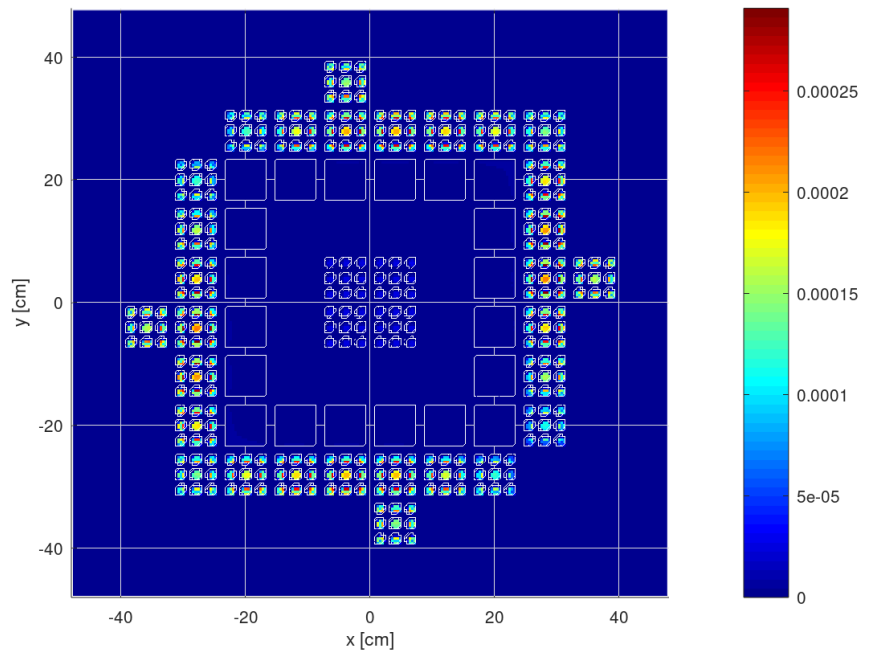


Figure F.13: Fission rate map for Design 2.

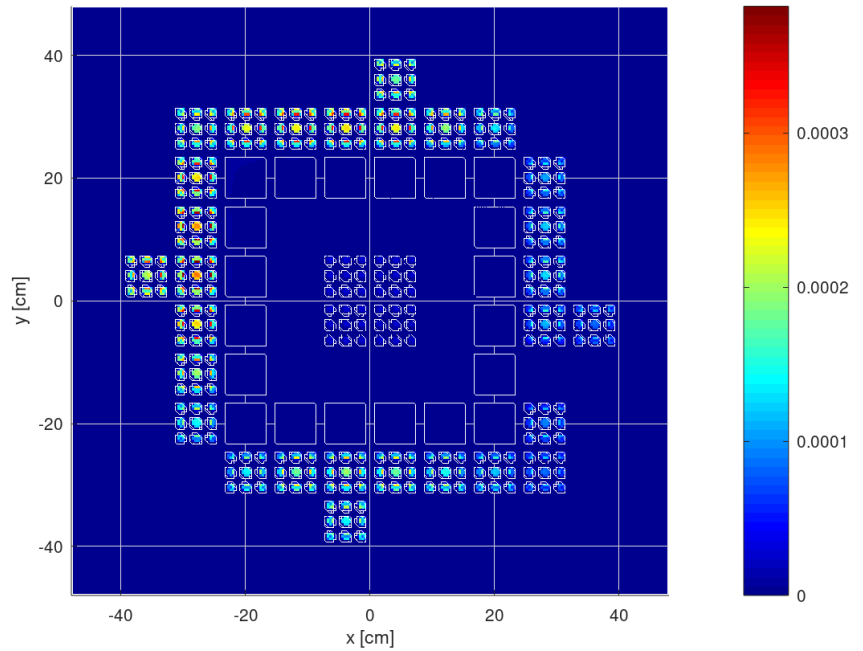


Figure F.14: Fission rate map for safety rod insertion in the Design 2 configuration.

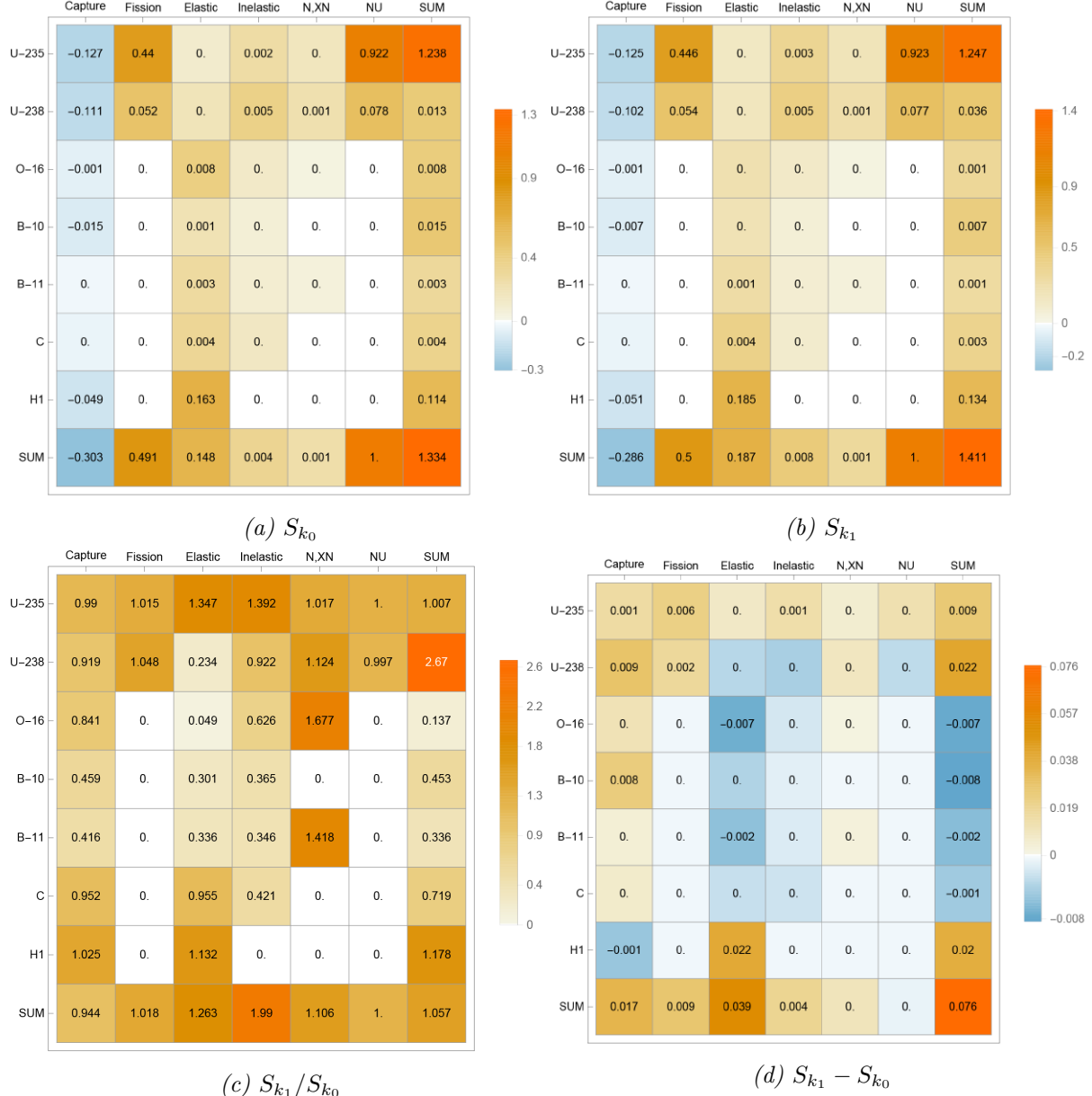


Figure F.15: Nuclear data sensitivity profiles for Design 2.

$$k_{ij}^{Design\ 2} = \begin{pmatrix} 0.32904 & 0.10665 & 0.02792 & 0.00775 & 0.00547 & 0.00300 & 0.00106 & 0.00065 & 0.00033 & 0.00016 \\ 0.52280 & 0.70968 & 0.39549 & 0.15535 & 0.07708 & 0.04441 & 0.01613 & 0.00922 & 0.00441 & 0.00198 \\ 0.03830 & 0.12588 & 0.29596 & 0.21470 & 0.07795 & 0.03562 & 0.01495 & 0.00657 & 0.00265 & 0.00111 \\ 0.00344 & 0.01282 & 0.05499 & 0.12659 & 0.04829 & 0.02493 & 0.00963 & 0.00365 & 0.00119 & 0.00047 \\ 0.00645 & 0.01758 & 0.05406 & 0.13394 & 0.28932 & 0.10131 & 0.07271 & 0.02918 & 0.01050 & 0.00389 \\ 0.00388 & 0.01052 & 0.02922 & 0.07264 & 0.10142 & 0.28990 & 0.13367 & 0.05406 & 0.01762 & 0.00644 \\ 0.00047 & 0.00118 & 0.00365 & 0.00965 & 0.02496 & 0.04819 & 0.12672 & 0.05505 & 0.01283 & 0.00344 \\ 0.00111 & 0.00266 & 0.00657 & 0.01499 & 0.03565 & 0.07794 & 0.21470 & 0.29655 & 0.12575 & 0.03826 \\ 0.00198 & 0.00442 & 0.00923 & 0.01613 & 0.04441 & 0.07693 & 0.15551 & 0.39549 & 0.70825 & 0.52280 \\ 0.00016 & 0.00033 & 0.00065 & 0.00106 & 0.00299 & 0.00548 & 0.00774 & 0.02798 & 0.10665 & 0.32937 \end{pmatrix}$$

Table F.5: Azimuthal k_{ij} coupling coefficients for Design 2.

Region	1	2	3	4	5
ℓ_i (μs)	2.1	1.4	1.3	2.8	2.2
β_i (pcm)	796	850	684	533	681
Region	6	7	8	9	10
ℓ_i (μs)	2.2	2.8	1.4	1.4	2.1
β_i (pcm)	683	533	686	850	796

Table F.6: ℓ_i and β_i for Design 2.

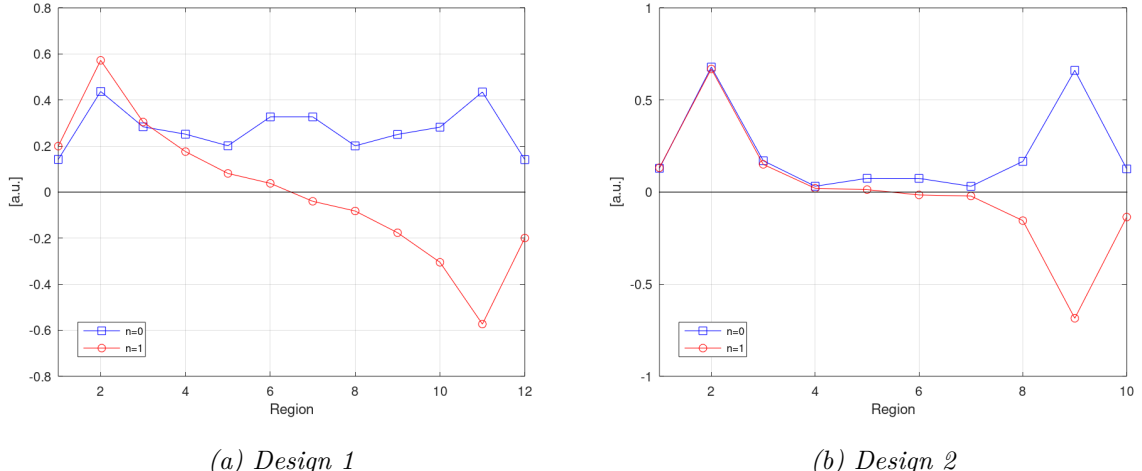


Figure F.16: Fundamental and first mode eigenvectors as calculated in ERANOS, for Design 1 and Design 2.

F.3 Résumé en français

F.3.1 Contexte et motivation

Dans le domaine de la physique des réacteurs nucléaires, les installations expérimentales jouent un rôle important. En fonction de leur objectif, elles peuvent comporter des cœurs spécialisés, centrés sur une certaine classe d'expériences, ou elles peuvent être conçues avec la polyvalence à l'esprit, permettant un large éventail d'applications. Les maquettes critiques appartiennent souvent à la deuxième catégorie, visant à fournir divers environnements de test. Parallèlement aux analyses numériques, ces installations sont utilisées pour à la fois améliorer notre compréhension de la nature multiphasique complexe des phénomènes des réacteurs nucléaires et soutenir l'industrie nucléaire.

Dans le cadre de ce dernier point, les réacteurs expérimentaux sont souvent utilisés pour simuler le comportement des grands cœurs, permettant l'étude de phénomènes liés au fonctionnement des réacteurs de puissance. Cependant, il y a des limites en termes de représentativité des grands cœurs avec des maquettes critiques. Une différence particulière entre elles et les grands cœurs est leur séparation des valeurs propres (SVP). C'est une grandeur qui décrit l'ampleur de l'effet des harmoniques de flux sur le flux neutronique et le couplage des différentes parties d'un système. Les harmoniques de flux sont des modes propres de l'équation de transport et, dans le cas général, sont perturbées différemment du mode fondamental, la forme du flux neutronique étant la somme pondérée des modes fondamental et harmonique. Une SVP élevée signifie que les modes fondamentaux et premier harmonique sont proches et que la dernière partie a une contribution significative au comportement global du flux. Les systèmes avec un SVP élevé présenteront un grand degré de découplage neutronique, ce qui signifie qu'une perturbation locale se propagera lentement. A l'inverse, une SVP bas signifie que la contribution des harmoniques diminuera rapidement, la perturbation se propagera rapidement dans le cœur et le mode fondamental s'établira plus rapidement.

Les grands cœurs de puissance sont généralement découplés et caractérisés par une séparation des valeurs propres particulièrement élevée, conduisant à des inclinaisons de puissance souvent assez importantes. Le problème est exacerbé dans les conceptions typiques de réacteur à eau légère en raison des hétérogénéités axiales résultant d'un fonctionnement normal, où il est communément appelé « axial offset anomaly » (AOA) [2]. L'AOA peut affecter les marges d'exploitation et oblige ainsi à fonctionner à des niveaux de puissance inférieurs, ce qui présente un problème important pour l'économie du cycle du combustible. Comme dans le cas axial, des études ont montré [3–5] que les grands cœurs présentent des problèmes de bascule de puissance similaires sur le plan azimutal,

surtout s'il est caractérisé par des hétérogénéités ou si un baffle lourd est utilisé, comme dans le cas de la conception du réacteur pressurisé européen (EPR).

Par conséquent, la séparation des valeurs propres et le comportement des harmoniques de flux sont d'un grand intérêt pour la recherche en physique des réacteurs. Malheureusement, il n'est pas possible de les calculer directement, sauf dans les cas où la géométrie respecte certaines symétries [8, 9]. Pour le cas général cependant, une autre approche doit être utilisée pour reconstruire les flux harmoniques. Ceci peut être réalisé avec des modèles cinétiques multipoints. Ils étendent le modèle de cinétique ponctuelle en plusieurs régions, chaque région étant décrite par la cinétique ponctuelle habituelle, plus les contributions de toutes les autres régions. Il fournit de bons résultats concernant le comportement cinétique d'un système, tout en étant relativement peu coûteux par rapport aux approches de modélisation cinétique complète. Le modèle introduit la notion de couplage neutronique, décrivant les interactions régionales qui ont lieu dans le système, ce qui permet ensuite d'étudier son comportement spatial.

Il est donc d'un grand intérêt de développer une méthodologie de conception de maquettes critiques avec une séparation de valeurs propres élevée. De telles conceptions pourront présenter des effets de cinétique spatiale de la même manière que les grands cœurs, ce qui permettra d'étudier ces problèmes de manière à la fois sûre et efficace. La polyvalence et la relative facilité d'utilisation de plusieurs maquettes critiques en font des bancs d'essai idéaux pour une variété d'études et de scénarios. Cependant, leur petite taille signifie qu'ils sont également, généralement, beaucoup plus couplés que les grands cœurs et sont caractérisés par de faibles valeurs de séparation des valeurs propres. Certaines conceptions surmontent cette limitation de manière innovante, comme par exemple la conception du cœur thermique rapide ZEPHYR [10–12], développée par le Commissariat à l'énergie atomique et aux énergies alternatives (CEA). ZEPHYR parvient à augmenter le découplage entre différentes régions du système en incorporant une conception radiale composée de diverses régions fissiles, fertiles et absorbantes de spectres neutroniques très différents.

Le but de la thèse est de développer une méthodologie basée sur la simulation pour analyser le comportement cinétique et de couplage des systèmes nucléaires en utilisant des approches cinétiques multipoints et enfin utiliser cette méthodologie pour produire des conceptions de réacteurs à puissance nulle qui présentent une séparation à valeur propre élevée. La thèse explore l'utilisation de deux modèles cinétiques multipoints - le modèle Transient Fission Matrix [13–19], fonctionnant dans le code Monte Carlo Serpent 2 [20] et le multipoint modèle cinétique de Kobayashi [21–24], fonctionnant dans le système ECCO / ERANOS de codes déterministes [25]. Les avantages, les limites et les applications de chaque modèle sont explorés tout au long d'une partie de la thèse, les modèles étant

d’abord utilisés pour analyser la conception du cœur couplé ZEPHYR. La dépendance de la séparation des valeurs propres sur divers facteurs est ensuite explorée et finalement la méthodologie est appliquée pour proposer des configurations de séparation de valeurs propres élevées dans la maquette critique VENUS-F du SCK CEN [27, 28].

F.3.2 Structure de la thèse

Le chapitre 2 établit un contexte théorique des deux principales approches cinétiques multipoints, en commençant par le modèle d’Avery [29]. Avery a basé son modèle sur un processus intuitif, introduisant le concept de «coefficients de couplage», des grandeurs qui décrivent le couplage neutronique ou la connexion entre différentes régions d’un système, qu’il s’agisse d’un seul cœur ou de plusieurs réacteurs interagissant les uns avec les autres. Ensuite, l’attention se déplace vers le modèle de Kobayashi, où il a vu la nécessité et a ensuite développé un modèle de cinétique multipoint plus rigoureusement dérivé. Une brève comparaison entre les deux approches est incluse, ainsi qu’une section décrivant l’implémentation du modèle de Kobayashi dans le code ERANOS. Enfin, le modèle de Transient Fission Matrix (TFM), récemment développé par A. Laureau, est présenté. Il décrit une approche hybride stochastique-déterministe, basée sur l’utilisation d’informations recueillies à partir d’un calcul de Monte Carlo comme entrée pour des équations cinétiques multipoints déterministes, et offre un regard détaillé sur le comportement cinétique d’un système.

Le chapitre 3 introduit les notions d’harmoniques de flux et de séparation de valeurs propres. Il décrit les comportements liés aux cœurs de séparation de valeurs propres élevées et relie la séparation des valeurs propres aux inclinaisons de puissance, en utilisant un modèle simple à deux régions. On discute de la manière dont les coefficients de couplage peuvent être utilisés pour accéder aux harmoniques du système, grâce à la reconstruction des distributions des sources de fission. Un modèle d’ordre réduit pour relier la séparation des valeurs propres aux caractéristiques intrinsèques du système est également présenté, permettant son estimation ainsi que montrant des façons de l’affecter en modifiant lesdites caractéristiques. Il est montré que la séparation des valeurs propres est largement déterminée par la capacité relative des neutrons à se déplacer dans une géométrie - les systèmes où la surface de migration est petite par rapport à la taille globale de la géométrie, sont largement découplés et caractérisés par des séparations de valeurs propres élevées et vice versa.

Le chapitre 4 décrit comment le modèle de matrice de fission transitoire et le modèle de cinétique multipoint de Kobayashi sont utilisés pour analyser le comportement cinétique de la géométrie du cœur thermique rapide ZEPHYR. Il sert de chapitre d’introduction

à la méthodologie développée au cours de la thèse, décrivant le processus, ainsi que l’interprétation des différents résultats que ces deux implémentations multipoint produisent. Le modèle TFM est utilisé pour analyser un scénario d’insertion de barre de contrôle et discuter des changements résultants dans le comportement de couplage. Certaines des manières dont les deux codes se complètent sont également mentionnées, avec plus de remarques à ce sujet dans le chapitre suivant. Il aborde également la possibilité d’accéder directement à la première harmonique de flux, en tirant parti des symétries du système. Malheureusement, le projet de réacteur ZEPHYR a été reporté par le CEA et cela a nécessité un changement d’orientation de la thèse.

Le chapitre 5 aborde brièvement la nécessité d’élargir le sujet de la thèse, suite au report de ZEPHYR et montre comment la méthodologie d’analyse précédemment développée est utilisée pour étudier comment la séparation des valeurs propres et le comportement de couplage en général sont affectés par la géométrie et les changements de matériaux. Un benchmark a été réalisé, constitué d’un système couplé de deux assemblages combustibles de type REP placés dans l’eau. Les assemblages sont libres de se déplacer le long d’un seul axe géométrique, en commençant l’un à côté de l’autre et en se terminant à 20 cm l’un de l’autre, augmentant le découplage à la fois en raison de la distance elle-même, ainsi que de l’eau entre eux. Les changements de matériaux consistent à changer le type de combustible, à insérer des barres de commande dans diverses parties de la géométrie et à introduire des quantités variables de bore dilué dans le modérateur. De plus, ce chapitre fournit de nombreuses données de comparaison entre TFM et le modèle de Kobayashi. La simplicité de la géométrie permet également une conversation plus approfondie concernant l’utilisation d’harmoniques d’ordre supérieur dans la détection ou la prédiction des inclinaisons de flux.

Le chapitre 6 décrit comment l’expérience acquise jusqu’à présent a été appliquée à la production de configurations de séparation à valeurs propres élevées dans le cœur VENUS-F du SCK CEN, servant de preuve de concept de la méthodologie développée. Cela se fait dans le cadre d’une potentielle collaboration entre le CEA et le SCK CEN et à ce titre, la maquette critique VENUS-F représente un candidat idéal pour tester des configurations de séparation à haute valeur propre et étudier les problèmes de cinétique transitoire liés aux grands coeurs. Après une première analyse du comportement de couplage du cœur en configuration CR0*, un processus d’optimisation progressive est suivi, aboutissant à deux conceptions candidates. Une discussion sur leur faisabilité et leurs marges de sécurité suit, suivie d’une description de leur comportement de couplage et de leur réponse à une perturbation.

Enfin, le chapitre 7 présente les conclusions de la thèse et propose quelques idées de projets futurs.

F.3.3 Conclusions

Le but de cette thèse était de développer une méthodologie d'analyse et de production de configurations de séparation à valeurs propres élevées. Ceci a été réalisé en comprenant les enjeux et les motivations de ce travail, présenté dans le chapitre 1, en rassemblant les connaissances et les approches existantes dans les chapitres 2 et 3, suivi d'un processus en trois parties, lui-même présenté dans la partie travail de la thèse, dans les chapitres 4, 5 et 6.

Analyse du cœur ZEPHYR

La première partie était consacrée au développement d'un processus efficace avec l'objectif d'analyser les conceptions de réacteurs existants à l'aide de modèles cinétiques multipoints. La géométrie de choix est basée sur le concept de cœur thermique rapide développé dans le cadre du programme ZEPHYR du CEA. Le système est d'abord analysé à l'aide du modèle Transient Fission Matrix, implémenté sur le code Serpent 2 Monte Carlo, qui permet actuellement la discrétisation de région unidimensionnelle. Cela permet d'étudier le comportement cinétique du système par son couplage, en indiquant les régions qui affectent le plus le système en termes d'importance et de changement d'importance, via les modes de distribution de source fondamental et de premier ordre. Le calcul des valeurs propres du système permet la détermination de sa séparation des valeurs propres. Dans le même temps, la réponse du système aux perturbations à l'aide de dispositifs de réactivité est étudiée. Pour rester dans les ressources de calcul disponibles pour les schémas de calcul personnalisés, l'approche cinétique multipoint de Kobayashi a été utilisée dans le code déterministe ECCO / ERANOS, pour les géométries XYZ. Cela a permis une analyse tridimensionnelle complète du système, qui permet d'observer le couplage entre des régions choisies arbitrairement. En fonction du schéma de discrétisation, on peut accéder à la fois aux harmoniques azimutales / axiales et radiales, obtenant des informations différentes de ce qui était possible via une analyse unidimensionnelle.

Benchmark d'assemblages combustibles couplés

La deuxième partie s'est concentrée sur l'étude de la façon dont les caractéristiques cinétiques et le comportement de couplage d'un système couplé de base, mais réaliste, se comportent en ce qui concerne les changements de géométrie et de matériau. L'analyse comprenait un changement partiel du matériau combustible du système, le combustible UOX étant remplacé par du MOX moins réactif dans l'un des deux assemblages, après quoi les différences de couplage ont été notées et expliquées. L'assemblage UOX a déter-

miné le comportement global du système, à la fois en raison de sa plus grande réactivité (et donc de sa plus grande production de neutrons, entraînant des coefficients de couplage plus élevés pour la partie la moins réactive du système) et en raison de l' ^{238}U plus élevé contenu, dont l'augmentation de la production de neutrons retardés avait un effet sur les termes de fraction de neutrons retardés par région. Les parties différemment réactives ont également aidé à illustrer comment les distributions de mode source plus élevées répondent aux asymétries dans le système. L'introduction partielle et complète de barres de commande dans l'un des deux ensembles a servi à illustrer comment la distribution de la source est affectée par les dispositifs de réactivité et a aidé à établir davantage un modèle de décalage du zéro du vecteur propre de premier ordre vers les parties du système qui affichaient la plus haute importance, indiquant effectivement que le point d'intersection en abscisse suit le centre d'importance du système. Enfin, l'effet de la dilution du bore dans le modérateur a été étudié, trouvant que le bore ajouté augmente la séparation des valeurs propres de manière linéaire, en raison de l'augmentation globale de la section efficace d'absorption du système. De plus, il a été montré que pour des géométries simples symétriques par rapport à l'axe de discréétisation utilisé pour les calculs de séparation des valeurs propres, ce dernier peut également être réalisé en calculant directement la premier harmonique de flux dans ERANOS. Le travail effectué dans ce chapitre a conduit à la production d'un benchmark qui comprend et compare deux méthodes différentes d'analyse cinétique multipoint et peut être utilisé comme base pour la validation de futurs schémas de calcul pertinents.

Produire des configurations de séparation à valeurs propres élevées dans le cœur VENUS-F

La troisième partie, prenant en compte l'analyse du comportement de séparation des valeurs propres donnée dans le chapitre 3, visait à appliquer les connaissances et l'expérience acquises jusqu'à présent, au développement de configurations de séparation à valeurs propres élevées dans un système existant. Dans la foulée de la décision du CEA de reporter le réacteur ZEPHYR, une collaboration potentielle entre le CEA et le SCK CEN a fait de la maquette critique VENUS-F un choix naturel pour démontrer les effets discutés. Il s'agit d'une installation polyvalente qui peut accueillir un certain nombre de configurations et des configurations de séparation à valeur propre élevée peuvent être utilisées pour atteindre une partie des objectifs du programme expérimental. Cette application réaliste était une partie importante du processus de thèse et a été utilisée comme un test de la méthodologie développée ici. En donnant la priorité à la taille du cœur actif et en commençant par 96 assemblages combustibles, le problème a été initialement traité comme une approche à géométrie fixe, après quoi des changements dans les matériaux du

système ont été utilisés pour affecter la séparation des valeurs propres. L'objectif principal restait d'augmenter la taille apparente du cœur, par rapport à la surface de migration. Ainsi, un changement vers un cœur plus thermique a été envisagé. Alors que les meilleurs résultats ont été obtenus avec l'utilisation d'un modérateur de polyéthylène riche en hydrogène, l'excès de réactivité généré à la suite du processus de thermalisation a nécessité une réduction de la taille du cœur, pour aider à garder la réactivité sous contrôle. En fin de compte, le processus a réussi à produire des configurations avec une séparation des valeurs propres plus élevée que la conception originale du cœur couplé ZEPHYR. De plus, la conception du candidat principal a été perturbée par une barre pilote et une barre de contrôle, ce dernier scénario générant une inclinaison de flux significative, indiquant que la géométrie peut être utilisée avec succès pour présenter les effets spatiaux de grands coeurs.

Bibliography

- [1] Imre Pázsit and Victor Dykin. The role of the eigenvalue separation in reactor dynamics and neutron noise theory. *Journal of Nuclear Science and Technology*, 55(5):484–495, 2018.
- [2] P.L. Frattini, J. Blok, S. Chauffriat, Jerzy Sawicki, and J. Riddle. Axial offset anomaly: Coupling PWR primary chemistry with core design. *Nuclear Energy*, 40:123–135, 04 2001.
- [3] A. Sargeni, K.W. Burn, and G. B. Bruna. Coupling effects in large reactor cores: The impact of heavy and conventional reflectors on power distribution perturbations. *Proc. PHYSOR 2014, Kyoto, Japan*, 2014.
- [4] A. Sargeni, K.W. Burn, and G.B. Bruna. The impact of heavy reflectors on power distribution perturbations in large PWR reactor cores. *Annals of Nuclear Energy*, 94:566–575, 2016.
- [5] Federico Rocchi, Roberto Pergalli, Franck Boreicha, Antonio Sargeni, and Giovanni Bruna. Azimuthal power disequilibrium estimate through control rod worth measurement for GEN III+ PWRs. *Proc. International Congress on Advances in Nuclear Power Plants - ICAPP 2015, Nice, France*, 2015.
- [6] Christophe Demazière. Core sim: A multi-purpose neutronic tool for research and education. *Annals of Nuclear Energy*, 38(12):2698–2718, 2011.
- [7] Nicolò Abrate, Giovanni Bruna, Sandra Dulla, and Piero Ravetto. Assessment of numerical methods for the evaluation of higher-order harmonics in diffusion theory. *Annals of Nuclear Energy*, 128:455–470, 2019.
- [8] Jean Tommasi, Maxence Maillot, and Gérald Rimpault. Calculation of higher-order fluxes in symmetric cores—I: Theory. *Nuclear Science and Engineering*, 184(2):174–189, 2016.

- [9] Maxence Maillot, Jean Tommasi, and Gérald Rimpault. Calculation of higher-order fluxes in symmetric cores—II: Implementation. *Nuclear Science and Engineering*, 184(2):190–207, 2016.
- [10] P. Blaise and et al. Experimental R&D innovation for Gen-II, III & IV neutronics studies in zprs: a path to the future ZEPHYR facility in Cadarache. *Proc. Int. Conf. IGORR-RRFM 2016, Berlin, Germany*, 2016.
- [11] P. Ros, P. Blaise, P. Leconte, H. Doger de Spéville, and M. Maillot. Fast-thermal coupled cores in ZPRs: a demonstration of feasibility and pertinence for the ZEPHYR project. *Ann. Nucl. Energy*, 110:290–305, 2017.
- [12] P. Blaise, B. Minot-Taioglou, P. Fougeras, M. Maillot, K. Routsonis, C. de Saint-Jean, and et al. Scientific needs for a new generation critical facility at CEA: the ZEPHYR (zero power experimental physics reactor) ZPR. *Proc. IGORR 19th - 19th Meeting of the International Group on Research Reactors, RRFM (European Research Reactor Conference), Mar 2019, Amman, Jordan*, 2019.
- [13] A. Laureau. *Développement de modèles neutroniques pour le couplage thermohydraulique du MSFR et le calcul de paramètres cinétiques effectifs*. PhD thesis, Université Grenoble Alpes, 2015.
- [14] A. Laureau, L. Buiron, and B. Fontaine. Local correlated sampling Monte Carlo calculations in the TFM neutronics approach for spatial and point kinetics applications. *EPJ Nuclear Sci. Technol*, 3, 2017.
- [15] A. Laureau, L. Buiron, and B. Fontaine. Towards spatial kinetics in a low void effect sodium fast reactor: core analysis and validation of the TFM neutronic approach. *EPJ Nuclear Sci. Technol*, 3, 2017.
- [16] A. Laureau, L. Buiron, B. Fontaine, and V. Pascal. Fission matrix interpolation for the TFM approach based on a local correlated sampling technique for fast spectrum heterogeneous reactors. *Proc. International Conference on Mathematics and Computational Methods Applied to Nuclear Science & Engineering (M&C 2017), Jeju, South Korea*, 2017.
- [17] A. Laureau, M. Aufiero, P.R. Rubiolo, E. Merle-Lucotte, and D. Heuer. Transient Fission Matrix: Kinetic calculation and kinetic parameters β_{eff} and λ_{eff} calculation. *Ann. Nucl. Energy*, 85:1035–1044, 2015.
- [18] A. Laureau, D. Heuer, E. Merle-Lucotte, P.R. Rubiolo, M. Allibert, and M. Aufiero. Transient coupled calculations of the molten salt fast reactor using the Transient Fission Matrix approach. *Nuclear Engineering and Design*, 316:112–124, 2017.

- [19] P. Blaise, A. Laureau, P. Ros, P. Leconte, and K. Routsonis. Transient Fission Matrix approach for assessing complex kinetics behavior in the ZEPHYR ZPR coupled core configurations. *Ann. Nucl. Energy*, 128:390–397, 2018.
- [20] J. Leppänen, M. Pusa, T. Viitanen, V. Valtavirta, and T. Kaltiaisenaho. The Serpent Monte Carlo code: Status, development and applications in 2013. *Annals of Nuclear Energy*, 82:142 – 150, 2015.
- [21] K. Kobayashi. Rigorous derivation of nodal equations for coupled reactors. *Annals of Nuclear Energy*, 18(1):13–18, 1991.
- [22] K. Kobayashi. Rigorous derivation of static and kinetic nodal equations for coupled reactors using transport equation. *Journal of Nuclear Science and Technology*, 28:5:389–398, 1992.
- [23] K. Kobayashi. Rigorous derivation of multi-point reactor kinetics equations with explicit dependence on perturbation. *Journal of Nuclear Science and Technology*, 29:110–120, 1992.
- [24] K. Kobayashi. A relation of the coupling coefficient to the eigenvalue separation in the coupled reactors theory. *Ann. Nucl. Energy*, 25:198–201, 1998.
- [25] G. Rimpault, D. Plisson, J. Tommasi, R. Jacqmin, and J.M. Rieunier. The ER-ANOS code and data system for fast reactor neutronic analyses. *PHYSOR 2002 International Conference, Seoul, South Korea*, 2002.
- [26] K. Routsonis, P. Blaise, and J. Tommasi. Numerical benchmark of strongly to loosely coupled assemblies using the Transient Fission Matrix method. *EPJ Web of Conferences*, 247:06038, 01 2021.
- [27] A. Krása, P. Baeten, L. Fiorito, J. Heyse, A. Kochetkov, S. Kopecky, N. Messaoudi, C. Paradela, P. Schillebeeckx, A. Stankovskiy, G. van den Eynde, G. Vittiglio, , and J. Wagemans. The VENUS-F reactor for nuclear data validation. *Reactor Dosimetry: 16th International Symposium, ASTM STP 1608, ASTM International*, pages 286 – 295, 2018.
- [28] VENUS-F: an accelerator driven system prototype. <https://science.sckcen.be/en/Facilities/VENUS>.
- [29] R. Avery. Theory of coupled reactors. *Proc. 2nd Int. Conf. Peaceful Uses At. Energy, 1958, New York, United States*, 1958.

- [30] Robert Avery. Coupled fast-thermal power breeder. *Nuclear Science and Engineering*, 3(2):129–144, 1958.
- [31] R. Avery, C. Branyan, G. S. Brunson, C. Cohn, G. F. Fischer, H. H. Hummel, W. Kato, F. Kirn, D. Meneghetti, F. W. Thalgott, and B. J. Toppel. Coupled fast-thermal power breeder critical experiment, 1958.
- [32] Keisuke Kobayashi. Physical meaning of kinetics parameter “lifetime” used in the new multi-point reactor kinetics equations derived using Green’s function. *Annals of Nuclear Energy*, 23(10):827–841, 1996.
- [33] Jean Tommasi and Giuseppe Palmiotti. Verification of iterative matrix solutions for multipoint kinetics equations. *Annals of Nuclear Energy*, 124:357–371, 2019.
- [34] G. Palmiotti, J.M. Rieunier, C. Gho, and M. Salvatores. BISTRO optimized two dimensional Sn transport code. *Topical Meeting on Advances in Reactor Physics, Mathematics and Computation, Paris, France, April 1987*, 1987.
- [35] G. Valocchi, J. Tommasi, and P. Ravetto. Reduced order models in reactor kinetics: A comparison between point kinetics and multipoint kinetics. *Annals of Nuclear Energy*, 147:107702, 2020.
- [36] G. Palmiotti, M. Salvatores, S. Sen, C. Rabiti, M. Aufiero, and J. Tommasi. Investigating decoupling effects in CFV type of reactors using avery s coupled reactor theory. *PHYSOR 2018: Reactor Physics paving the way towards more efficient systems, Cancun, Mexico*, 2018.
- [37] Santosh K. Pradhan, K. Obaidurrahman, Kannan N. Iyer, and Avinash J. Gaikwad. Development, validation and application of multi-point kinetics model in RE-LAP5 for analysis of asymmetric nuclear transients. *Nuclear Engineering and Design*, 300:506–516, 2016.
- [38] Sean Carney, Forrest Brown, Brian Kiedrowski, and William Martin. Theory and applications of the fission matrix method for continuous-energy Monte Carlo. *Annals of Nuclear Energy*, 73:423–431, 2014.
- [39] Forrest Brown, Sean Carney, Brian Kiedrowski, and William Martin. Fission matrix capability for MCNP Monte Carlo. *Transactions of the American Nuclear Society*, 107:03502, 06 2014.
- [40] G. Kępisty and J. Cetnar. Dominance ratio evolution in large thermal reactors. *Annals of Nuclear Energy*, 102:85–90, 2017.

- [41] E. Dumonteil and T. Courau. Dominance ratio assessment and Monte Carlo criticality simulations: Dealing with high dominance ratio systems. *Nuclear Technology*, 172:120 – 131, 2010.
- [42] M. Maillot, J. Tommasi, and G. Rimpault. A search for theories enabling analyses of spatial effects in highly coupled SFR cores. *PHYSOR 2016: Unifying Theory and Experiments in the 21st Century, Sun Valley, United States*, 2016.
- [43] Takanori KITADA and Toshikazu TAKEDA. Evaluation of eigenvalue separation by the Monte Carlo method. *Journal of Nuclear Science and Technology*, 39(2):129–137, 2002.
- [44] Gérald Rimpault, L. Buiron, Bruno Fontaine, Pierre Sciora, and J. Tommasi. Flux harmonics in large SFR cores in relation with core characteristics such as power peaks. *Proc. International Conference on Mathematics and Computational Methods Applied to Nuclear Science & Engineering (M&C 2013), Sun Valley, Idaho, United States, 2013*, 2:985–995, 2013.
- [45] Om Pal Singh and K. Obaidurrahman. Investigations on neutronic decoupling phenomenon in large nuclear reactors. *Energy Procedia*, 7:384 – 390, 2011. Asian Nuclear Prospects 2010.
- [46] G. Palmiotti and M. Salvatores. Use of integral experiments in the assessment of large Liquid-Metal Fast Breeder Reactor Basic Design parameters. *Nuclear Science and Engineering*, 87(3):333–348, 1984.
- [47] Yoshiki KATO, Toshihisa YAMAMOTO, Takanori Kitada, Toshikazu TAKEDA, Kengo HASHIMOTO, Seiji SHIROYA, Hironobu Unesaki, and Otohiko AIZAWA. Analysis of first-harmonic eigenvalue separation experiments on KUCA coupled-core. *Journal of Nuclear Science and Technology - J NUCL SCI TECHNOL*, 35:216–225, 03 1998.
- [48] S.B. Brumbach, R.W. Goin, and S.G. Carpenter. Studies of spatial decoupling in heterogeneous LMFBR critical assemblies. *Proc. ANS Topical Meeting on Reactor Physics and Shielding, 17-19 September 1984, Chicago*, 1984.
- [49] Kenji NISHIHARA, Keisuke KOBAYASHI, and Nobuo OHTANI. Numerical validation of the theory of coupled reactors for the Heavy Water Critical Assembly DCA. *Journal of Nuclear Science and Technology*, 36(3):265–272, 1999.
- [50] Keisuke Kobayashi. A relation of the coupling coefficient to the eigenvalue separation in the coupled reactors theory. *Annals of Nuclear Energy*, 25(4):189–201, 1998.

- [51] Sandra Dulla, Piero Ravetto, and Paolo Saracco. Some new thoughts on the multipoint method for reactor physics applications. *Proc. International Conference on Mathematics and Computational Methods Applied to Nuclear Science & Engineering (M&C 2017), Jeju, South Korea*, 2017.
- [52] G. Chiba. Nuclear data-induced uncertainty calculation for fast reactor eigenvalue separation. In *Proc. NDS2008: 2008 annual symposium on nuclear data, Tokai, Ibaraki (Japan), 20-21 Nov 2008*, 2009.
- [53] Avinash J. Obaidurrahman, K. and Gaikwad. Investigations on neutronic coupling aspects of thorium fuelled AHWR. *Proceedings of the international thorium energy conference: gateway to thorium energy, Mumbai, India*, 2015.
- [54] D. C. Wade and R. A. Rydin. An experimentally measurable relationship between asymptotic flux tilts and eigenvalue separation. *Dynamics of Nuclear Systems*, 1972.
- [55] E. Salvatores and T. Blaise. Internal communication and seminar, 2016.
- [56] Patrick Blaise, Marat Margulis, L. Buiron, G. Prulhière, Bruno Fontaine, and Erez Gilad. Representativity studies of ZEPHYR fast/thermal coupled cores for SFR-like reactivity effects during core meltdown. *Proc. International Congress on Advances in Nuclear Power Plants - ICAPP 2017, Fukui/Kyoto, Japan*, 04 2017.
- [57] M. Margulis, P. Blaise, L. Buiron, and E. Gilad. ZPR core representativity of SFR reactivity effects during core meltdown. *Proc. ANS Winter Meeting, Oct 2017, Washington, United States*, 04 2017.
- [58] Marat Margulis, Patrick Blaise, and Erez Gilad. Modeling representative Gen-IV molten fuel reactivity effects in the ZEPHYR ZPR - LFR analysis. *International Journal of Energy Research*, 43(2):829–843, 2019.
- [59] J. R. Lamarsh and A. J Baratta. *Introduction to nuclear engineering*. Prentice Hall, Upper Saddle River, N.J 07458, 2001.
- [60] Kazuki Ishitani, Yoshihiro Yamane, Akira Uritani, Testuo Iguchi, and Seiji Shiroya. Measurement of eigenvalue separation by using position sensitive proportional counter. *Annals of Nuclear Energy*, 25(10):721 – 732, 1998.
- [61] Masaki ANDOH, Tsuyoshi MISAWA, Kojiro NISHINA, and Seiji SHIROYA. Measurement of flux tilt and eigenvalue separation in axially decoupled core. *Journal of Nuclear Science and Technology*, 34(5):445–453, 1997.

- [62] Philippe Fougeras, Jean-Pascal Hudelot, Muriel Antony, Frédéric Mellier, Patrick Blaise, Stephane Cathalau, and Nicolas Thiollay. EOLE, MINERVE and MASURCA facilities and their associated neutron experimental programs. *In Proc. ICONE 13 - 13th International Conference on Nuclear Engineering, Beijing, China, 05 2005.*
- [63] P. Ros, P. Leconte, and P. Blaise. Integral cross sections of fission products in fast reactors. re-interpretation of the ERMINE V experiment : Interest of fast-thermal coupled cores. *Proc. Int. Conf ND2016, Bruges, Belgium, 2016.*
- [64] Jan Dufek and Gustaf Holst. Correlation of errors in the Monte Carlo fission source and the fission matrix fundamental-mode eigenvector. *Annals of Nuclear Energy*, 94:415–421, 2016.
- [65] Abdelhamid Dokhane, Hakim Ferroukhi, and Andreas Pautz. On out-of-phase higher mode oscillations with rotation and oscillation of symmetry line using an advanced integral stability methodology. *Annals of Nuclear Energy*, 67:21–30, 05 2014.
- [66] K. Routsonis, P. Blaise, J. Tommasi, and G. Valocchi. Transient Fission Matrix analysis of rod drop experiments in coupled cores for addressing high dominance ratio configurations. *Proc. International Conference on Mathematics and Computational Methods Applied to Nuclear Science & Engineering (M&C 2019), Portland, OR, United States, 2019.*
- [67] D. Schneider, F. Dolci, F. Gabriel, J.-M. Palau, M. Guillo, and et al. APOLLO3® CEA/DEN deterministic multi-purpose code for reactor physics analysis. *Proc. PHYSOR 2016 – Unifying Theory and Experiments in the 21st Century, Sun Valley, United States, 2016.*
- [68] Seiji Shiroya. Research on reactor physics using the Kyoto University Critical Assembly (KUCA). *Proc. Seminar on reactor physics experiments with critical assemblies; Kumatori, Osaka (Japan); 26 Nov 1987, 1988.*
- [69] KUCA - Kyoto University Critical Assembly. <https://www.rri.kyoto-u.ac.jp/en/facilities/ca>.
- [70] N. Horelik, B. Herman, B. Forget, and K. Smith. Benchmark for evaluation and validation of reactor simulations (BEAVRS), v1.0.1. *Proc. International Conference on Mathematics and Computational Methods Applied to Nuclear Science & Engineering (M&C 2013), Sun Valley, Idaho, United States, 2013, 2013.*
- [71] Stephane Cathalau, Philippe Fougeras, Patrick Blaise, Nicolas Thiollay, Alain Santamarina, Toru Yamamoto, Y. Iwata, and R. Kanda. Full MOX recycling in ALWR

- : Lessons drawn through the MISTRAL program. *PHYSOR 2002 International Conference, Seoul, South Korea*, 10 2002.
- [72] Y. Nagaya and K. Kobayashi. Solution of 1-D multi-group time-dependent diffusion equations using the coupled reactors theory. *Annals of Nuclear Energy*, 22(7):421 – 440, 1995.
 - [73] H. Parhizkari, M. Aghaie, A. Zolfaghari, and A. Minuchehr. Analysis of control rod drop accident in PWRs with multipoint kinetics method. *Annals of Nuclear Energy*, 88:194–203, 2016.
 - [74] H. Jasak, A. Jemcov, and Ž. Tukovíc. OpenFOAM: A C++ library for complex physics simulations. *International Workshop on Coupled Methods in Numerical Dynamics, IUC, Dubrovnik, Croatia*, 2007.